The Pennsylvania State University

The Graduate School

Department of Mechanical and Nuclear Engineering

HYDROGEN DISTRIBUTION IN ZIRCALOY UNDER A TEMPERATURE GRADIENT: MODELING, SIMULATION AND EXPERIMENTS

A Thesis in

Nuclear Engineering

by

Olivier F. Courty

© 2013 Olivier F. Courty

Submitted in Partial Fulfillment
of the Requirements
for the Degree of

Master of Science

August 2013

The thesis of Olivier F. Courty was reviewed and approved* by the following:

Arthur T. Motta
Professor of Mechanical and Nuclear Engineering
Professor of Materials Science and Engineering
Chair of Nuclear Engineering
Thesis Advisor

Kostadin N. Ivanov
Distinguished Professor of Nuclear Engineering

Maria N. Avramova
Assistant Professor of Nuclear Engineering

Karen A.Thole
Department Head of Mechanical and Nuclear Engineering
Professor of Mechanical Engineering

*Signatures are on file in the Graduate School

ABSTRACT

As a result of corrosion during normal operation in nuclear reactors, hydrogen can enter the zirconium fuel cladding and precipitate as brittle hydride particles, which can severely degrade the cladding ductility. According to previous observations, the distribution of the hydrides in the cladding is not homogeneous and responds to temperature and stress gradients. Due to the heterogeneity of the temperature distribution, hydrides tend to accumulate in the colder areas. This accumulation creates local spots of weak cladding that can favor crack initiation. Therefore, the estimation of the average concentration of the hydrides in the cladding is not sufficient to accurately estimate the risk of cladding failure. An estimation of the local hydride distribution is necessary to help predict future and this is the subject of the current work.

The hydride distribution is governed by three competing phenomena. Hydrogen in solid solution diffuses under a concentration gradient due to Fick's law and under a temperature gradient due to the Soret effect. Finally, precipitation of hydrides occurs once the hydrogen solubility limit is reached. This precipitation has its own kinetics. All of these phenomena are strongly temperature dependent. The complex interplay of these separate phenomena can explain why the hydrogen and hydride distribution depends on temperature. In the current study, different models describing these phenomena have been developed in order to study the behavior of hydrogen in the cladding.

Due to the complexity of the modeling, it is usually not possible to find an analytical solution for the hydrogen and hydride distribution for nuclear fuel rod geometries, and so numerical solutions were obtained from the implementation of the model in computer. A 1-D difference code has been created to compute hydrogen distribution in simple geometries. A more detailed model was then implemented in the 3D fuel performance code BISON in order to calculate the hydrogen distribution for more sophisticated geometries, such as a nuclear fuel rod.

The results shown by these simulations explain the formation of specific radial distribution of hydrides. The simulations predict that before precipitation occurs, hydrogen tends to accumulate in the colder spots due to the Soret effect. Once the solubility limit is reached, hydrogen precipitates and forms a rim close to the outer edge of the cladding. This is due to the competition between precipitation and diffusion. The simulation also show an axial transfer of hydrogen from the top of the rod, where the oxidation rate is high, to the bottom of the rod, where the hydrogen will precipitate. In the future, the implemented model will be able to provide additional information on the azimuthal hydrogen distribution.

The model used to describe hydrogen behavior is semi-empirical. In particular, two empirical constants have to be determined that do not have consistent values in the literature. Therefore, two experiments were designed and performed in order to measure these constants. The first constant is the heat of transport Q*, which determined the Soret effect. This was measured by applying a gradient to a Zircaloy plate that was previously charged with hydrogen. The measured value for Q* was 58.5 kJ/mol and is higher than previous measurement. The results confirm the large variability of the measurement of the heat of transport. The second constant is the rate of precipitation α^2 from Marino, which describes the rate at which the supersaturated hydrogen in solid solution precipitates into zirconium hydrides. This rate is measured through an in situ X-Ray diffraction experiment in transmission, at the Advanced Photon Source of the Argonne National Laboratory. The results are between 0.013 $s^{-1/2}$ and 0.034 $s^{-1/2}$ and are in the same range of values as found in previous experiments. However, no clear trend of temperature dependence has been identified.

The current work involves preliminary approach to calculate an estimation of the thickness of the hydride rim. The simulations directly based on the model predict a very high concentration in the rim that is not seen experimentally. However, once a limit to the concentration of hydrides was set, the simulations provide rim thickness close to 100 microns,

which is consistent with experimental observation. The work also proposes suggestions to improve the model governing hydrogen and hydrides distribution in the future.

TABLE OF CONTENTS

LIST OF FIGURES viii

LIST OF TABLES xiii

ACKNOWLEDGEMENTS xv

Chapter 1: Introduction and background 1

1.1 Zirconium Alloys for Nuclear Fuel Cladding 1
1.2 Origin of hydrogen in the LWR fuel cladding 3
1.2.1 Reactions producing hydrogen in the cladding in LWR 3
1.2.2 Kinetics of the cladding oxidation 3
1.2.3 Empirical Hydrogen Pick-up in LWR cladding 6
1.3 Hydrogen flux entering the cladding 7
1.3.1 Shape of hydrogen overall concentration 8
1.3.2 Hydrogen flux at the coolant/cladding interface 9
1.4 Redistribution of hydrogen in the cladding 10
1.4.1 Consequence of hydrides on Zircaloy cladding properties 11
1.4.2 Previous observations and measurements of hydride formation in Zr alloys 12
1.4.3 Hydrogen diffusion in Zircaloy 19
1.4.4 Hydride precipitation and dissolution (TSS laws) 24
1.4.5 Kinetics of precipitation 27
1.4.6 Summary of the balance equations governing hydrogen concentration 30
1.5 Motivation of the study and thesis outline 33

Chapter 2: Modeling and simulation of hydrogen distribution 35

2.1 Creation of “HydruLab”: a 1D Finite difference simulation code on Matlab 36
2.1.1 Derivation of the hydrogen balance equations for HydruLab 36
2.1.2 Structure of the code HydruLab 39
2.2 Implementation of the model in the 3D fuel performance code BISON 40
2.2.1 BISON and MOOSE overview 41
2.2.2 Derivation of the equations according to Galerkin finite element theory 42
2.2.3 Hydrogen model source files for BISON 52
2.3 Calculation of the temperature distribution based on DeCART, CTF and BISON 53
2.3.1 Overview of the COBRA-TF/DeCART coupling 54
2.3.2 Definition of the boundary conditions for BISON 55
2.3.3 Calculation of the temperature distribution with BISON 55
2.4 Benchmark of HydruLab and BISON 56
2.4.1 Benchmark 1: Diffusion equilibrium without precipitation 56
2.4.2 Benchmark 2: Precipitation model 62
2.5 BISON results on a small piece of cladding 65

2.5.1 Geometry of the piece of cladding....65
2.5.2 Case 1: Hydrogen distribution under temperature gradient before precipitation....66
2.5.3 Case 2: Formation of the rim....69
2.5.4 Case 3: Simulation of the consequences of a reactor shutdown....75
2.5.5 Conclusions simulations of hydrogen behavior in a piece of cladding....81
2.5.6 Simulation with a limitation of the amount of hydrogen in hydrides....82
2.6 Results of 5-pellet rod simulation using BISON....85
2.6.1 Geometry and boundary conditions....85
2.6.2 Hydrogen distribution in hot 5 pellets rod....88
2.6.3 Hydrogen distribution in a cold 5 pellets rod....92
2.6.4 Full rod results with BISON....95
2.7 Conclusions on Chapter 2 results....98

Chapter 3: Experimental work on the model....99

3.1 Measurement of the heat of transport Q*....99
3.1.1 Scattered previous measurements of the heat of transport....99
3.1.2 Experimental design for measurement of Q*....102
3.1.3 Sample preparation....109
3.1.4 Experimental procedure....109
3.1.5 Results of the heat of transport experiment....114
3.1.6 Conclusion of the results of the Q* measurement....116
3.2 Measurement of the rate of precipitation....119
3.2.1 A significant lack of measurement....119
3.2.2 Experimental technique....119
3.2.3 Sample preparation....125
3.2.4 Experimental procedure....126
3.2.5 Results....130
3.2.6 Conclusion of the results....132

Chapter 4: Preliminary work for further investigations....135

4.1 Analytical estimation of the rim....135
4.2 Physical parameters affecting the TSSp and TSSd....136
4.3 Ideas and concerns regarding the hydrogen model....146
4.4 Improvement of the diffusion experiments....146
4.5 Next measurement of the precipitation parameter....147

Chapter 5: Conclusions....148

References....151

Appendices....156

Appendix A: HydruLab code simulating hydrogen behavior in Zircaloy plate....156
Appendix B: BISON Kernels source code....161
Appendix C: BISON Auxiliary Kernel source code....165
Appendix D: Hydrogen picked up flux BISON boundary condition....166

Appendix E: Input files for the BISON piece of cladding runs 168
Appendix F: Rough estimation of the axial diffusion flux through a full fuel rod 176
Appendix G: Derivation of the analytical rim calculation 179

LIST OF FIGURES

Figure 1-1: Growth of the cladding oxide layer according to oxidation kinetics models in Table 1-1 6

Figure 1-2: Evolution of the average cladding hydrogen concentration with time at 320°C, using kinetics models of Table 1-1 9

Figure 1-3: Hydride distribution and morphology in HBR rod F07 cladding near b650 mm above midplane (740-wppm H)[17].....12

Figure 1-4: Optical micrographs of the hydride distribution and oxide layers on Zircaloy-4 irradiated for 6 cycles in PWR [18] 13

Figure 1-5: Increase of the oxide layer thickness with elevation in a PWR reactor (burnup close to 70 MWd/kgU) [19] 14

Figure 1-6: Azimuthal variations of the hydride distribution 15

Figure 1-7: Axial macrograph of a fuel rod 16

Figure 1-8: Cladding temperature profile (K) around the inter-pellet gap as calculated with BISON.....16

Figure 1-9: Hydride distribution at the inter-pellet gap cladding compared to mid-pellet cladding [21] 17

Figure 1-10: Hydride blister due to oxide spallation[22].....18

Figure 1-11: Main measurement of hydrogen diffusion coefficient in Zircaloy-4 [24].....20

Figure 1-12: Illustration of the precipitation hysteresis [34] 26

Figure 1-13: Hydrogen boundary condition schematic.....27

Figure 1-14: Kammenzind measurement of the rate of precipitation as a function of temperature.....29

Figure 2-1: Structure of the implementation of the hydrogen model in HydruLab 40

Figure 2-2: Coupling between CTF, DeCART and BISON 53

Figure 2-3: Mesh of the plate used for BISON calculation 56

Figure 2-4: BISON temperature profile using boundary conditions of 600°C and 700°C for benchmark 1 58

Figure 2-5: Comparison between the steady-state distribution of hydrogen in solid solution exposed to a linear temperature gradient of 600°C-700°C calculated by BISON and HydruLab and the analytical solution.....59

Figure 2-6: 3D view of the hydrogen profile calculated with BISON using a 600°C-700°C linear temperature gradient 60

Figure 2-7: Hydrogen distribution after 8 hours calculated by HydruLab and BISON when submitted to a 700°C-600°C temperature gradient.....61

Figure 2-8: Comparison of the hydride concentration profile calculated with BISON and the analytical solution, in the case of pure precipitation of hydrogen.....64

Figure 2-9: Geometry and mesh of the piece of cladding.....66

Figure 2-10: Temperature gradient applied to the plate, corresponding to a typical cladding gradient (330°C-360° for 660 microns).....67

Figure 2-11: Hydrogen (solid solution) profile after 1 year under a typical cladding radial temperature gradient (320°-340°C for 660 microns) 68

Figure 2-12: Hydrogen in solid solution vs. r, after the TSS has been reached at the outer edge of the cladding 71

Figure 2-13: Hydrogen in hydrides vs. r, after the TSS has been reached at the outer edge of the cladding.....71

Figure 2-14: Location of the nodes of interest for case 2 72

Figure 2-15: Hydrogen in solid solution vs. time during the formation of the hydride rim 73

Figure 2-16: Hydrogen in hydrides vs. time during the formation of the hydride rim 74

Figure 2-17: Reactor shutdown cladding temperature evolution with time.....76

Figure 2-18: Evolution of the cladding temperature difference in the cladding during a 24 hour reactor shutdown.....77

Figure 2-19: Nodes tracked in the temporal analysis of case 3.....79

Figure 2-20: Temperature vs. time for case 3 79

Figure 2-21: Hydrogen in solid solution vs. time for case 3.....80

Figure 2-22: Hydrogen in hydride vs. time for case 3 80

Figure 2-23: Hydride profile after 6 months of precipitation with a limit of 1000wt.ppm of hydrogen in hydrides, calculated with HydruLab 83

Figure 2-24: Hydrogen (solid solution) profile after 6 months of precipitation with a limit of 1000wt.ppm of hydrogen in hydrides, calculated with HydruLab 84

Figure 2-25: Evolution of the thickness of the rim with time during 6 months of precipitation with a limit of 1000wt.ppm of hydrogen in hydrides, calculated with HydruLab 84

Figure 2-26: Five pellet geometry for BISON simulation 87

Figure 2-27: Axial temperature profile for the hot 5 pellets mesh at the outer edge of the cladding, after 4 years 89

Figure 2-28: Radial temperature profile for the hot 5 pellets mesh at z=2.75 cm, after 4 years 89

Figure 2-29: Evolution of the cladding temperature for the hot 5 pellets at z=3.0 cm and r=4.15mm and 4.2mm (in green, inner edge), and r=4.67mm and 4.72mm (blue, outer radius), between 0 years and 4 years 90

Figure 2-30: Axial hydrogen profile for the hot 5 pellet mesh at the outer edge of the cladding, after 4 years 91

Figure 2-31: Radial hydrogen profile for the hot 5 pellets mesh at z=2cm, after 4 years 91

Figure 2-32: Axial temperature profile for the 5 pellets mesh at the coldest spot of the fuel at the outer edge of the cladding, after 4 years 92

Figure 2-33: Radial temperature profile for the hot 5 pellets mesh at z=3cm, after 4 years 93

Figure 2-34: Radial hydrogen profile for the cold 5 pellets mesh at z=, after 4 years 94

Figure 2-35: Radial hydride profile for the cold 5 pellets mesh at z=, after 4 years 94

Figure 2-36: Hydrogen profile in a 360-pellets fuel cladding after 1 hour, with an initial homogeneous concentration of 60 wt.ppm 96

Figure 2-37: Hydrogen profile in a 360-pellets fuel cladding after 1 day, with an initial homogeneous concentration of 60 wt.ppm 97

Figure 2-38: Evolution of the difference average concentration between high (z=3m) and low (z=1m) elevations 97

Figure 3-1: Measurement of Q* with respect to the temperature 101

Figure 3-2: Heat of transport measured by Kammenzind 102

Figure 3-3: 3-D View of the 304 Stainless Steel holders and the Zircaloy-4 plate sample 103

Figure 3-4: Heaters, holders and sample in the heat of transport experiment.....104

Figure 3-5: Temperature controller front and back views 105

Figure 3-6: Schematic of the temperature control for the diffusion experiment.....106

Figure 3-7: Air flow regulator.....107

Figure 3-8: Connection between the air tube and the holder 107

Figure 3-9: Design of the insulation of the experiment 108

Figure 3-10: Thermocouples on the sample.....108

Figure 3-11: Sample damaged after 750°-650° experiment.....109

Figure 3-12: Temperature and hydrogen steady state profile under 650°-550° gradient.....110

Figure 3-13: Hydrogen profile before starting 660°C-560°C gradient experiment 111

Figure 3-14: Kinetics of the concentration profile (one line per 10 hours) with a 650°-550°C gradient 112

Figure 3-15: Difference with steady state (one line per 10 hours) with a 650°-550°C gradient.....112

Figure 3-16: Sample after 660°C-560°C experiment.....113

Figure 3-17: Temperature profile for diffusion experiment.....115

Figure 3-18: Result of the diffusion experiment.....116

Figure 3-19: Comparison of experimental results with Kammenzind's data [24].....117

Figure 3-20: Heat of transport Q* measured in the literature as a function of the temperature gradient 118

Figure 3-21: Illustration of Bragg's law. 120

Figure 3-22: Advanced Photon Source synchrotron and position of the beamline used in our experiment. 121

Figure 3-23: Schematic representation of beamline 1-ID experimental set-up. 124

Figure 3-24: Picture of the experimental set-up at beamline 1-ID.....125

Figure 3-25: Data Analysis procedure for X-Ray diffraction data collected at beamline 1-ID. 125

Figure 3-26: Evolution of temperature and hydrides concentration during synchrotron experiment.....127

Figure 3-27: Linear regression and alpha calculation.....129

Figure 3-28: Measured precipitation parameter $\boldsymbol{\alpha 2}$ with respect to 1/T, with different initial concentration (300, 400, 502 and 644 wt. ppm) 131

Figure 3-29: Measured precipitation parameter $\boldsymbol{\alpha}$ with respect to 1/T, with different initial concentration (300, 400, 502 and 644 wt. ppm).....132

Figure 3-30: Measured precipitation parameter $\boldsymbol{\alpha}$ with respect to 1/T, in log scale and with Kammenzind interpolation.....134

Figure 4-1: Comparison of McMinn's equations for the TSSd and TSSp of unirradiated and irradiated material [40].....138

Figure 4-2: Zirconium crystal structure with hydrogen (c) and oxygen (b) in interstitial solid solution [74] 139

Figure 4-3: TSS Data points for Zircaloy with 2540 to 2860 ppm O compared to Zircaloy with 1000 to 1200 ppm O (solid and dashed curves) [40] 140

Figure 4-4: Solubility of hydrogen in zirconium alloys [28] 141

Figure 4-5: The effect of alloying elements on TSSd of hydrogen in zirconium [77].....142

Figure 4-6: Hydride dissolution solvus, comparative effect of temperature and stress[78].....143

LIST OF TABLES

Table 1-1: Empiric oxidation kinetics parameters 5

Table 1-2: Diffusion driving forces and fluxes 21

Table 1-3: Hydrogen model constants 32

Table 2-1: Summary of the dissolution and precipitation conditions 36

Table 2-2: MOOSE capabilities 41

Table 2-3: Strong form, weak form and Jacobian of the hydrogen kernel in case of precipitation (case 1) 46

Table 2-4: Strong form, weak form and Jacobian of the hydrogen kernel in case of dissolution (case 2) 47

Table 2-5: Summary of the dissolution and precipitation conditions 48

Table 2-6: Boundary and initial condition for benchmark 1 58

Table 2-7: Statistical comparison of the difference between BISON and HydruLab calculations 62

Table 2-8: Boundary and initial condition for benchmark 2 63

Table 2-9: Shutdown decay power constants 76

Table 2-10: Pellet geometry in the PWR simulations 86

Table 2-11: Condition for five pellet DeCART-CTF coupling 86

Table 3-1: Summary of heat of transport of hydrogen in Zircaloy measurements 100

Table 3-2: Temperature controller Specifications 105

Table 3-3: PID values of the thermal controllers 106

Table 3-4: Estimators of the difference between transient and steady state profile (650°C-550°C) 113

Table 3-5: Temperature in the plate during the diffusion experiment 114

Table 3-6: Overall hydrogen concentration in the APS samples 126

Table 3-7: Measurement of the kinetics parameter alpha^2 (s) 130

Table 3-8: Measurement of the kinetics parameter alpha ($s^{-1/2}$).....130

ACKNOWLEDGEMENTS

First, I would like to thank my advisor, Arthur Motta, for his help and guidance during these two years at The Pennsylvania State University. It has been a great experience and I have learned a lot, not only about material sciences and experimental technique but also on how to conduct research in an academic structure. I want to thank Ian Davis who has been an excellent research partner during these two years. Thanks to his reliability and rigor, our collaboration led to very interesting work, at the intersection of most of the nuclear fields. His advisors, Dr. Ivanov and Dr. Avramova, were also very helpful during these two years. I also want to thank Dr. Thole for her help.

We are thankful for the financial support for this research program provided by the United States Department of Energy through the NEUP project 11-2987. In particular, the guidance from Brady Hanson was very useful to conduct the project. I would also like to thank Jon Almer and Jun-Sang Park from Argonne National Laboratory for their help running the experiments at the APS and analyzing the data. I also want to thanks Mark Daymond from Queen's University for sharing his knowledge regarding the APS data analysis. The simulation part of this work could not have been done without the strong support of Jason Hales and Richard Williamson from Idaho National Laboratory. By allowing us to collaborate into the BISON project and by supporting our efforts through the modifications of the code and the run of the simulation, they made our 3D simulation possible. I also want to thank the University of Michigan for allowing us to use their DeCART software.

At The Pennsylvania State University, I would like to thank all the students past and present of the Nuclear Materials Group. I would also like to thank the staff from the Nanofab for their help preparing samples. I would like to thank Dave Shelleman and Eric Sagmuller for their help with the design of the diffusion experiment. I want to thank Daniel Nunez, Charles

Pasgrimmaud and Kevin Cass who help me during the summer semesters. I thank and wish the best to Christopher Piotrowski who is going to continue this research over the next years and with whom I collaborated during the last 2 months of my research.

I want to thank Centrale Paris staff and professors who allow me to end my engineering study through a joint degree with The Pennsylvania State University. I would like to also thank Celine Lascar (Areva), Herve de Barbeyrac (McKinsey), Pascal Yvon (CEA), Nicolo Galante (McKinsey), Franck Enguehard (ECP), Jean-Luc Salanave (ECP) and Dominique Pareau (ECP) who encouraged me to pursue a Master of Science in the United States.

Finally, I would like to thank Benoit for his continuous support and help during these two years. The solving of neutronics, mathematics, physics, biology and bridge problems over many nights will stay in my memory. I want to thank Maïlys for her continuous support and patience. I also want to thank Thibault Bertrand and Max Fratoni for their precious advices on how academic research works in the United States. I would finally like to thank my family for their support.

Nomenclature

In the current work, the following symbols are used:

C_{ss} is the concentration of hydrogen in solid solution in zirconium (in wt.ppm)

C_p is the amount of hydrogen in the zirconium hydrides (in wt.ppm)

Q* is the heat of transport of hydrogen in Zr

α is the rate of precipitation

Chapter 1: Introduction and background

This chapter provides the fundamental understanding of the hydrogen behavior in the LWR fuel cladding. The section 1.1 gives the general background of the role of zirconium alloy as a material for the cladding. It is followed, in section 1.2, by the description of the oxidation mechanisms that produce hydrogen at the interface between the coolant and the fuel cladding. In section 1.3, the mechanism of the hydrogen pick-up is briefly explained as a prelude to the calculation of the incoming hydrogen flux in the zirconium cladding. Section 1.4 presents the key elements to understanding the redistribution of hydrogen in the cladding, starting with the experimental observations (sections 1.4.1 and 1.4.2) followed by a description of physical understanding through different models (section 0, 1.4.4, 1.4.5 and 1.4.6). Finally, the motivation and purpose of this study are detailed in section 1.5 .

1.1 Zirconium Alloys for Nuclear Fuel Cladding

The core of a Light Water reactor (LWR) contains fuel assemblies that are cooled by water. Each assembly is made of a series of fuel rods (approximately 4 m in height and 9.6 mm in diameter) that contain fissile material in the form of uranium dioxide pellets (UO_2). These fuel rods are sheathed in the nuclear fuel cladding, made of zirconium alloy, which serves as the primary barrier to contain fission products between the nuclear fuel and the primary coolant water.

Zirconium alloys have been chosen as cladding material primarily for their very low thermal neutron absorption cross section (0.185 barns (or $0.185 \times 10^{-24} cm^2$) for 0.0253eV neutrons) which allow for a good neutron economy [1] . Zirconium alloys also exhibit good corrosion

resistance, good heat transfer properties, appropriate mechanical strength for LWR conditions and are, to a certain extent, resistant to radiation damage [2].

During in-reactor operation, the zirconium cladding is subject to environmental degradation. The cladding tube is under stress from the pressure of the fission gases emitted from the uranium pellet and can eventually chemically bond with the pellet itself. The typical temperature of the inner cladding wall is about 380 ºC. The outer wall of the cladding is in contact with the cooling water and its temperature is approximately 330 ºC. At this boundary, waterside corrosion occurs. The corrosion reaction generates hydrogen, some of which is picked up by the cladding [3]. Additional sources of hydrogen production are water radiolysis and hydrogen added to the reactor core primary water. Radiation damage also affects the properties of the cladding. Typically during the 3 year operating lifetime of the fuel rod, each atom in the zirconium cladding is displaced 20 times (20 dpa). This causes an alteration of the material properties. [2]

Historically, the alloy most often used in Pressurized Water Reactors (PWR) is Zircaloy-4, while Zircaloy-2 is used in Boiling Water Reactors (BWR). Recently, PWRs have started to use more modern alloys such as ZIRLO® and M5®, which exhibit improved corrosion resistance, compared to Zircaloy-4 [4, 5]. Another zirconium alloy, Zr-2.5Nb is also used in heavy water reactors such as CANDU reactors. Although the alloying elements are added in small quantities, they have a strong impact on the in-service behavior of the alloy strongly, especially its corrosion resistance. There are other alloys, especially Russian alloys that are not covered by this study.

1.2 Origin of hydrogen in the LWR fuel cladding

1.2.1 Reactions producing hydrogen in the cladding in LWR

As stated above, the hydrogen produced in the LWR cores comes from three main sources. The first source is the waterside corrosion reaction shown in equation 1-1.

$$Zr + 2H_2O \rightarrow ZrO_2 + 4H \qquad \textbf{1-1}$$

Second, hydrogen can be generated by radiolysis [6] according to the following reaction:

$$H_2O \rightarrow_{\gamma,n} H^+ + OH^- \qquad \textbf{1-2}$$

Third, hydrogen can be purposefully added to the primary water to limit oxidation. Other factors, such as hydrogen present in the fuel pellets, can make additional hydrogen atoms available to enter the cladding.

1.2.2 Kinetics of the cladding oxidation

The oxidation kinetics have been formulated with semi empirical models, which are detailed in the Waterside Corrosion report, produced by the International Atomic Energy Agency (IAEA) [7]. These models separate two different kinetic behaviors. At first, oxidation weight gain kinetics is governed by a cubic rate law:

$$w^3 = k_c * t, with\ k_c = A_{kc} * \exp(-\frac{Q_{kc}}{RT}) \qquad \textbf{1-3}$$

With:

w the weight gain (per unit area)
A_{kc} the pre-transition frequency factor (in $\mu m^3/d$)
Q_{kc} the pre-transition activation energy for oxide growth
R the gas constant, T the temperature (K)

Assuming that all oxygen weight gain is used to produce ZrO_2 and that no ZrO_2 oxide is lost by spallation or dissolution, the oxide layer thickness is proportional to the weight gain [8]:

$$\delta(\mu m) = \frac{w\left(\frac{mg}{dm^2}\right)}{14.7} = \frac{(k_c * t)^{\frac{1}{3}}}{14.7} = K_c^{\frac{1}{3}} * t^{\frac{1}{3}} \qquad \textbf{1-4}$$

Then, the oxide thickness follows a cubic law and oxidation gradually falls down. The equations above reflect the volume expansion of the oxide relative to the metal. The new constant is defined as:

$$K_c = \frac{k_c}{(14.7)^3} \qquad \textbf{1-5}$$

At about an alloy dependent thickness ($\delta \approx 2\ \mu m$ for Zircaloy-4), a kinetic transition is observed. At this point, the oxidation kinetics returns to the initial value seen at the start of the corrosion of the bare metal [9]. Afterwards, the oxidation kinetics can be approximated with a linear rate law:

$$w = k_l * (t - t^*) + w^*, k_l = A_{kl} * \exp\left(-\frac{Q_{kl}}{RT}\right) \qquad \textbf{1-6}$$

With:

w the weight gain
k_l the proportionality constant
t* the transition time
w* the weight gain at the transition.

In terms of oxide thickness,

$$\delta = \delta^* + K_L * (\delta - \delta^*) \qquad \textbf{1-7}$$

Experimental data has been used to calculate the kinetic proportionality constants. According to [7], the values given in Table 1-1 have been considered in previous work and fuel performance codes:

Table 1-1: Empiric oxidation kinetics parameters

Source / model	*Pre transition frequency factor (cubic)*	*Pre transition activation energy (Q/R)*	*Post transition frequency factor (linear)*	*Post transition activation energy (Q/R)*	*Transition oxide thickness S=A*exp(-B/T)* [μm] *t [days] for CEA*	
					A	B
	$\mu m^3 \cdot d^{-1}$	K^{-1}	$\mu m \cdot d^{-1}$	K^{-1}	*μm/days*	K^{-1}
MATPRO [10]	$4.976*10^9$	15,660	$8.288*10^7$	14,080	7.749	790
EPRI KWU/C-E	$1.78*10^{10}$	16,250	$8.04*10^7$	13,766	$2.14*10^7$	$-\frac{5417}{T} - 0.0117T$
COCHISE (CEA)	$11.4*10^{10}$	17,171	$4.0*10^{11}$	18,391	$8.857*10^{10}$	$\frac{921}{T} - 0.035T$
Motta (private com.)	535	4533	$8.1*10^6$	12,500	4.35	550

Figure 1-1 represents the evolution of the Zircaloy-4 oxide layer thickness, at 320°C, for 9 years. The curves have been drawn following to the equations 1-4 and 1-7 and using the model constants given in Table 1-1.

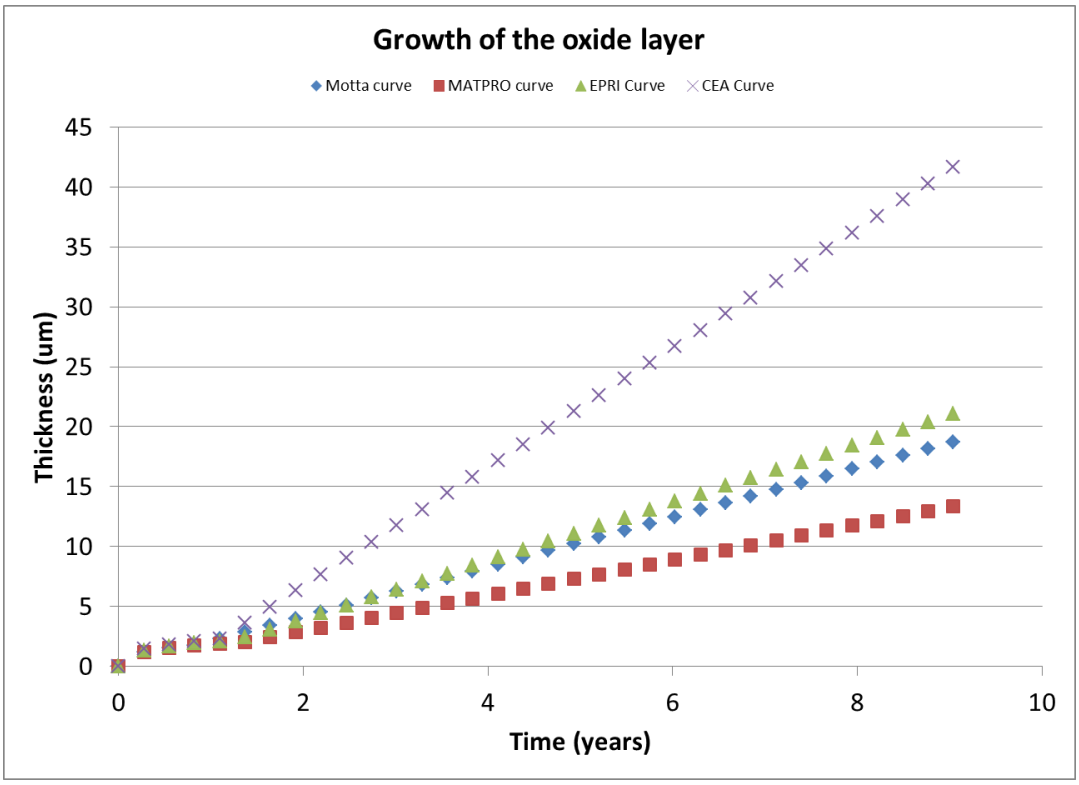

Figure 1-1: Growth of the cladding oxide layer according to oxidation kinetics models in Table 1-1

1.2.3 Empirical Hydrogen Pick-up in LWR cladding

Some of the hydrogen atoms produced by the mechanisms detailed in the section 1.2.2 are transported to the oxide-metal interface and can be absorbed into the cladding. This process is called hydrogen pick-up. The absorbed hydrogen migrates through the material in response to thermodynamic driving forces, which will be detailed in the next sections. For Zircaloy-4, 10% to 20% of the hydrogen liberated from corrosion is typically absorbed into the cladding. Factors influencing hydrogen pick-up may include:

- Oxide film characteristics (thickness, morphology and crystal structure)
- Second phase particles of various characteristics
- Zirconium alloy composition and microstructure

- Residual stresses
- The ratio of area/volume exposed to corrosion
- Water chemistry and more specifically radiolysis of the water during irradiation

The work from Adrien Couet [11, 12] gives information on the pick-up mechanisms. While no accurate model has been proposed at this time, a typical value of 15% is admitted as an average pick-up.

1.3 Hydrogen flux entering the cladding

According to the previous section, it is possible to calculate the hydrogen flux that enters the cladding at the coolant interface. The quantity of Zr oxide in the oxide layer, per unit of surface, is given by:

$$n_{ZrO_2} = \delta * \frac{\rho(ZrO_2)}{M(ZrO_2)} \qquad \textbf{1-8}$$

With δ the oxide thickness, $\rho(ZrO_2)$ the oxide density and $M(ZrO_2)$ the oxide molar mass.

According to the oxidation reaction 1-9, there are 4 atoms of hydrogen for each molecule of Zr oxide.

$$Zr + 2H_2O \rightarrow ZrO_2 + 2H_2 \qquad \textbf{1-9}$$

Assuming f=15%, the hydrogen pick-up fraction, the amount of hydrogen picked up by the cladding is given by:

$$n_H = 4f * \delta * \frac{\rho(ZrO_2)}{M(ZrO_2)} \qquad \textbf{1-10}$$

The mass of hydrogen picked up is:

$$m_H = 4f * \delta * \frac{\rho(ZrO_2)}{M(ZrO_2)} * M_H \qquad \textbf{1-11}$$

With δ the oxide thickness, $\rho(ZrO_2)$ the oxide density M_H the hydrogen molar mass and $M(ZrO_2)$ the oxide molar mass.

It is common to use wt. ppm for the concentration of hydrogen. Thus, it is necessary to evaluate the amount of zirconium (per unit of surface) in the cladding, which is given by equation 1-12.

$$m_{Zr} = \rho(Zr) * (thickness - \delta) \qquad \textbf{1-12}$$

With δ the oxide thickness and $\rho(Zr)$ the density of pure zirconium.

The thickness corresponds to the thickness of the cladding, which is usually close to 650 microns.

Finally, the average concentration of hydrogen in the cladding is given by the equation 1-13.

$$C_H[wt.ppm] = 4f * \frac{\frac{\rho(ZrO_2)}{M(ZrO_2)} * \delta}{\frac{\rho(Zr)}{M(Zr)} * (thickness - \delta)} * \frac{M_H}{M_{Zr}} = \frac{4f}{1.56} \frac{\delta}{(thickness - \delta)} * \frac{M_H}{M_{Zr}} \qquad \textbf{1-13}$$

1.3.1 Shape of hydrogen overall concentration

Figure 1-2 gives the average hydrogen concentration evolution with time, assuming a constant hydrogen pick-up fraction of 15%, using a cladding/coolant interface temperature of 320°C and a cladding thickness of 0.6 mm.

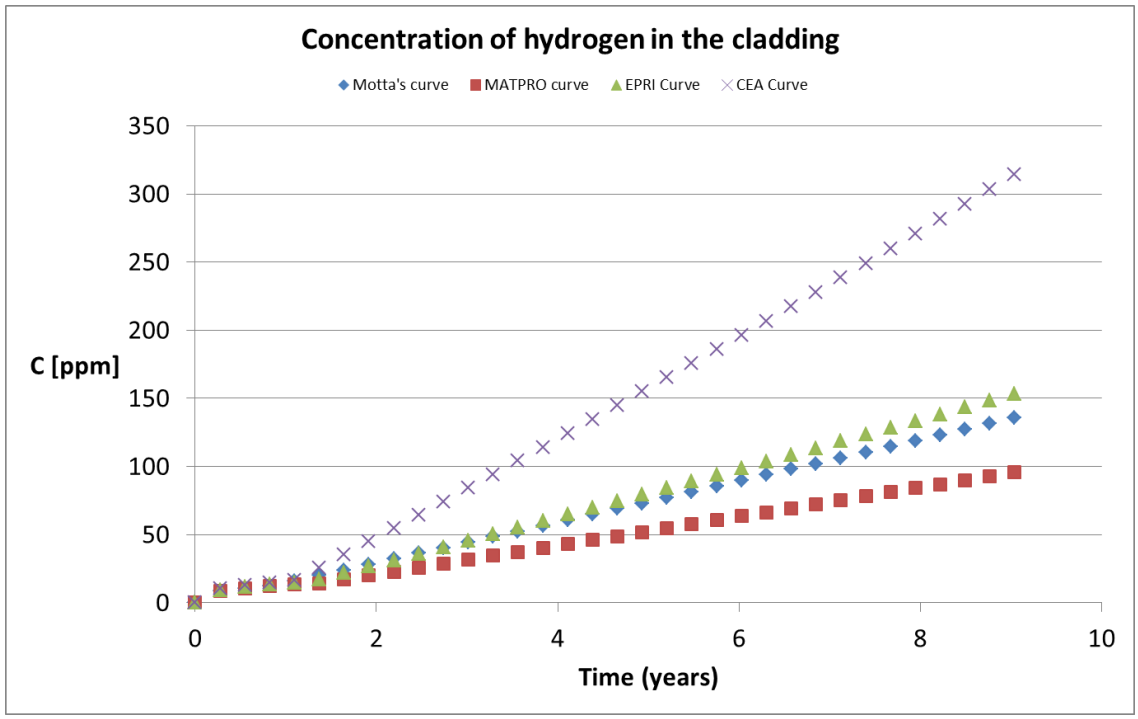

Figure 1-2: Evolution of the average cladding hydrogen concentration with time at 320°C, using kinetics models of Table 1-1

1.3.2 Hydrogen flux at the coolant/cladding interface

The rate of the increase of the oxide layer is:

- For the cubic regime (according to equation1-4)

$$\frac{d(\delta)}{dt} = (K_c)^{\frac{1}{3}} * \frac{1}{3} t^{-\left(\frac{2}{3}\right)} \qquad \textbf{1-14}$$

- For the linear regime (according to equation1-7)

$$\frac{d(\delta)}{dt} = K_L \qquad \textbf{1-15}$$

The rate of the increase of hydrogen in the cladding is given by:

$$\frac{dC_H}{dt} = \frac{d}{dt}\left(\frac{4f}{1.56}\frac{\delta}{(thickness - \delta)} * \frac{M_H}{M_{Zr}}\right)$$

$$\frac{dC_H}{dt} = \frac{4f}{1.56} * \frac{M_H}{M_{Zr}} * \frac{d}{d\delta}\left(\frac{\delta}{(thickness - \delta)}\right) * \frac{d\delta}{dt}$$

$$\frac{dC_H}{dt} = \frac{4f}{1.56} * \frac{M_H}{M_{Zr}} * \left(\frac{(thickness)}{(thickness - \delta)^2}\right) * \frac{d\delta}{dt} \qquad \textbf{1-16}$$

By conservation of species:

$$\frac{dC_H}{dt} * V = J * S \qquad \textbf{1-17}$$

Where V is the volume of cladding considered and J is the flux of hydrogen coming into this volume through the cross-section S. The cross-section S multiplied by the cladding thickness is equal to the volume V.

Therefore:

$$J = thickness * \frac{4f}{1.56} * \frac{M_H}{M_{Zr}} * \left(\frac{(thickness)}{(thickness - \delta)^2}\right) * \frac{d\delta}{dt}$$

$$J = \frac{4f}{1.56} * \frac{M_H}{M_{Zr}} * \left(\frac{thickness^2}{(thickness - \delta)^2}\right) * \frac{d\delta}{dt} \quad (wt.ppm/cm^2\ /s) \qquad \textbf{1-18}$$

In a first approximation, the thickness factor can be neglected. The equation becomes:

$$J = \frac{4f}{1.56} * \frac{M_H}{M_{Zr}} * \frac{d\delta}{dt} \quad (wt.ppm/cm^2\ /s) \qquad \textbf{1-19}$$

1.4 Redistribution of hydrogen in the cladding

Once the hydrogen enters the cladding, it can exist within two different phases. The hydrogen in solid solution corresponds to H atoms occupying interstitial sites in the hcp zirconium structure. At higher concentrations, hydrogen precipitates and forms hydrides (mostly delta hydrides) [13, 14] The distribution of hydrogen within these two species is strongly interdependent and the specific hydrogen distributions can reduce cladding ductility and create

other critical challenges for the nuclear industry. The main purpose of this thesis will be to study, model and simulate this distribution.

1.4.1 Consequence of hydrides on Zircaloy cladding properties

According to various work including Robert Daum's mechanical project ([15, 16]), a local high concentration of hydrides has a significant impact on the Zircaloy-4 fuel cladding.

Daum's study showed that local accumulation of hydrogen (>5900 wt. ppm) in a hydride rim at the outer surface of the cladding could result in the precipitation of a mixture of hydride phases. Thick rims appear to be susceptible to cracking at 300°C or temperatures close to normal reactor operation and a hot zero power condition.

According to his testing, the propagation of these cracks through the cladding wall is highly dependent on temperature and hydride-rim thickness. Cladding with thin rims (<100 μm) appears to have considerable resistance to unstable crack propagation at temperatures >300°C. A hydride-rim thickness of 100 μm is at the higher end of usual thicknesses formed in typical intermediate and high burnup Zircaloy-4 cladding. For cladding with thicker rims or blisters, surface crack nucleation and subsequent mixed propagation is expected to occur at relatively low plastic strains or, in the case of his study, <2% far field hoop strain.

At higher temperatures (375°C), the cladding is ductile even at a hydride-rim thickness of 210 μm. However, such thick rims are likely to induce a loss of ductility due to the presence of small cracks within the rim.

1.4.2 Previous observations and measurements of hydride formation in Zr alloys

According to the following observations, the hydrogen in Zr cladding redistributes because of temperature gradients. The hydrogen tends to move to the cold areas and to precipitate there.

1.4.2.1 Radial distribution of hydrogen in Zircaloy cladding

A radial gradient in the hydride distribution has been observed regularly for cross-sectional samples coming from LWR. At high burnup, a high concentration region is observed, constituting a hydride "rim". Figure 1-3 is a cross-sectional metallography of a cladding coming from a PWR reactor. As in similar studies, the hydride rim is located close to the outer edge of the cladding, where the temperature is the lowest. This is consistent with the assumption that hydrogen diffuses in Zircaloy according to temperature gradients.

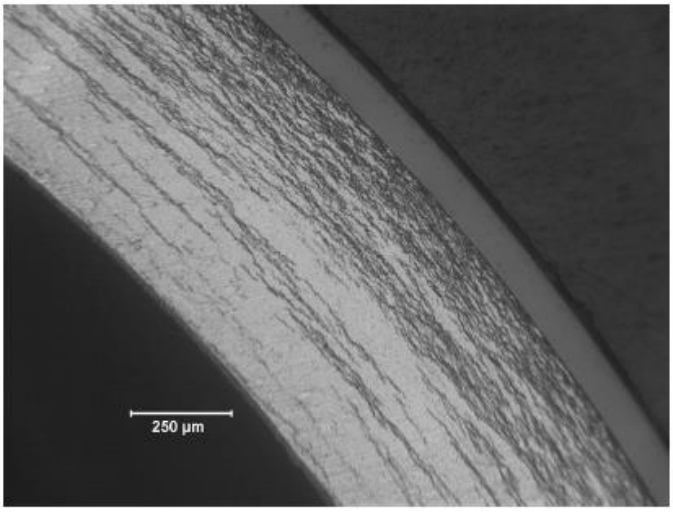

Figure 1-3: Hydride distribution and morphology in HBR rod F07 cladding near b650 mm above midplane (740-wppm H)[17]

A study of Bossis and al. [18] shows that at high burnup, the average concentration in the rim can go up to 1300 wt.ppm, when the cladding average concentration is 430 wt.ppm. Figure

1-4 shows the metallography related to this observation. The hydride rim is also located close to the cladding/coolant interface.

Figure 1-4: Optical micrographs of the hydride distribution and oxide layers on Zircaloy-4 irradiated for 6 cycles in PWR [18]

1.4.2.2 Axial oxidation behavior and consequences on hydrogen production

Because of the heat production in the fuel, the coolant temperature gradually increases along the axial direction. It also decreases locally close to the spacer grids, due to the presence of elements that are mixing the coolant flow (mixing vanes or castellations). Figure 1-5 shows the oxide thickness as a function of the elevation. It shows that the oxide growth follows the same profile as the temperature, increasing generally and decreasing locally at the spacer grids locations [19].

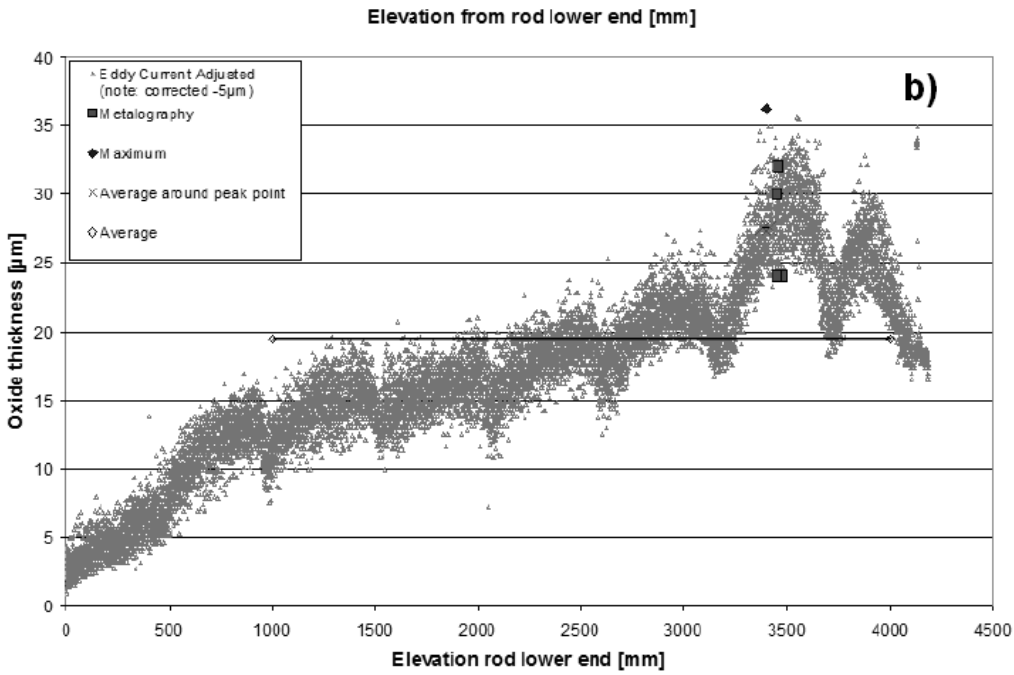

Figure 1-5: Increase of the oxide layer thickness with elevation in a PWR reactor (burnup close to 70 MWd/kgU) [19]

No precise measurement giving hydrogen concentration as a function of axial elevation has been found. Rough estimations have been provided by Zhang in his work [20]. Image treatment has been used on cross sectional metallography in order to estimate the hydride concentration. However, the results do not seem to be usable, due to very high uncertainties.

1.4.2.3 Azimuthal distribution of hydrogen in the cladding

Due to the heterogeneity of the core geometry, the cladding is subjected to a heterogeneous temperature distribution. Guide tubes, corners and sides of the assemblies create colder boundary conditions and, therefore, affect the hydrogen distribution. This phenomenon has been observed by Billone and coworkers [17]. Figure 1-6 is a collection of irradiated cladding metallography coming from one of their ring compression test. The average total hydrogen concentration has been measured with hot vacuum extraction for different azimuthal sections. The variations between different sections are greater than 150 wt.ppm. Moreover, the result of the

test shows that the crack is formed where the concentration is the highest. This confirms the fact that hydrides weaken the cladding.

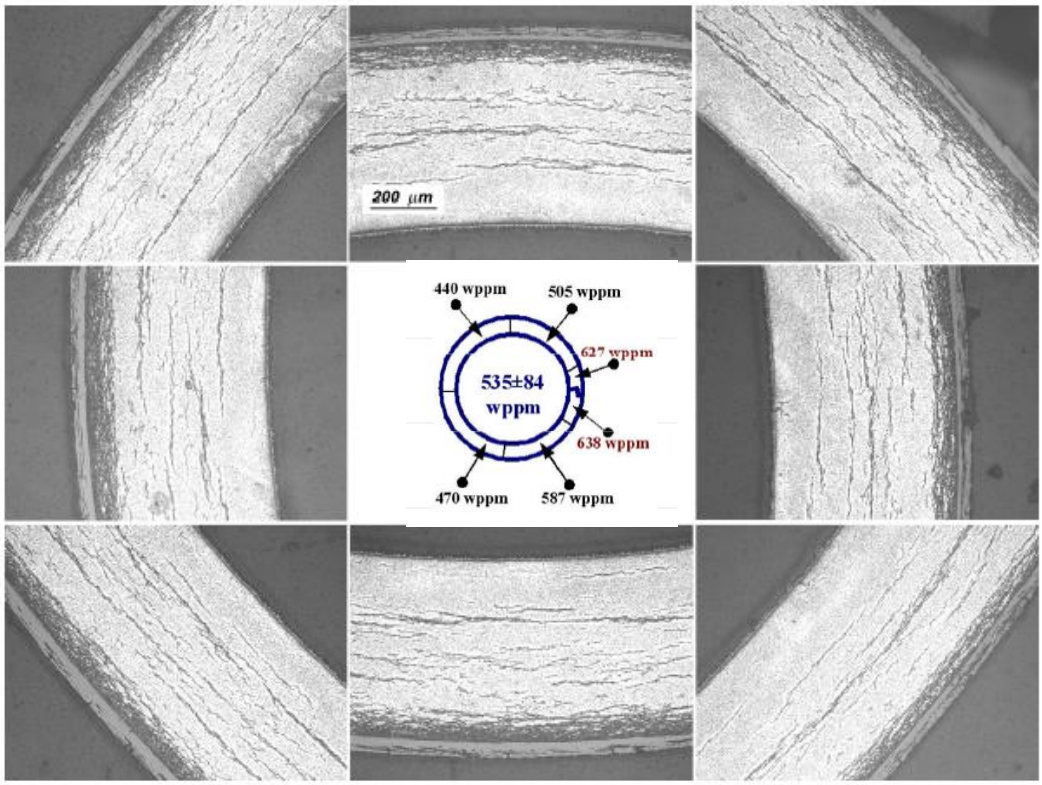

Figure 1-6: Azimuthal variations of the hydride distribution

1.4.2.4 Inter Pellet gap hydride distribution

Another classical observation regarding the temperature dependence of hydrogen distribution is the enhancement of the concentration of hydride at the inter pellet gap. The mechanical stress due to pellet expansion led to the creation of chamfers, at the top and bottom of the pellets. Figure 1-7 is a metallography of showing a full pellet and its neighboring pellets. The inter-pellet gap forms at the interface between two pellets and has been circled in red.

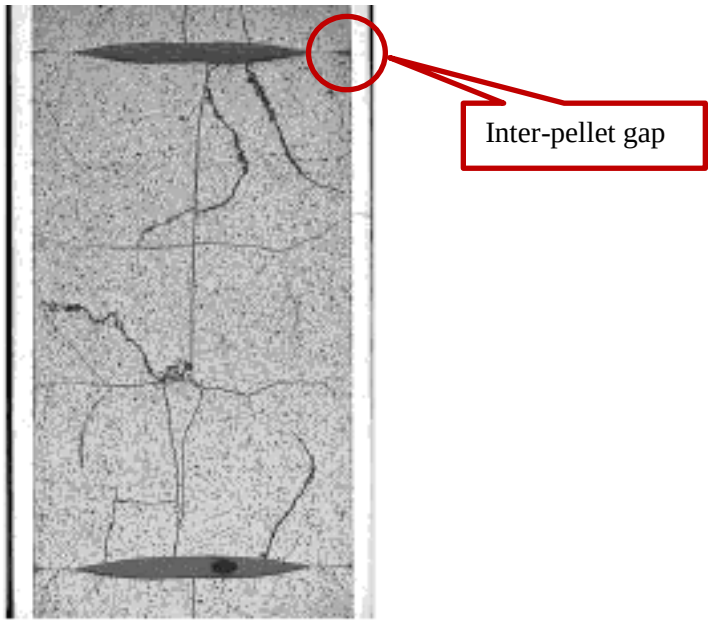

Figure 1-7: Axial macrograph of a fuel rod

The presence of chamfers leads to lower temperatures at their locations, which creates a cold spot in the cladding, as it can be seen from a fuel performance calculation (BISON). Figure 1-8 shows the temperature profile at the inter-pellet gap. The pellet is represented in green and its temperature is not displayed. At the inter-pellet gap, a decrease of about 20°C is observed. This is mainly due to the fact that there is less energy deposition at the inter-pellet gap and that the gap created by the chamfers is filled by the fission gases and the initial helium, which have a significant thermal resistance.

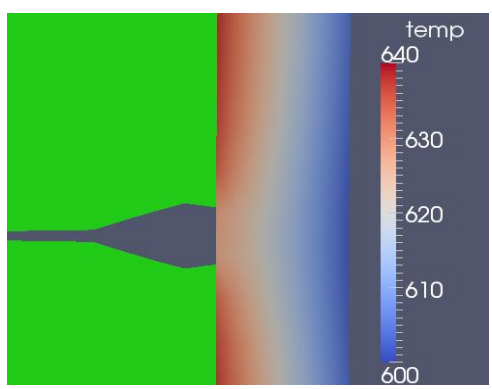

Figure 1-8: Cladding temperature profile (K) around the inter-pellet gap as calculated with BISON

The work by Smith [21] shows a very high concentration of hydrides close to the inter-pellet gap, compared to the mid-pellet cladding. Figure 1-9 shows three different micrographs, coming from the same road. The picture a, on the left, shows the hydride distribution far from the inter-pellet gap. The rim can be seen. On the contrary, the pictures b and c show hydride distribution in the inter-pellet gap. Almost the full thickness is covered by hydrides. This is consistent with the temperature profile shown above.

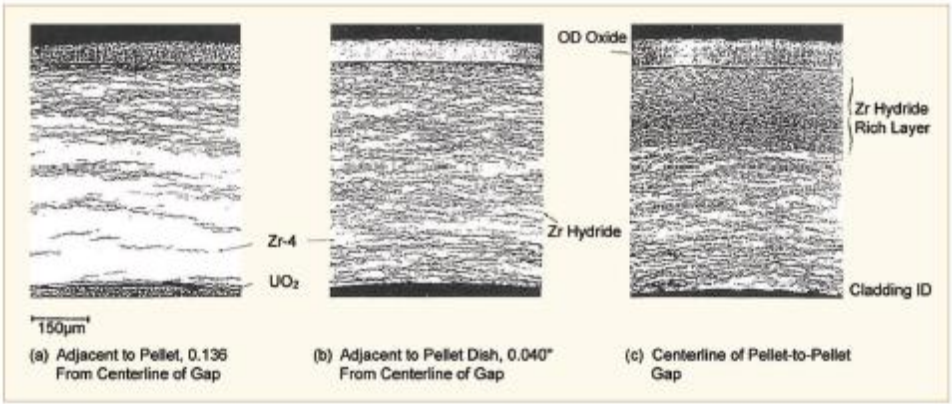

Figure 1-9: Hydride distribution at the inter-pellet gap cladding compared to mid-pellet cladding [21]

1.4.2.5 Oxide spallation

When the oxide thickness reaches a very high value (> 80µm), oxide spallation can occur[22]. At the spallation, the metallic cladding is directly in contact with the coolant, and its temperature decreases quickly. Previous observations show the formation of a hydride blister (pure hydride) at the location of the spallation. Figure 1-10 shows a metallography of a cladding portion where the spallation has occurred. A blister formed at the outer edge.

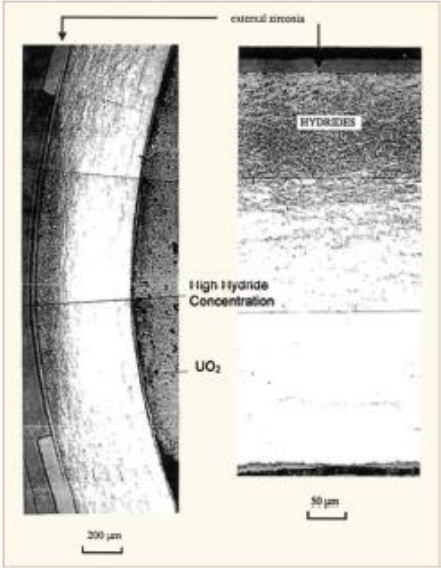

Figure 1-10: Hydride blister due to oxide spallation[22]

According to these observations, a high concentration of hydrides is usually observed at the lower temperature spots in the nuclear fuel cladding.

1.4.3 Hydrogen diffusion in Zircaloy

In order to study the formation of the specific hydride distribution, it is necessary to understand the phenomena that govern the distribution of hydrogen in solid solution. One of these phenomena is the diffusion of hydrogen. The hydrogen diffusion in solid solution in the zirconium matrix is governed by two driving forces: the concentration gradient and the temperature gradient.

1.4.3.1 Fick's law and diffusion coefficient

A concentration gradient in the hydrogen distribution generates a flux according to Fick's law. This concerns only the hydrogen in solid solution, as the hydrogen in hydrides is immobilized within that place.

$$J_{Fick} = -D(T) * \nabla C_{ss} \qquad \textbf{1-20}$$

J_{Fick} is the diffusion flux due to concentration gradient

C_{ss} is the concentration of hydrogen in solid solution

D(T) is the diffusion coefficient, which is governed by an Arrhenius law:

$$D = A_D * \exp(-\frac{Q_D}{RT}) \qquad \textbf{1-21}$$

The coefficients have been measured by Kearns [23]:

$$\boldsymbol{A_D = 7.90 * 10^{-7} m^2/s} \qquad \textbf{1-22}$$

$$\boldsymbol{Q_D = 4.49 * 10^4 J/mol} \qquad \textbf{1-23}$$

Figure 1-10Figure 1-11 shows the most usual correlations, that have been compiled by Kammenzind [24]. All these calculation are close to each other.

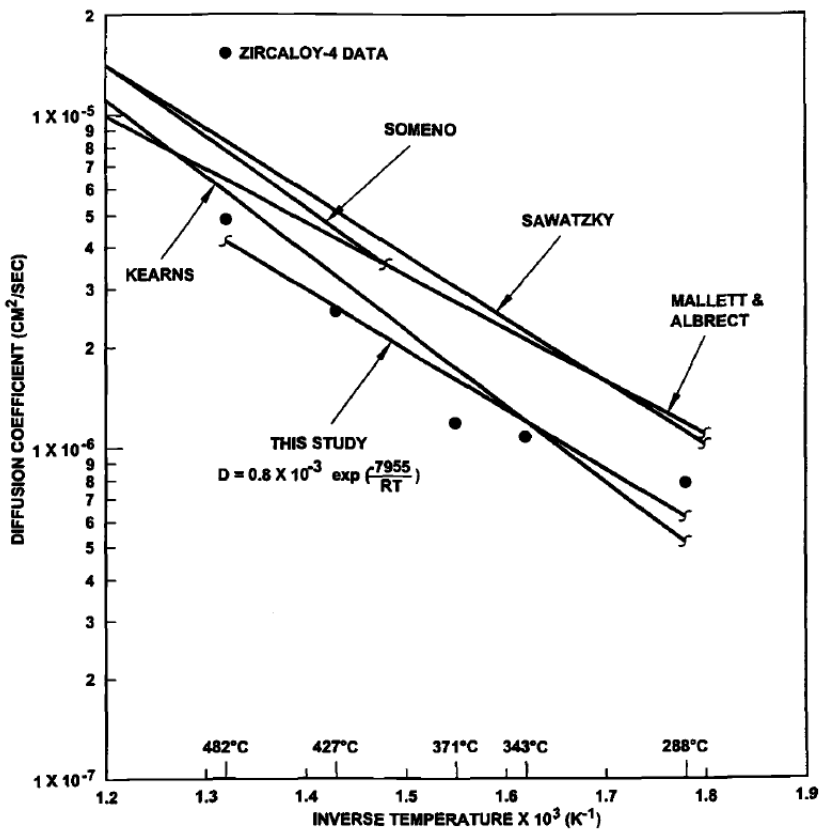

Figure 1-11: Main measurement of hydrogen diffusion coefficient in Zircaloy-4 [24]

1.4.3.2 Soret Effect and heat of transport

As observed by Sawatzky and confirmed in several studies, hydrogen diffusion is also driven by a temperature gradient. According to the linear thermodynamic model [25], there is a coupling between thermal diffusion and species diffusion. The connection between a species diffusion flux and temperature gradient has different names. This phenomenon is called Soret effect (flux of particles induced by temperature gradient) or Dufour effect (heat flux induced by concentration gradient). The thermoelectric phenomena (Seebeck and Peltier effects) that govern the thermocouple laws are also described by the linear thermodynamics theory. This theory also

includes the Onsager reciprocal relations. The fundamental assumption of this model is that there is a linear relation between the driving forces and the fluxes, as presented in Table 1-2.

Table 1-2: Diffusion driving forces and fluxes

	Driving force	**Flux**
Heat transfer	$\nabla(\frac{1}{T})$	J_Q
Species diffusion	$-\frac{\nabla\mu_k}{T}$	J_D

The proportionality between the driving forces and the fluxes is assumed. The proportionality coefficients are called L_{xx} for direct relations and L_{xy} for coupled relations. The following set of equations is obtained [25]:

$$J_D = L_{ii} * -\frac{\nabla\mu_k}{T} + L_{ij} * \nabla(\frac{1}{T})$$
$$J_Q = L_{jj} * \nabla\left(\frac{1}{T}\right) + L_{ji} * \frac{\nabla\mu_k}{T} \qquad \textbf{1-24}$$

With

μ_k the chemical potential of the species k,
L_{ii} and L_{jj} the direct proportionality coefficient (based on the linear approximation)
L_{ij} and L_{ji}, the coupling proportionality coefficient

According to Onsager reciprocal relation:

$$L_{ij} = L_{ji} \qquad \textbf{1-25}$$

This equality is a consequence of the symmetries of the equations. The full demonstration can be found on page 355 of *Modern Thermodynamics* [25].

According to the relationship between the activity and chemical potential for chemical species:

$$\mu_k(T) = \mu_0 + RT\ln(a_k) \qquad \textbf{1-26}$$

With a_k the activity of the species k.

For particle species in solution:

$$a_k = C_{ss} \qquad \textbf{1-27}$$

With C_{ss} the concentration in solid solution.

Thus,

$$J_D = -L_{ii} * R * \frac{\nabla C_{ss}}{C_{ss}} + L_{ij} * \nabla(\frac{1}{T}) \qquad \textbf{1-28}$$

Then, factorized by $L_{ii} * \frac{R}{C}$:

$$J_D = -L_{ii} * \frac{R}{C_{ss}}\left(\nabla C - \frac{L_{ij}}{L_{ii}} * \frac{C_{ss}}{R} * \nabla\left(\frac{1}{T}\right)\right) \qquad \textbf{1-29}$$

The heat of transport is then defined as:

$$Q^* = \frac{L_{ij}}{L_{ii}} \qquad \textbf{1-30}$$

Then,

$$J_D = -L_{ii} * \frac{R}{C_{ss}}\left(\nabla C - Q^* \cdot \frac{C_{ss}}{R} * \nabla\left(\frac{1}{T}\right)\right) \qquad \textbf{1-31}$$

By definition of the diffusion coefficient:

$$D = L_{ii} * \frac{R}{C_{ss}} \qquad \textbf{1-32}$$

Then,

$$J_D = -D\left(\nabla C_{ss} + Q^* \frac{C_{ss}}{RT^2} * \nabla \mathrm{T}\right) \qquad \textbf{1-33}$$

The first part of the equation corresponds to Fick's law. It can be observed that the temperature dependence of the diffusion coefficient does not appear in this equation. This is due to the fact that in the framework of the linear thermodynamics, the temperature dependence is assumed to be negligible. This assumption is approximately valid if the temperature does not vary

excessively in the region of interest. The second part of the equation corresponds to the Soret effect:

$$J_{Soret} = -\frac{DC_{ss}Q^*}{RT^2}\nabla T \qquad \textbf{1-34}$$

1.4.3.3 Consequences of the Soret effect

If the concentration of hydrogen in solid solution is low, there is no hydride precipitation (see next section). In simple 1-D geometry, the analytical steady state solution can be calculated. Considering a plate exposed to two different temperatures (T_{hot} and T_{cold}) on its two extremities and assuming adiabatic boundary condition on the other sides:

According to the conservation of mass,

$$\frac{dC_{ss}}{dt} = -\nabla J_D = -\nabla\left[-D\left(\nabla C_{ss} + Q^*\frac{C_{ss}}{RT^2} * \nabla \mathrm{T}\right)\right] \qquad \textbf{1-35}$$

The terms corresponding to the derivative of D with respect to x (or to T) are neglected.

Assuming steady state and 1-D geometry, equation 1-35 becomes:

$$\frac{d}{dx}\left[-D\left(\frac{\mathrm{d}}{\mathrm{dx}}C_{ss} + Q^*\frac{C_{ss}}{RT^2} * \frac{\mathrm{d}}{\mathrm{dx}}\mathrm{T}\right)\right] = 0 \qquad \textbf{1-36}$$

Assuming no mass transfer at the cold and hot boundary:

$$-D\left(\frac{\mathrm{d}}{\mathrm{dx}}C_{ss} + Q^*\frac{C_{ss}}{RT^2} * \frac{\mathrm{d}}{\mathrm{dx}}\mathrm{T}\right) = 0$$

$$\frac{dC_{ss}}{dx} = -Q^*\frac{C_{ss}}{RT^2} * \frac{\mathrm{dT}}{\mathrm{dx}}$$

$$\frac{dC_{ss}}{C_{ss}} = -Q^*\frac{dT}{RT^2} \qquad \textbf{1-37}$$

Integrating between x=0 and x:

$$\ln(C_{ss}) - \ln(C_0) = Q^* \left(\frac{1}{RT} - \frac{1}{RT_0}\right) \qquad \textbf{1-38}$$

$$C_{ss} = K_{int} * \exp\left(\frac{Q^*}{RT}\right) \qquad \textbf{1-39}$$

The integration constant K_{int} can be calculated using the conservation of mass and the initial average concentration:

$$\int (C_{ss})dx = \text{cst} \qquad \textbf{1-40}$$

The transient calculation, using series expansion, has been performed by Sawatzky and Vogt [26]. This complex calculation has not been reproduced in this thesis. The first part of the publication gives the transient of the case presented above. The second part, however, tries to model the two phase equilibrium and has to be considered carefully.

1.4.4 Hydride precipitation and dissolution (TSS laws)

This section is inspired from the introduction of Kimberly Colas PhD's thesis [27].

When the hydrogen content reaches the solubility limit in the α-zirconium matrix, the hydrogen precipitates as zirconium hydride. This limit is called the Terminal Solid Solubility (TSS). The determination of the TSS is essential for a better understanding of the behavior of zirconium hydrides. Kearns' study on the terminal solubility limit using the diffusion couple method has been widely used as the reference for TSS determination [28]. This study states that below 550ºC (above which recrystallization occurs), the following equation determines the TSS:

$$TSS\ (wt.ppm) = 120000\ exp\left(-\frac{4302}{T}\right) \qquad \textbf{1-41}$$

where T is the temperature in Kelvin.

A hysteresis phenomenon has been observed in several studies between the TSS for dissolution (TSSd) and the TSS for precipitation (TSSp). This temperature hysteresis is a result of the work associated with volume expansion which is required for hydride precipitation, as illustrated in Figure 1-12. When a small plate-shaped hydride precipitate is nucleated, reversible elastic work is done on the surrounding matrix, yielding the following expression for the nucleation solvus [29, 30]:

$$C_{nucl} = C_s \, exp\left(\frac{w_e}{RT}\right) \qquad \textbf{1-42}$$

where C_{nucl} is the amount of hydrogen in solution until hydride precipitation, C_s is a theoretical "stress-free" or equilibrium solvus, w_e is the elastic accommodation energy of the matrix and hydride precipitate per mole hydrogen (which is influenced by the orientation relationship of the precipitate and the matrix), and T is the temperature. Because the hydride is performing work on the matrix as it precipitates, the hydrogen concentration in the matrix is elevated relative to the equilibrium solvus C_s. When a hydride grows past a critical size (typically sub-micron [31, 32]), the accommodation energy is no longer purely elastic and the expression must account for plastic accommodation of the hydride [33]:

$$C_{cool} = C_s exp\left(\frac{w_{e,p} + w_p}{RT}\right) = C_s exp\left(\frac{Q_{cool}}{RT}\right) \qquad \textbf{1-43}$$

where w_p is the plastic accommodation energy, $w_{e,\,p}$ is the elastic contribution in the presence of plastic deformation, and Q_{cool} represents the total accommodation energy upon cooling. The solvus expression for hydride dissolution, C_{Heat}, is similar to that of precipitation, the difference being the plastic work required to precipitate the hydride is not reversible (and therefore the contribution from w_p is negligible on heating):

$$C_{heat} = C_s \exp\left(\frac{w_{e,p} + w_p}{RT}\right) = C_s \exp\left(\frac{Q_{heat}}{RT}\right) \qquad \textbf{1-44}$$

In the case of zirconium, it is the plastic work term that dominates during cooling and for this reason the hydrogen concentration on dissolution C_{heat} is often approximated as C_s. It should also be noted that the hydrogen concentration on precipitation C_{cool} is not unique and is affected by the previous thermo-mechanical history of a specimen [29, 30, 34].

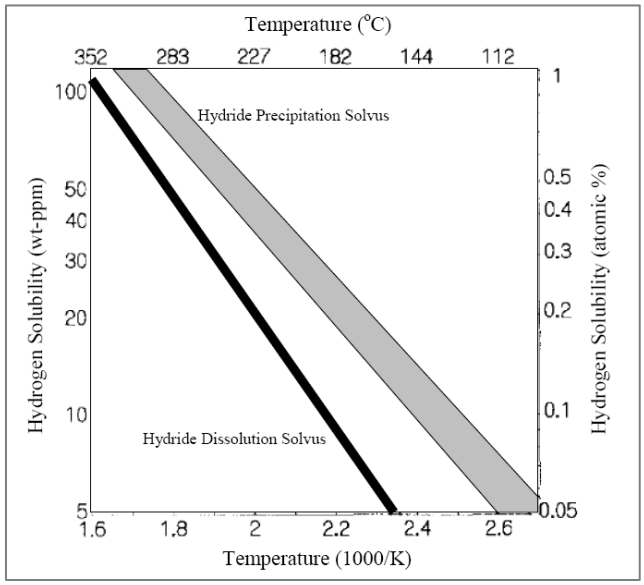

Figure 1-12: Illustration of the precipitation hysteresis [34]

According to McMinn [35] and without any additional effects, the TSSd and the TSSp can be approximated by the following equations:

$$\begin{cases} TSSd = 106446.7 * exp\left(-\frac{4328.67}{T}\right) \\ TSSp = 138746.0 * exp\left(-\frac{4145.72}{T}\right) \end{cases} \quad \textbf{1-45}$$

In addition to temperature, the main factors that influence hydride dissolution and precipitation in zirconium and its alloys are:

- Irradiation
- Oxygen in solid solution
- Alloying elements
- Thermal cycles.

Detailed information is provided in section 4.2. Since these effects are not taken into account into our current modeling, they have not been detailed in the current section.

1.4.5 Kinetics of precipitation

1.4.5.1 Necessity of the precipitation kinetics understanding

The kinetics of precipitation is a critical aspect of hydrogen redistribution in the cladding. While the TSSp and TSSd give the equilibrium value between the hydrogen in solid solution and in the precipitated hydrides, the kinetics provide information regarding the transient behavior between a non-equilibrated initial condition and the final steady state equilibrium. The detailed kinetics of hydride precipitation is likely one of the main causes of the rim feature and specific hydrogen distributions that occur in the nuclear fuel cladding. Because the kinetics are difficult to model, in his initial work, Sawatzky tried to explain the hydride redistribution without taking the kinetics into account [36].

However, he considered an initial homogeneous concentration of zirconium and applied a temperature gradient. Then, he observed a local increase of the hydride concentration that looks like a rim, but is completely different from the rim that is seen in reactor condition. It can, however, be considered in calculations for dry-cask storage.

In the case of reactor operation, the initial concentration of hydrogen starts at about 0 wt. ppm. The cladding is submitted to a temperature gradient of about 40°C for a thickness of 0.6 mm. The hydrogen flux is coming from the coolant interface, as shown below:

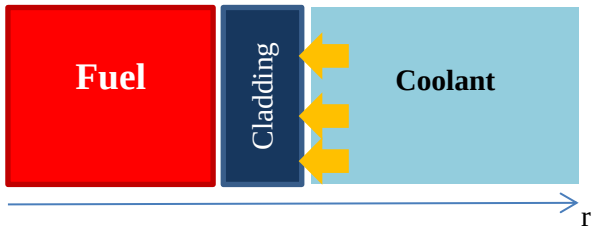

Figure 1-13: Hydrogen boundary condition schematic

As already noticed by Shewmon [37], it is impossible to predict the redistribution solely from the diffusion laws and the Terminal Solid Solubility. Indeed, as long as the hydrogen

concentration does not reach the TSSp, the equilibrium will be established in a quasi-steady-state manner, with a solution close to the one explained in section 1.4.3.3. It means that the highest concentration of hydrogen will occur in the colder area, which is the coolant/cladding interface.

Moreover, the TSSp decreases when the temperature decreases. Therefore the lowest temperature area also has the lowest TSSp. Thus, the point where hydrogen reaches the TSSp first is at the cladding/coolant interface. If instantaneous precipitation is assumed, there is no reason for the hydrogen to diffuse into the cladding. It will precipitate instantaneously upon entry into the cladding. This would however lead to the formation of a solid hydride, and it is not what is observed (see section1.4.2.1). Therefore, the role of precipitation kinetics needs to be examined. This precipitation will explain why hydrogen can diffuse into the cladding. If all the hydrogen in solid solution does not precipitate instantaneously, it remains supersaturated in the solid state. In that case, the previous diffusion equilibrium is modified and hydrogen diffuses toward the fuel/cladding interface.

1.4.5.2 Model of precipitation kinetics developed by Marino

This section follows the mode developed by Marino [38, 39]. In his papers, he proposed a precipitation rate proportional to the difference between supersaturated hydrogen in solid solution concentration C_{ss} and the equilibrium value (given by the TSSp):

$$\frac{dC_{ss}}{dt} = -\alpha^2(C_{ss} - TSSp) \qquad 1\text{-}46$$

The kinetics parameter α^2 has been studied by Kammenzind, who measured it in his experiment and proposed an Arrhenius law to describe its dependence on temperature [24]. Figure 1-14 shows Kammenzind's measurements and the linear interpolation of his data. The value of α is plotted against the inverse of the temperature (in Kelvin).

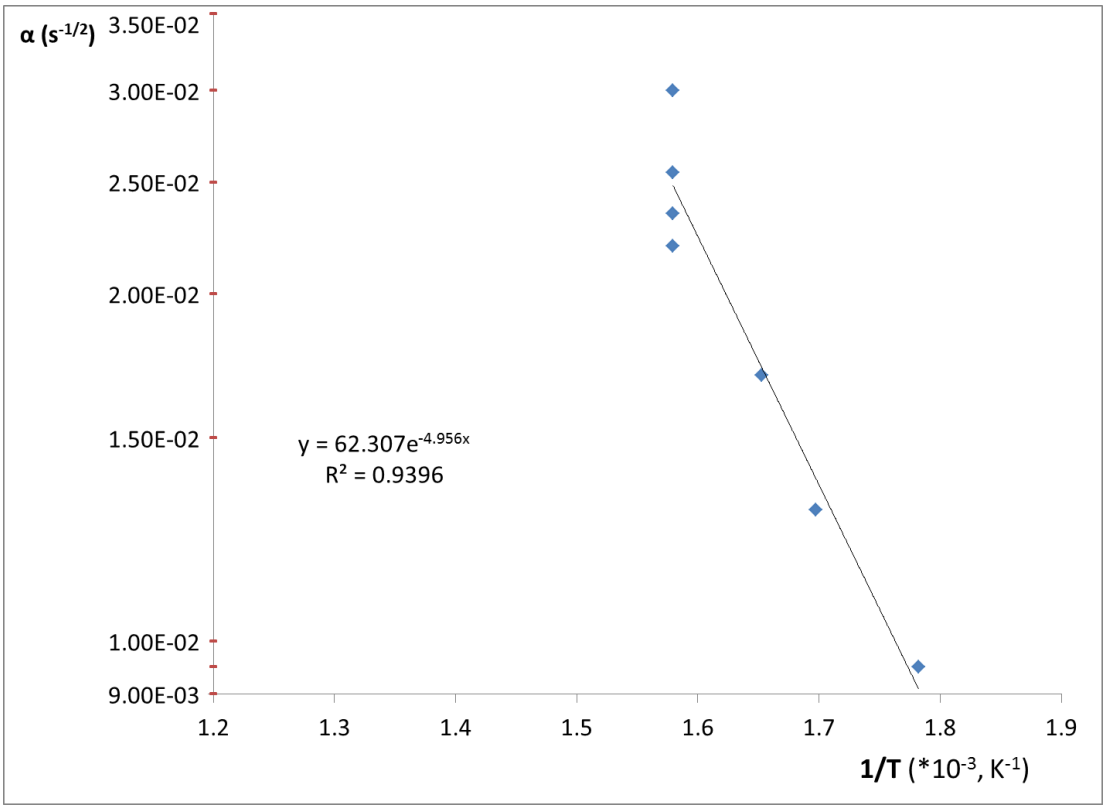

Figure 1-14: Kammenzind measurement of the rate of precipitation as a function of temperature

The equation found for the kinetics parameter is:

$$\alpha = A_\alpha * exp\left(-\frac{Q_\alpha}{RT}\right) \qquad \textbf{1-47}$$

With $A_\alpha \approx 62.3\ s^{1/2}$ and $Q_\alpha \approx 4.12 * 10^4\ J$

1.4.6 Summary of the balance equations governing hydrogen concentration

From the precipitation, dissolution and diffusion model explained in the previous sections, the balance equation for hydrogen in solid solution and hydride concentration can be deduced. The variation of hydrogen in solid solution per unit of time is given by the sum of the net flux, the hydrogen created by the dissolution of hydride minus the hydrogen transformed into hydride due to precipitation.

Based on the Sawatzky diffusion model given by equation 1-33, the diffusion flux is equal to:

$$J = -D\nabla C_{ss} - \frac{DC_{ss}Q^*}{RT^2}\nabla T \qquad \textbf{1-48}$$

Hydride precipitation occurs when the C_{ss} surpasses the TSSp. Hydride dissolution occurs when the C_{ss} becomes lower than the TSSd. The TSSp and TSSd values measured by McMinn [40] have been used for the current work. Recalling equations 1-45,

$$\begin{cases} TSSd\ (wt.ppm) = 106446.7 * exp\left(-\frac{4328.67}{T\ (K)}\right) \\ TSSp\ (wt.ppm) = 138746.0 * exp\left(-\frac{4145.72}{T\ (K)}\right) \end{cases} \qquad \textbf{1-49}$$

According to Marino's equation 1-46, the rate of precipitation (in wt.ppm/s) is given by:

$$R_{precipitation} = -\alpha^2(C_{ss} - TSSp) \qquad \textbf{1-50}$$

The dissolution is assumed instantaneous by most authors and is assumed here. In order to simplify our future calculations, we assume a linear law for the dissolution, with a characteristic time very small compared to the precipitation characteristic time:

$$R_{dissolution} = \beta^2(C_{ss} - TSSp) \qquad \textbf{1-51}$$

Note: $\beta \gg \alpha, \beta \gg \frac{l^2}{D}$

The diffusion coefficient is calculated using Kearns' correlation [23]

$$D = A_{diff} * exp(-\frac{Q_{Diff}}{RT}) \qquad \textbf{1-52}$$

Four different cases have to be taken into account for the writing of the balance equations.

In the first case, the concentration of hydrogen in solid solution is greater than the TSSp. Then, precipitation occurs according to the laws described above.

- Precipitation:

$$if\ C_{ss} > TSSp, \begin{Bmatrix} \frac{dC_{ss}}{dt} = -\nabla.J - \alpha^2(C_{ss} - TSSp) \\ \frac{dC_p}{dt} = \alpha^2(C_{ss} - TSSp) \end{Bmatrix} \qquad \textbf{1-53}$$

In the second case, the concentration in solid solution is between the TSSp and the TSSd. This is the "hysteresis" area, where neither diffusion nor precipitation occurs.

- Hysteresis:

$$if\ TSSp \geq C_{ss} > TSSd, \begin{Bmatrix} \frac{dC_{ss}}{dt} = -\nabla \cdot J \\ \frac{dC_p}{dt} = 0 \end{Bmatrix} \qquad \textbf{1-54}$$

In the third case, the concentration in solid solution is below the TSSd. The hydrogen in the precipitated hydrides (C_p) is dissolving so that the C_{ss} matches the TSSd value. This is possible only if there are hydrides ($C_p > 0$).

- Dissolution:

$$if\ TSSd \leq C_{ss}\ and\ C_p > 0\ and\ \nabla J$$

$$> 0, \begin{Bmatrix} \frac{dC_{ss}}{dt} = -\nabla \cdot J + \beta^2(TSSd - C_{ss}) \\ \frac{dC_p}{dt} = -\beta^2(TSSd - C_{ss}) \end{Bmatrix} \qquad \textbf{1-55}$$

In the fourth and last case, the concentration in solid solution is below the TSSd but there are no more hydrides to dissolve. In that case, the only change to hydrogen concentration comes from net diffusion flux.

- Diffusion only:

$$if\ TSSd \geq C_{ss}\ and\ C_p = 0, \begin{Bmatrix} \frac{dC_{ss}}{dt} = -\nabla.J \\ \frac{dC_p}{dt} = 0 \end{Bmatrix} \quad \textbf{1-56}$$

The model constants have been taken from the literature and are summarized in Table 1-3.

Table 1-3: Hydrogen model constants

Phenomenon	Parameter	Value	Unit	Source	Comments
Fick's law	A_{Dff}	$7.90*10^{-7}$	m^2/s	[41]	Longitudinal diffusion
	Q_{Diff}	$4.49*10^4$	J/mol	[41]	Longitudinal diffusion
Soret effect	Q*	$2.51*10^4$	J/mol/K	[24]	Average value
Precipitation	A_P	$1.39*10^5$	wt. ppm	[40]	Unirradiated
	Q_P	$3.45*10^4$	J/mol	[40]	Unirradiated
Dissolution	A_D	$1.06*10^5$	wt. ppm	[40]	Unirradiated
	Q_D	$3.60*10^4$	J/mol	[40]	Unirradiated
Precipitation kinetics	A_α	$6.23*10^1$	$s^{1/2}$	[24]	
	Q_α	$4.12*10^4$	J/mol	[24]	

1.5 Motivation of the study and thesis outline

According to the previous sections, hydride precipitation in nuclear fuel cladding can increase the risk of cladding failure. Moreover, the hydrogen does not distribute homogeneously and shows specific features (rim, blisters) that create high local concentration of hydrides, and strongly affects the cladding mechanical properties. The understanding of this specific distribution requires the study of the hydrogen redistribution in the cladding. According to the model detailed above, it is mainly the results of three different processes: diffusion under concentration gradient, diffusion under temperature gradient and precipitation.

The first goal of this work is to combine these models, following the balance equations 1-53 to 1-56, and implement them into computer codes. Following this, the estimation of the local hydrogen concentration and of the hydride volume fraction will be possible. As a consequence, it will allow the identification of “high risk areas” due to the hydrides. This is the purpose of Chapter 2. Since all of the hydrogen phenomena are closely related to temperature, we used the fuel performance code BISON, developed by Idaho National Laboratory, to obtain the temperature distribution in the fuel rod. This code requires precise boundary conditions (coolant temperature and energy deposition due to fission reaction. To obtain these, a coupling with COBRA-TF and DeCART has been developed. This parallel project is detailed in Ian Davis Master of Science thesis [42] and is briefly summarized in the second chapter.

The second goal of the work is to improve our understanding of hydrogen behavior with fundamental experiments. The model detailed above uses constants that are not very well known (heat of transport and rate of precipitation). Because of this, two different experiments were designed in order to get more data about the Soret effect and the precipitation kinetics. These are described in Chapter 3. The heat of transport has been studied through a benchtop experiment, as detailed in section 3.1. The precipitation rate has been measured using an X-Ray diffraction in

situ experiment, at the APS synchrotron as detailed in section 3.2. Finally, preliminary calculations and reviews are shown in Chapter 4, which provide ideas for future development of the model and its derivations. Conclusions of the work are given in Chapter 5.

Chapter 2: Modeling and simulation of hydrogen distribution

Using the model described in Chapter 1, it is possible to predict the distribution of hydrogen in solid solution and precipitated hydrides if the temperature distribution is well known. Due to the complexity of the reactor core geometry, it is not possible to have reliable analytical profiles of the temperature distribution. Moreover, the hydrogen model does not provide analytically solvable results when diffusion and precipitations of hydrogen occur simultaneously. For both of these reasons, the prediction of hydrogen distribution required the use of computer codes.

As a first step, a simple 1D Matlab code has been created, which allows the calculation of simple temperature profiles. Its primary goal is to understand the consequences of the physical model and try basic calculations. The Matlab code structure and content is detailed in section 2.1.

The seconds step included the use of a fuel performance code developed by Idaho National Laboratory called BISON [43]. In this study, a contribution to this computer code has been created in the form of the hydrogen model explained in section 2.2. To work properly, this code requires a neutronics input (volumetric energy deposition) and a thermo-hydraulic boundary condition (coolant or outer cladding temperature). This data is provided through a coupling with DeCART (neutronics code) and COBRA-TF (thermal-hydraulics code) as detailed in section 2.3.1. Both of the codes have been tested and benchmarked. These results are presented in section 2.4. Finally, BISON has been run on typical fuel rod geometries and the results are given in section 2.5, 2.6.3 and 2.6.4 that respectively deal with cuboid, 5-pellets rod and 360-pellets rod geometries.

2.1 Creation of "HydruLab": a 1D Finite difference simulation code on Matlab

The model presented in the previous section now should be implemented in Matlab. A one-dimensional geometry is considered. The equations are expressed according to the finite difference theory. A steady state temperature gradient is assumed. This code has been named HydruLab.

2.1.1 Derivation of the hydrogen balance equations for HydruLab

The set of equations changes, depending on the concentration of hydrogen in solid solution. Table 2-1 describes the conditions.

Table 2-1: Summary of the dissolution and precipitation conditions

#	Case	C_{ss} condition	C_p condition	Precipitation term	Dissolution term
1	Precipitation	C_{ss} > TSSp	C_p >0	Yes	No
			C_p =0 (<0)	Yes	No
2	Hysteresis	TSSd < C_{ss} < TSSp	C_p >0	No	No
			C_p =0 (<0)	No	No
3	Dissolution	C_{ss} < TSSd	C_p >0	No	Yes
4	Diffusion only		C_p =0 (<0)	No	No

In Table 2-1, C_{ss} is the amount of hydrogen in solid solution and C_p is the amount of hydrogen in the precipitated hydrides. The equations are derived for each case.

2.1.1.1 Case 1: Precipitation

In this case, the concentration in solid solution is greater than the TSSp. Recalling equation 1-53:

$$if\ C_{ss} > TSSp, \begin{Bmatrix} \frac{dC_{ss}}{dt} = -\nabla.J - \alpha^2(C_{ss} - TSSp) \\ \frac{dC_p}{dt} = \alpha^2(C_{ss} - TSSp) \end{Bmatrix} \qquad \textbf{2-1}$$

$$with\ J = -D\nabla C_{ss} - \frac{DC_{ss}Q^*}{RT^2}\nabla T \qquad \textbf{2-2}$$

In one dimension and Cartesian geometry, it becomes:

$$\begin{gathered} \frac{dC_{ss}}{dt} = -\frac{d}{dx}J - \alpha^2(C_{ss} - TSSp) \\ \frac{dC_p}{dt} = \alpha^2(C_{ss} - TSSp) \\ J = -D\frac{dC_{ss}}{dx} - \frac{DC_{ss}Q^*}{RT^2} * \frac{dT}{dx} \end{gathered} \qquad \textbf{2-3}$$

Considering a δx unit cell and a δt time step, the finite difference form is:

$$\begin{Bmatrix} C_{ss}(t_n + 1) - C_{ss}(t_n) = -\frac{\delta t}{\delta x}\big(J(x_n + 1) - J(x_n)\big) - \delta t \cdot \alpha^2(C_{ss}(t_n, x_n) - TSSp) \\ C_p(t_n + 1) - C_p(t_n) = \delta t \cdot \alpha^2(C_{ss}(t_n, x_n) - TSSp) \\ J = -D\frac{C_{ss}(t_n, x_{n+1}) - C_{ss}(t_n, x_n)}{\delta x} - \frac{DC_{ss}C_{ss}(t_n, x_n)Q^*}{RT^2} * \frac{T(t_n, x_{n+1}) - T(t_n, x_n)}{\delta x} \end{Bmatrix} \qquad \textbf{2-4}$$

2.1.1.2 Case 2: Hysteresis

Similarly, the equation can be transformed:

$$if\ TSSp \geq C_{ss} > TSSd, \begin{Bmatrix} \frac{dC_{ss}}{dt} = -\nabla.J \\ \frac{dC_p}{dt} = 0 \end{Bmatrix} \qquad \textbf{2-5}$$

Equation 2-5 is transformed into:

$$C_{ss}(t_n+1) - C_{ss}(t_n) = -\frac{\delta t}{\delta x}\big(J(x_n+1) - J(x_n)\big) \qquad \textbf{2-6}$$
$$C_p(t_n+1) - C_p(t_n) = 0$$

2.1.1.3 Case 3: Dissolution

In case of dissolution:

$$if\ TSSd \le C_{ss}\ and\ C_p > 0\ and\ \nabla J$$

$$> 0, \begin{Bmatrix} \frac{dC_{ss}}{dt} = -\nabla.J + \beta^2(TSSd - C_{ss}) \\ \frac{dC_p}{dt} = -\beta^2(TSSd - C_{ss}) \end{Bmatrix} \qquad \textbf{2-7}$$

Note: $\beta \gg \alpha, \beta \gg \frac{l^2}{D}$

Thus:

$$C_{ss}(t_n+1) - C_{ss}(t_n) = -\frac{\delta t}{\delta x}\big(J(x_n+1) - J(x_n)\big) - \delta t \cdot \beta(C_{ss}(t_n,x_n) - TSSd)$$
$$C_p(t_n+1) - C_p(t_n) = \delta t \cdot \beta(C_{ss}(t_n,x_n) - TSSd) \qquad \textbf{2-8}$$
$$J = -D\frac{C_{ss}(t_n,x_{n+1}) - C_{ss}(t_n,x_n)}{\delta x} - \frac{DC_{ss}C_{ss}(t_n,x_n)Q^*}{RT^2} * \frac{T(t_n,x_{n+1}) - T(t_n,x_n)}{\delta x}$$

2.1.1.4 Case 4: Diffusion only

Finally, in case of pure diffusion,

$$if\ TSSd \ge C_{ss}\ and\ C_p = 0, \begin{Bmatrix} \frac{dC_{ss}}{dt} = -\nabla.J \\ \frac{dC_p}{dt} = 0 \end{Bmatrix} \qquad \textbf{2-9}$$

Becomes:

$$C_{ss}(t_n+1) - C_{ss}(t_n) = -\frac{\delta t}{\delta x}\big(J(x_n+1) - J(x_n)\big) \qquad \textbf{2-10}$$
$$C_p(t_n+1) - C_p(t_n) = 0$$

2.1.2 Structure of the code HydruLab

The code assumes 1D geometry and divides the one dimension into n cells. It also divides the time into timesteps that are much shorter than the characteristic times for the phenomena studied. The code corresponds to the implementation of equations from the previous section (2.1.1), using finite differences. For a given time step, the code updates the temperature if needed. Then, it calculates the TSSp, TSSd, diffusion and alpha coefficient values using this new temperature. After that, the net flux between each cell is calculated. From the flux and according to the condition on the hydrogen concentration, the new values of the concentration of precipitated hydrogen and in solid solution hydrogen are calculated in each cell. Figure 2-1 illustrates the structure of the code.

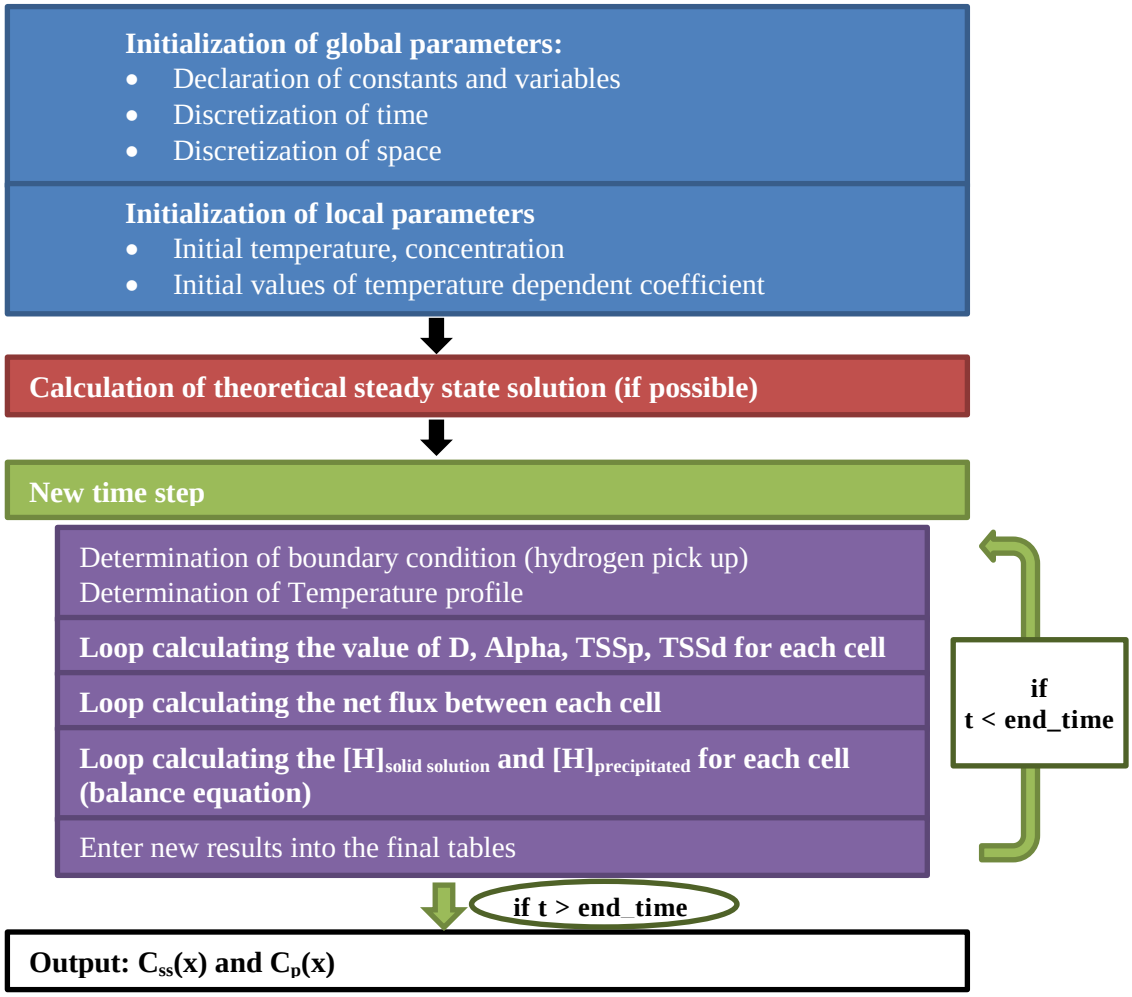

Figure 2-1: Structure of the implementation of the hydrogen model in HydruLab

The full code can be found in Appendix A.

A benchmark of the code is described in section 2.4. Results are given in the sections 2.5.

2.2 Implementation of the model in the 3D fuel performance code BISON

The temperature in the core is heterogeneous not only along the axial direction, but also along the radial and circumferential directions. This is why HydruLab is not sufficient to calculate hydrogen distribution in more complicated cases. Because of this, a 3D computer code

(BISON) has been developed by Idaho National Laboratory. This code is based on the framework MOOSE [44]. BISON provides accurate 3D temperature distributions in the fuel and in the cladding. Thanks to the modularity of these codes, it has also been possible to implement the hydrogen model into it, and thus to obtain 2D and 3D hydrogen distribution evolution.

2.2.1 BISON and MOOSE overview

MOOSE, for Multiphysics Object Oriented Simulation Environment, is a framework for solving computational engineering problems in a well-managed and coordinated manner[44]. It is part of an Idaho National Laboratory project and designed to reduce the expense and time required to develop new applications. According to its authors, its strengths are that it uses very robust solution methods, is designed to be easily extended and maintained and it is efficient on both a few (quick simulations) and many processors (sophisticated simulation). The MOOSE solver is based on the Galerkin Finite Element theory[45]. Its main capabilities are summarized in Table 2-2.

Table 2-2: MOOSE capabilities

Capability	Interest regarding the project
1D, 2D and 3D	Allow axial, radial and azimuthal simultaneous calculations
Finite Element Based (Continuous and discontinuous Galerkin)	Precision able to solve the temperature variation at the inter-pellet gap
Fully Coupled, Fully implicit	Limit numerical inconsistencies
Unstructured Mesh	Allow all geometries
Mesh adaptivity	Allow a refined mesh in specific areas
Parallelism	Strongly decrease computational time
High order shape functions	High polynomial fitting provides accurate interpolation

BISON is a nuclear fuel performance analysis code, built on top of the MOOSE framework. It is used primarily for analysis of UO_2 fuel, but has also been used to model TRISO fuel and rod and plate metal fuel [46]. Since it is based on MOOSE, it is also an implicit and fully

coupled core, capable of running in parallel. It uses the library from ELK (mechanical properties) and FOX (materials properties). The BISON current capabilities are [43]:

- Oxide fuel behavior
  - Temperature and burnup dependent material properties (density, thermal conductivity from MATPRO[10])
  - Volumetric heat generation (given a fission rate input)
  - Thermal, fission product swelling, densification strains
  - Thermal and irradiation creep
  - Fuel fracture via relocation and smeared cracking
  - Fission gas release (Model currently being improved)
- Gap/Plenum behavior
  - Gap heat transfer
  - Mechanical contact
  - Plenum pressure function of evolving gas volume, gas mixture and temperature
- Cladding behavior
  - Thermal and irradiation creep
  - Thermal expansion
  - Irradiation growth
  - Plasticity
- Coolant Chanel: Closed channel thermal hydraulics with heat transfer coefficient

2.2.2 Derivation of the equations according to Galerkin finite element theory

As stated above, because of its modularity, it is possible to implement new models and equations into BISON. However, a transformation of the equations is necessary. Since BISON is based on the Galerkin Finite Element theory, the equation has to be transformed into their weak form [45]. The weak form corresponds to the scalar product (in the function space) of the equation and a given shape function:

$$WeakForm(f) = (f, \psi) = \iiint_V f(x, y, z) \cdot \psi_i(x, y, z) dV \qquad \textbf{2-11}$$

The function scalar product is represented by (f ,g), where f and g are space and time dependent functions. In the case of the second derivative, the weak form requires integration by parts, to

remove the second order derivative. For instance (applying the divergence theorem for the second term):

$$WeakForm(\nabla^2 T) = \iiint_V \nabla^2 T(x,y,z) \cdot \psi_i(x,y,z) dV \qquad \textbf{2-12}$$

$$WeakForm(\nabla^2 T) \qquad \textbf{2-13}$$

$$= -\iiint_V \nabla T(x,y,z) \cdot \nabla \psi_i(x,y,z) dV$$

$$+ \iint_S \psi_i(x,y,z) \cdot \nabla T(x,y,z) \cdot d\boldsymbol{S}$$

Once the weak form of an entire equation is obtained, each term is considered individually. This piece of the equation (in its weak form) is called a Kernel, and it is what has to be implemented in the code. In order to evaluate the convergence of the code toward a solution (through iteration), MOOSE uses a mathematical tool called the Free Jacobian Newton Krylov. This is considerably faster than the calculation of the residuals of each variable. This Jacobian has to be calculated for each kernel, and is obtained by calculating the derivative of the kernel weak form with respect to the primary variable. Details are provided in MOOSE documentation [44].

2.2.2.1 Kernels

The equations from the model given in section 1.4.6 are written below. Each member of the equations is represented with a different color that corresponds to the kernels. The following kernels will be created:

- Diffusion (only for hydrogen in solid solution) - red
- Precipitation/Dissolution for hydrogen in solid solution - green
- Precipitation/Dissolution for precipitated hydrides - orange
- Time derivative (Implemented in MOOSE) - blue

The MOOSE structure implies that a given kernel can be used with different variables. The time derivative $\frac{d}{dt}$ is the same for many equations. Therefore, the same kernel is called for

each equation. Then, in the input file, the variables on which the kernel applies are specified. Typically, the time derivative is used for the hydrogen in solid solution, the precipitated hydride, the temperature and all the partial differential equation that include time derivative of the primary variable. The diffusion flux is given by:

$$J = -D\nabla C_{ss} - \frac{DC_{ss}Q^*}{RT^2}\nabla T \qquad \textbf{2-14}$$

The rate of precipitation (in wt.ppm/s) is given by:

$$R_{precipitation} = -\alpha^2(C_{ss} - TSSp) \qquad \textbf{2-15}$$

The rate for dissolution is given by:

$$R_{dissolution} = \beta^2(C_{ss} - TSSp) \qquad \textbf{2-16}$$

The diffusion coefficient is given by:

$$D = A_{diff} * exp(-\frac{Q_{Diff}}{RT}) \qquad \textbf{2-17}$$

The balance equations are slightly rearranged to have a 0 term on the right hand side.

- Precipitation:

$$if\ C_{ss} > TSSp, \begin{Bmatrix} \frac{dC_{ss}}{dt} + \nabla.J + \alpha^2(C_{ss} - TSSp) = 0 \\ \frac{dC_p}{dt} - \alpha^2(C_{ss} - TSSp) = 0 \end{Bmatrix} \qquad \textbf{2-18}$$

In the second case, the concentration in solid solution is between the TSSp and the TSSd. This is the “hysteresis” area, where neither diffusion nor precipitation occurs.

- Hysteresis:

$$if\ TSSp \geq C_{ss} > TSSd, \begin{Bmatrix} \frac{dC_{ss}}{dt} + \nabla.J = 0 \\ \frac{dC_p}{dt} = 0 \end{Bmatrix} \qquad \textbf{2-19}$$

In the third case, the concentration in solid solution is below the TSSd. The hydrogen in the precipitated hydrides (C_p) is dissolving so that the C_{ss} matches the TSSd value. This is possible only if there are hydrides ($C_p > 0$).

- Dissolution:

$if\ TSSd \leq C_{ss}\ and\ C_p > 0\ and\ \nabla J > 0,$

$$\begin{cases} \frac{dC_{ss}}{dt} + \nabla . J - \beta^2 (TSSd - C_{ss}) = 0 \\ \frac{dC_p}{dt} + \beta^2 (TSSd - C_{ss}) = 0 \end{cases} \qquad \textbf{2-20}$$

In the fourth and last case, the concentration in solid solution is below the TSSd but there is no more hydride to dissolve. In that case, only remains the net diffusion flux.

- Diffusion only:

$$if\ TSSd \geq C_{ss}\ and\ C_p = 0, \begin{cases} \frac{dC_{ss}}{dt} + \nabla . J = 0 \\ \frac{dC_p}{dt} = 0 \end{cases} \qquad \textbf{2-21}$$

In Table 2-3 and Table 2-4, the strong form, the weak form, the general weak form and the Jacobian of each kernel are specified. The general weak form is the weak form with the primary variable replaced by the undefined variable, u. This allows the multiple use of the same kernel in different equations. Table 2-3 corresponds to the equation in the case of precipitation. Table 2-4 corresponds to the equation in the case of dissolution.In the absence of precipitation and dissolution (“Hysteresis”or “Diffusion only”), all the forms of the diffusion/precipitation kernels are equal.

Table 2-3: Strong form, weak form and Jacobian of the hydrogen kernel in case of precipitation (case 1)

Kernel name	HydrogenDiffusion	HydrogenPrecipitation	HydridePrecipitation	TimeDerivative
Description	Net diffusion flux (including Fick's law and Soret effect)	Precipitation and dissolution laws, applied to hydrogen in solid solution	Precipitation and dissolution laws, applied to hydrogen in precipitated hydrides	Time derivative kernel created by MOOSE developers
Strong form	$-\nabla \cdot \left(D\nabla C_{ss} + \frac{DC_{ss}Q^*}{RT^2}\nabla T\right)$	$\alpha^2(C_{ss} - TSSp)$	$-\alpha^2(C_{ss} - TSSp),$	$\frac{dC_{ss}}{dt}$
Weak form	$\left(D\nabla C_{ss} + \frac{DC_{ss}Q^*}{RT^2}\nabla T, \nabla\psi_i\right)$	$(\alpha^2(C_{ss} - TSSp), \psi_i)$	$(-\alpha^2(C_{ss} - TSSp), \psi_i)$	$\left(\frac{dC_{ss}}{dt}, \psi\right)$
General weak form	$\left(D\nabla u + \frac{DuQ^*}{RT^2}\nabla T, \nabla\psi_i\right)$	$(\alpha^2(u - TSSp), \psi_i)$	$(-\alpha^2(C_{ss} - TSSp), \psi_i)$	$\left(\frac{du}{dt}, \psi\right)$
Jacobian	$\left(D\nabla\psi_i + \frac{D\psi_i Q^*}{RT^2}\nabla T, \nabla\psi_j\right)$	$(\alpha^2\psi_i, \psi_j)$	No Jacobian	$\left(\frac{1}{\Delta t}\psi_j, \psi_i\right)$

Table 2-4: Strong form, weak form and Jacobian of the hydrogen kernel in case of dissolution (case 2)

Kernel name	HydrogenDiffusion	HydrogenPrecipitation	HydridePrecipitation	TimeDerivative
Description	Net diffusion flux (including Fick's law and Soret effect)	Precipitation and dissolution laws, applied to hydrogen in solid solution	Precipitation and dissolution laws, applied to hydrogen in precipitated hydrides	Time derivative kernel created by MOOSE developers
Strong form	$-\nabla \cdot \left(D\nabla C_{ss} + \frac{DC_{ss}Q^*}{RT^2}\nabla T\right)$	$-\beta^2(TSSd - C_{ss})$	$\beta^2(TSSd - C_{ss})$	$\frac{dC_{ss}}{dt}$
Weak form	$\left(D\nabla C_{ss} + \frac{DC_{ss}Q^*}{RT^2}\nabla T, \nabla\psi_i\right)$	$(-\beta^2(TSSd - C_{ss}), \psi_i)$	$(\beta^2(TSSd - C_{ss}), \psi_i)$	$\left(\frac{dC_{ss}}{dt}, \psi\right)$
General weak form	$\left(D\nabla u + \frac{DuQ^*}{RT^2}\nabla T, \nabla\psi_i\right)$	$(-\beta^2(TSSd - u), \psi_i)$	$(\beta^2(TSSd - C_{ss}), \psi_i)$	$\left(\frac{du}{dt}, \psi\right)$
Jacobian	$\left(D\nabla\psi_i + \frac{D\psi_i Q^*}{RT^2}\nabla T, \nabla\psi_j\right)$	$(\beta^2\psi_i, \psi_j)$	No Jacobian	$\left(\frac{1}{\Delta t}\psi_j, \psi_i\right)$

2.2.2.2 Summary of the conditions:

Different parts of the kernels are used, depending on the value of the concentration of hydrogen in solid solution (C_{ss}). These conditions are summarized in Table 2-5.

Table 2-5: Summary of the dissolution and precipitation conditions

#	Case	C_{ss} condition	C_p condition	Precipitation term	Dissolution term
1	Precipitation	C_{ss} > TSSp	$C_p > 0$	Yes	No
			$C_p = 0$ (<0)	Yes	No
2	Hysteresis	TSSd < C_{ss} < TSSp	$C_p > 0$	No	No
			$C_p = 0$ (<0)	No	No
3	Dissolution	C_{ss} < TSSd	$C_p > 0$	No	Yes
4	Diffusion only		$C_p = 0$ (<0)	No	No

2.2.2.3 Auxiliary Kernel

The equation governing the balance of hydrogen in the precipitated hydride is not a classic Partial Differential Equation (PDE). The time derivative of this concentration is a function of the concentration of hydrogen in solid solution:

$$\frac{dC_p}{dt} = f(C_{ss}) \qquad \text{2-22}$$

Therefore, this equation does not have to be solved as a PDE. Once the C_{ss} solution is known, the calculation of C_p is straightforward. This is the reason why the HydridePrecipitation kernel does not have a Jacobian. In order to accelerate the calculation, BISON allows the use of a finite difference calculation for this type of equation. The kernel is then replaced by what is called an Auxiliary kernel. Recalling the equations 1-53 to 1-56:

- Precipitation:

$$if\ C_{ss} > TSSp,\quad \frac{dC_p}{dt} - \alpha^2(C_{ss} - TSSp) = 0 \qquad \textbf{2-23}$$

- Hysteresis:

$$if\ TSSp \geq C_{ss} > TSSd,\quad \frac{dC_p}{dt} = 0 \qquad \textbf{2-24}$$

- Dissolution

$$if\ TSSd \leq C_{ss}\ and\ C_p > 0\ and\ \nabla J > 0,\quad \frac{dC_p}{dt} + \beta^2(TSSd - C_{ss}) = 0 \qquad \textbf{2-25}$$

- Diffusion only:

$$if\ TSSd \geq C_{ss}\ and\ C_p = 0,\quad \frac{dC_p}{dt} = 0 \qquad \textbf{2-26}$$

The equations 2-23 to 2-26 become:

- Precipitation:

$$if\ C_{ss} > TSSp,\ \ C_p(t_{n+1}) = C_p(t_n) + \delta t * \alpha^2 * (C_{ss} - TSSp) \qquad \textbf{2-27}$$

- Hysteresis:

$$if\ TSSp \geq C_{ss} > TSSd,\quad C_p(t_{n+1}) = C_p(t_n) \qquad \textbf{2-28}$$

- Dissolution

$$if\ TSSd \leq C_{ss}\ and\ C_p > 0\ and\ \nabla J > 0,\quad C_p(t_{n+1}) = C_p(t_n) - \delta t * \beta^2 * (TSSd - C_{ss}) \qquad \textbf{2-29}$$

- Diffusion only:

$$if\ TSSd \geq C_{ss}\ and\ C_p = 0,\ \ C_p(t_{n+1}) = C_p(t_n) \qquad \textbf{2-30}$$

2.2.2.4 Boundary condition

- **General comments on the boundary conditions for hydrogen**

In order to solve the second order partial differential equations that govern the hydrogen in solid solution concentration, it is necessary to specify the boundary conditions. There are two ways to express these boundary conditions. The first one is to impose a given concentration at a boundary:

$$C_{ss}(x_0, y, z) = C_{BC} \qquad \textbf{2-31}$$

The second one is to impose a flux at the boundary:

$$\boldsymbol{J} \cdot \boldsymbol{dS}(x_0) = J_0 \qquad \textbf{2-32}$$

It has to be noted that the flux is given by equation 1-33 and is not directly proportional to the concentration gradient. Therefore, a zero-flux boundary condition does not imply that the solid solution concentration profile is flat. Indeed, if there is a temperature gradient, the concentration profile has to show a gradient in order to compensate for the flux induced by the Soret effect:

$$\boldsymbol{J} \cdot \boldsymbol{dS}(x_0) = 0 \qquad \textbf{2-33}$$

$$\boldsymbol{\nabla} C_{ss} \cdot \mathbf{dS} = -\frac{D C_{ss} Q^*}{RT^2} \boldsymbol{\nabla} T \cdot \mathbf{dS} \qquad \textbf{2-34}$$

As shown by equation 2-34, the concentration gradient ∇C_{ss} is not equal to 0.

- **Expressing the Boundary condition in MOOSE**

Regarding the Galerkin finite element theory, the boundary conditions appear naturally in the weak forms, as a consequence of the integration by parts of terms that have a second order spatial derivative (∇^2). In the finite element theory [45], a condition on a flux is called a “natural boundary condition” or a Neumann boundary condition. A condition on a scalar is called a Dirichlet boundary condition. In order to clarify the MOOSE boundary condition, the example of a simple diffusion case is reproduced below, from the MOOSE documentation [44].

- *Derivation of the weak form in MOOSE documentation of a simple diffusion case*

The equation considered is a typical diffusion equation, steady state and with a source term.

$$-\nabla \cdot \nabla u - f = 0 \qquad \textbf{2-35}$$

Multiplying by a given shape function ψ_i and integrating over the domain Ω:

$$\int_{\Omega} -\nabla . \nabla u * \psi_i d\Omega + \int_{\Omega} f * \psi_i d\Omega = 0 \qquad \textbf{2-36}$$

Integrating by parts:

$$\int_{S} -\nabla u * \psi_i dS + \int_{\Omega} \nabla u * \nabla \psi_i * d\Omega + \int_{\Omega} f * \psi_i * d\Omega = 0 \qquad \textbf{2-37}$$

The red part of the equation 2-37 is the boundary condition, called the "NeumannBC". This boundary condition corresponds to the gradient of the primary variable (u in this case). Any boundary condition is written with brackets:

$$\int_{S} -\nabla u * \psi_i dS = \langle -\nabla u, \psi_i \rangle \qquad \textbf{2-38}$$

- *Derivation for the weak form for the hydrogen model (simplified: diffusion only)*

The precipitation and dissolution phenomena do not interfere with the boundary condition since they are governed by first-order equations and do not feature any spatial derivative (gradient) in their formulation. Therefore, we simplify the derivation by considering the hysteresis case. Recalling equation 2-20:

$$\frac{dC_{ss}}{dt} + \nabla . J = 0 \qquad \textbf{2-39}$$

Multiplying by a shape function ψ and integrating over the domainΩ,

$$\int_{\Omega} \frac{dC}{dt} * \psi_i * \ d\Omega + \int_{\Omega} \nabla . \left(-D\nabla C - \frac{DCQ^*}{RT^2} \nabla T \right) * \psi_i * \ d\Omega = 0 \qquad \textbf{2-40}$$

Integrating equation 2-40 by parts:

$$\int_{\Omega} \frac{dC}{dt}\, d\Omega + \int_{S} \left(-D\nabla C - \frac{DCQ^{*}}{RT^{2}} \nabla T * \psi_i\right) . dS \qquad \textbf{2-41}$$

$$- \int_{\Omega} \left(-D\nabla C - \frac{DCQ^{*}}{RT^{2}} \nabla T\right) * \nabla \psi_i * d\Omega = 0$$

In our case and by analogy, the Neumann boundary condition corresponds to:

$$\int_{S} -D\nabla C - \frac{DCQ^{*}}{RT^{2}} \nabla T * \psi_i dS = \langle J . dS \rangle \qquad \textbf{2-42}$$

Therefore, in the hydrogen model, the Neumann boundary condition corresponds to the specific flux boundary condition and not to the derivative of the primary variable. A specific boundary condition has been created for the hydrogen model. This boundary condition calculates the hydrogen flux, assuming the oxide kinetics are known, as explained in section 1.2.2, following the derivation in section 1.3.

2.2.3 Hydrogen model source files for BISON

According to the BISON/MOOSE code structure, each piece of code (kernel, auxiliary kernel and boundary condition) is split into two files. This structure is based on the high level Object-Oriented Programming rules. These rules specify that each piece of physics (Hydrogen Diffusion Kernel, hydrogen boundary condition,…) is a class that derives from their respective general class (Kernel, boundary condition,…). It is said that they “inherit” the properties of their global class. The header file (name.h) refers to and declares the variables and classes used. This file also defines the heredity properties. The main file (name.C) corresponds to the calculation and the transcription of the physics equations.

The source code of the Kernels is given in Appendix B. The source code of the Auxiliary Kernel is given in Appendix C. The source code of the Boundary Condition can be found in Appendix D.

2.3 Calculation of the temperature distribution based on DeCART, CTF and BISON

The NEUP project that supports this work also includes the work of Dr. Kostadin Ivanov, Dr. Maria Avramova and Ian Davis on the coupling between COBRA-TF, DeCART and BISON. Since the hydrogen behavior is mainly based on temperature gradient, an accurate prediction of the temperature in the core is necessary. This is why a coupling between the neutronics code DeCART [47], the thermo-hydraulics code COBRA-TFTF [48] and BISON has been developed. The present section, written in strong collaboration with Ian Davis, gives an overview of this coupling. More details can be found in his thesis [42]. Figure 2-2 summarized the interactions between the codes that are explained in the next sections.

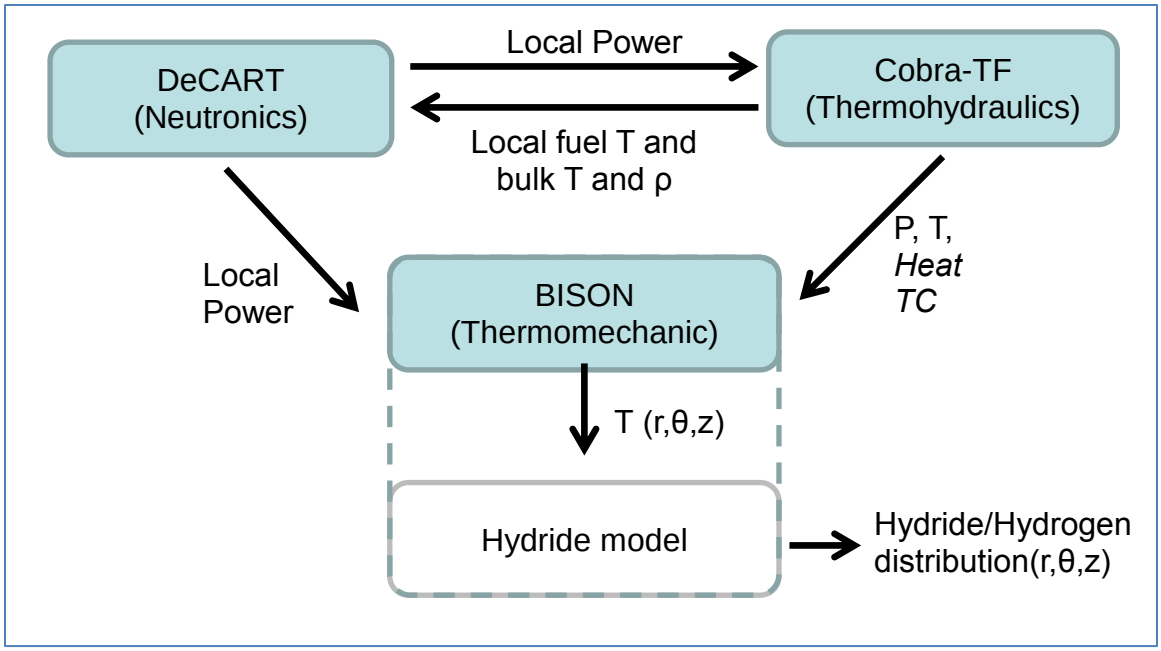

Figure 2-2: Coupling between CTF, DeCART and BISON

The hydride model corresponds to the implementation of the hydrogen model as explained in section 2.2.

2.3.1 Overview of the COBRA-TF/DeCART coupling

COBRA-TF is a two fluid, three field sub-channel thermal-hydraulics code that was modernized and further developed at the Pennsylvania State University. The Pennsylvania State University's version of COBRA-TF is called CTF. DeCART is a method of characteristics neutronics code capable of modeling single pin models to full core calculations of 3D neutron flux. Further development of DeCART has taken place at the University of Michigan. The benefit of coupling a neutronics code with a thermal-hydraulics comes from the mutual feedback between the two codes. The strong heat transfer and fluid flow models in CTF allow for a better prediction of the bulk coolant temperature and density. CTF also contains simplified 3D heat conduction models for nuclear fuel rods to calculate temperatures in the cladding and fuel pellet. DeCART uses the bulk coolant temperature, bulk coolant density, and fuel temperature as feedback for cross-section generation, which affects the 3D neutron flux calculations. Neutronics models in DeCART allow for better prediction of the axial power shape, radial power shape, as well as the relative power of each fuel rod compared to the average power of the array/lattice. CTF uses the total power, the power shapes and the in-pellet radial power factors as feedback for the heat generation in the fuel rod, which enhances the thermal-hydraulics predictions. Feedback between the codes is provided externally using a driver written in Python. DeCART and CTF must converge upon a steady-state solution before depleting to the next time step in the calculation. Coupled CTF-DeCART calculations can then be used to provide boundary condition data to BISON.

2.3.2 Definition of the boundary conditions for BISON

BISON requires certain boundary conditions to run a fuel performance simulation. One of these boundary conditions comes from the thermal-hydraulics calculations. BISON needs a temperature boundary condition on the outside of the fuel rod. Internally, BISON contains the Dittus-Bolter correlation, which can calculate the temperature on the outside of the fuel rod using flow conditions and a given heat transfer coefficient. Though this model is available, it does not include some important characteristics of two phase flow that are available in sub-channel thermal-hydraulics codes. Also, since BISON models one fuel rod at a time, there is not feedback from cross-flow to the heat transfer calculations. Therefore, CTF is used to generate the outer clad temperature profile for BISON. Similar to the temperature boundary conditions, BISON requires fission rates in its calculations. One way to provide these fission rates is through a linear heat rate combined with and axial power shape. Both parameters are calculated as a function of time, and then converted to a fission rate distribution using a constant energy per fission value. As mentioned before, both sets of boundary conditions are generated from coupled CTF-DeCART calculations.

2.3.3 Calculation of the temperature distribution with BISON

Once the temperature of the outer cladding (from CTF) and the energy deposition (from DeCART) are given to BISON, the fuel performance code calculates the temperature distribution in the fuel rod. Based on the physical models described in section 2.2.1 and the fine meshes that are used for the fuel and cladding geometries, BISON provides accurate results not only for temperature, but also for stress and other mechanical parameters. This high fidelity calculation is

then internally used to provide the temperature distribution to the hydrogen model implemented in BISON, as described in section 2.2.2.

2.4 Benchmark of HydruLab and BISON

In order to validate the implementation of the hydrogen model into BISON and HydruLab, a benchmark of the codes has been performed. For some cases, the analytical solution can be calculated and then, used for the benchmarking exercises. For the other cases, the two codes (HydruLab and BISON) have been compared and the reliability of the results has been checked.

The benchmark cases use a simple geometry. In most cases, the geometry is a 3cm x 1cm x 0.6 cm plate. This geometry has been chosen since it corresponds to the one used in the set up for the experiment presented in section 3.1. In HydruLab, a 1D slab of 3 cm or 0.06cm length is used. Because BISON does not have the capability of creating a mesh, the mesh has been generated using the Trelis code, developed by Sandia National Laboratory [49]. Figure 2-3 shows the plate mesh, represented using the visualization tool Paraview [50]:

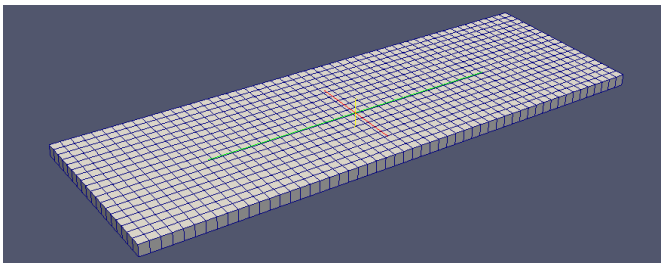

Figure 2-3: Mesh of the plate used for BISON calculation

2.4.1 Benchmark 1: Diffusion equilibrium without precipitation

The first benchmark aims to validate the implementation of the diffusion equation. In this problem, an initial concentration of hydrogen is considered, which is lower than the TSSp. The

external hydrogen incoming flux is zero and a linear temperature gradient is applied to the sample. The balance equation gives:

$$\frac{dC_{ss}}{dt} = -\nabla J = -\frac{d}{dx}J = \frac{d}{dx}(D\nabla C_{ss} + \frac{Q^{*}C_{ss}}{RT^{2}}\nabla T) \quad \textbf{2-43}$$

2.4.1.1 Steady State calculation

The steady state of this equation can be solved analytically:

$$\nabla J(x) = cst \quad \textbf{2-44}$$

Since no flux is assumed at the boundaries, the constant is equal to 0. Therefore:

$$\nabla C_{ss} + \frac{Q^{*}C_{ss}}{RT^{2}}\nabla T = 0 \quad \textbf{2-45}$$

$$\frac{\mathrm{d}C_{ss}}{\mathrm{dx}} = -\frac{Q^{*}C_{ss}}{RT^{2}} * \frac{\mathrm{d(T)}}{\mathrm{dx}} \quad \textbf{2-46}$$

Solving the problem in T,

$$\frac{dC_{ss}}{dx} = \frac{dC_{ss}}{dT} * \frac{C_{ss}T}{dx} \quad \textbf{2-47}$$

Then,

$$\frac{dC_{ss}}{dT} = -\frac{Q^{*}C_{ss}}{RT^{2}} \quad \textbf{2-48}$$

$$\frac{dC_{ss}}{C_{ss}} = -\frac{Q^{*}}{R} * \frac{dT}{T^{2}} \quad \textbf{2-49}$$

Integrating on the x variable,

$$\ln(C_{ss}) - \ln(C_{x0}) = \frac{Q^{*}}{RT(x)} - \frac{Q^{*}}{RT(x_0)} \quad \textbf{2-50}$$

Taking the exponential:

$$C_{ss} = \exp\left(\frac{Q^{*}}{RT(x)}\right) * \exp\left(ln\left(C_{x0} - \frac{Q^{*}}{RT(x_0)}\right)\right) \quad \textbf{2-51}$$

Equation 2-51 can be rewritten as:

$$C_{ss} = C_0 * \exp(\frac{Q^*}{RT}) \qquad \textbf{2-52}$$

The integration constant can be calculated by conservation of mass:

$$\frac{1}{l} * \int_0^l C_0 \exp\left(\frac{Q^*}{RT(x)}\right) dx = C_{ini} \qquad \textbf{2-53}$$

For the calculation, the values assumed for the boundary and initial conditions are detailed in Table 2-6.

Table 2-6: Boundary and initial condition for benchmark 1

Condition	**Value**
Initial hydrogen concentration	600 wt. ppm
Temperature gradient type	Linear
Lowest temperature	600 °C
Highest temperature	700 °C

According to Fourier's heat conduction law and assuming constant conductivity, the temperature gradient is linear. The following picture shows the temperature profile calculated from a 3D BISON simulation (top view).

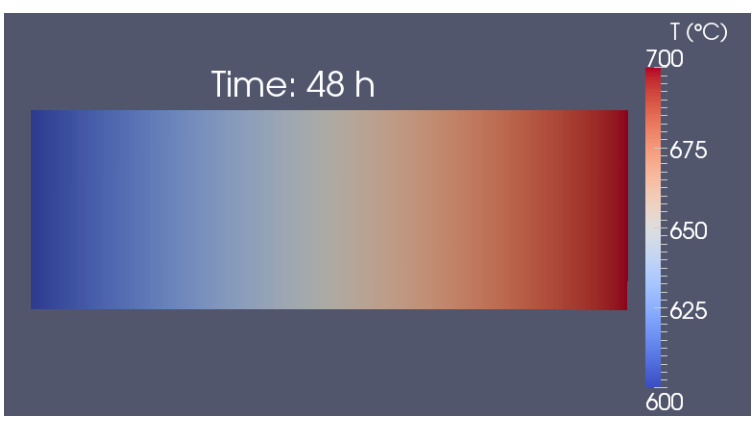

Figure 2-4: BISON temperature profile using boundary conditions of 600°C and 700°C for benchmark 1

The steady state is obtained after 24h, which is also confirmed by the analysis of the difference between the steady state and the transient values. The following figure shows the hydrogen profile as given by HydruLab, BISON and the analytical solution.

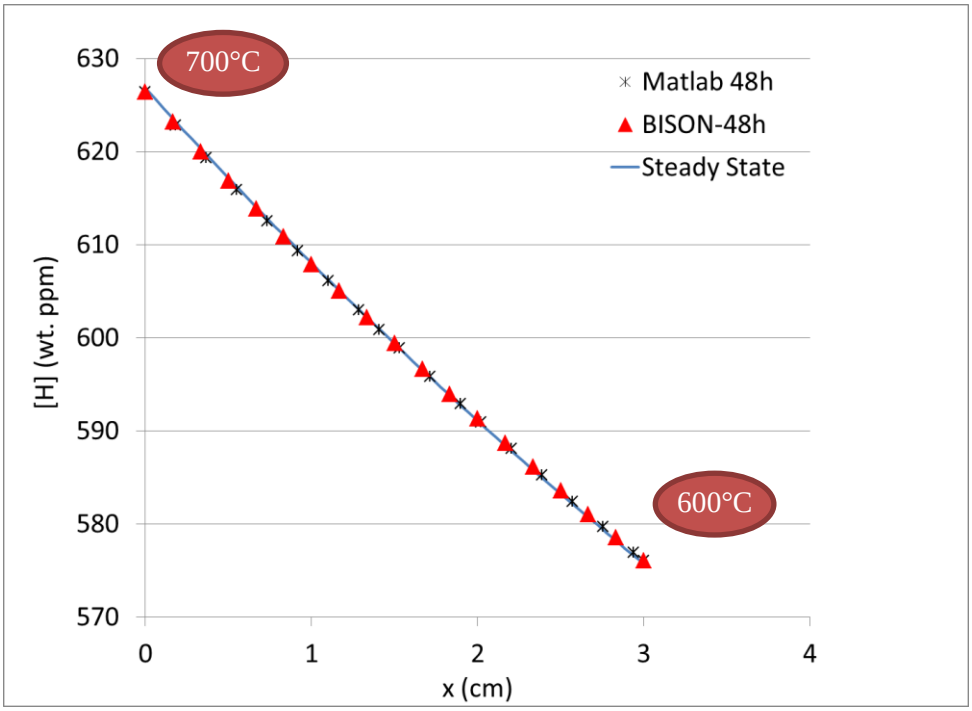

Figure 2-5: Comparison between the steady-state distribution of hydrogen in solid solution exposed to a linear temperature gradient of 600°C-700°C calculated by BISON and HydruLab and the analytical solution

The numerical calculations (BISON and HydruLab) agree well with the analytical solution. Additionally, BISON allows showing a 3D view of the hydrogen concentration, as shown in Figure 2-6.

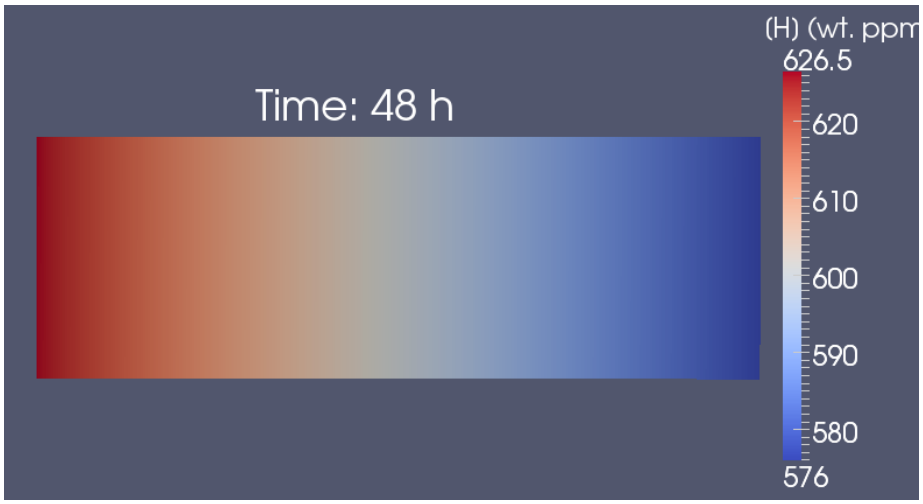

Figure 2-6: 3D view of the hydrogen profile calculated with BISON using a 600°C-700°C linear temperature gradient

This 3D view is not necessary in this benchmark since this is a 1D problem (no axial and azimuthal variations). However the 3D results confirm that BISON does not predict any hydrogen diffusion along the other directions.

2.4.1.2 Transient calculation

As explained in section 1.4.3.3, the analytical solution for the diffusion problem is complex. However, the transient calculated with BISON can be compared to the transient calculated with HydruLab. As an example, the profiles after 8 hours calculated by both of the codes, in the case described in the previous section (Homogeneous initial hydrogen concentration exposed to a 600°C-700°C temperature gradient) have been compared. Since the HydruLab mesh is not the same as the BISON mesh, a linear interpolation has been performed to the HydruLab results, in order to have a better comparison. Figure 2-7 shows both of the calculations.

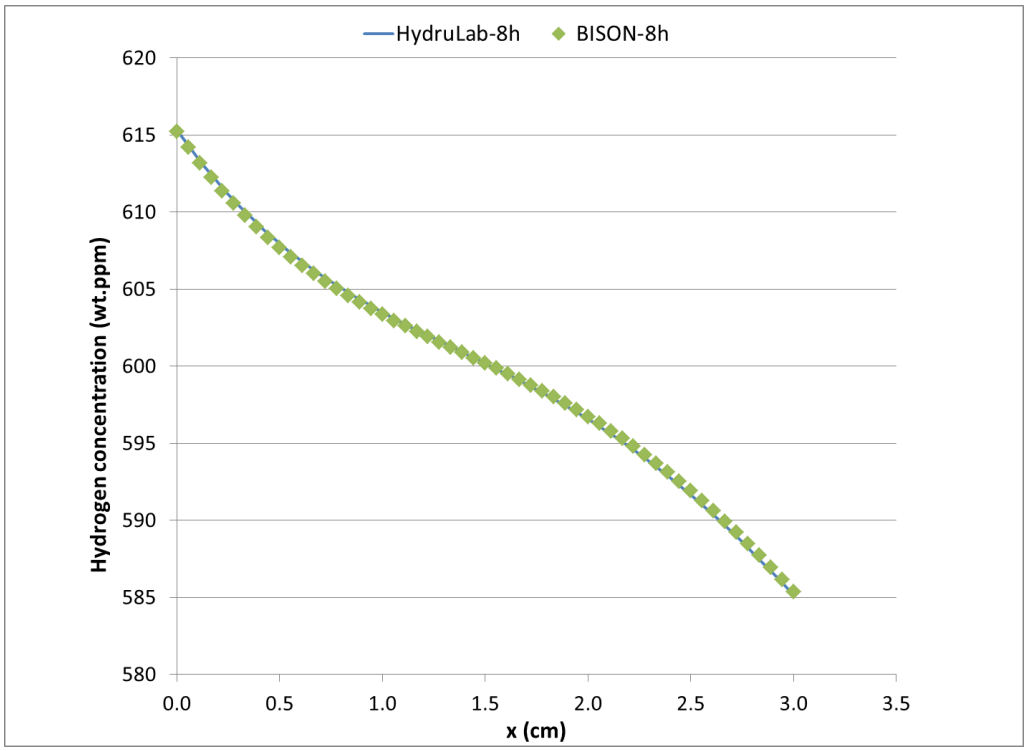

Figure 2-7: Hydrogen distribution after 8 hours calculated by HydruLab and BISON when submitted to a 700°C-600°C temperature gradient

The value of the hydrogen in solid solution under a temperature gradient of 700°C-600°C for 8 hours as calculated by both of the codes are very similar. In order to assess this comparison, a systematic statistical analysis has been performed. For each hour, from 0 to 48 hours and for each of the 55 mesh points, the BISON and the HydruLab calculation have been compared. Defining the mean error as:

$$\mu = \frac{1}{n}\sum(c_{bison} - c_{matlab}) \qquad \textbf{2-54}$$

And the standard deviation as:

$$\sigma = \frac{1}{n-1}\sqrt{\sum((c_{bison} - c_{matlab})^2 - \mu^2)} \qquad \textbf{2-55}$$

The following results were obtained:

Table 2-7: Statistical comparison of the difference between BISON and HydruLab calculations

Parameter	Value
Mean Error	0.016 wt. ppm (.002%)
Standard deviation	0.13 wt. ppm (.02%)

This shows that the calculated values of hydrogen in solid solution provided by the codes, during a simple diffusion experiment under a temperature gradient, are very close. This good agreement helps to validate the implementation of the hydrogen model in BISON.

2.4.2 Benchmark 2: Precipitation model

In order to benchmark the hydride precipitation model, a case without any diffusion has been simulated. In that case, the balance equations are reduced to:

$$\left\{\begin{array}{l} \frac{dC_p}{dt} = \alpha^2(C_{SS} - TSSp) \\ \frac{dC_{ss}}{dt} = -\alpha^2(C_{SS} - TSSp) \end{array}\right\} \qquad \textbf{2-56}$$

The second differential equation is independent and can be solved:

$$C_{SS}(t) = Aexp(-\alpha^2 t) + TSSp \qquad \textbf{2-57}$$

When t=0, $C_{ss}(0) = C_{ini}$

So,

$$C_{SS}(t) = (C_{ini} - TSSp)\, exp(-\alpha^2 t) + TSSp \qquad \textbf{2-58}$$

And the first equation can be solved as:

$$\frac{dC_p}{dt} = \alpha^2(C_{ini} - TSSp)\, exp(-\alpha^2 t) \qquad \textbf{2-59}$$

So,

$$C_p(t) = -(C_{ini} - TSSp)\, exp(-\alpha^2 t) + A \qquad \textbf{2-60}$$

When t = 0, $C_H(0) = C_{Hini}$, so:

$$C_{Hini} + C_{ini} - TSSp = A \qquad \textbf{2-61}$$

$$C_p(t) - C_{Hini} = (C_{ini} - TSSp)(1 - exp(-\alpha^2 t)) \qquad \textbf{2-62}$$

The simulated case uses the following boundary and initial conditions described in Table 2-8:

Table 2-8: Boundary and initial condition for benchmark 2

Condition	**Value**
Initial hydrogen concentration	400 wt. ppm
Temperature gradient type	No gradient
Constant temperature	300 °C

At this temperature, the TSSp and the kinetics parameter alpha have the following values:

$$\alpha = 1.09 * 10^{-02} [s^{-\frac{1}{2}}] \qquad \textbf{2-63}$$

$$TSSp(300°C) = 99.51\ [wt.ppm] \qquad \textbf{2-64}$$

Figure 2-7 shows the analytical results as calculated in equation 2-62 compared to the BISON results. The solutions match very well. The mean error is equal to 0.06 wt. ppm and the standard deviation is 0.015 wt. ppm. This helps to validate the implementation of the hydride precipitation kinetics model in BISON.

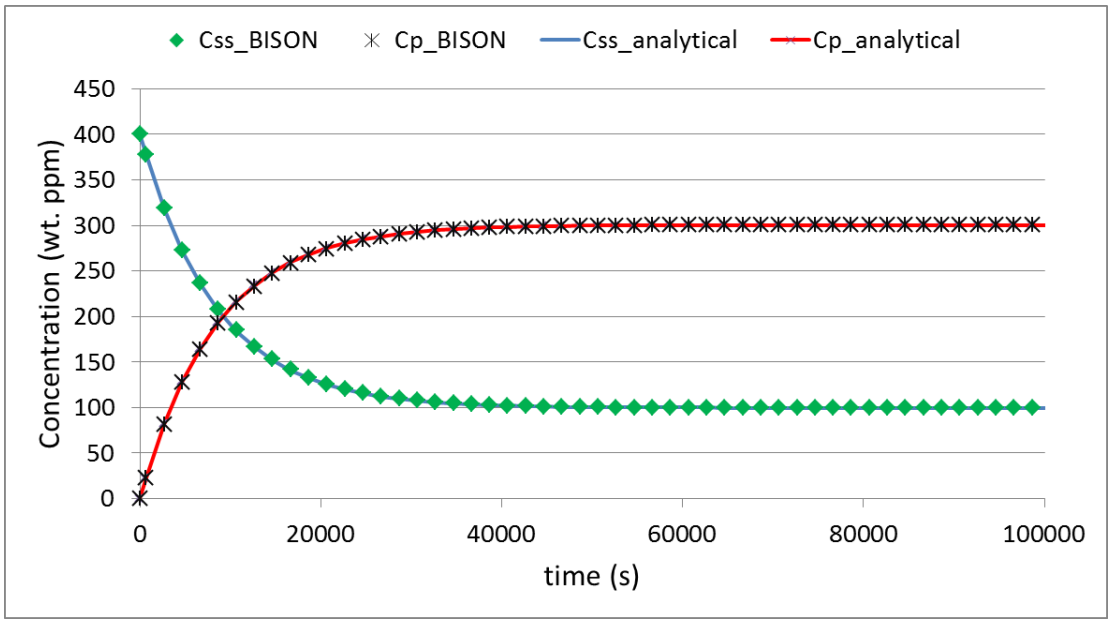

Figure 2-8: Comparison of the hydride concentration profile calculated with BISON and the analytical solution, in the case of pure precipitation of hydrogen

2.5 BISON results on a small piece of cladding

The purpose of this section is to show the calculations made by BISON of diffusion and precipitation of hydrogen. By examining these results, a greater understanding of the hydrogen redistribution in the cladding can be achieved. A simple geometry has been chosen, in order to perform fast calculations. Doing these calculations will also help the analysis of more sophisticated geometries. Most of the results have been analyzed with the help of *Kevin Cass*, undergraduate student and summer intern at the Pennsylvania State University, in the framework of the *Toshiba-Westinghouse Fellows Program.* The BISON input files have been reproduced in Appendix E.

2.5.1 Geometry of the piece of cladding

The geometry used is a plate. Its dimensions are 660 μm x 1.2 mm x 1.2 mm. In the simulations performed on this mesh, the temperature varies along the 660 μm direction. This thickness is typical for a PWR Zircaloy-4 cladding. Figure 2-9 shows the geometry and the mesh of this piece of cladding. In the thickness direction, the mesh has 21 nodes.

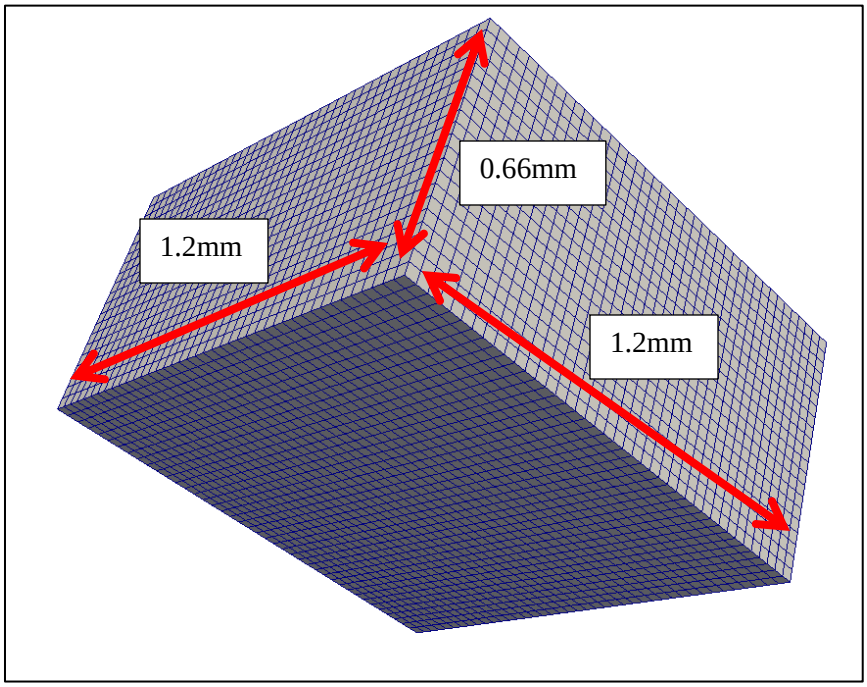

Figure 2-9: Geometry and mesh of the piece of cladding

2.5.2 Case 1: Hydrogen distribution under temperature gradient before precipitation

This first simulation reproduces the first step in hydrogen redistribution. A constant temperature gradient of 40°C for 660 µm in the y direction has been assumed. The temperature goes from 320°C at the coolant/cladding interface to 360°C at the fuel/cladding interface. These are typical temperature values in zirconium fuel cladding. The temperature gradient is represented in Figure 2-10. Since there is no heat source in the cladding and since the conductivity is almost constant, the temperature gradient is linear. The hydrogen flux due to oxidation is calculated at the coolant/cladding interface according to section 0.

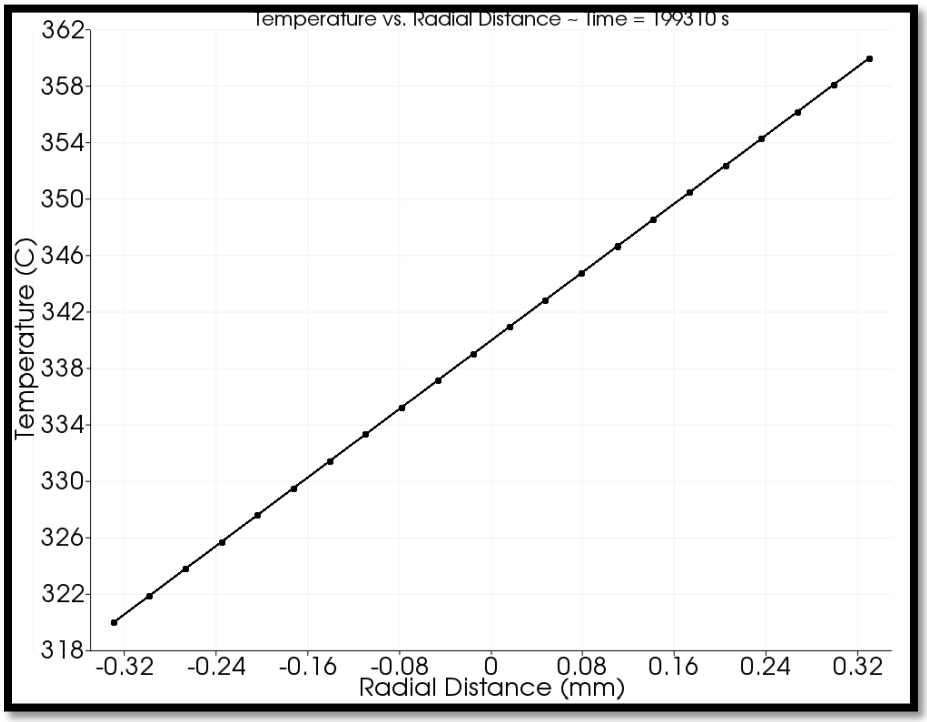

Figure 2-10: Temperature gradient applied to the plate, corresponding to a typical cladding gradient (330°C-360° for 660 microns)

At each time step, the distribution of hydrogen is very close to the steady state profile (without any incoming flux at the boundaries). The steady state profile is given by the equation 1-39. Figure 2-11 shows this profile after 1 year. After 1 year, the average hydrogen concentration is small (about 8 wt. ppm), as calculated in section 1.3.1. This hydrogen redistribute in the cladding in response to the temperature gradient.

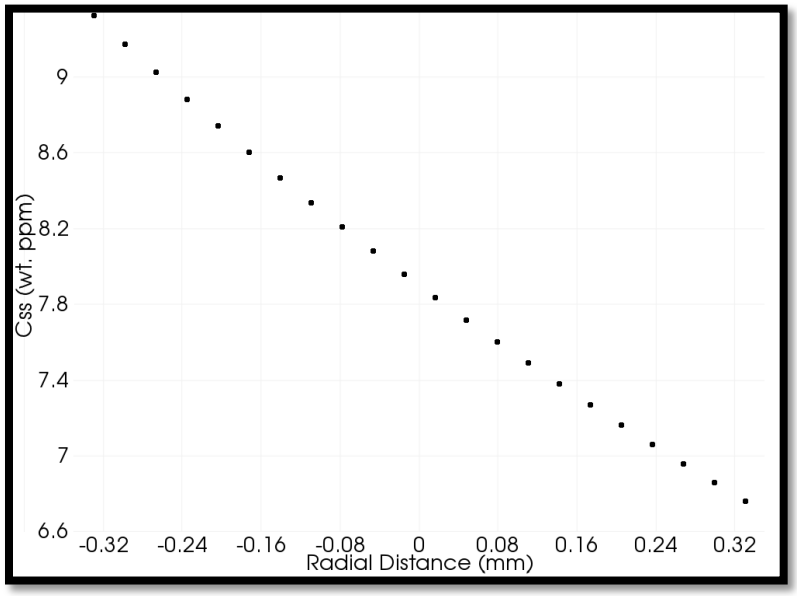

Figure 2-11: Hydrogen (solid solution) profile after 1 year under a typical cladding radial temperature gradient (320°-340°C for 660 microns)

It is observed that the hydrogen profile is strictly identical by either:

- Running the calculation for 1 year
- Running the calculation for 1 day, starting with an initial hydrogen concentration equal to the theoretical value obtained after 364 days.

From this observation, it can be concluded that the time to equilibrium is short compared to the hydrogen absorption time. The characteristic time for the diffusion in the plate at 320°C is given by the equation

$$\tau_{Diffusion} = \frac{l^2}{D} \qquad \textbf{2-65}$$

With D the diffusion coefficient
L the characteristic length

$\tau_{Diffusion}$ is equal to 5000s (about 2 hours) at 320°C. Considering that the steady state is obtained after 10*$\tau_{Diffusion}$, it is consistent to have a quasi-steady state profile in a day or less. The quasi-steady state situation is confirmed only if, during this time, the amount of hydrogen coming from the boundary is small. The increase of the average hydrogen concentration in 1 day,

according to the MATPRO model detailed in section 1.3.1, is about 0.03 wt.ppm, at 320°C and goes up to 0.13 wt. ppm at 360°C (above the maximum temperature observed at the outer edge of the cladding in a PWR). This confirms the fact that a quasi-steady state assumption is reliable in the case of pure diffusion of hydrogen.

Since the TSSp decreases when the temperature decreases, the lowest TSSp is observed at the outer edge of the cladding. According to the results above, it is also the place where the concentration of hydrogen in solid solution is at its highest (with respect to the radial profile). As long as this concentration is below the TSSp at 320°C, there is no precipitation and we observe the classic equilibrium solution, as derived in section 1.4.3.3.

2.5.3 Case 2: Formation of the rim

In the second calculation, the formation of the hydride rim is studied. The calculation has been run for about 115 days (10^7 seconds). The temperature conditions are the same as in case 1. The outer cladding temperature is set to 320°C and the inner cladding is set at 360°C. An initial hydrogen concentration of 125 wt. ppm in solid solution has been chosen. The TSSp at 320° is equal to 127 wt. ppm according to equation 1-45.The temperature profile is kept constant for the run.

Figure 2-12 shows the radial profile of hydrogen concentration in solid solution. Figure 2-13 shows the radial profile of the concentration of hydrogen in precipitated hydride. The concentration in solid solution is slightly higher than the steady state profile. At the same time, a rim appears in the hydrides. This can be explained by looking how the hydride concentration is calculated within the model.

First, at the end of a given timestep, the concentration of hydrogen in the first node reaches the TSSp. This will create a driving force for precipitation $\Delta C = C_{ss} - TSSp$. During the

next timestep, precipitation terms appear in the equation (Correspondingly, inn BISON, the HydrogenPrecipitation kernel is activated). The appearance of this precipitation terms means that during a timestep δt, the fraction $\alpha \cdot \Delta C \cdot \delta t$ precipitates. The other fraction $(1-\alpha) \cdot \Delta C \cdot \delta t$ stays in supersaturation in the node. This disturbs the solid solution equilibrium and, due to Fick's law, increases the diffusion flux toward the next node. The concentration of this second node will subsequently increase.

Examining the further behavior of the second node, two outcomes can occur. It is important to notice that the TSSp in the second node is higher than the TSSp in the first. Therefore in the first case, the hydrogen diffused from the first node may not initially be sufficient to reach the new local TSSp. In that case, a new solid solution profile is obtained which follows the standard equilibrium, as expressed in equation 1-39. In the second case, the concentration is greater that the new TSSp, which implies a precipitation. Again, a fraction of the hydrogen in solid solution will precipitate and another fraction will stay in solid solution.

Furthermore, regarding the first node, at one point the hydrogen flux coming from the boundary will be equal to the sum of the hydrogen diffusing and the hydrogen precipitating. Once this equilibrium is reached, the concentration in solid solution becomes constant in the location where the hydrogen has precipitated.

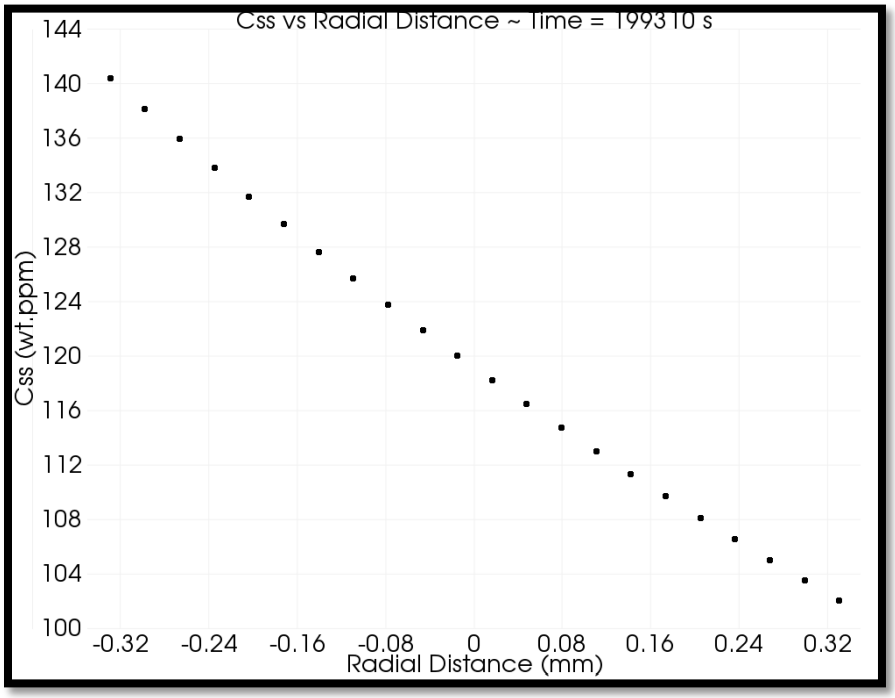

Figure 2-12: Hydrogen in solid solution vs. r, after the TSS has been reached at the outer edge of the cladding

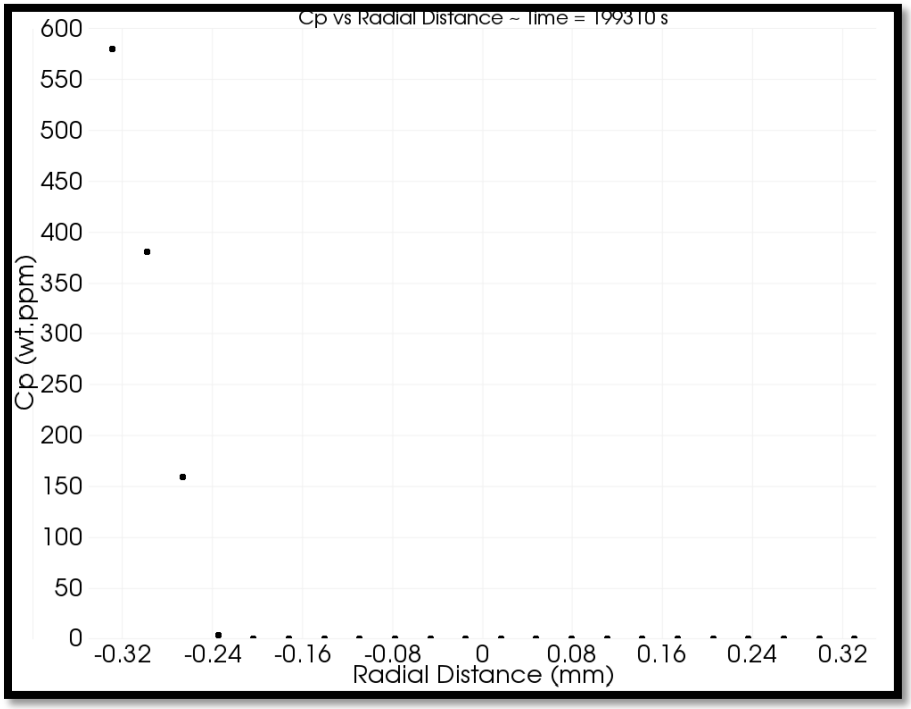

Figure 2-13: Hydrogen in hydrides vs. r, after the TSS has been reached at the outer edge of the cladding

The temperature, concentration in solid solution and concentration of precipitated hydrogen (in hydrides) have been tracked for three points, corresponding to the first three radial nodes starting from the coolant/cladding interface. The nodes are highlighted in Figure 2-14.

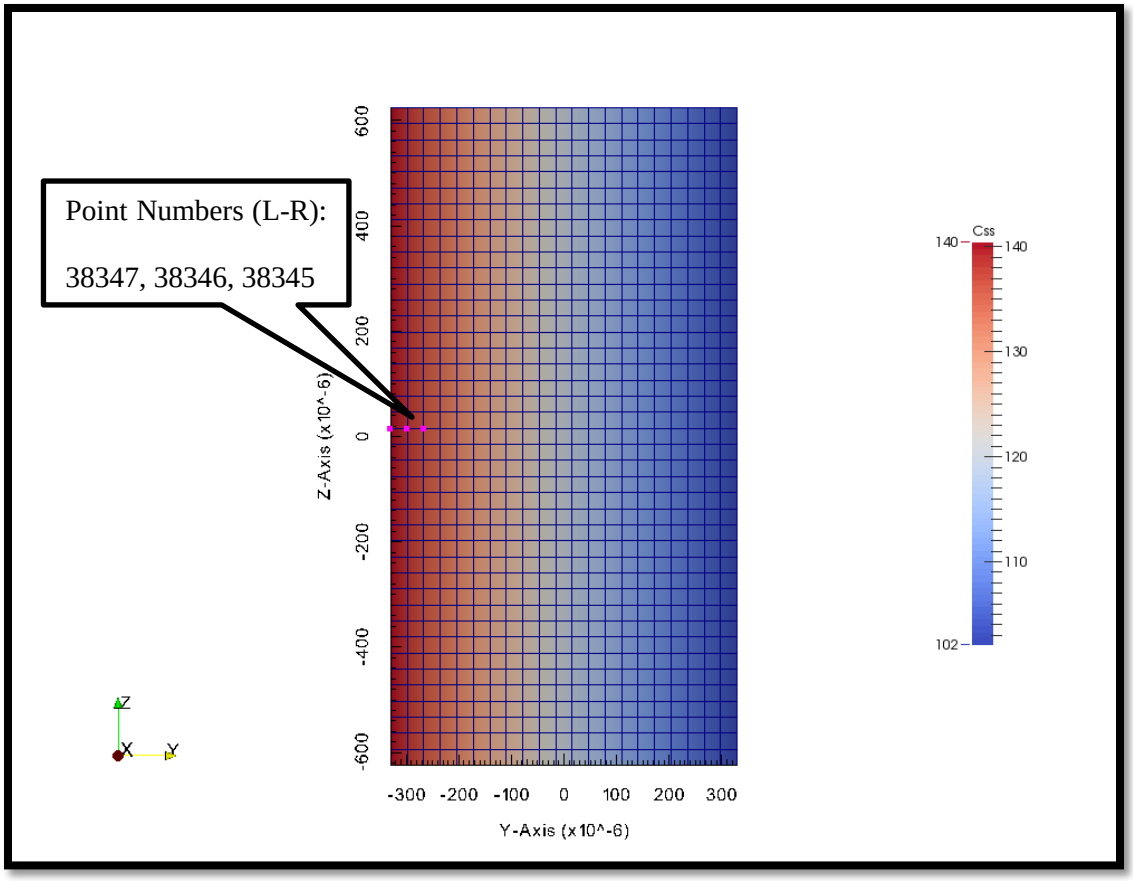

Figure 2-14: Location of the nodes of interest for case 2

Figure 2-15 and Figure 2-16 show the evolution with respect to time of the hydrogen in solid solution, and of the hydrogen in the hydrides concentration respectively. These temporal profiles are plotted at the three locations showed in Figure 2-14. Regarding the solid solution points, it appears that the local equilibrium is reached quickly.

Regarding the hydrogen precipitated, the concentration is increasing considerably and reaches the 18 000 wt. ppm limit in less than 50 days. This limit corresponds to a full hydride. The limit is reached because the rim is thin (less than 100 microns). This is essentially due to the

choice made for the variable α and the precipitation kinetics in the model. If α were smaller, the rim would be thicker and the concentration of hydrogen in hydride would be smaller. This will be discussed in section 4.3.

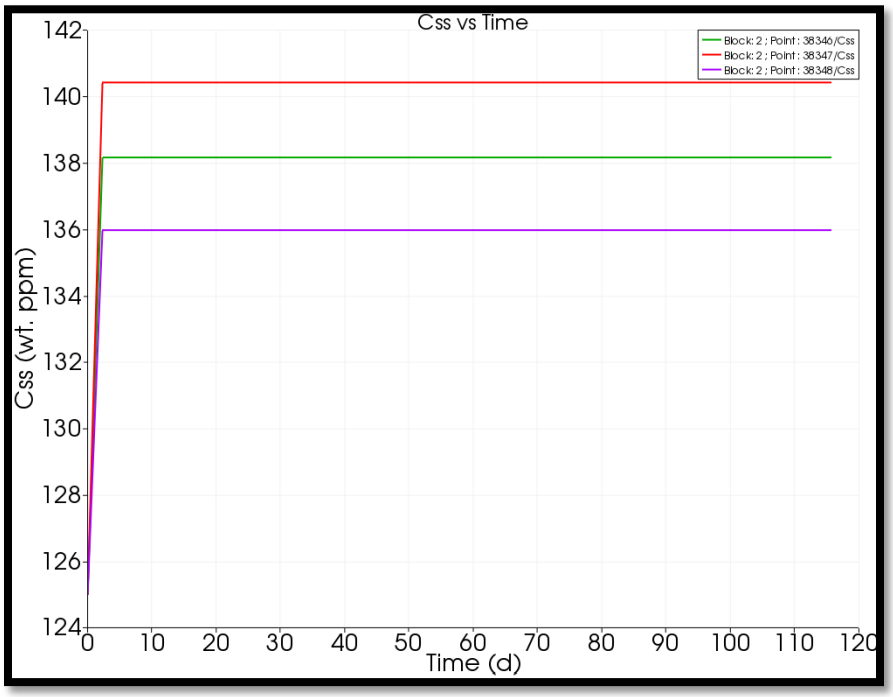

Figure 2-15: Hydrogen in solid solution vs. time during the formation of the hydride rim

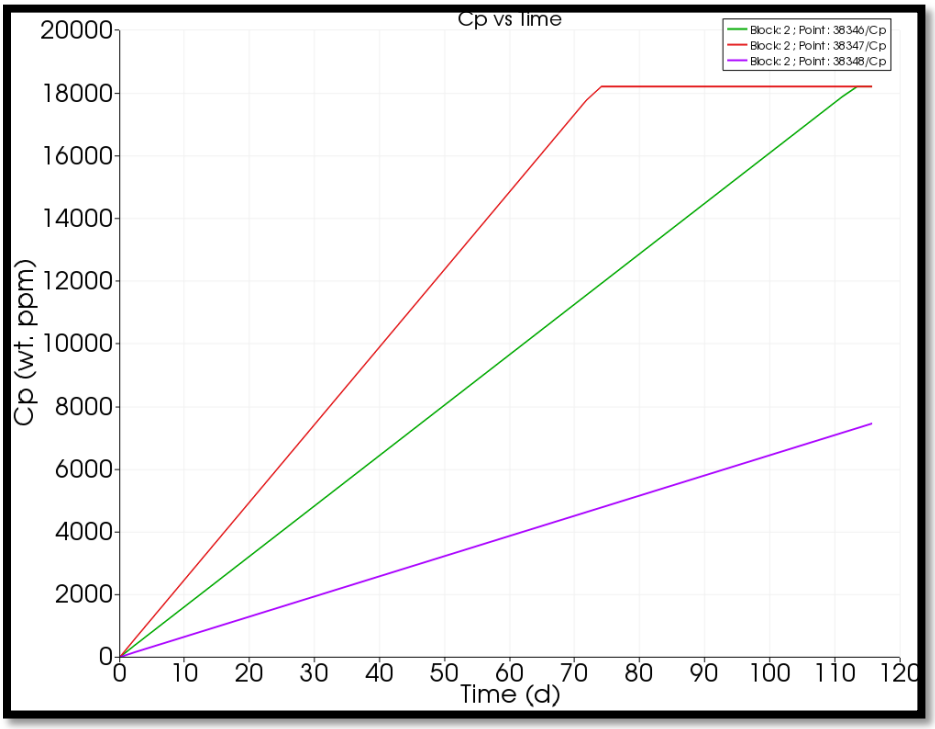

Figure 2-16: Hydrogen in hydrides vs. time during the formation of the hydride rim

2.5.4 Case 3: Simulation of the consequences of a reactor shutdown

Almost all the hydrogen measurement and cross-sectional pictures performed that exist in the literature are post-facto measurements (RIA test, ring compression tests, etc.)[17, 51]. Therefore, what is usually measured is not the hydrogen distribution during reactor operation but the distribution after a normal reactor shutdown. The influence of the shutdown on the distribution is studied in Case 3. The geometry is the same as in Case 2.

2.5.4.1 Reactor shutdown parameters

The reactor shutdown takes place in two phases. First, the control rods are moved down in order to stop the chain reaction. The reactor goes from Hot Full Power (HFP) to Hot Zero Power (HZP). This operation takes about two minutes. Once the control rods are down, only the heat produced by the radioactive decay of the fission products remains. At this point, the temperature in the core is almost homogeneous due to the relatively low heat rate. Then the main and auxiliary cooling systems are used to bring temperature and pressure to room and atmospheric conditions. Usually, the temperature is decreased linearly within 24 hours, as explained in the NRC Standard Technical Specification[52] The pressure is kept below the saturation pressure. Figure 2-17 shows the evolution of the cladding temperature with time during the shutdown.

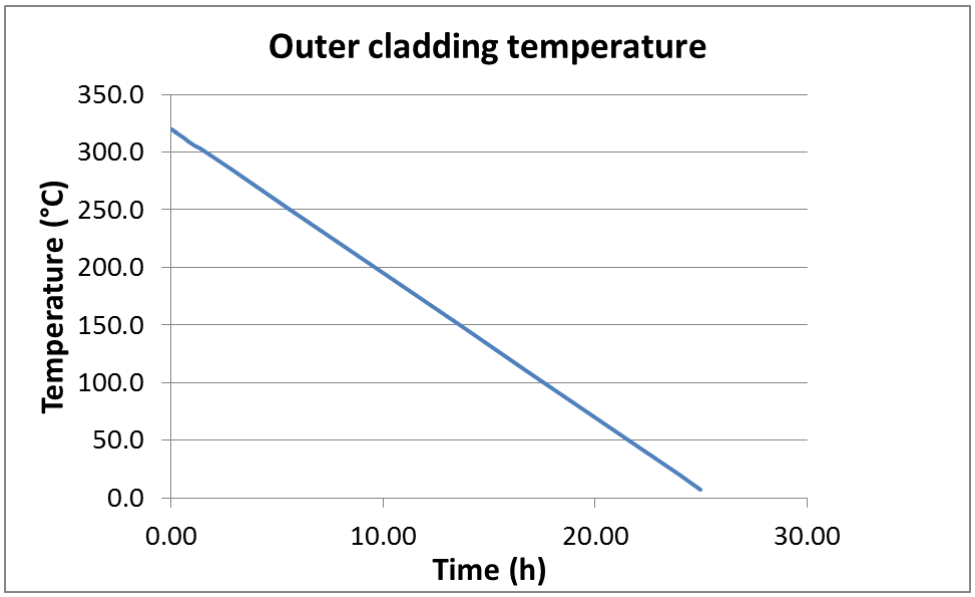

Figure 2-17: Reactor shutdown cladding temperature evolution with time

Regarding the decay heat, the value is given as a percentage of the nominal power by the American Nuclear Society standard, described on page 293 of *The Nuclear Fuel Cycle*, by Robert Cochran and Nicholas Tsoulfanidis. [53] Equation 9.7 found in this book provides the power from decay heat as a function of time (starting at HZP):

$$P(t,\infty) = P_0 * A * t^{-a} \qquad \textbf{2-66}$$

The infinity sign means the equation approximates an infinite time of operation before the shutdown. P_0 is the nominal power. **A** and **a** are the constants given by Table 2-9.

Table 2-9: Shutdown decay power constants

Time Interval (s)	A	a
$0.1 < t < 10$	0.0603	0.0639
$10 < t < 150$	0.0766	0.181
$150 < t < 4x10^6$	0.130	0.283
$4x10^6 < t < 2x10^8$	0.266	0.335

Regarding Case 3, by knowing the heat rate and the outer cladding temperature, the inner cladding temperature can be calculated using the equation:

$$T_{inner} = T_{outer} + \Delta T \qquad \textbf{2-67}$$

With:

$$\Delta T = \frac{q'_{nominal}}{k_{cladding}} \cdot \frac{P}{P_0} \cdot \frac{1}{2\pi R_{inner}} \qquad \textbf{2-68}$$

With:

$q'_{nominal}$ the nominal linear heat rate
$k_{_cladding}$ the conductivity of the cladding
P/P_0 the factor given by equation 2-66
R_{inner} the inner cladding radius

Assuming a linear heat rate of 18.5 kJ/m (used in fuel rod calculations in the following sections), the inner cladding temperature is very close to that of the outer cladding. Figure 2-18 shows the evolution of the temperature difference between the inner edge and the outer edge of the cladding with respect to time.

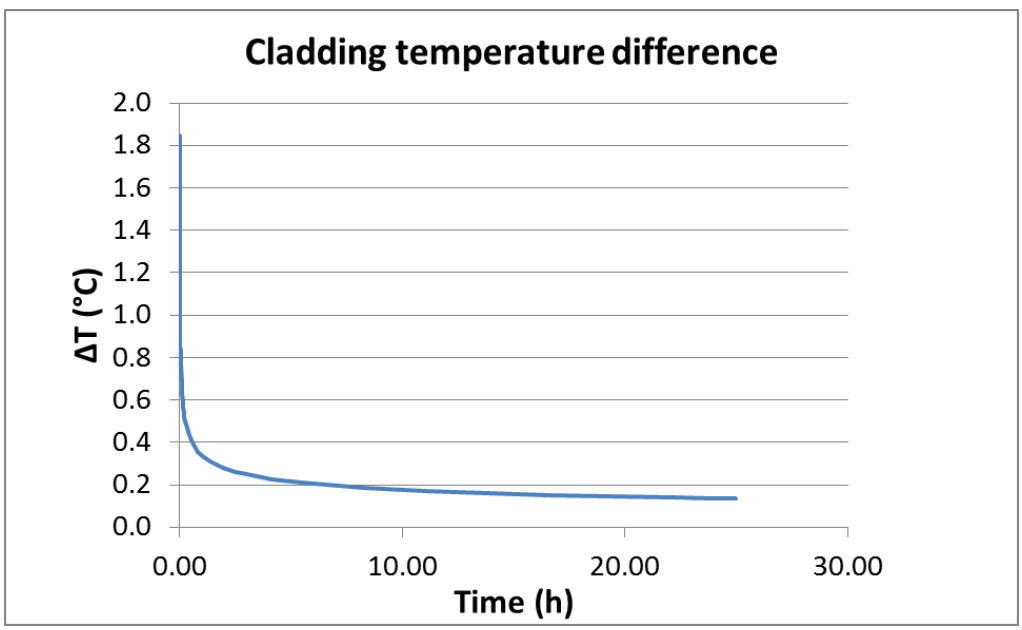

Figure 2-18: Evolution of the cladding temperature difference in the cladding during a 24 hour reactor shutdown

2.5.4.2 Simulation of the hydrogen redistribution during shutdown

The simulation considers a shutdown at a time where the hydrogen content is 120 wt. ppm. The simulation was run for about 2.31 days using typical operation temperature. This leads to the formation of a small rim. The shutdown starts at 2.31 days and takes 24 hours. After the shutdown, temperature is held at 20°C held for 3 more days, in order to verify that there is no further hydrogen evolution at room temperature.

Figure 2-19 shows the nodes where the evolutions of temperature and hydrogen concentration were followed. Figure 2-20 shows the evolution of temperature with respect to time for these nodes. The temperature profiles are consistent with the conditions detailed in section 2.5.4.1. The temperature gradient disappears when the shutdown begins, since the difference in temperature due to decay heat is too small to be seen on the graphs. Following shutdown, the temperature decreases linearly to room temperature in 24 hours. Figure 2-21 shows the evolution of the hydrogen in solid solution. The C_{ss} profile is suddenly homogenized when the conditions go from HFP to HZP. Indeed, without a temperature gradient, the Soret effect disappears. Only Fick's law remains and this diffusion homogenizes the C_{ss} concentration in the cladding. Following the homogenization, the cladding is cooled down and the TSSp decreases progressively. Hydrogen in solid solution precipitates and its concentration is solid solution decreases. Once the temperature is lower than 280°C, the precipitation kinetics slow down, which is why not all the hydrogen is precipitated at the end. The concentration of hydrogen in the hydrides is shown in Figure 2-22 and follows, before the reactor shutdown, a similar rim as shown in Case 2. The main difference is that the rim formation is simulated for less than 3 days. Therefore, the concentration of hydrogen in hydrides is smaller than 350 wt.ppm. The rim is located close to the outer edge of the cladding. Once the shutdown happens, hydrides appear in the cladding, as a result of precipitation of the hydrogen from solid solution.

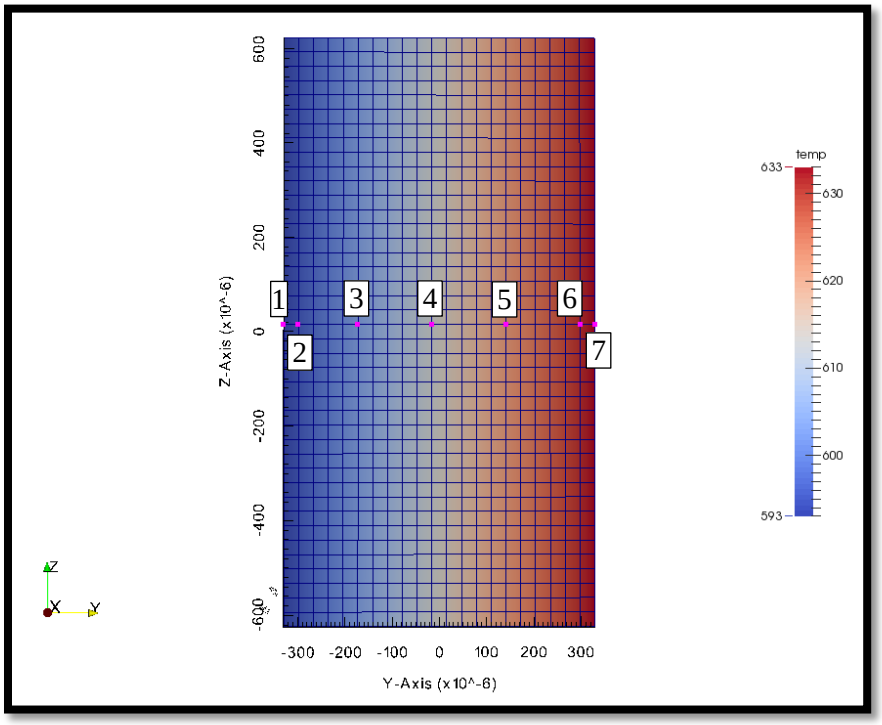

Figure 2-19: Nodes tracked in the temporal analysis of case 3

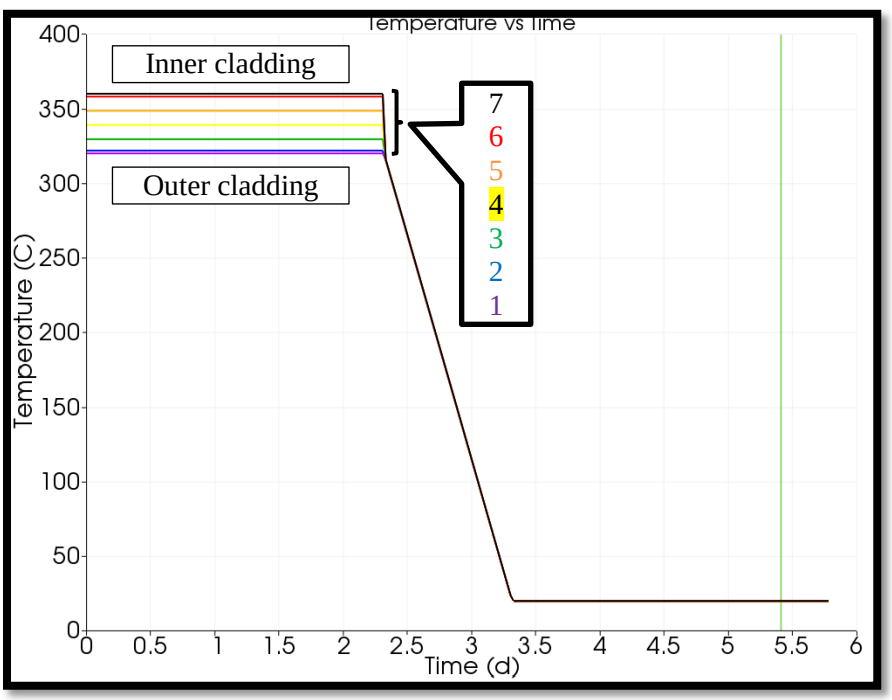

Figure 2-20: Temperature vs. time for case 3

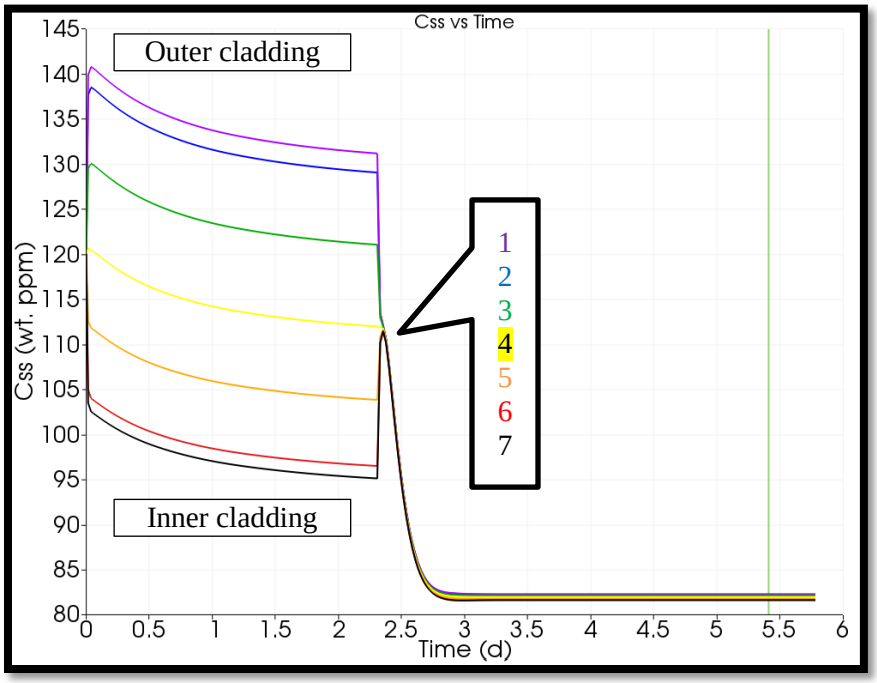

Figure 2-21: Hydrogen in solid solution vs. time for case 3

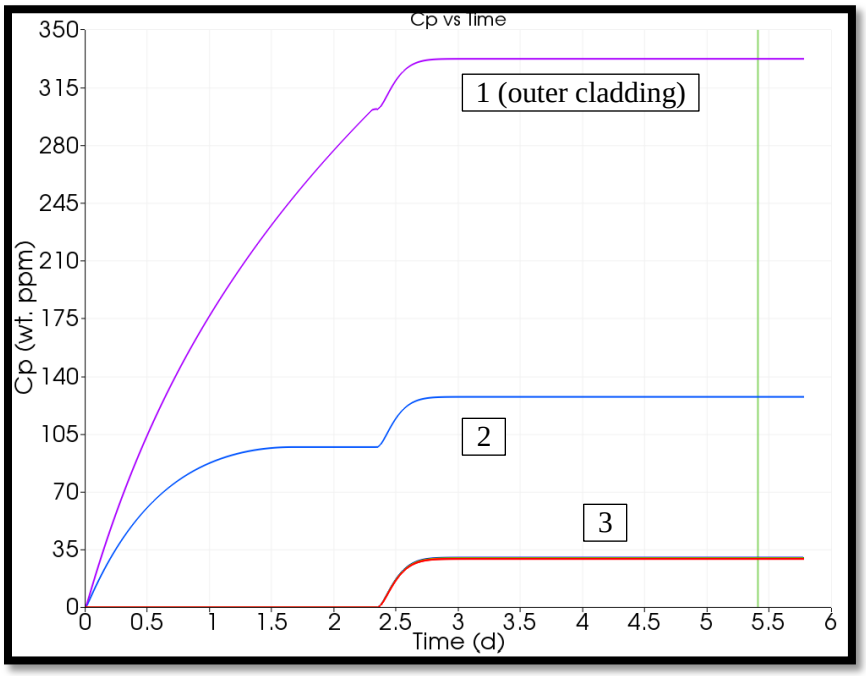

Figure 2-22: Hydrogen in hydride vs. time for case 3

In conclusion, the results of this case show that the shutdown does not affect the hydrides formed during reactor operation. However, hydrogen that was in solid solution during operations redistributes and almost homogenously precipitates. This would explain why, in experimental rim pictures, some hydrides are also seen in the metal substrate underneath the rim (see Figure 1-3).

2.5.5 Conclusions simulations of hydrogen behavior in a piece of cladding

The first simulation predicts distribution of hydrogen that is consistent with previous observations and that is due to the combination of Soret effect and Fick's law. This behavior was expected, since the code was partially benchmarked on this case (see section 2.4.1.1). The second simulation provides an interesting understanding of the formation of the rim. The third simulation shows that the reactor shutdown has a limited effect on the hydride distribution. However, three important deficiencies can be observed in these simulations:

- The rim hydrogen concentration is considerably too high after long exposure (see Figure 2-16)
- The temperature conditions and the hydrogen initial concentration have been chosen arbitrarily.
- All axial and azimuthal transfers of hydrogen have been neglected.

In order to take these phenomena into account, it was decided to perform additional simulations with the fuel rod geometry.

2.5.6 Simulation with a limitation of the amount of hydrogen in hydrides

In order to address the very high concentrations of hydrogen found for the rim after a few months in the previous simulation (see section 2.5.3), it was decided to set an upper limit to the value of the concentration of hydrogen in hydrides. Theoretically, the maximum limit is given by the concentration of hydrogen in a full hydride:

$$C_{pmax} = 1.66 * \frac{M(H)}{M(Zr)} * 10^6 \qquad \textbf{2-69}$$

Where 1.66 is the hydrogen stoichiometry in $ZrH_{1.66}$ (δ hydrides), M(H) and M(Zr) are the molar masses of hydrogen and zirconium and the 10^6 factor transform a mass fraction in wt.ppm. This value is equal to 18,197 wt.ppm. The maximum observed value for concentration of hydrogen in the rim is usually about 1000-1200 wt.ppm. The only time a solid hydride is observed is when hydride blisters form or when hydrogen is charged by electrolytic means. There are several physical reasons why the hydrogen concentration of the rim is usually much smaller than this theoretical limit:

- The equilibrium between hydrogen in solid solution and hydrides may be affected by the hydrides that have already precipitated
- The precipitation kinetics may be changed by the increase of hydride nuclei

Further developments are given in section 4.3.

HydruLab has been modified in order to decrease the maximum hydrogen concentration in hydride from 18297 to 1000 wt. ppm. The simulation goes from 3.4 years to 4.0 years. The initial concentration at 3.4 years is assumed to be equal to 125 wt.ppm and there is no initial precipitate. The temperature gradient goes from 330°C to 360°C. Figure 2-23 shows the profile of hydrogen in the hydride at t=4 years. The rim appears thicker than in the previous calculation, and is consistent with experimental observations, as described in section 1.4.2. Figure 2-24 shows the concentration of hydrogen in solid solution. It can be noticed the hydrogen concentration in

solid solution is higher than in previous cases. This is due to the fact that the cells close to the coolant interface are filled with the maximum hydride concentration. Thus, the lowest TSSp that causes precipitation is the one of the first cell that does not have a 1000 wt.ppm hydride concentration. This cell is more inside the cladding and has a higher value, because of the temperature gradient in the cladding. Therefore, the profile of hydrogen in solid solution is higher than the one without any precipitation. With this calculation, it is also possible to show the evolution of the rim, as shown in Figure 2-25. The plateaus are due to the mesh used. These results are consistent with what is seen experimentally. However the 1000 wt. ppm limit has no physical meaning and requires more investigation in the future.

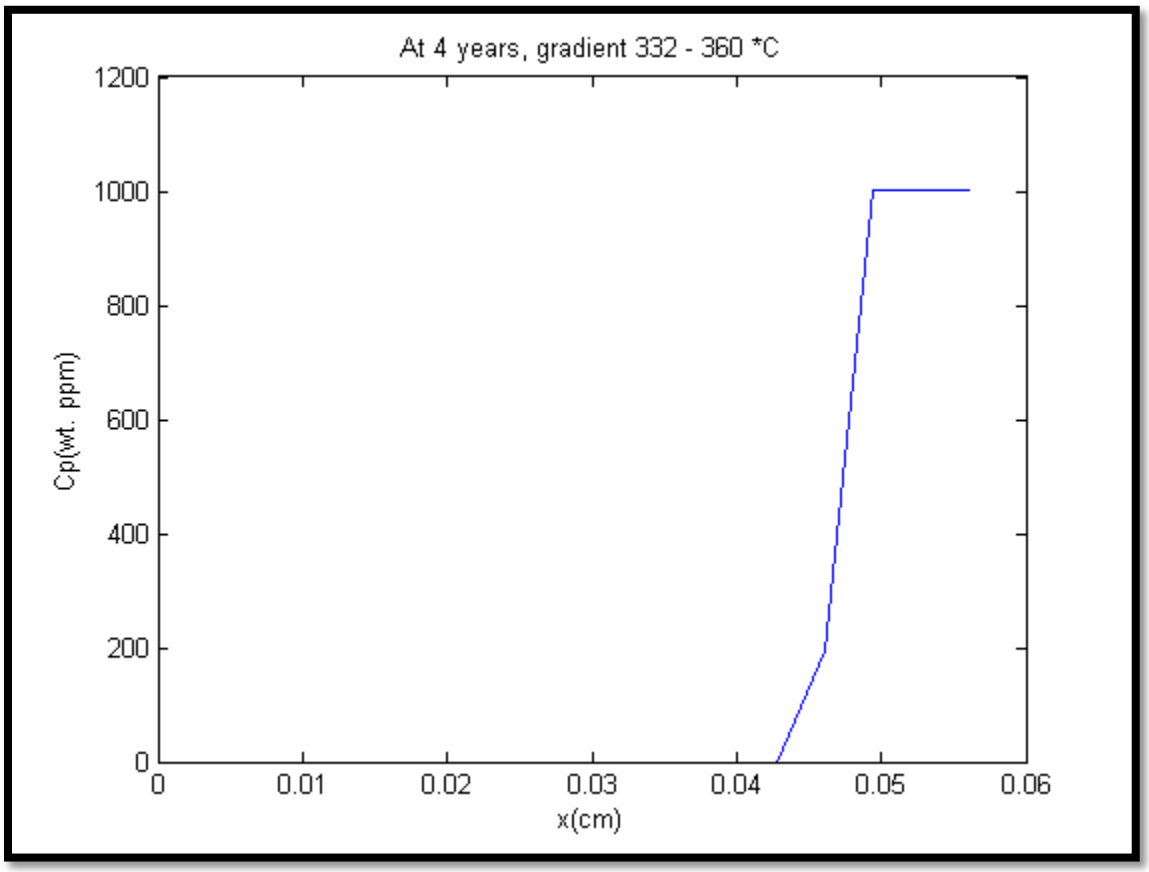

Figure 2-23: Hydride profile after 6 months of precipitation with a limit of 1000wt.ppm of hydrogen in hydrides, calculated with HydruLab

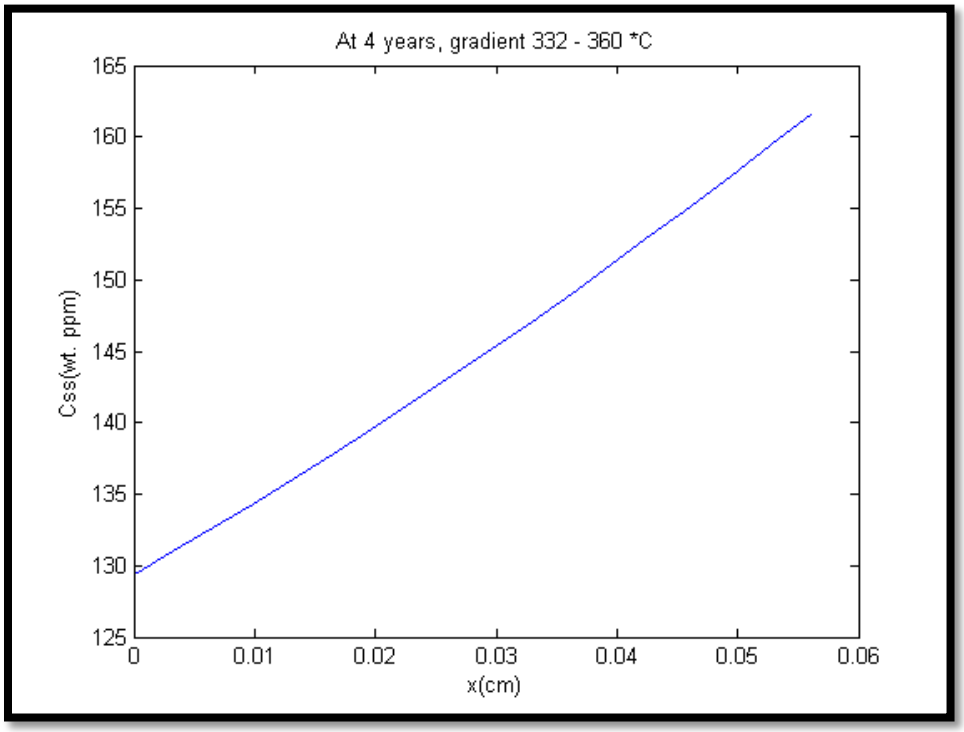

Figure 2-24: Hydrogen (solid solution) profile after 6 months of precipitation with a limit of 1000wt.ppm of hydrogen in hydrides, calculated with HydruLab

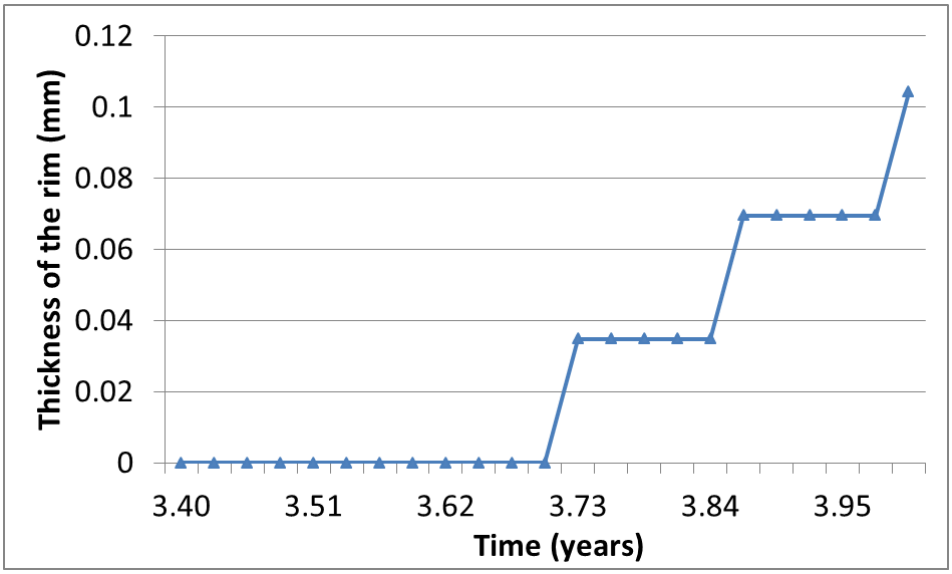

Figure 2-25: Evolution of the thickness of the rim with time during 6 months of precipitation with a limit of 1000wt.ppm of hydrogen in hydrides, calculated with HydruLab

2.6 Results of 5-pellet rod simulation using BISON

According to section 2.5 it is difficult to obtain realistic results with a simple 1D geometry. The main reason for this is that the temperature profile is set manually, and does not change with time. In addition, the 1D geometry does not take into account the axial transfer of hydrogen down the length of the rod. Due to limited computational resources, it is impossible to run a full rod hydrogen calculation for a long time. Some simulations covering a small amount of time have been made and are presented in section 2.6.4. Therefore, it was decided to extract 5 pellets and the contiguous cladding and to run the analysis on this geometry.

2.6.1 Geometry and boundary conditions

The geometry consists of five UO_2 stacked pellets with typical PWR pellets dimensions. Each pellet has dishes and chamfers. The pellets are surrounded by a Zircaloy-4 fuel cladding. The dimensions are given in Table 2-10. The geometry is in 2 dimensions (radial and axial). Figure 2-26 shows the simulation mesh, represented as half of each pellet and the cladding on one side (in blue), due to the invariance per rotation.

The two main inputs that have to be provided to BISON are the burnup and the outer cladding temperature. This data are obtained from the high fidelity calculation using CTF and DeCART, made by Ian Davis and described in section 2.3.1. The calculations are made for a 4x4 assembly with the conditions described in Table 2-11.

Table 2-10: Pellet geometry in the PWR simulations

Type	Value	Units
Reactor	PWR	
Layout	4 x 4	
Fuel	UO2	
Enrichment	3.45%	
Fuel density	10.4	g/cc
% of theoretical density (10.96 g/cc)	95%	
Burnable poison	None	
Clad	Zircaloy-4	
Clad density	6.55	g/cc
Coolant	H_2O	
Fill gas	Helium	
Fill gas density	0.0002	g/cc
Fuel pellet radius	0.4095	cm
Clad inner radius	0.418	cm
Clad outer radius	0.475	cm
Clad thickness	570	microns
Pin pitch	1.26	cm
Active fuel height	365.76	cm
Top reflector height	35.512	cm
Bottom reflector height	35.512	cm
Array power	1.0808	MW
Average linear heat rate	18.5	kW/m
Core pressure	15.5	Mpa
Mass flow rate	4.86	kg/s
BOC boron loading	1400	ppm
Inlet temperature	287	°C

Table 2-11: Condition for five pellet DeCART-CTF coupling

Condition	Value
Geometrical parameters	PWR standard values*
Nominal Power	1.0808 MW
Inlet temperature	287°C
Pressure	15.5 MPa
Mass Flow Rate	4.8 kg/s
Isotopic fractions, Xenon, boron, depletion test	PWR standard values*

* Detailed values are reported in Ian Davis's thesis [42]

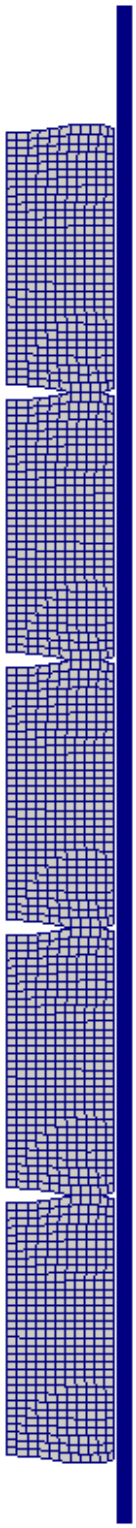

Figure 2-26: Five pellet geometry for BISON simulation

The DeCART-CTF provides temperature and heat deposition distributions for each of the fuel rod of the simulated assembly. Each fuel rod contains 360 UO_2 pellets. A five pellet section is selected and the boundary conditions (Cladding temperature and energy deposition) are extracted from the CTF-DeCART calculation. It is assumed in the calculation that there is no axial heat flux and no axial hydrogen diffusion flux. Two different axial sections were chosen. The first one is where the highest temperature is observed in the cladding. It will be called the "hot 5 pellet rod" in the next sections. The second section is located close to the inlet and will be called the "cold 5 pellets rod" in the next sections.

2.6.2 Hydrogen distribution in hot 5 pellets rod

Figure 2-27 shows the axial temperature profile for this geometry. It can be observed that the temperature profile is similar from one pellet to another. This is due to the fact that the elevation of the temperature of the coolant is negligible for the small elevation corresponding to 5 pellets (about 6 cm). The cladding is subjected to a temperature gradient going from 330°C to 360°C, as shown in Figure 2-28. The temperature in the cladding does not change significantly with time, as shown in Figure 2-29. According to the MATPRO model described in section 1.2.2, the average concentration of hydrogen after 4.5 years at 330°C will be about 70 wt. ppm. The TSSp at this temperature is 140 wt.ppm. Therefore, no precipitation can be seen for this temperature. A BISON calculation confirms this observation. Figure 2-31 shows a radial distribution that is very similar to what has been observed in section 2.5. Figure 2-30 shows the axial distribution that follows the same kind of pattern. The hydrogen moves toward the bottom of the cladding, as a result of the Soret effect. A small drop is observed at the location of the inter-pellet gap. Even if this difference is small, it creates a local cold spot where hydrogen will precipitate preferentially in the future, according to the observation made in Figure 1-9.

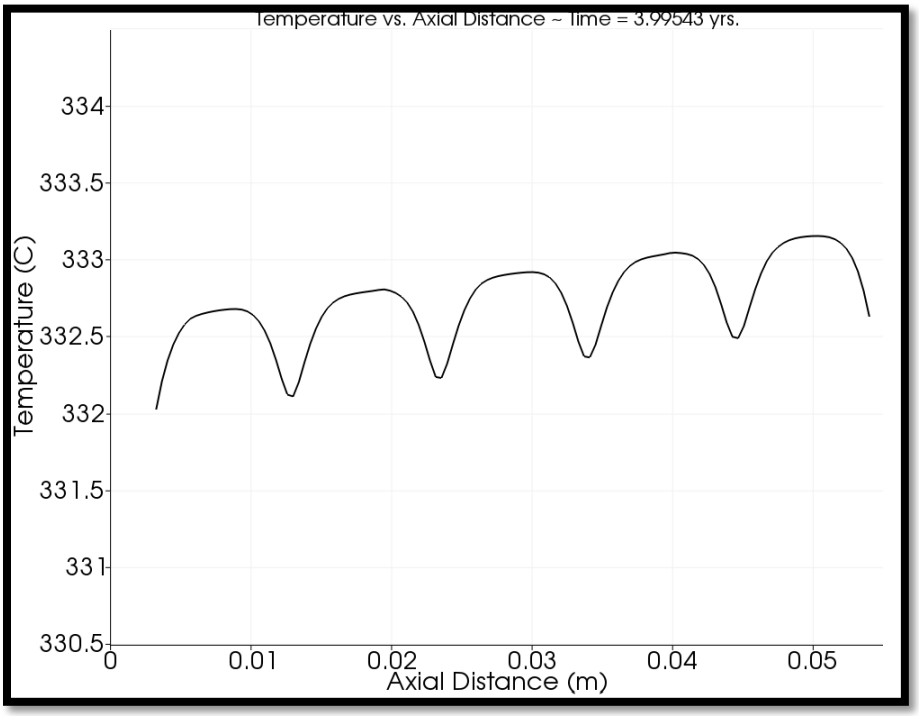

Figure 2-27: Axial temperature profile for the hot 5 pellets mesh at the outer edge of the cladding, after 4 years

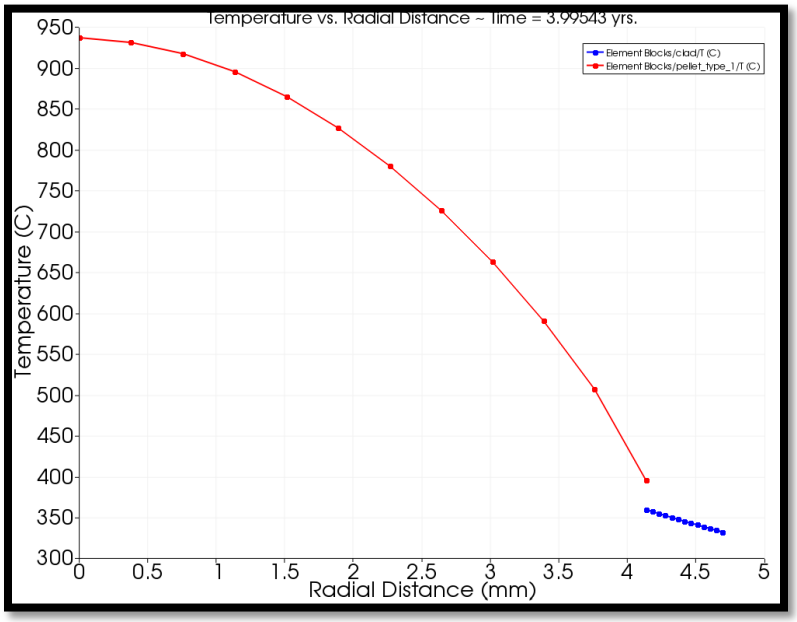

Figure 2-28: Radial temperature profile for the hot 5 pellets mesh at z=2.75 cm, after 4 years

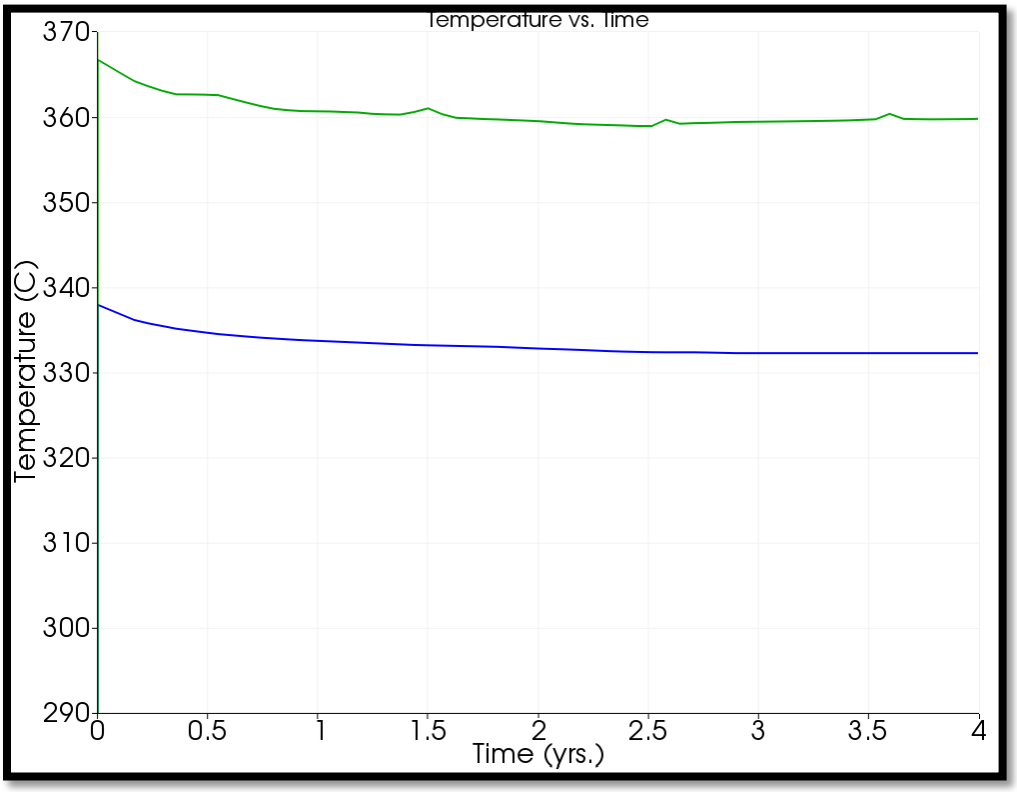

Figure 2-29: Evolution of the cladding temperature for the hot 5 pellets at z=3.0 cm and r=4.15mm and 4.2mm (in green, inner edge), and r=4.67mm and 4.72mm (blue, outer radius), between 0 years and 4 years

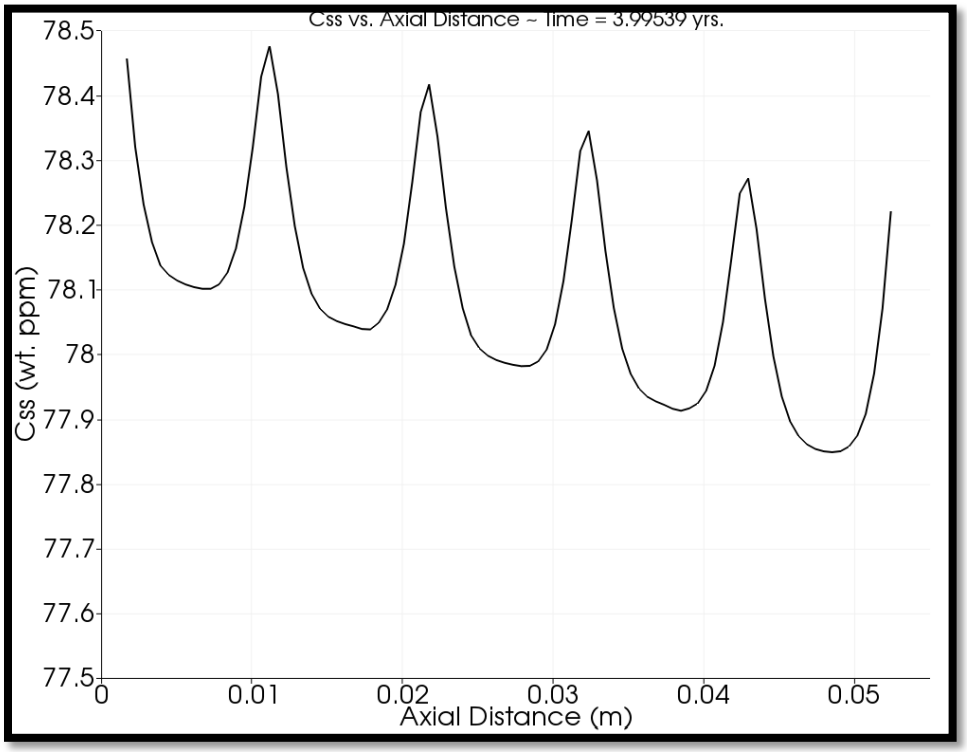

Figure 2-30: Axial hydrogen profile for the hot 5 pellet mesh at the outer edge of the cladding, after 4 years

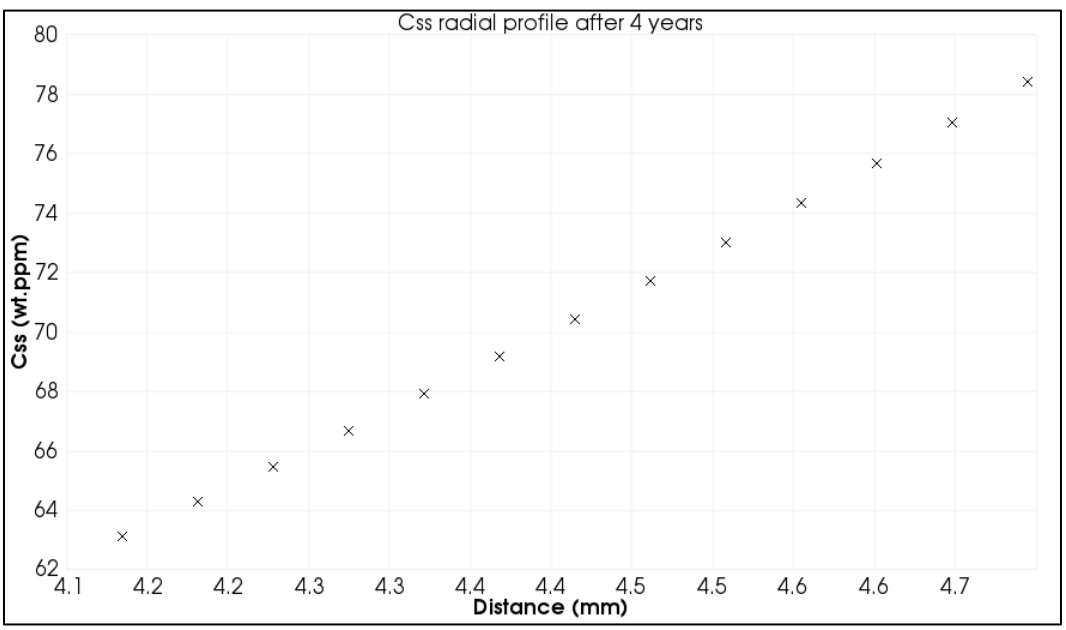

Figure 2-31: Radial hydrogen profile for the hot 5 pellets mesh at z=2cm, after 4 years

2.6.3 Hydrogen distribution in a cold 5 pellets rod

Figure 2-32 shows the axial temperature profile for this simulation, after 4 years. Again, the temperature distribution depends mainly on the pellet geometry but does not show a significant increase relative to the coolant. Figure 2-33 shows the radial distribution of hydrogen. The temperature goes from 300°C to 315°C. At 300°C, the average concentration of hydrogen after 4 years is about 22 wt.ppm and the TSSp is 99wt.ppm. Therefore no precipitation should be observed.

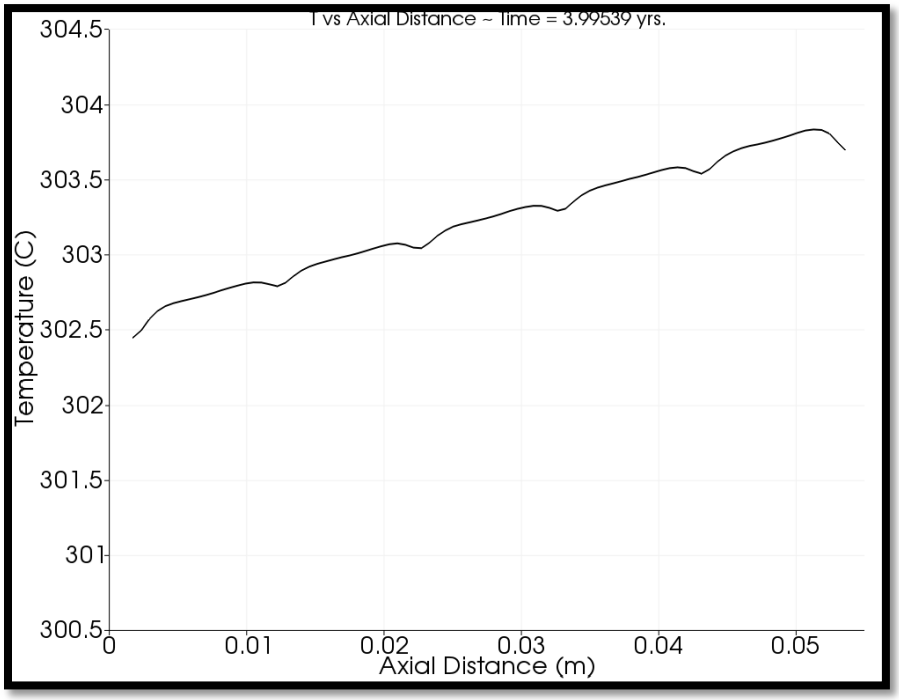

Figure 2-32: Axial temperature profile for the 5 pellets mesh at the coldest spot of the fuel at the outer edge of the cladding, after 4 years

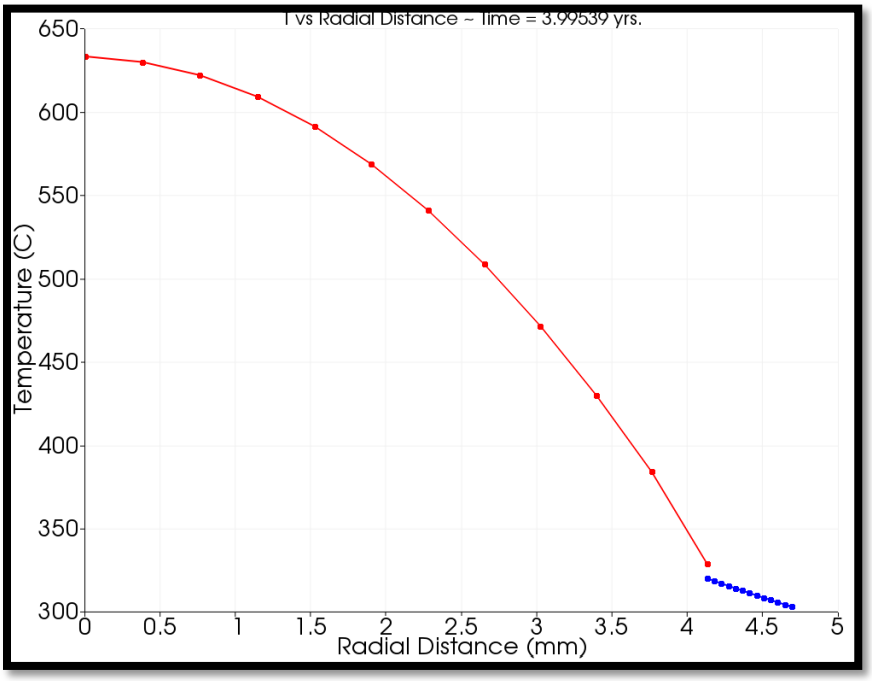

Figure 2-33: Radial temperature profile for the hot 5 pellets mesh at z=3cm, after 4 years

However, the hydrogen diffuses from the top to the bottom of the rod. Because of this diffusion, the hydrogen concentration at the lower part of the cladding can reach the TSSp. Appendix F shows a rough estimation of this axial transfer. In order to study the behavior of hydrogen in this case, the simulation was run with an initial concentration of 125 wt.ppm. Figure 2-34 shows the variation of the hydrogen concentration with the axial dimension. The profile shows similar shape to the one seen in section 2.5.3 and corresponds to the formation of the rim. Figure 2-35 shows the concentration of hydrogen in the hydrides as a function of radial distance. The radial direction is divided into 14 nodes. Only the last node shows precipitation, since once precipitation occurs, the hydrogen tends to migrate there. Thus, there is a very high (more than 6000 wt.ppm) concentration of precipitated hydrogen in the first node and none in the others. As explained in section 2.5.6, this can be corrected with a limit to the amount of precipitated hydrogen per unit of volume. This feature has not yet been implemented in BISON.

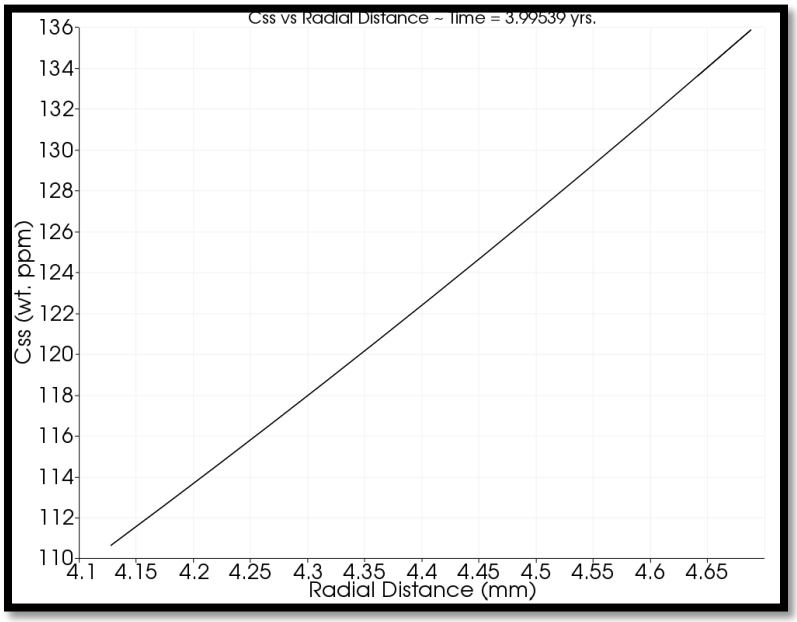

Figure 2-34: Radial hydrogen profile for the cold 5 pellets mesh at z=, after 4 years

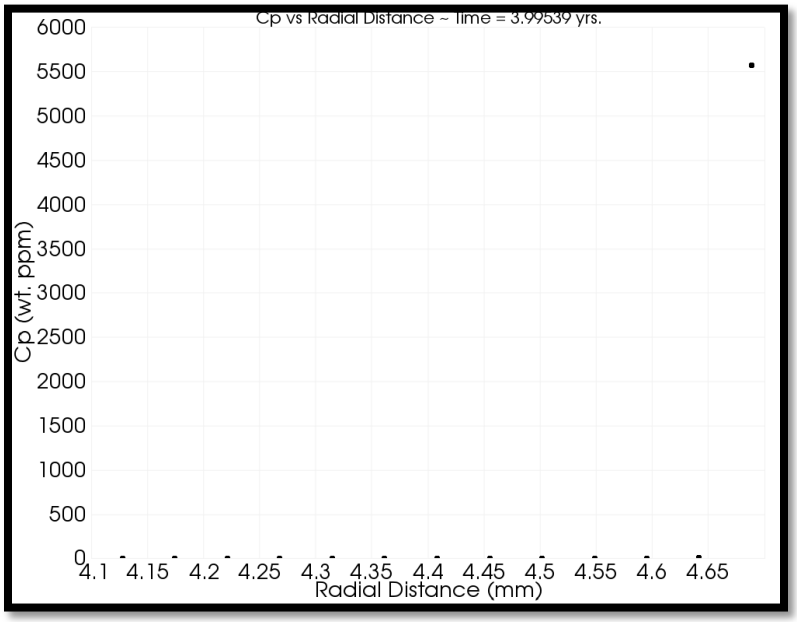

Figure 2-35: Radial hydride profile for the cold 5 pellets mesh at z=, after 4 years

2.6.4 Full rod results with BISON

As mentioned previously, the simulation of an entire fuel rod is not computationally feasible yet. This is due to the fact that the minimum time step required to run the hydrogen model is 200 seconds, which has to be done over a mesh of 360 pellets, requiring more than 65,000 nodes. The temperature calculation can be run separately using a large timestep (1E6 seconds) and takes about 12 hours for a 4-year simulation. The calculation of the evolution of the hydrogen distribution for 1 day took about 12 hours. Therefore, it has been decided to run the hydrogen calculation only for 1 day. This calculation is still useful because at operating temperature, the typical diffusion length of hydrogen is about 1 cm, so that significant diffusion can occur. The purpose of this calculation is to confirm the axial redistribution of hydrogen. The initial hydrogen content was chosen at 60 wt.ppm. Figure 2-36 shows the axial hydrogen profile after 1 hour. All the mesh points are represented in the figure. The upper line corresponds to the outer cladding. The second line is the second axial row of node (at a smaller radius). The third line is the third row. The bottom line corresponds to the inner cladding. The difference that occurs during the first hour corresponds to radial redistribution that is very fast. Figure 2-37 represents the same distribution after 1 day. When compared to Figure 2-36, a slight shift of the hydrogen concentration towards the bottom of the fuel can be observed. Figure 2-38 shows the evolution of the radially averaged concentration of hydrogen for several elevations. This evolution is described by equation 2-70

$$DC_{ss} = [\bar{H}]_{3m} - [\bar{H}]_{1m} \qquad \textbf{2-70}$$

Although the change is small, this confirms that the concentration is increasing at the bottom of the cladding and decreasing at the highest part of the cladding, thus confirming the fact that an axial diffusion occurs in the cladding in the time period observed (one day).

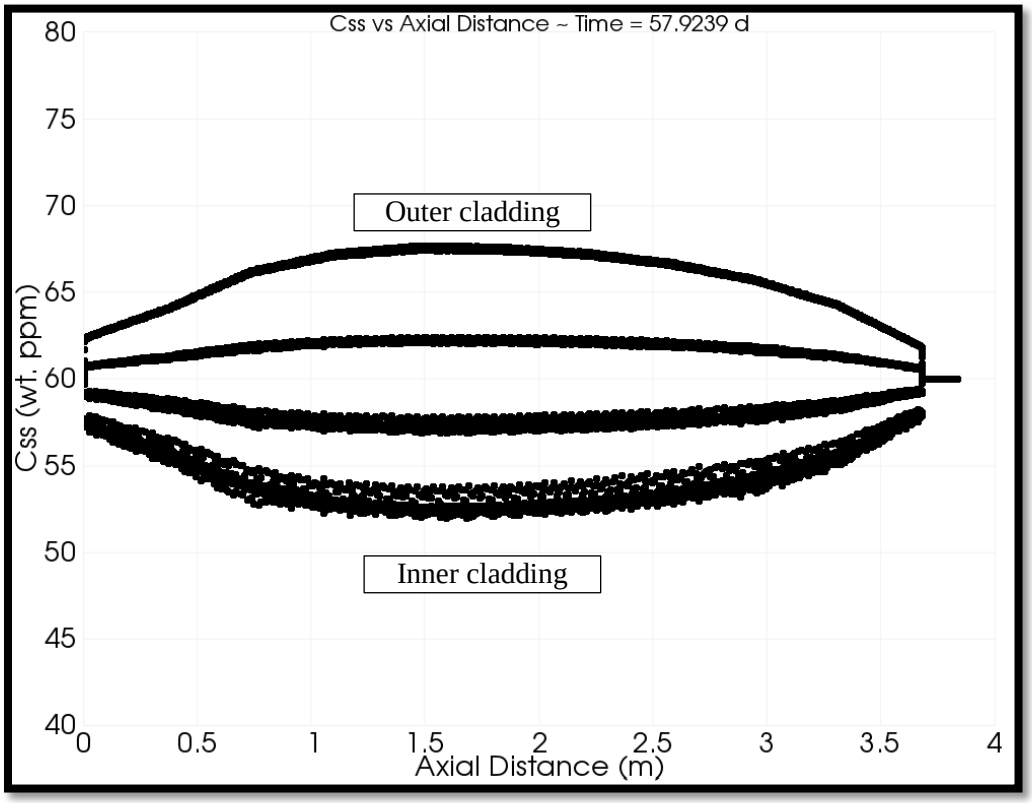

Figure 2-36: Hydrogen profile in a 360-pellets fuel cladding after 1 hour, with an initial homogeneous concentration of 60 wt.ppm

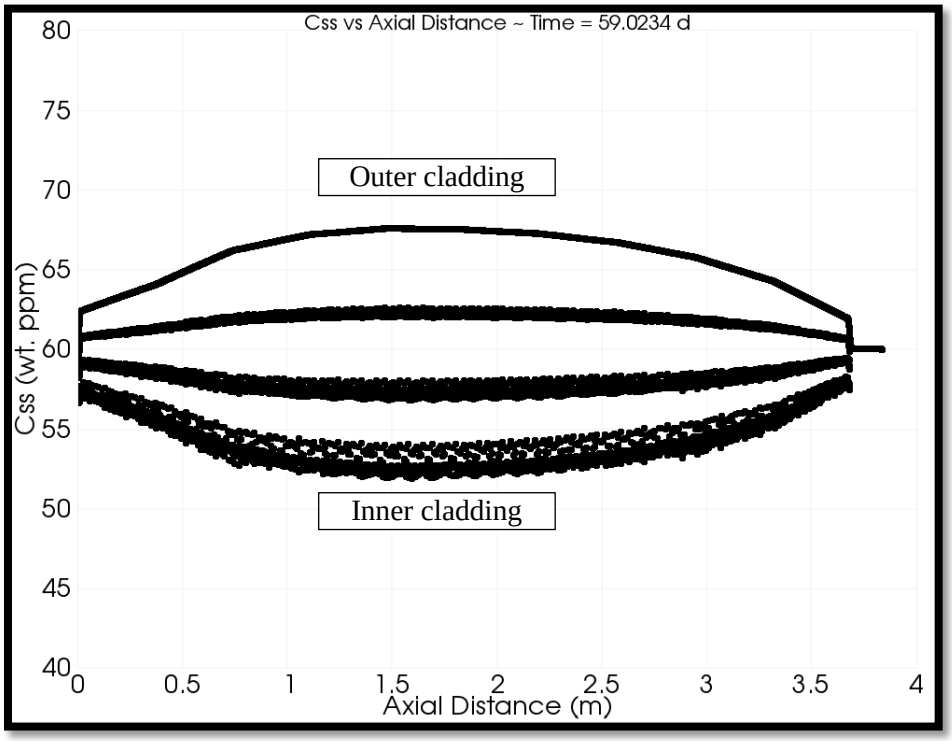

Figure 2-37: Hydrogen profile in a 360-pellets fuel cladding after 1 day, with an initial homogeneous concentration of 60 wt.ppm

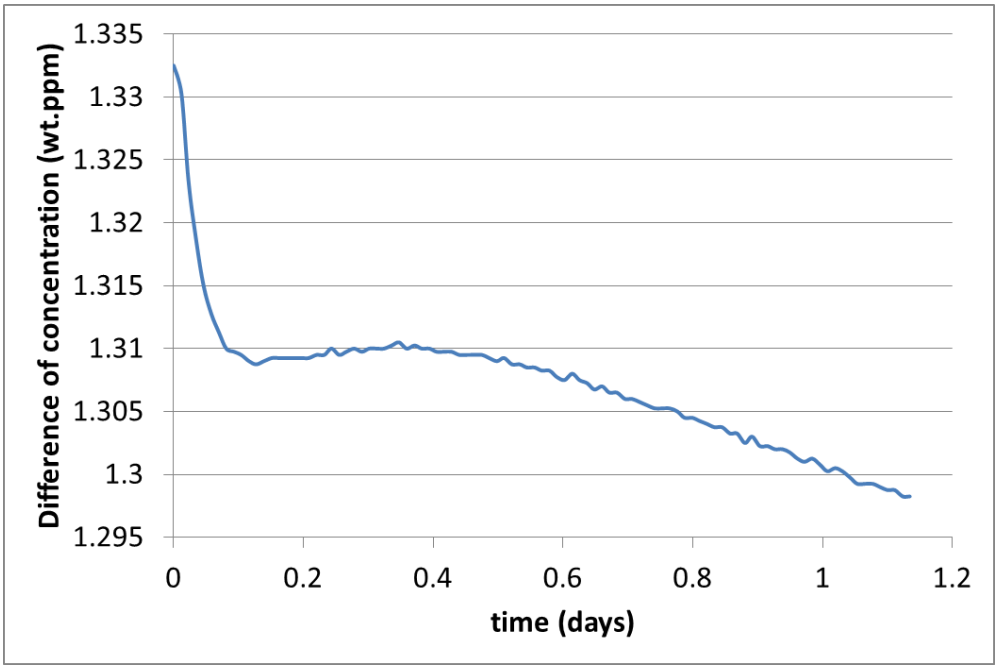

Figure 2-38: Evolution of the difference average concentration between high (z=3m) and low (z=1m) elevations.

2.7 Conclusions on Chapter 2 results

From the section 2.5, 2.6.3 and 2.6.4, the formation of the rim can be explained by a competition between diffusion and precipitation, localized at the coldest parts of the cladding, where the TSSp is the lowest. The existence of hydrides needs to take into account the axial transfer of hydrogen from the top of the cladding, where the oxidation is the highest, to the bottom part of the cladding, where the TSSp is the lowest. Without any limitation to the amount of hydrogen in hydrides, the calculated rim is very small (<50 microns), as shown in Figure 2-13. The rim thickness is explained by the precipitation kinetics. The fact that hydrogen needs time to precipitates creates a small amount of hydrogen in supersaturation that diffuses into the cladding. However, this effect is small and implies a very high concentration (full hydride) close to the outer edge of the cladding. In Figure 2-23, a limitation was applied to the amount of hydrogen in precipitated hydrides. This leads to a much more reliable thickness for the rim (~100 microns) after 4 years. However, even if this limitation has qualitative explanations (see section 2.5.6), the quantitative limitation is only based on rough estimation from previous observation.

Chapter 3: Experimental work on the model

This Chapter describes two experiments which were set up and performed in order to measure the data regarding two empirical constants: the heat of transport and the rate of precipitation.

3.1 Measurement of the heat of transport Q*

3.1.1 Scattered previous measurements of the heat of transport

Previous measurements of the heat of transport (Q*), for hydrogen in Zircaloy-4, show significant dispersion among measured values. These measurements were gathered and presented by Menibus in his thesis [54], and his table is reproduced in Table 3-1. Figure 3-1 shows the average value of each experiment against the temperature range that is used. All the measurements follow similar procedures. A zirconium (or Zircaloy) plate is initially charged with hydrogen. Then the plate is submitted to a constant temperature gradient over a long time period. At the end of the experiment, the hydrogen distribution is assumed to have a steady state profile, as given in section 1.4.3.3. In some experiments (as in the one made by Jovanovic [55]), the initial concentration of hydrogen is chosen to avoid any precipitation in the sample. In others, (e.g. Hong [56]) precipitation is observed. In the second case, the results, analysis and the calculation of Q* are more complicated because hydride precipitation affects hydrogen distribution.

Table 3-1: Summary of heat of transport of hydrogen in Zircaloy measurements

Material	**Temperature (°C)**	**H (wt.ppm)**	**Q* (kJ/mol)**	**# of exp.**	**Source**	**ΔT / Δx (°C/cm)**
Zr-α	300-500	60	24.7 ± 0.6	2	Sawatzky [57]	167
	350-400	<55	29.5 ± 0.7	2	Sugiaski [58]	n/a
	200-480	10	22.2	1	Morozumi [59]	175
	350-560	55	11+0.026 T	11	Hashizume [60]	137, 150
Zircaloy-2	295-450	300	14.2	1	Markowitz [61]	n/a
	300-500	60	22.6 ±4.2	2	Sawatzky [26]	167
Zircaloy-4	260-648	46-250	26.9 ± 5.4	11	Kammenzind [24]	66, 87
	300-340	60	28.1	1	Hong[56]	13
Zr-α-1%Nb	200-480	10	24.7	1	Morozumi[59]	175
Zr-α-2.6%Nb	300-500	68	23.4 ± 1.8	2	Sawatzky[57]	163
Zr-α-2.5%Nb	240-500	28-108	19.3 ± 1.8	8	Jovanovic [55]	43, 47, 50
Zircaloy-2 / Deuterium	300-500	120	27.2 ± 1.8	2	Sawatzky [57]	133
Zr-Tritium	250-350	<55	24.3 ± 2	3	Sugiaski [58]	n/a

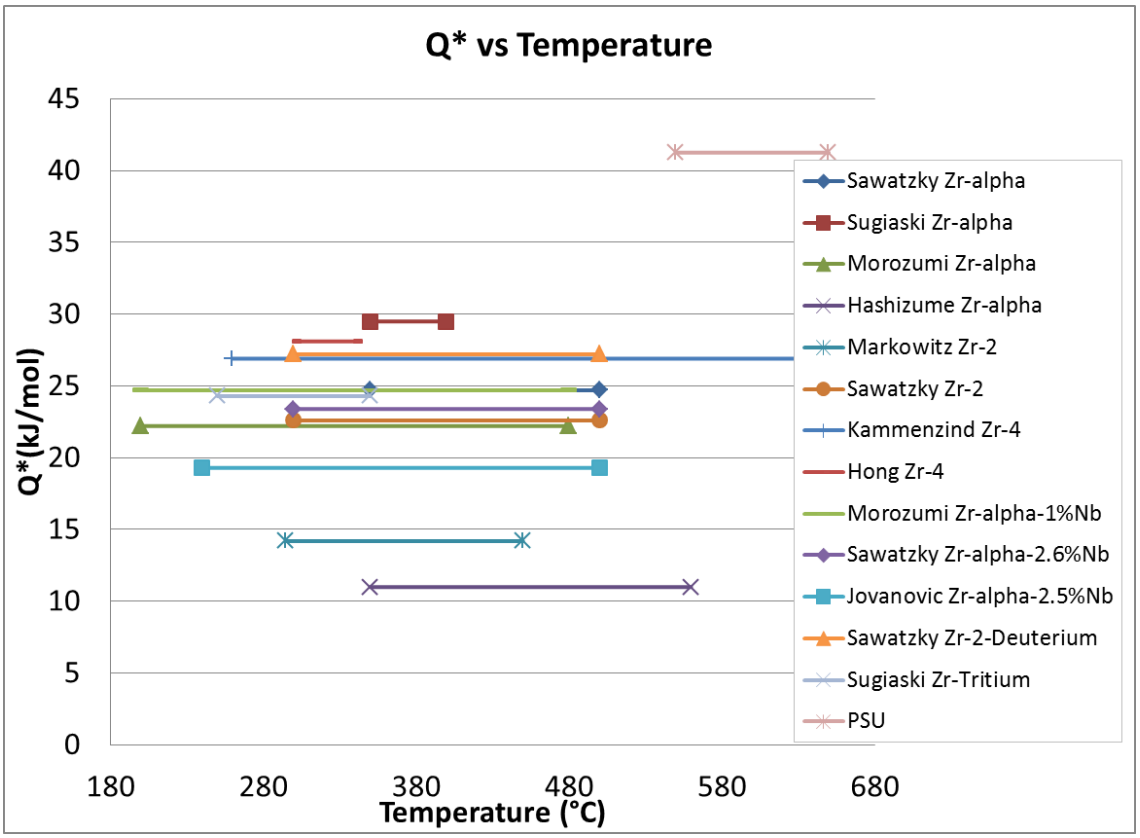

Figure 3-1: Measurement of Q* with respect to the temperature

Only two studies are devoted to Zircaloy-4. The Kammenzind's study shows a variation of the heat of transport with the temperature, but also with the gradient applied. However, no clear law seems to be deducible from his measurements [62].Figure 3-2 shows the measured values of Q* versus the inverse of the absolute temperature. Kammenzind's experimental results show a high dispersion. Regarding Hong's measurement, its correlation includes a two phase area, which should be driven by the TSSp equilibrium and not by the Soret-Fick equilibrium. This approximation may affect the calculation. Nevertheless, none of the Zircaloy-4 measurements give conclusive results. Since this parameter is critical in the diffusion model and that it cannot be calculated, an experiment was designed to measure the value of Q*.

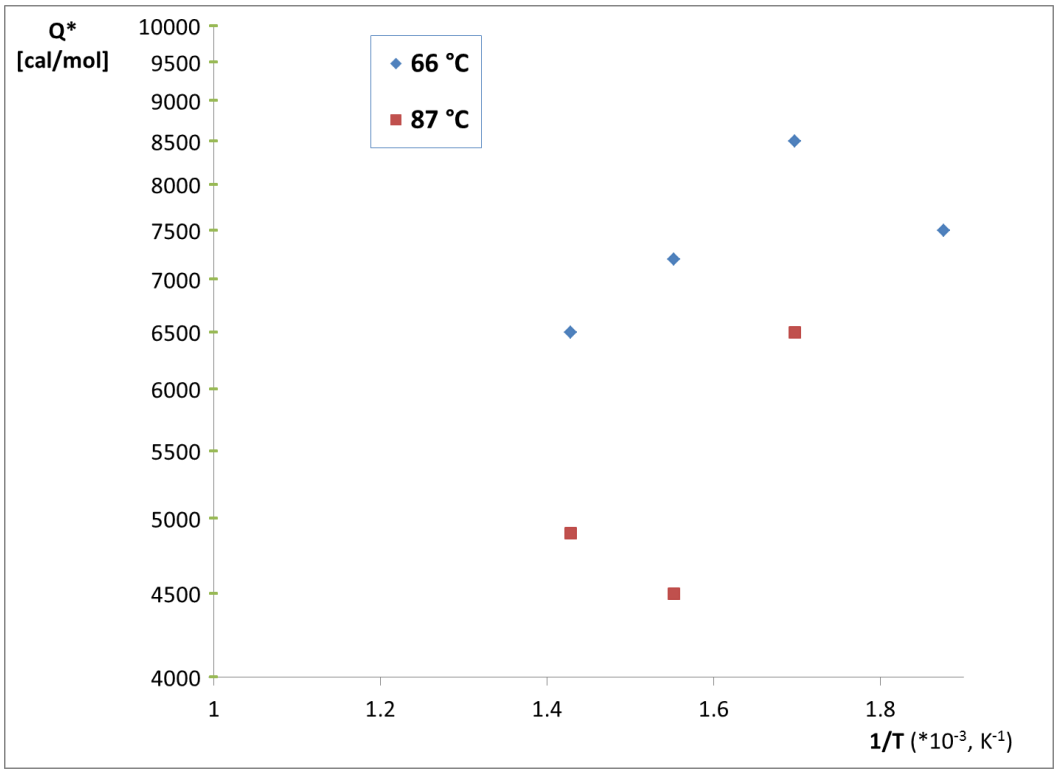

Figure 3-2: Heat of transport measured by Kammenzind

3.1.2 Experimental design for measurement of Q*

The experiment was designed[1] to observe the redistribution of hydrogen under a temperature gradient in the absence of precipitation, as done by Jovanovic et al. but not by Hong [55, 56]. In this case, the steady state equilibrium hydrogen concentration in solid solution is given by:

$$C_{ss}(x) = C_0 * \exp\left(\frac{Q^*}{RT}\right) \qquad \textbf{3-1}$$

[1] *The experiment was designed with the help of Daniel Nunez, undergraduate student and summer intern at the Pennsylvania State University, within the framework of the Toshiba-Westinghouse Fellows Program.*

The sample chosen for the study is a Zircaloy-4 plate, measuring 1cm x 3.4cm x 0.06cm. The sample is stacked between two stainless steel holders, as shown in Figure 3-3.

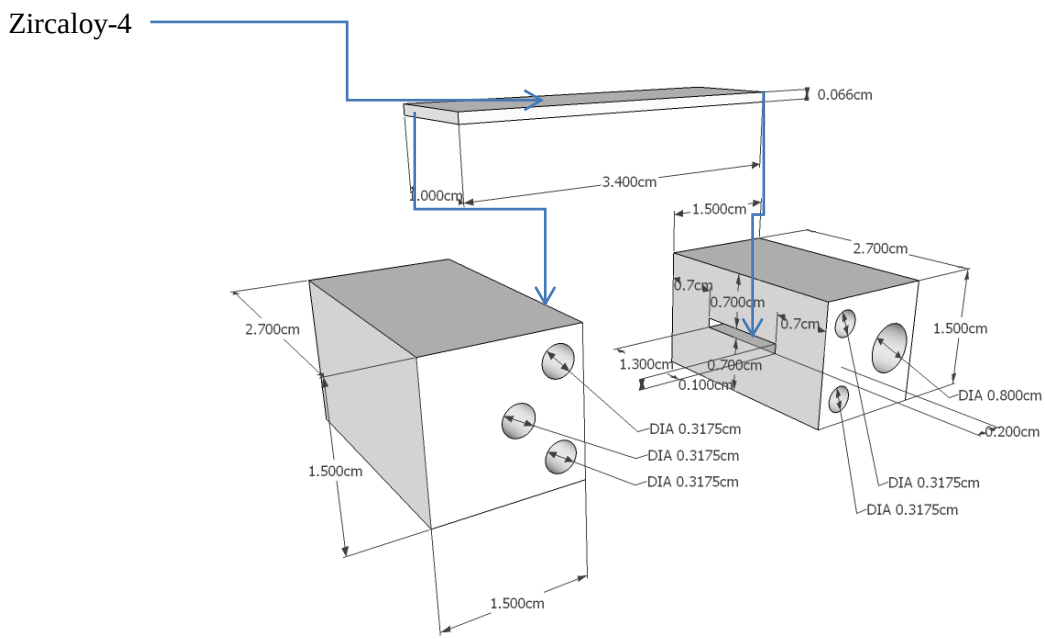

Figure 3-3: 3-D View of the 304 Stainless Steel holders and the Zircaloy-4 plate sample

The holder with 3 small holes is heated to the higher temperature and the second one is one heated to a lower temperature. The plate is inserted about 2 mm into the slot in each holder, which means that the experimentally usable section of the sample is 3 cm long. The holders were heated with silicon carbide surface igniters[63]. These igniters can reach a temperature greater than 1000°C, and allow obtaining high temperatures in a localized spot. The igniters are placed on the outside of the holders, as shown in Figure 3-4.

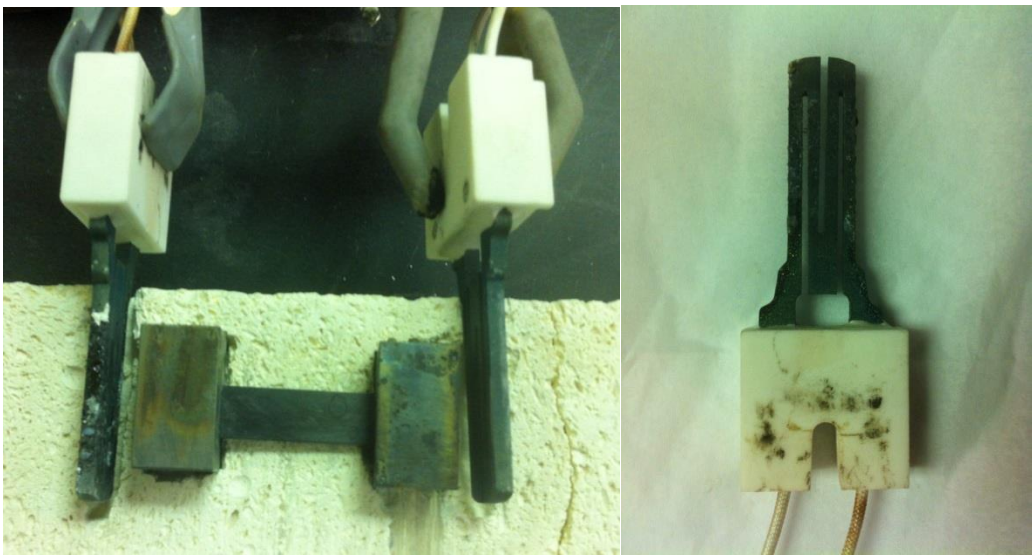

Figure 3-4: Heaters, holders and sample in the heat of transport experiment

The 0.3175 cm holes drilled into both of the heaters were to be used for heat cartridges. Because of systematic failures of the Omega ® cartridge heaters at 400°C, these holes are no longer used in the current design. The heat cartridges have been replaced by surface igniters.. Both of the silicon carbide igniters are controlled with Benchtop Temperature Controllers. Figure 3-5 and Table 3-2 below show the front and back view of the controllers, and their main specifications.

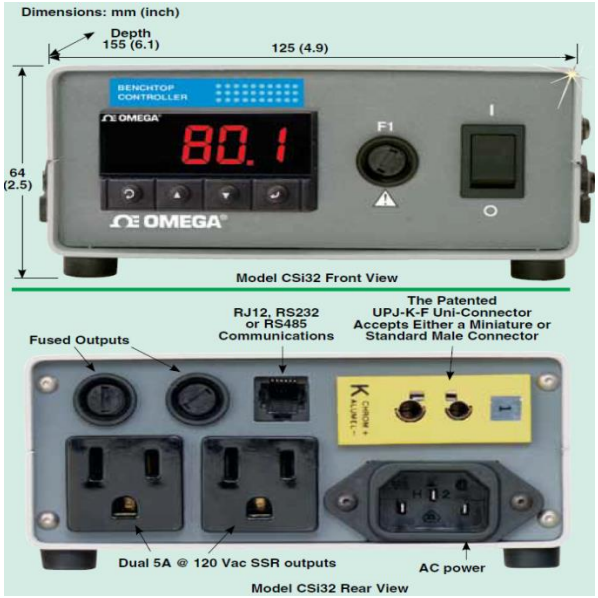

Figure 3-5: Temperature controller front and back views

Table 3-2: Temperature controller Specifications

Specification	***Value***
Resolution:	1°/0.1°; 10 µV process
Temperature Stability:	RTD: 0.04°C/°C
Reading Rate:	3 samples per second
Display:	4-digit, 9-segment LED;
Input Types	Thermocouple, RTD, analog voltage, analog current
Thermocouple Lead Resistance	100 Ω (max)
Digital Filter:	Programmable

These controllers are configured in a Proportional-Integral-Derivative mode. The controlled temperature is given by a type-K thermocouple, attached to the extremity of the plate (But not in the holder). Figure 3-6 shows the control loop pattern.

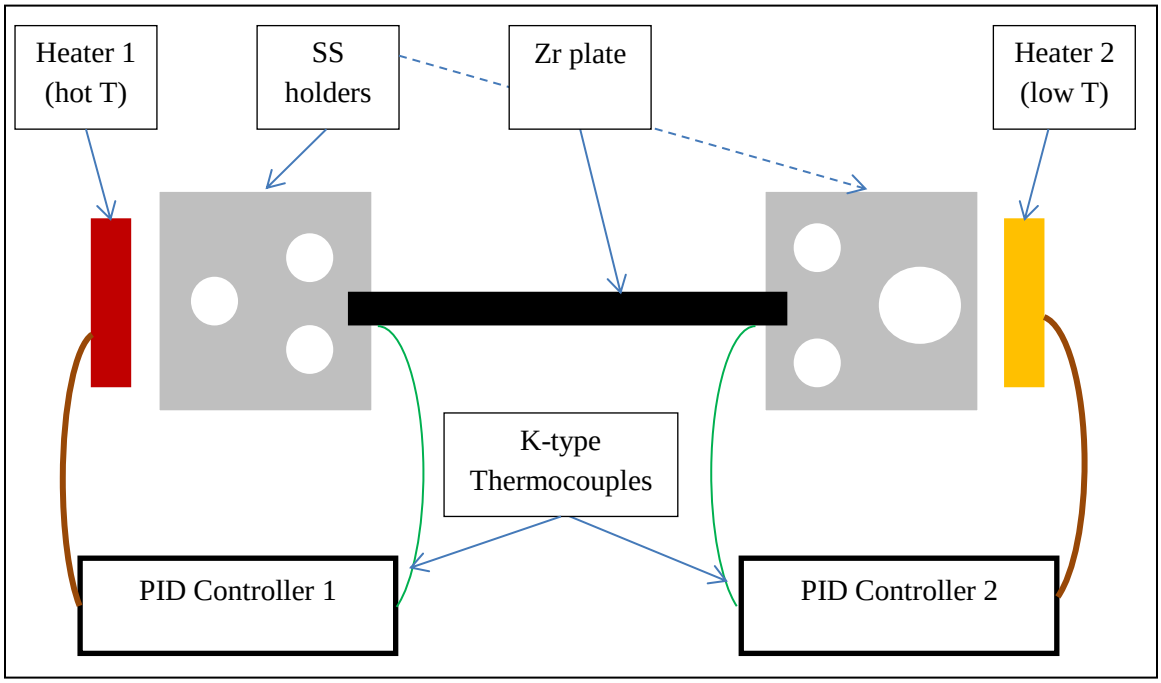

Figure 3-6: Schematic of the temperature control for the diffusion experiment

The PID values have been chosen using a manual configuration. Table 3-3 reproduces the values chosen.

Table 3-3: PID values of the thermal controllers

Parameter	PID controller 1	PID controller 2
P	50	300
I	100	150
D	6.0	25

Since there is a heat transfer from the hot side to the cool side of the plate, a thermal flux is created toward the “cool” holder, where the heat is removed using an air cooling system connected to this holder. The air flow is controlled by a regulator (Figure 3-7). Air is blown through a glass tube into the main hole of the second holder (Figure 3-8). However, due to heat loss caused by natural convection, this system is not used in most of the experiments.

Figure 3-7: Air flow regulator

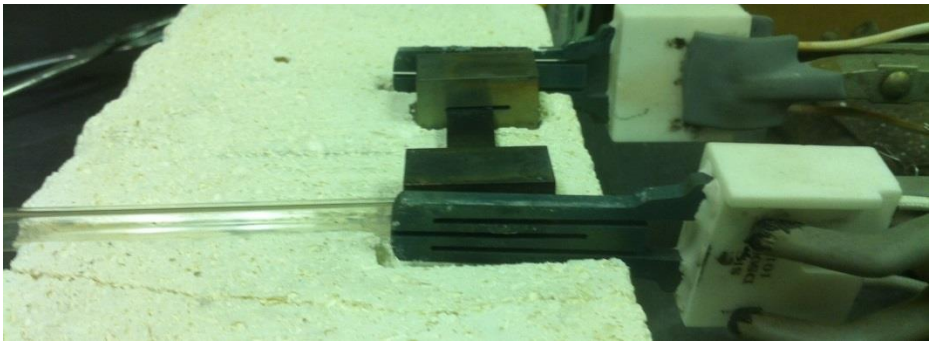

Figure 3-8: Connection between the air tube and the holder

In order to minimize heat losses, two different types of insulation have been installed. First, the entire setup (holder, heating elements, sample and thermocouples) is contained within two insulating bricks. Second, insulation blankets are used to wrap the sample to provide additional thermal insulation. The design of the insulation is shown in Figure 3-9. A second brick covers the experiment.

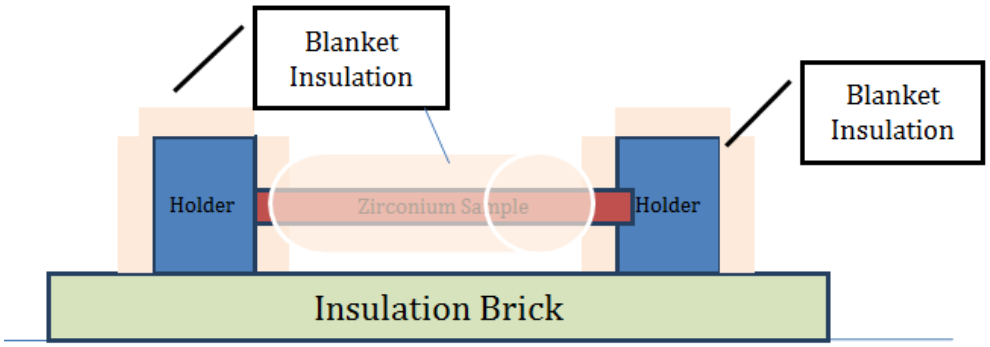

Figure 3-9: Design of the insulation of the experiment

Once the second brick covers the experimental set up and the specimen is at temperature, the temperature measured outside of the experimental setting is smaller than 25 °C (for a room temperature of 20°C). This indicates a small heat loss and good thermal insulation.

The temperature profile was measured nonlinear in the sample, using a thermocouple in the middle of the plate. This indicates the presence of temperature losses. After several attempts, it was not possible to obtain a linear gradient. Nevertheless, the steady state hydrogen concentration profile is expressed as a function of temperature. Therefore, by knowing the temperature profile, the hydrogen concentration profile can be calculated. In order to accurately obtain the steady state temperature profile, 5 thermocouples have been attached to the plate, as shown in Figure 3-10.

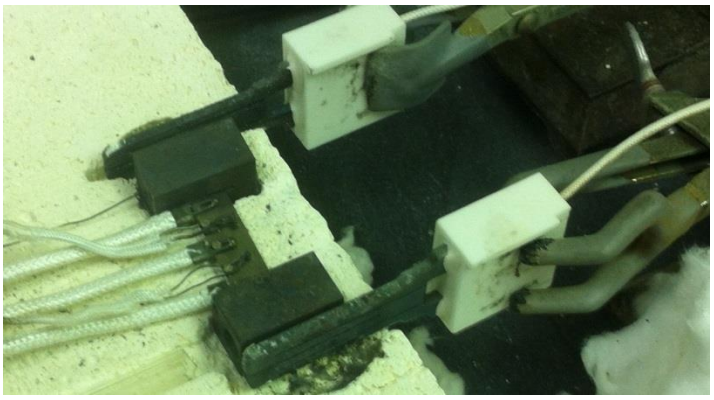

Figure 3-10: Thermocouples on the sample

3.1.3 Sample preparation

The preparation of the samples requires the following steps.

- Since the sample is exposed to high temperature (~ 500-700°C), the sample may recrystallize. To avoid change to the microstructure during the experiment, the sample is subject to a recrystallization heat treatment before the experiment starts.
- To prevent oxidation, the samples are coated with a deposited 100 nm layer of Nickel.
- Hydrogen is put into the sample using to the hydrogen charging equipment at PSU.

3.1.4 Experimental procedure

In a first attempt, the experiment was run with a 750°C-650°C temperature difference. The sample had been charged with an initial concentration of 1000 wt. ppm. After 40 hours, the experiment was stopped and the sample quenched. Unfortunately, the sample broke during the experiment as shown in Figure 3-11. On the hot side, almost 20% of the sample was destroyed and transformed into oxide dust. Moreover, the sample was significantly bent. The sample failure is probably due to a strong oxidation and a low yield stress that have allowed plastic deformation. The high oxidation rate due to high temperature and issues with the Ni coating probably leads to the formation of a “destructive” oxide layer. Then, at high temperature, the yield stress is significantly lower and thus allows plastic deformation.

Figure 3-11: Sample damaged after 750°-650° experiment

In order to prevent these phenomena, a new run with a lower gradient (650°C-550°C) was performed. In this case, the initial concentration has to be 650 wt. ppm in order to prevent hydride precipitation. The hydrogen charging does not allow a precise concentration. The hydrogen concentration has been measured after the charging and was equal to 709°C wt.ppm. Therefore, the temperatures conditions were moved to 660°C-560°C to avoid precipitation. During preliminary tests, the temperature profile has been measured to estimate the heat loss. Assuming a constant linear heat loss, and using a sample length l=3 cm,

$$T(x) = \frac{q}{2k} * x^2 - \frac{q}{2k} l * x + T_{maxi} \qquad \textbf{3-2}$$

Where q is the linear heat loss, k is the thermal conductivity and T_{maxi} is the temperature at the hot end. It has been determined experimentally that $\frac{q}{2k} = 27K.cm^{-2}$.

The steady state profile hydrogen profile (and the TSSp) obtained for this temperature profile are given in Figure 3-12. The steady state profile confirms the fact that there should not be any precipitation. In order to perform the calculation, the value heat of transport was assumed equal to $2.51 * 10^4\ J/mol$. This average value comes from Kammenzind work. [64]

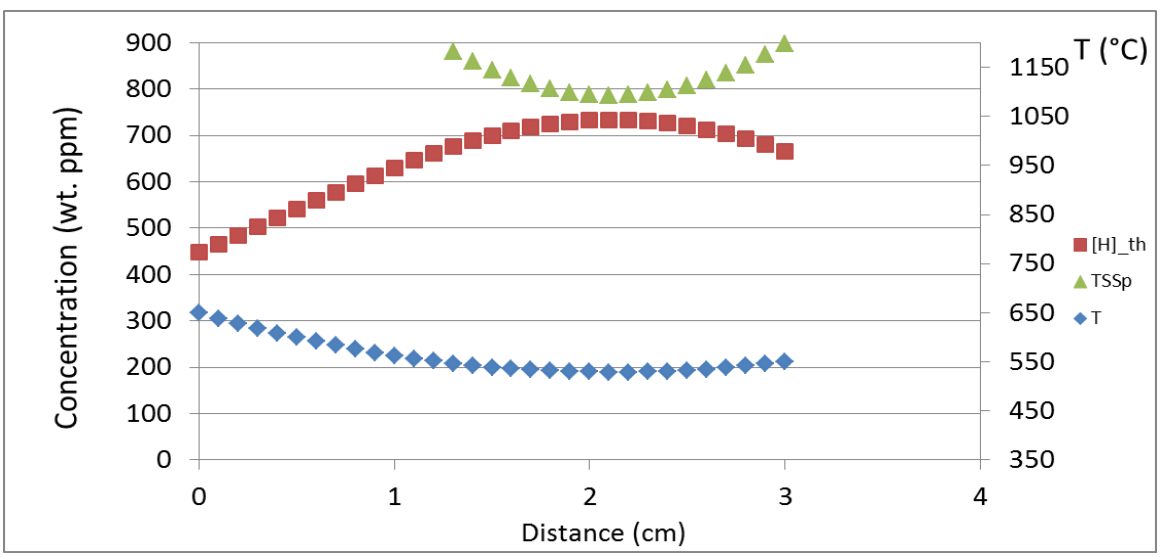

Figure 3-12: Temperature and hydrogen steady state profile under 650°-550° gradient

To perform the experiment, dissolution of all the hydrides is required. To dissolve the hydrides, it is necessary to heat up the sample to a temperature higher than the dissolution TSS (TSSd) in the sample before applying the temperature gradient. Assuming the same quadratic profile, a temperature of 680°C applied at each side of the sample is necessary. According to a steady state calculation, the application of this temperature to the sample implies a full dissolution of the hydrogen, as shown in Figure 3-13.

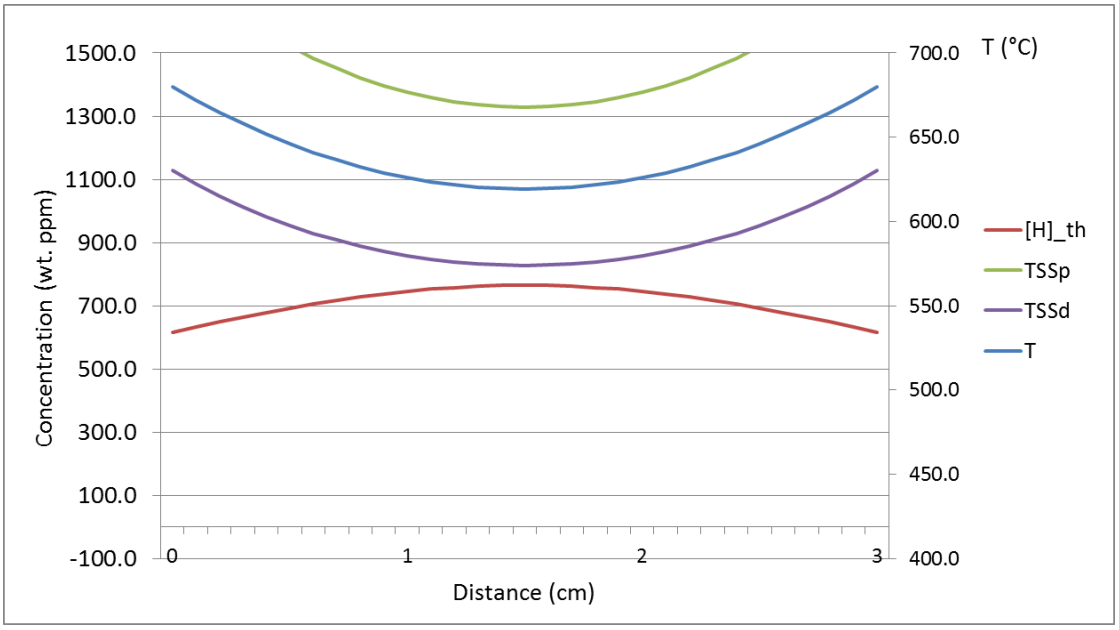

Figure 3-13: Hydrogen profile before starting 660°C-560°C gradient experiment

After the dissolution step, the 660°C-560°C gradient has been applied. Using the HydruLab code developed in the frame of this project and presented in section 2.1, the transient profile has been calculated, assuming an initial constant hydrogen profile. The transient profiles are represented on Figure 3-14 and Figure 3-15 for hydrogen in solid solution and hydrides respectively. Each line represents 10 hours. Table 3-4 shows a numerical estimation of the difference between the steady state profile and each transient profile, by calculating the maximum, minimum and average difference of the 200 mesh points. Considering that the

uncertainty of the hydrogen measurement is 20 wt.ppm, it can be concluded that after 60 hours, the transient is sufficiently close to the steady state (with a difference of about 5 wt. ppm).

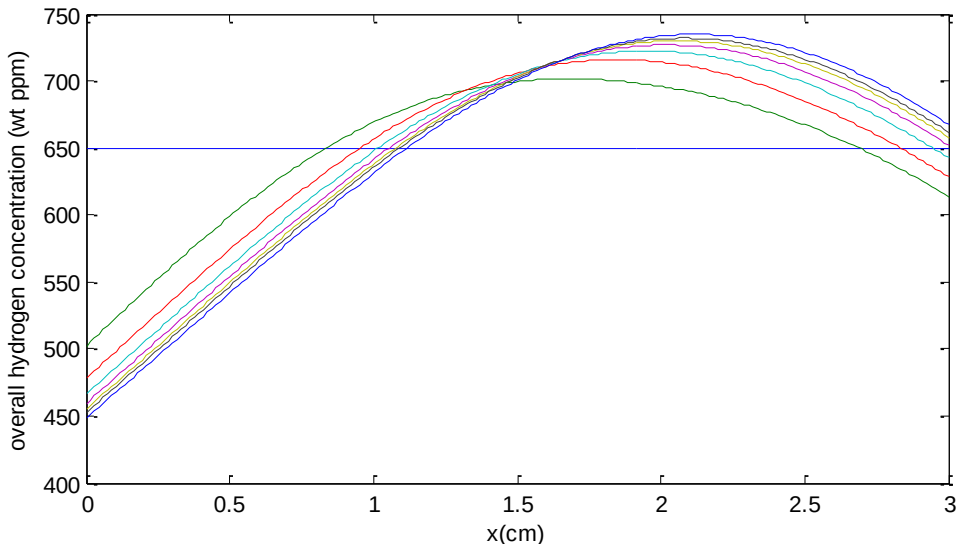

Figure 3-14: Kinetics of the concentration profile (one line per 10 hours) with a 650°-550°C gradient

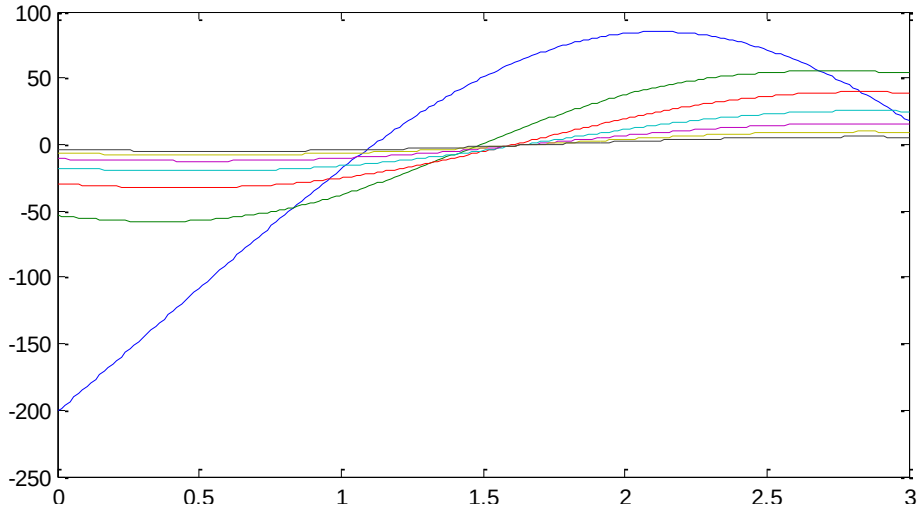

Figure 3-15: Difference with steady state (one line per 10 hours) with a 650°-550°C gradient

Table 3-4: Estimators of the difference between transient and steady state profile (650°C-550°C)

time (h)	average difference with SS	maximum difference with steady state	minimum difference with steady state	standard deviation
0.0	198.8	84.8	-200.6	86.3
10.0	53.9	55.5	-58.0	44.9
20.0	29.6	39.5	-32.6	27.9
30.0	17.8	25.3	-19.9	17.4
40.0	10.9	15.7	-12.4	10.8
50.0	6.7	9.6	-7.8	6.7
60.0	4.1	5.7	-4.9	4.1

Figure 3-16 shows the sample after 60 hours. There is some oxidation on the surface, but it is mostly a black protective layer. After measurement of the oxygen content, the oxide layer is thinner than 20 microns.

Figure 3-16: Sample after 660°C-560°C experiment

3.1.5 Results of the heat of transport experiment

The temperature profile has been measured during the experiment at five different locations on the plate. The temperature was measured constant during the 60 hours of the experiment. Table 3-5 provides the temperatures and the locations of these thermocouples. The length of the sample in which analysis is judged to be reliable, goes from the first to the last thermocouple, which corresponds to a length of 2.6 cm

Table 3-5: Temperature in the plate during the diffusion experiment

Location of the thermocouple	Temperature (°C)
0.4	550
1	567
1.7	581.5
2.4	607
3	660

This temperature profile cannot be estimated with the simplified profile described by equation 3-2. The heat losses are modeled with by convective heat transfer with the air. The equation 3-3 describes the steady state equilibrium

$$k\nabla^2 T + \frac{2 \cdot h}{l_{Zr}}(T - T_{air}) = 0 \qquad \textbf{3-3}$$

With k the conductivity of the Zircaloy-4, l_{Zr} the length of the plate, h the heat transfer coefficient for Zircaloy in air and T_{air} the temperature of the air. Equation 3-3 has for solution:

$$T(x) - T_{cool} = (T_{cool} - T_{air}) \cdot \cosh\left(\frac{x}{\sqrt{\frac{2 \cdot h}{l_{Zr}}}}\right) + \left[T_{hot} - T_{air} - (T_{cool} - T_{air}) * \coth\left(\frac{2.6}{\sqrt{\frac{2 \cdot h}{l_{Zr}}}}\right)\right] \cdot \sinh\left(\frac{x}{\sqrt{\frac{2 \cdot h}{l_{Zr}}}}\right) \quad \text{3-4}$$

The temperature of the air is assumed to be equal to the temperature of the coolest side. The h is assumed to be equal to 45 K^{-1} and the conductivity is 2100 m/K.[65] Figure 3-16 shows the calculated profiles and the measured thermocouple data points, showing that the temperature model given by equation 3-3 provides a good estimate of the actual temperature profile.

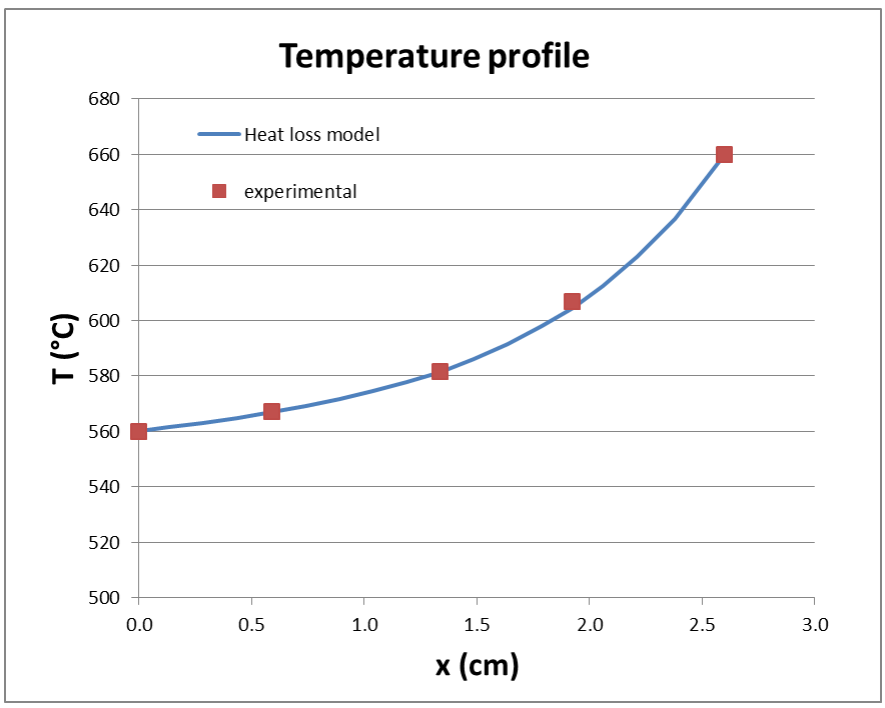

Figure 3-17: Temperature profile for diffusion experiment

Subsequent to the experiment, the plate was cut into small samples 1.5 mm wide, and the hydrogen measured in each slice using hot vacuum extraction (performed by Luvak company [66]. Figure 3-18 shows the natural logarithm of the concentration (multiplied by the gas constant R) as a function of the inverse of temperature. The slope of the curve is Q* in J/mol.

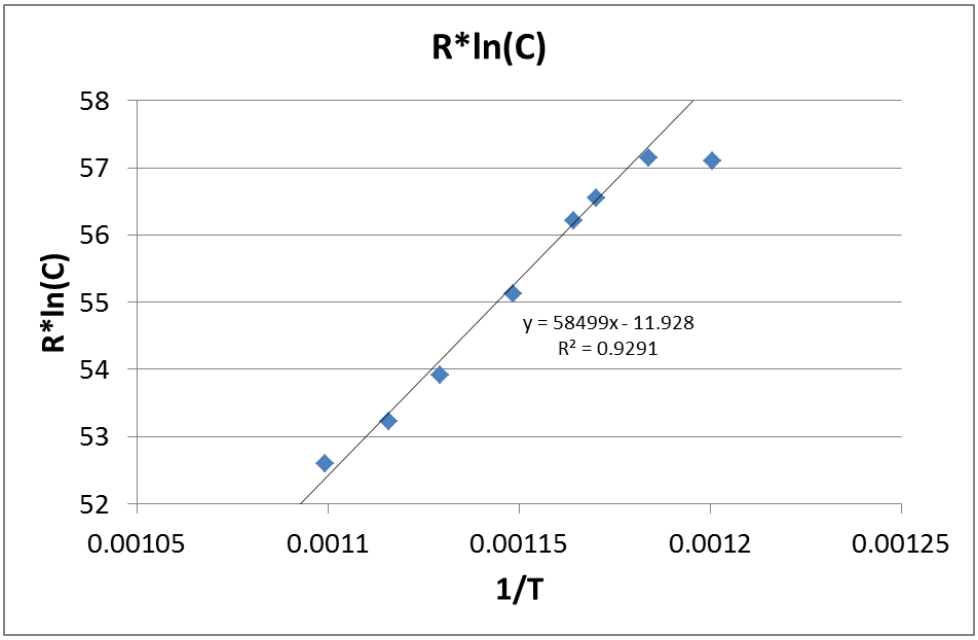

Figure 3-18: Result of the diffusion experiment

The value find for Q* is 58.50 kJ/mol.

3.1.6 Conclusion of the results of the Q* measurement

The value for Q* found in this work is higher than Kammenzind's measurements and in fact higher than all the measurements reported in Table 3-1The order of magnitude is comparable, as shown in Figure 3-19. Considering Kammenzind data, it is possible that the value of the temperature gradient has an impact on the value of Q*. This trend seems to be confirmed by the measurement made during this work. The temperature gradient was 38°C/cm, which is significantly lower than Kammenzind's data. However, the comparison of all the measurements

versus the temperature gradient, as shown in Figure 3-20, does not confirm such a trend. This result should be confirmed with other temperature gradient in order to validate or not the conjecture. If the value of Q* is dependent on the temperature gradient, the model of the Soret effect should be modified.

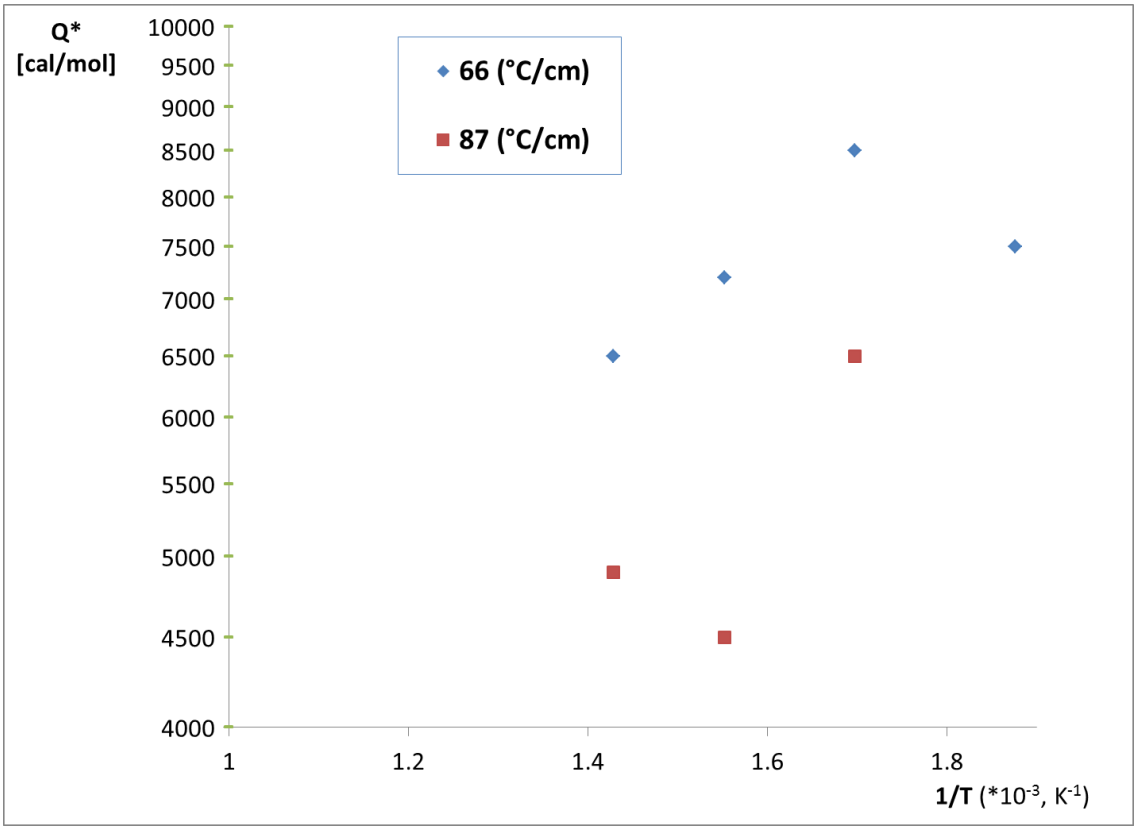

Figure 3-19: Comparison of experimental results with Kammenzind's data [24]

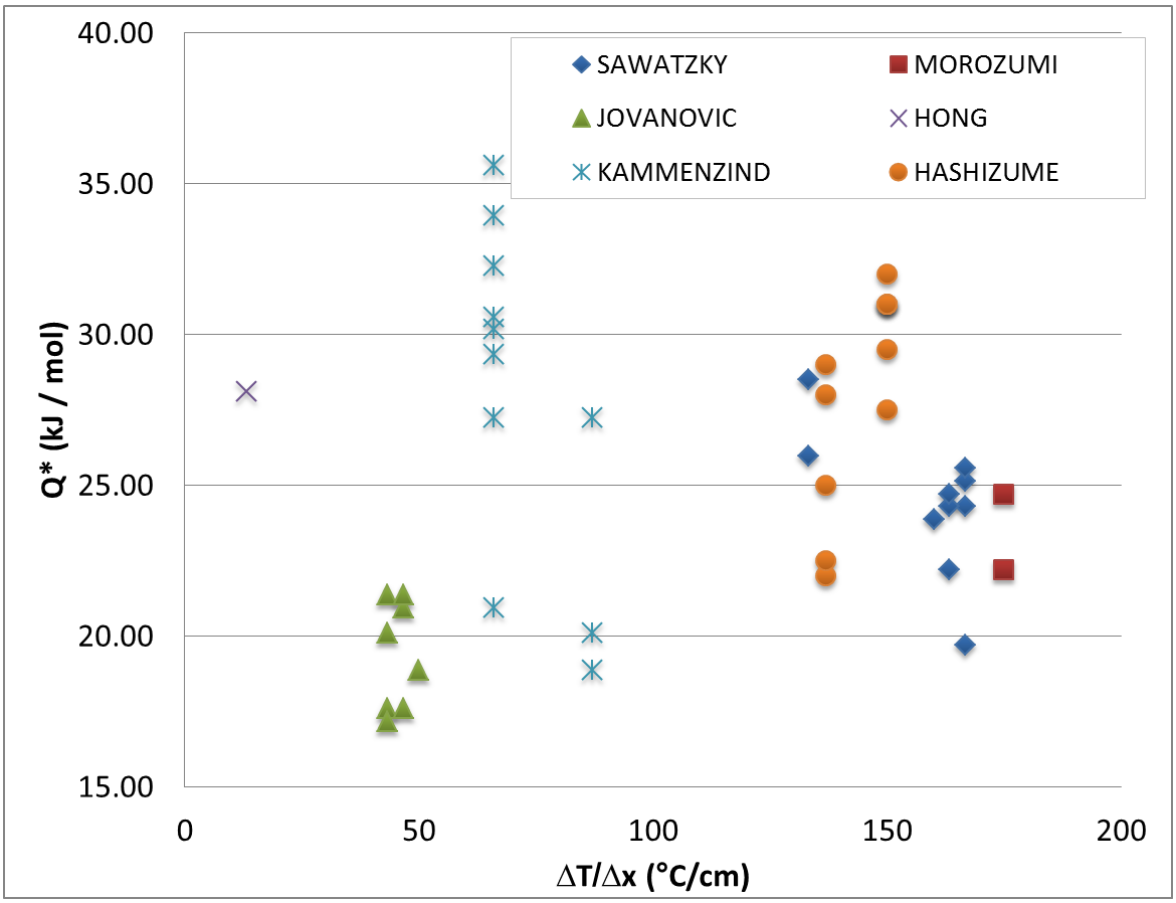

Figure 3-20: Heat of transport Q* measured in the literature as a function of the temperature gradient

3.2 Measurement of the rate of precipitation

3.2.1 A significant lack of measurement

The rate of hydride precipitation in Zr alloys has been poorly studied. Except for Kammenzind's measurements and his Arrhenius law correlation, as shown in Figure 1-14, no extensive study has been performed to measure this rate. The main difficulty in the calculation of rate of precipitation is that it contains kinetic parameters, and therefore has to be studied in-situ. Zanellato and al., have measured the precipitation kinetics at 300°C, using a similar technique to the one used in the experimented presented below. They found a value of $\alpha^2 = 0.012 s^{-1}$ which corresponds to $\alpha = 0.11\ s^{-1/2}$ [67]. This value is about 10 times what Kammenzind found in equation 1-47. His correlation gives $0.0109\ s^{-1/2}$ at 300°C.

3.2.2 Experimental technique

The current section is directly inspired from Kimberly Colas PhD thesis [27].

3.2.2.1 General Description of XRD using Synchrotron Radiation

The technique used in this study is synchrotron radiation X-Ray diffraction at the Advanced Photon Source (APS) at Argonne National Laboratory (Argonne, Ill). X-Ray diffraction is the process of the coherent scattering of an X-Ray beam by planes of atoms in a crystal and is governed by Bragg's law [68, 69]:

$$\lambda = 2\, d\, sin(\theta) \qquad \textbf{3-5}$$

where λ is the wavelength of the x-ray beam (m), d is the inter-planar spacing of the atoms (m) and θ is the diffraction angle (radians) as illustrated in Figure 3-21. The quality of X-Ray diffraction data is directly related to the quality of the X-Ray source used. In this study, the X-

Ray source is the APS synchrotron. The APS is a third generation synchrotron which produces X-rays at a very high brilliance which allows enhanced resolution and high energy radiation compared to conventional laboratory X-ray sources such as Cu-Kα for example. The brilliance is a measure of the intensity (photons per second per unit area) and directionality of the X-ray beam through its divergence (milliradians squared). The brilliance of the APS is 6 to 10 orders of magnitude higher than that of a conventional X-Ray source such as Cu-Kα [70]. This very high brilliance allows quick acquisition of data, high resolution and low background. This enables the detection of small volume fractions of phases that would otherwise not be detected. In addition, the high photon flux can be produced over a wide range of energies. This enables either the use of a monochromatic beam with a high and well known energy for our material or the use of a polychromatic beam.

In the next section, the beamline used for our experiments (designated 1-ID,) is described. Its position along the APS synchrotron ring is shown in Figure 3-22. This beamline operates at very high energy (e.g. 80 KeV) which allows the X-Ray beam to transmit through the thickness of a 1 mm thick sample, thus providing bulk information on the sample studied.

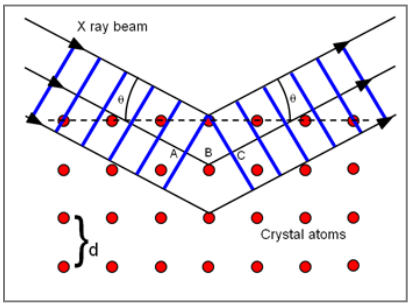

Figure 3-21: Illustration of Bragg's law.

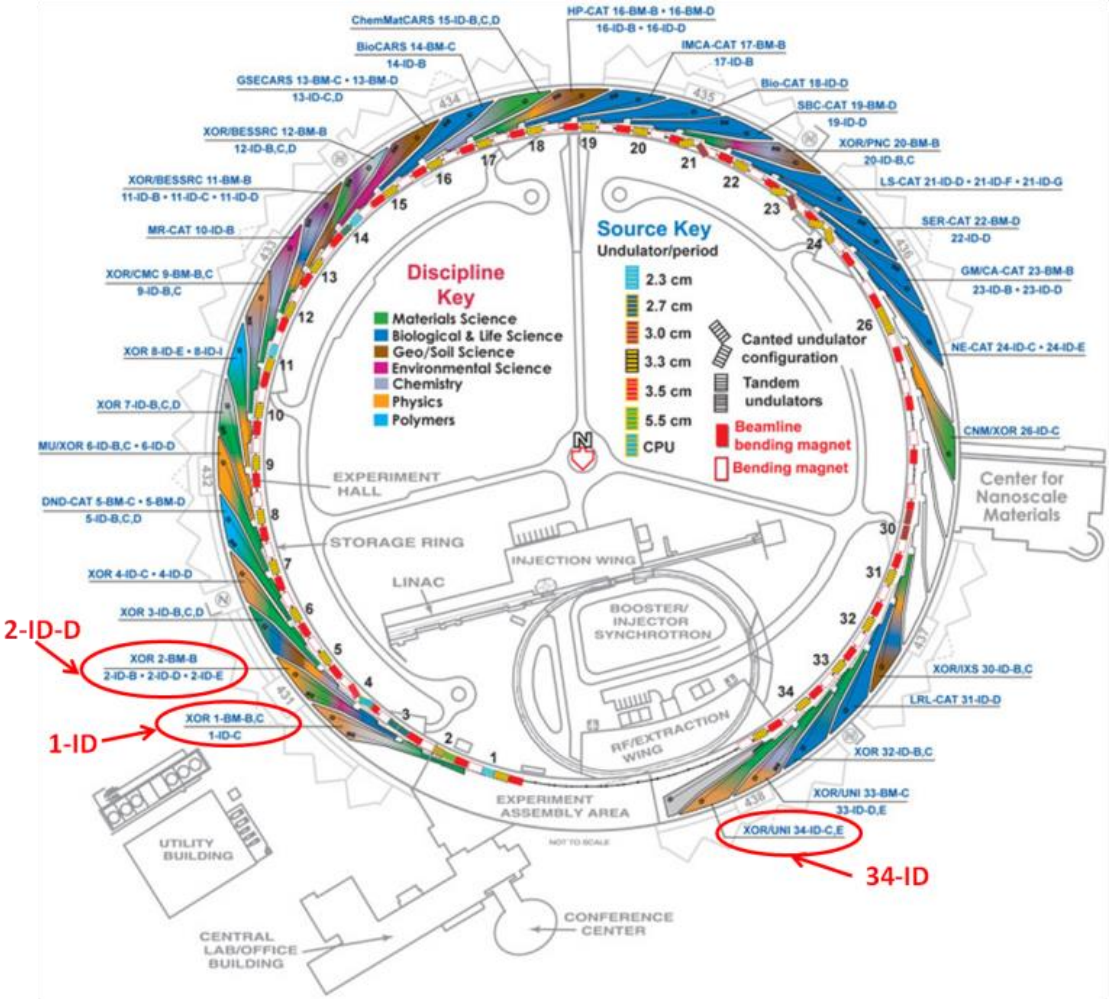

Figure 3-22: Advanced Photon Source synchrotron and position of the beamline used in our experiment.

3.2.2.2 Beamline 1-ID: High Energy In-Situ Transmission XRD

- ***Beamline properties***

Beamline 1-ID has the unique capability to operate at very high photon energies (more than 80 keV) allowing X-Rays to penetrate through the sample, while operating in transmission X-Ray diffraction. This allows data to be averaged over the full sample thickness which provides very good statistics. This beamline is also equipped with a fast amorphous silicon GE detector that allows very fast data collection rates. The beam is focused to a rectangular shape with slits which can be as small as 50 x 50 μm [71]. The geometry of the beamline, illustrated

schematically in Figure 3-23, allows the full diffraction rings to be recorded, which helps reveal in-plane texture.

The 1-ID beamline is also equipped with an MTS® load frame. This load frame is used for applying stresses to samples by computer monitoring of the applied force, the displacement, or the displacement rate. In addition, an optical furnace can heat the samples up to 900ºC while continuously gathering X-Ray diffraction data. The heating and cooling rates can be monitored by temperature controllers using K-type thermocouples, spot welded onto the sample surface as feedback. The load frame and furnace can be seen in Figure 3-24.

- ***Experimental procedures***
    - **Sample Preparation**

One of the advantages of the 1-ID beamline is that very little sample preparation is needed in order to obtain reliable X-Ray diffraction data. Since the high energy X-Rays penetrate through the entire sample thickness, no particular surface preparation is needed, although having two parallel surfaces through the sample thickness simplifies the calculation of sample to detector distance. The only requirement is to allow full transmission of X-Rays through the sample. In the case of zirconium atoms probed by 80 keV X-Rays, a maximum thickness of 2 mm is allowed for the samples.

    - **Calibration**

A calibration sample of a APS ceria powder is run at the beginning of every experiment in order to measure the exact beam position, angle and sample-to-detector distance. The X-Ray diffraction data from this sample is fitted, and the results of the fit are used to measure the volume fraction of hydrides in the zirconium matrix.

    - **Data Acquisition**

The data is acquired on a large two-dimensional plate detector that allows the recording of the full diffraction ring. The detector recording area is 2048 x 2048 pixels big with each pixel measuring 200 x 200 μm, which gives an angular resolution of 4.6 x 10^{-3} ^{o} with our typical set-up. In the experiments performed at beamline 1-ID, continuous recording of data was performed while heating and cooling of samples under load. This allowed studying the kinetics of hydride precipitation *in situ*. One diffraction frame was recorded as ten consecutive images with a typical exposure time of 1 second (to avoid saturation of the detector). While recording data, the temperature and load were monitored and recorded by control computers. The temperature is measured with a thermocouple that is screwed to the sample, as for the diffusion experiment (see section 3.1.2)

- **Data Analysis**

Several steps were needed to analyze the raw two-dimensional diffraction frames. The ten images recorded for one frame were summed and averaged by a Matlab® routine developed by J. Almer [71] and the background was subtracted, as described below. Using the Matlab® routine, full diffraction rings were integrated over the whole azimuth (360°). The integration files obtained were then reduced to a one dimensional GSAS file by the Matlab® routine as illustrated in Figure 3-25. The GSAS peaks obtained were then analyzed using GSAS/Rawplot® [72]. This software program is primarily a Rietveld refinement program that can fit all the different parameters that would affect peak height, shape and position (these parameters can be sample characteristics such as composition, crystal structure, atom positions, etc. or exterior parameters such as sample-to-detector distance, temperature, pressure, etc). However GSAS also allows a faster refinement by only fitting the peak shape, position and intensity of the raw data in a sub routine called Rawplot. For our peak fitting, the precision and amount of information given by Rawplot were sufficient. The peaks are fitted to a pseudo-Voigt function which is a convolution

of Gaussian and Lorentzian peak shapes. Only the Gaussian full-width at half-maximum (FWHM) was fitted while the Lorentzian FWHM remained constant; this Gaussian FWHM gives an understanding of the sample contribution to broadening. The background was modeled using a third-degree polynomial function and several refinement steps were iterated (usually 10 successive refinements for each parameter we chose to refine). This allowed us to fit the diffraction peaks and obtain (i) the integrated intensity, (ii) the Gaussian full width at half maximum (FWHM), (iii) the peak positions for the desired peaks. Additional details on the data analysis procedure can be found in Kimberly Colas thesis [27].

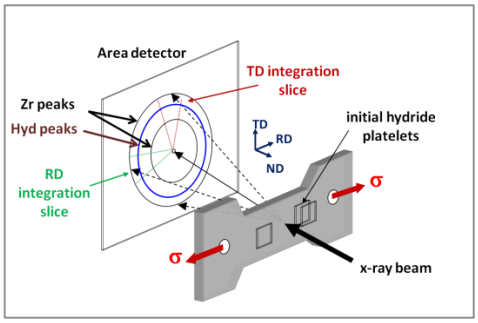

Figure 3-23: Schematic representation of beamline 1-ID experimental set-up.

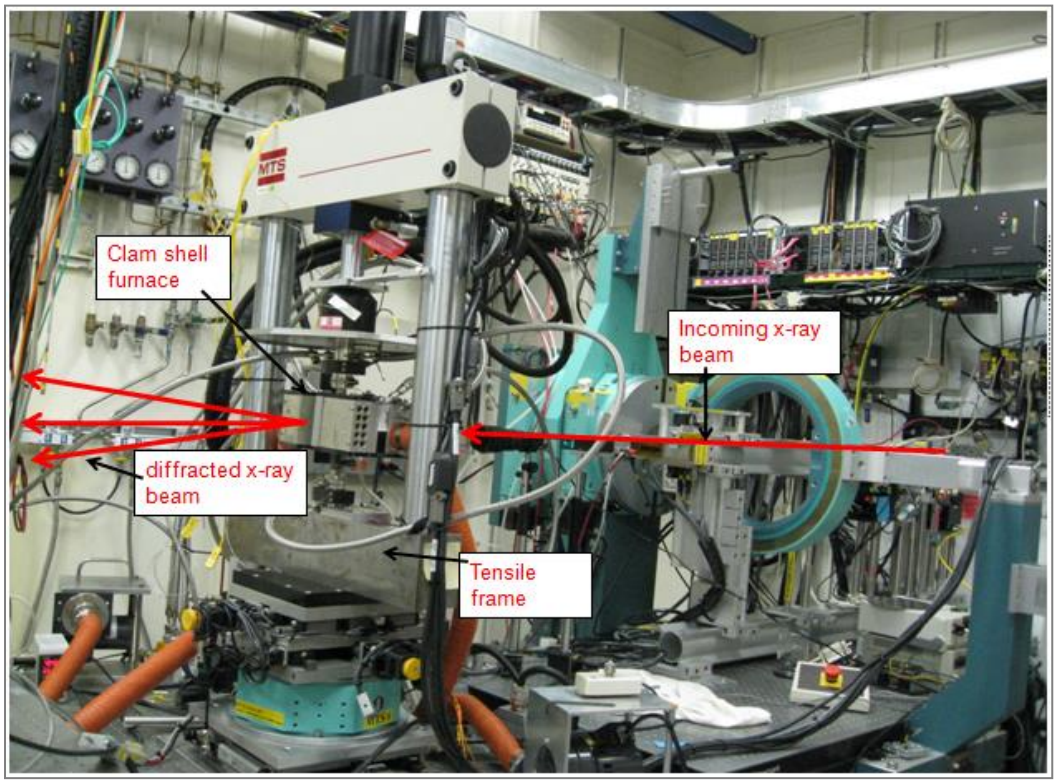

Figure 3-24: Picture of the experimental set-up at beamline 1-ID.

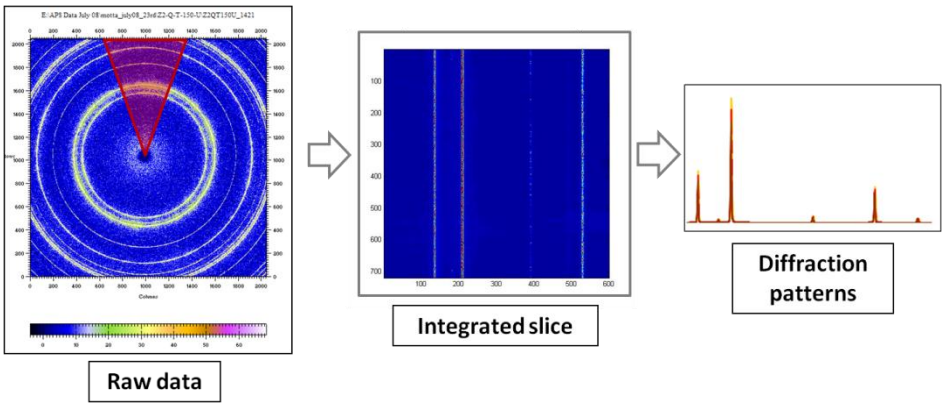

Figure 3-25: Data Analysis procedure for X-Ray diffraction data collected at beamline 1-ID.

3.2.3 Sample preparation

The preparation of the samples requires the following steps.

- Since the sample is exposed to high temperature (~ 500-700°C), the sample may recrystallize. To avoid change to the microstructure during the experiment, the sample is subject to a recrystallization heat treatment before the experiment starts.
- To prevent oxidation, the samples are coated with a deposited 100 nm layer of Nickel.
- Hydrogen is put into the sample using to the hydrogen charging equipment at PSU. The concentrations were checked by performing a hydrogen hot vacuum extraction on small parts of the samples. The hydrogen content of the samples are gathered in Table 3-6.

Table 3-6: Overall hydrogen concentration in the APS samples

Sample name	Content (wt.ppm)
H_310	310
H_400	400
H_502	502
H_644	644

3.2.4 Experimental procedure

Figure 3-26 shows the evolution of the area under the 111 delta hydride peak and the evolution of temperature with respect to time. The samples were heated to the dissolution temperature, in order to dissolve all the hydrides. This maximum temperature is held for 20 minutes, in order to reach a steady state. Then, the sample is cooled as fast as possible (about 1°C/s) to the target temperature (330°C in Figure 3-26). The sample is then held at this temperature, while the supersaturated hydrogen precipitates. The resulting increase of the hydride peak intensity allows measuring the kinetics of precipitation. In this case, indeed, the equations 1-53 can be reduced to:

$$\left\{\begin{array}{l} \dfrac{dC_H}{dt} = \alpha^2(C_{SS} - TSSp) \\ \dfrac{dC_{ss}}{dt} = -\alpha^2(C_{SS} - TSSp) \end{array}\right\} \qquad \textbf{3-6}$$

With α and TSSp constant.

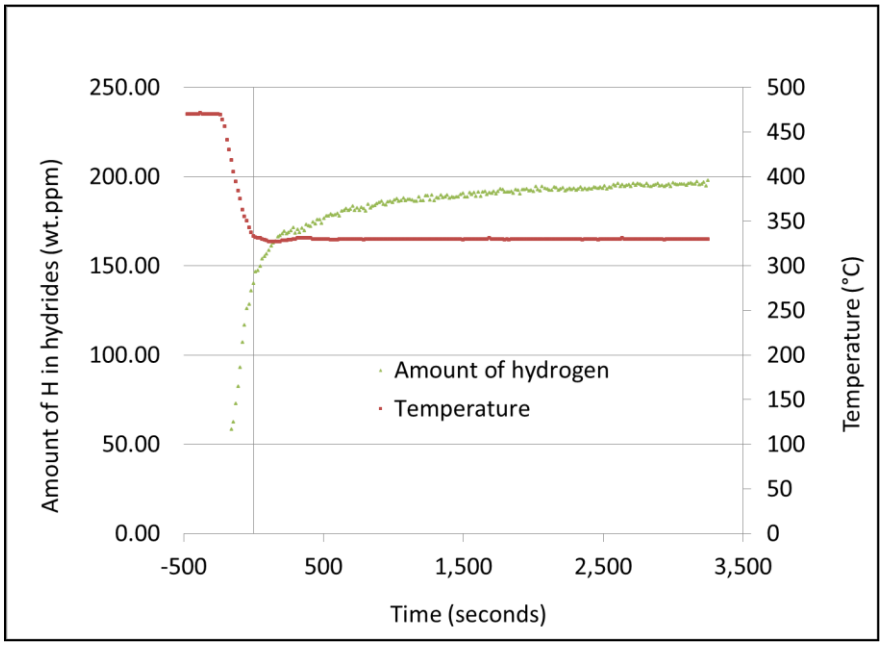

Figure 3-26: Evolution of temperature and hydrides concentration during synchrotron experiment

The second differential equation can be solved independently:

$$C_{ss}(t) = Aexp(-\alpha^2 t) + TSSp \qquad \textbf{3-7}$$

When t=0, $C_{ss}(0) = C_{ini}$,

$$C_{ss}(t) = (C_{ini} - TSSp) \cdot exp(-\alpha^2 t) + TSSp \qquad \textbf{3-8}$$

Then, the second equation of system 3-6 can be solved:

$$\frac{dC_p}{dt} = \alpha^2 (C_{ini} - TSSp)\, exp(-\alpha^2 t) \qquad \textbf{3-9}$$

So,

$$C_p(t) = -(C_{ini} - TSSp)\, exp(-\alpha^2 t) + A \qquad \textbf{3-10}$$

When t=0, $C_p(0) = C_{Pini}$, so:

$$C_{Pini} + C_{ini} - TSSp = A \qquad \textbf{3-11}$$

$$C_p(t) - C_{Pini} = (C_{ini} - TSSp)(1 - exp(-\alpha^2 t)) \quad \textbf{3-12}$$

$$\frac{C_p(t) - C_{Pini}}{(C_{ini} - TSSp)} = (1 - \exp(-\alpha^2 t)) \quad \textbf{3-13}$$

$$\frac{C_p(t) - C_{Pini}}{(C_{ini} - TSSp)} - 1 = -\exp(-\alpha^2 t) \quad \textbf{3-14}$$

$$\frac{C_p(t) - C_{Pini} - C_{ini} + TSSp}{(C_{ini} - TSSp)} = -\exp(-\alpha^2 t) \quad \textbf{3-15}$$

Recalling:

$$C_{TOT} = C_{ini} + C_{Pini} = C_p(t) + C_{SS}(t) \quad \textbf{3-16}$$

When t → infinity,

$$C_p(\infty) = C_{TOT} - TSSp \quad \textbf{3-17}$$

So,

$$\frac{C_p(\infty) - C_p(t)}{C_{TOT} - C_{Pini} - TSSp} = \exp(-\alpha^2 t) \quad \textbf{3-18}$$

Taking the logarithm of the previous expression:

$$-\log\left(C_p(\infty) - C_p(t)\right) = \alpha^2 t - \log(C_{TOT} - C_{Hini} - TSSp) \quad \textbf{3-19}$$

Plotting the log of the concentration against time allow the estimation of α^2 with a linear regression.

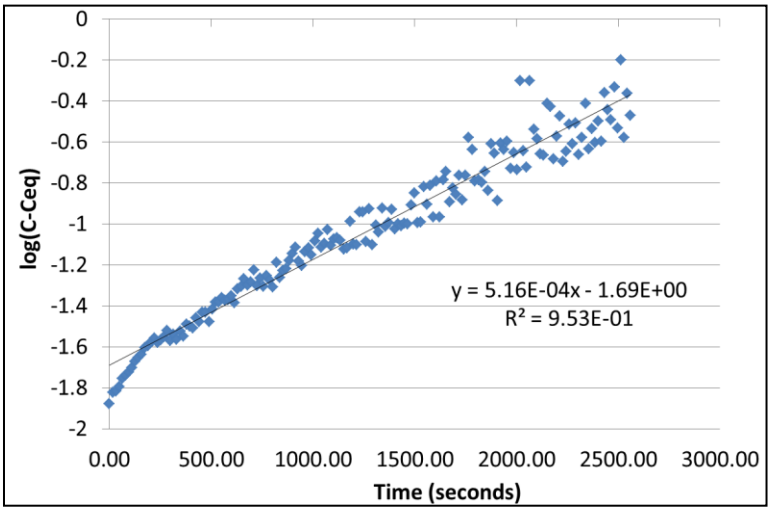

Figure 3-27: Linear regression and alpha calculation

In Figure 3-27 case, the regression gives $\alpha^2(330°C) = 5.16 * 10^{-4} s^{-1}$ *and* $\alpha = 0.023\ s^{-1/2}$ at 320°C and with an initial hydrogen content of 310 wt. ppm.

3.2.5 Results

In addition to the preliminary experiment detailed in the previous section, the hydride precipitation rate has been determined for five different temperatures and with three different initial concentrations using the approach illustrated in Figure 3-27. The measured values of α^2 are summarized in Table 3-7, while the value for α are given in Table 3-8. Figure 3-28 shows the value of α^2 agains the inverse of the absolute temperature. Figure 3-29 shows the α values against the inverse of temperature, and also displays the values reported by Kammenzind. [64]

Table 3-7: Measurement of the kinetics parameter alpha^2 (s)

	Initial total concentration			
Temperature	**310 wt. ppm**	**400 wt. ppm**	**502 wt. ppm**	**644 wt. ppm**
288°C	n/a	1.69E-04	1.69E-04	1.23E-03
316°C	n/a	2.56E-04	1.69E-04	2.56E-04
330°C	5.29E-04	n/a	n/a	n/a
332°C	n/a	3.24E-04	2.25E-04	5.29E-04
360°C	n/a	2.89E-04	1.69E-04	2.56E-04
380°C	n/a	n/a	1.96E-04	4.00E-04
400°C	n/a	n/a	1.69E-04	n/a

Table 3-8: Measurement of the kinetics parameter alpha ($s^{-1/2}$)

	Initial total concentration			
Temperature	**310 wt. ppm**	**400 wt. ppm**	**502 wt. ppm**	**644 wt. ppm**
288°C	n/a	0.013	0.013	0.035
316°C	n/a	0.016	0.013	0.016
330°C	0.023	n/a	n/a	n/a
332°C	n/a	0.018	0.015	0.023
360°C	n/a	0.017	0.013	0.016
380°C	n/a	n/a	0.014	0.020
400°C	n/a	n/a	0.013	n/a

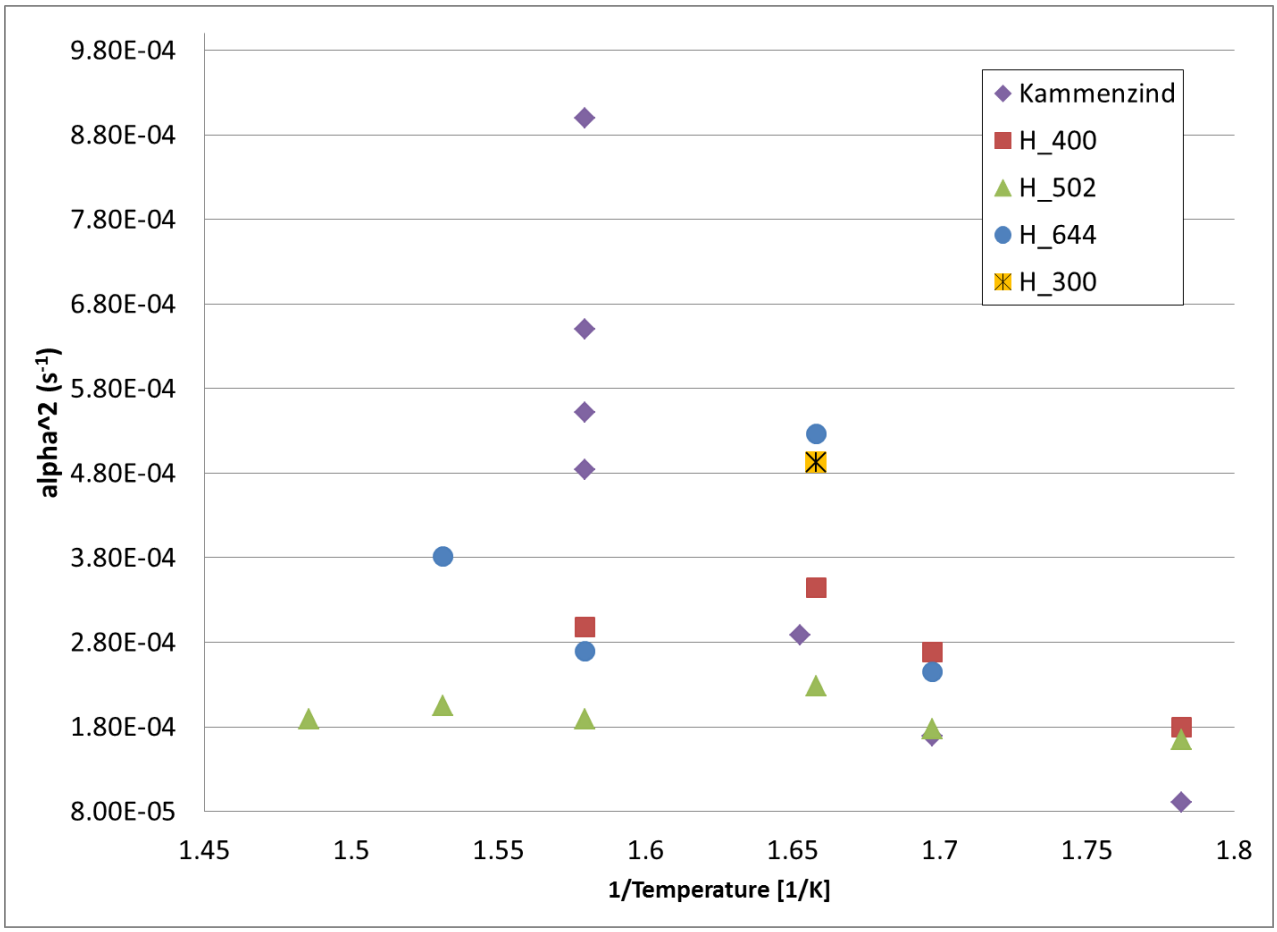

Figure 3-28: Measured precipitation parameter α^2 with respect to 1/T, with different initial concentration (300, 400, 502 and 644 wt. ppm)

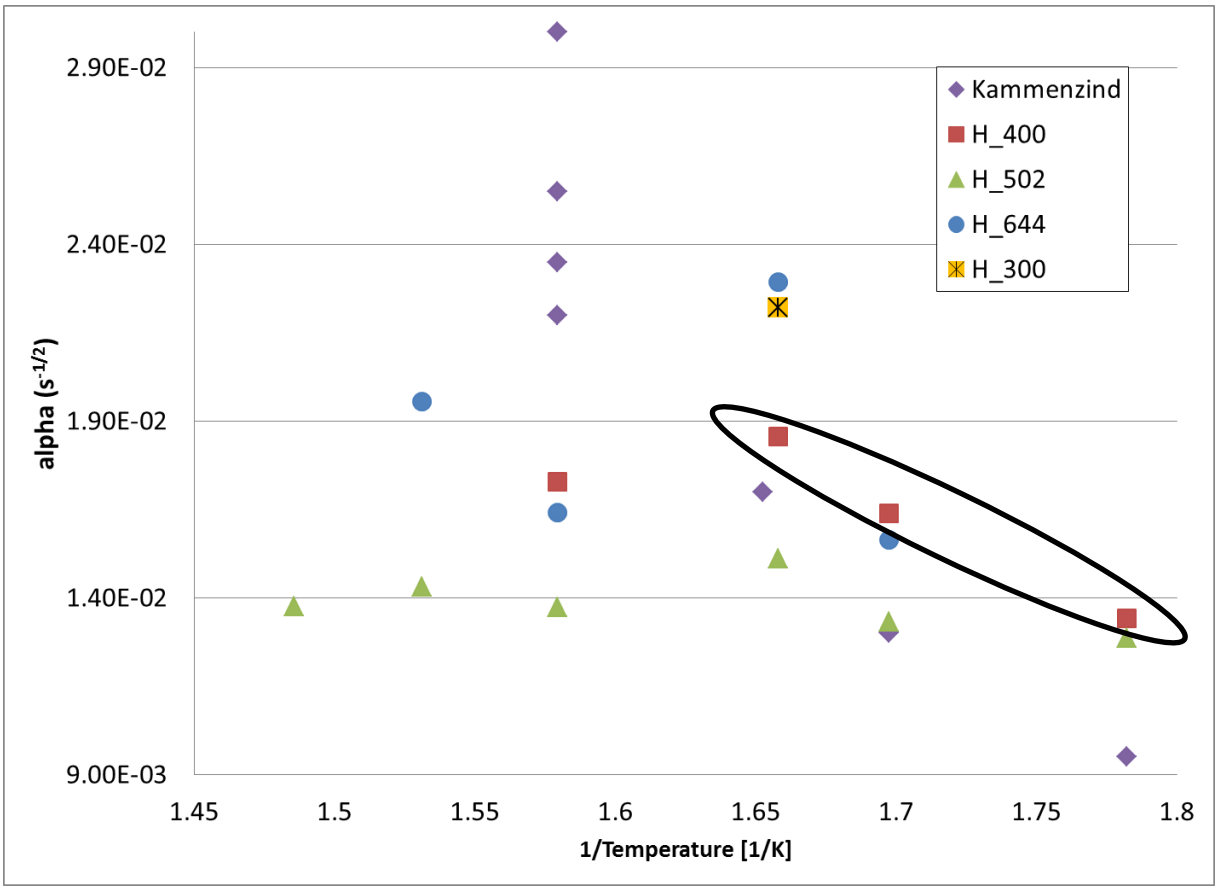

Figure 3-29: Measured precipitation parameter α with respect to 1/T, with different initial concentration (300, 400, 502 and 644 wt. ppm)

3.2.6 Conclusion of the results

Kammenzind suggested using a fitting with an Arrhenius law in his work [64]. The fitting of his results is reproduced in Figure 3-30. It is clear that the results obtained in this work, and which are also shown in Figure 3-30 cannot be fitted with the same law. The results obtained and shown in Figure 3-29 do not confirm these measurements. In fact, several observations can be made regarding the results. First, three of the four alpha values (circled in Figure 2-29) obtained for the sample with a low initial concentration (400 wt.ppm) show a similar temperature dependence as in Kammenzind's data (as shown in Figure 3-30), with an offset of about 0.03 s-

$^{1/2}$. In contrast contrary, the data obtained with the 502 wt.ppm initial concentration shows a value of α that is almost constant with temperature. We should note that the temperature profiles imposed on the samples at APS varied somewhat in the intended temperature ramps , leading us to believe that these results are more reliable. This variation was smallest in the 502 wt.ppm set of measurements and the circled data points in Figure 2-29. For example with the 644 wt.ppm sample, the results are very heterogeneous.

At this point, several interpretations can be made.

It is possible that the value of α does not depend on temperature. The values are only changing from 0.009 to 0.024, with a high number of data points between 0.015 and 0.022. Then, the variations could be caused by uncertainties in the temperature profile and the temperature measurements. As stated above, the least scattered data values are obtained in the sample with 502 wt.ppm, which shows a constant profile. It is also possible that α does depend on temperature. There is a global trend showing higher values of alpha when the temperature increases.it could be expected that the precipitation kinetics would be faster at higher temperature because of higher diffusion. The observation of constant alpha could also indicate a temperature independent process such as interface absorption of hydrogen into the hydrides.

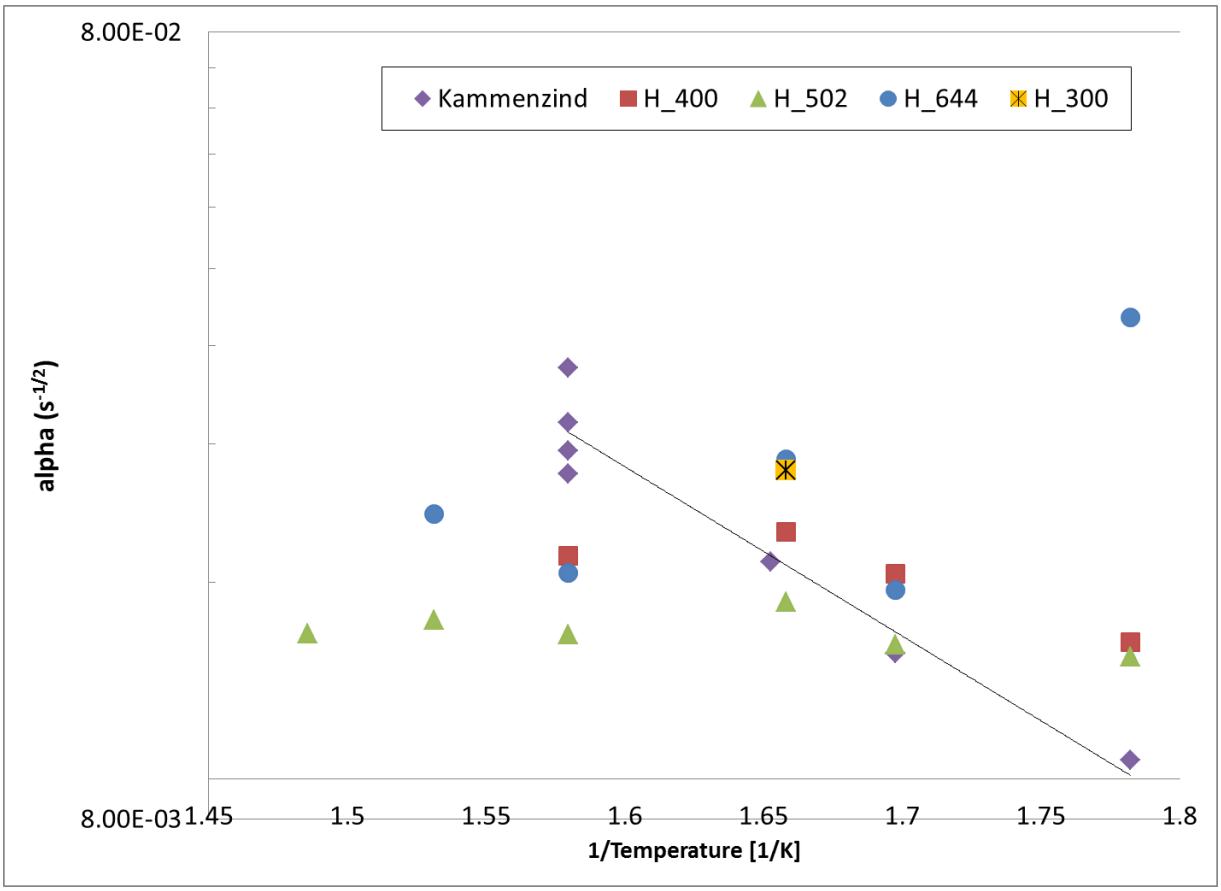

Figure 3-30: Measured precipitation parameter α with respect to 1/T, in log scale and with Kammenzind interpolation

.

Chapter 4: Preliminary work for further investigations

The purpose of this chapter is to open ways for future investigations. In the section 4.1, the analytical calculation of the rim has been attempted. Although it does not provide simple results, this derivation might be considered in the future as a way to obtain a rough estimation of the rim thickness. In section 0, physical phenomena that can improve the modeling are described. In particular, the hydrogen model used in this study is primarily temperature dependent. However, other elements can impact the hydrogen distribution, such as stress, oxygen… Their description is the purpose of this section. In section 4.3, some improvement and concerns regarding the modeling of the hydrogen behavior are shared. Section 4.4 focuses on the issues with the diffusion experiment and the calculation of Q*, whereas section 4.5 proposes future measurement techniques of the precipitation coefficient.

4.1 Analytical estimation of the rim

A way to try to estimate the thickness of the rim is to solve analytically the equation 4-1. This equation does not take into account the Soret effect and assume that the parameters D and α are constant with temperature.

$$D\frac{d^2C}{dx^2} - \alpha^2 C = \alpha TSS \qquad \textbf{4-1}$$

With C the hydrogen in solid solution, D the diffusion coefficient, α the rate of precipitation, TSS is the Terminal Solid Solubility for precipitation. Solving this equation will give a profile for the hydrogen in solid solution. The full derivation of this calculation is given in Appendix G. First, two areas have to be considered. The first one is consisted of hydrogen in solid solution only. Due to Fick's law and in the absence of any thermodiffusion, the concentration of hydrogen in solid solution is constant with x. The second area is consisted of two

phases: hydrogen in solid solution and hydrides. At the interface, there is conservation of the hydrogen flux and of the concentration of hydrogen. The boundary between the two areas is moving and this is what has to be calculated to solve the problem. First, the equation for the two phase area is solved using an approximated value for the TSS. Second, the equations governing the coordinate of the moving boundary are given. Unfortunately, no simple solution has been found.

A second option is to consider the model propose in section 2.5.6 with an limitation to the amount of hydride per unit of volume. In that case, and neglecting the kinetics, an estimation of the rim can be estimated by conservation of mass:

$$J_0 * t = \delta_{rim} \cdot C_{pMAX} + \int_0^{\delta_{rim}} TSSp\big(T(x)\big)dx \qquad \textbf{4-2}$$

Where J_0 is the flux at the coolant/cladding interface, t is the time, δ_{rim} is the thickness of the rim and TSSp(T(x)) is the TSSp calculated at the point x using the temperature of the point x.

However this equation is strongly dependent on the artificial limit C_{pMAX}. It can be solved numerically, but it does not have a strong physical meaning.

4.2 Physical parameters affecting the TSSp and TSSd

The hydride precipitation and dissolution limits TSSp and TSSd have been extensively studied in the literature, including the effects of irradiation, oxygen concentration, alloying elements and stress. This section, which presents a brief summary of these studies is based on the section 1.2.2 of Kimberly Colas' thesis [27].

4.2.1.1 Effect of irradiation

Using differential scanning calorimetry, McMinn studied the effect of different parameters on the TSSd and the TSSp [40]. For unirradiated Zircaloy materials, the TSS equations were found to be:

$$TSSd\ (wt.ppm)\ =\ 106\,446.7\ exp\left(-\frac{4328.67}{T}\right) \qquad \textbf{4-3}$$

$$TSSp\ (wt.ppm) =\ 138\,746.0\ exp\left(-\frac{4145.72}{T}\right) \qquad \textbf{4-4}$$

where TSSd and TSSp are the hydrogen terminal solid solubility for dissolution and precipitation respectively in wt.ppm; T is the temperature in Kelvin.

For irradiated Zircaloy materials, the TSS equations were found to be:

$$TSSp\ (wt.ppm) = 24236.1\ exp\ \left(-\frac{3391.16}{T}\right) \qquad \textbf{4-5}$$

$$TSSp\ (wt.ppm)\ =\ 212.1\ exp\ \left(-\frac{1003.6}{T}\right)\ for\ T < 170ºC \qquad \textbf{4-6}$$

$$TSSp\ (wt.ppm)\ =\ 66\,350.1\ exp\ \left(-\frac{3557.2}{T}\right)\ for\ T > 170ºC \qquad \textbf{4-7}$$

where TSSd and TSSp are the dissolution and precipitation hydrogen concentrations respectively in wt.ppm; T is the temperature in Kelvin. These equations illustrate the fact that the behavior for dissolution and precipitation is very different for irradiated material compared to unirradiated material, as illustrated in Figure 4-1. In the irradiated material, the difference between TSSd and TSSp becomes more prevalent than in the non-irradiated case. The increase of solubility due to irradiation was also confirmed by Vizcaino et al. [73]. It is important to note that McMinn showed that the “increase in solubility” can be recovered by suitable post-irradiation thermal anneals. From the data shown in these studies, it can be concluded that hydrogen exists in three forms in irradiated Zircaloy: soluble hydrogen, hydrides, and hydrogen trapped by irradiation produced defects. The latter can be released by post-irradiation annealing.

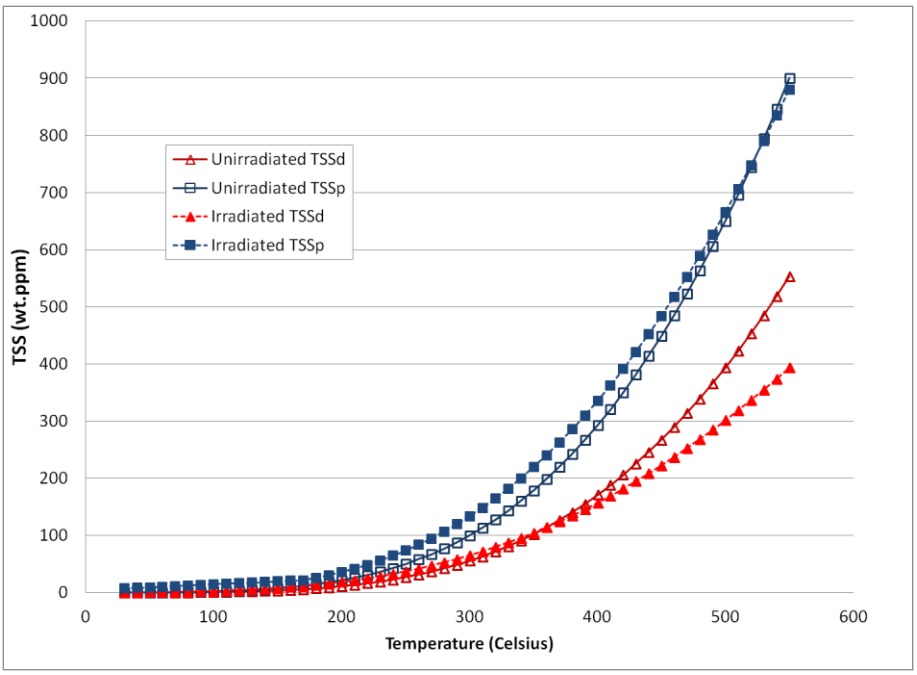

Figure 4-1: Comparison of McMinn's equations for the TSSd and TSSp of unirradiated and irradiated material [40]

4.2.1.2 Effect of oxygen

The hydrogen atoms in solution in hcp zirconium occupy the tetrahedral sites in the zirconium hexagonal closed packed crystal structure indicated as in (C) on Figure 4-2 [74]. Oxygen (O), always present in zirconium alloys, occupies the octahedral sites (B), and the interaction between the O and the H interstitials affects the solubility of hydrogen as a function of oxygen content. Increasing occupation of the sites by O decreases the ability to retain H in solid solution. Several studies have been conducted on this subject and produced conflicting data. In particular, the effect of O on the solubility of H in the α-zirconium phase is not clear. Yamanaka et al. [74] found that the H solubility in zirconium first increases then decreases at the higher O content. McMinn [40] and Bertolino [75] found that, in oxygen-strengthened tungsten inert gas (TIG) welded material, the high O material showed higher solubility for H, as shown in Figure 4-3. They also showed that O decreases the dissolution and precipitation temperatures. These authors concluded that there is general agreement that H solubility decreases with increasing O

content in the β phase of zirconium [40, 74-76]. The effect of O on the H solubility in the α-phase is uncertain at O levels of practical interest and could either increase or decrease. In either case, the effect is expected to be small.

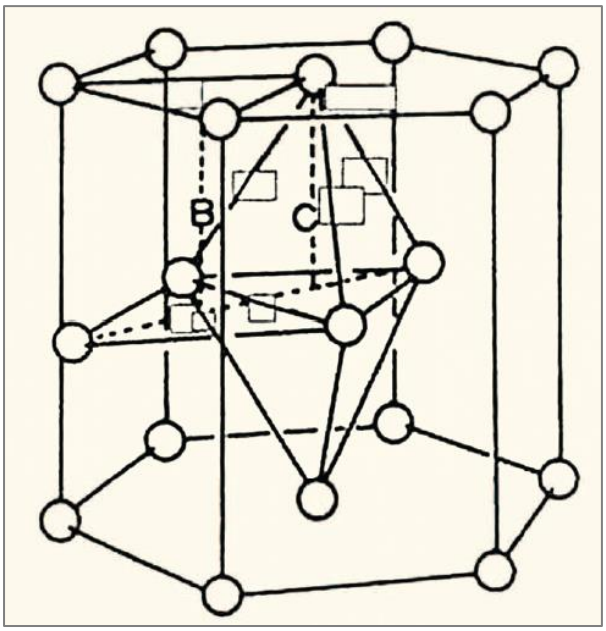

Figure 4-2: Zirconium crystal structure with hydrogen (c) and oxygen (b) in interstitial solid solution [74]

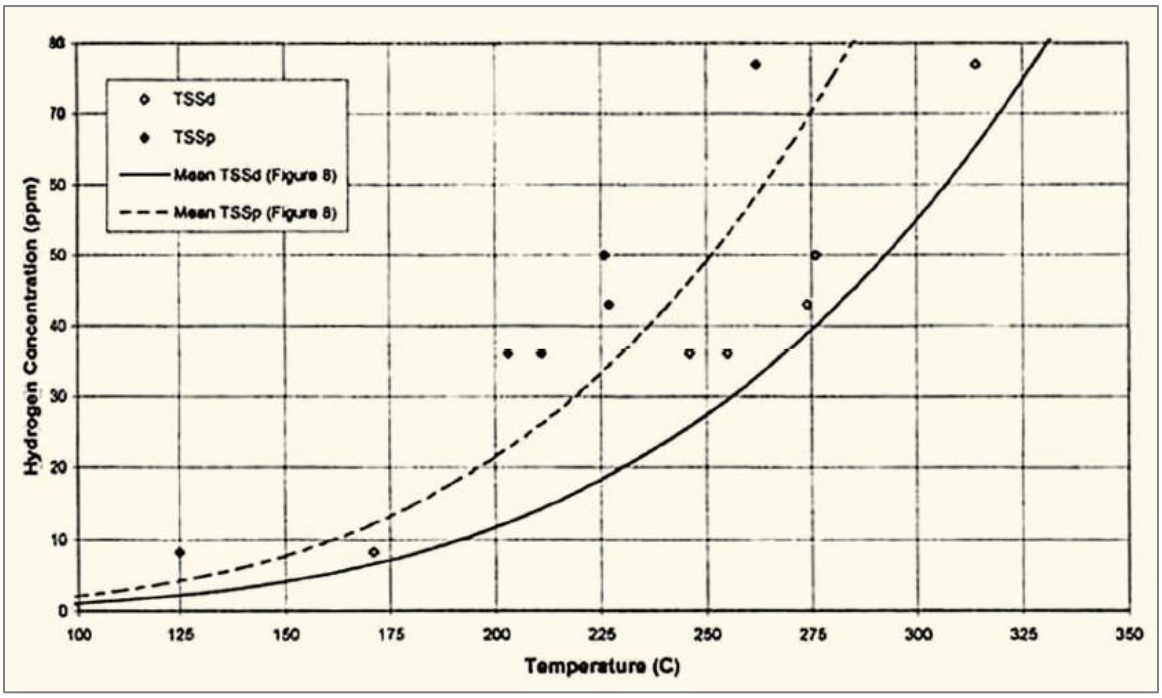

Figure 4-3: TSS Data points for Zircaloy with 2540 to 2860 ppm O compared to Zircaloy with 1000 to 1200 ppm O (solid and dashed curves) [40]

4.2.1.3 Effect of alloying elements

The solubility of H in pure zirconium and Zircaloys has been measured several times. Early measurements from Kearns [28] shown in Figure 4-4 were later confirmed by Kammenzind [64]. The effect of individual alloying elements on the TSSd of hydrogen in zirconium was measured by comparing unalloyed zirconium and Zircaloy-2 materials of various Fe levels by Setoyama et al. [77]. The results are shown in Figure 4-5. Binary additions of Ni and Cr to Zr had the most significant effect in increasing the hydrogen solubility while Fe and Sn had very little effect. Since Ni can vary from 0.03 to 0.08% and Cr from 0.05 to 0.15%, the hydrogen solubility could vary slightly for Zircaloy-2 made to the same specifications.

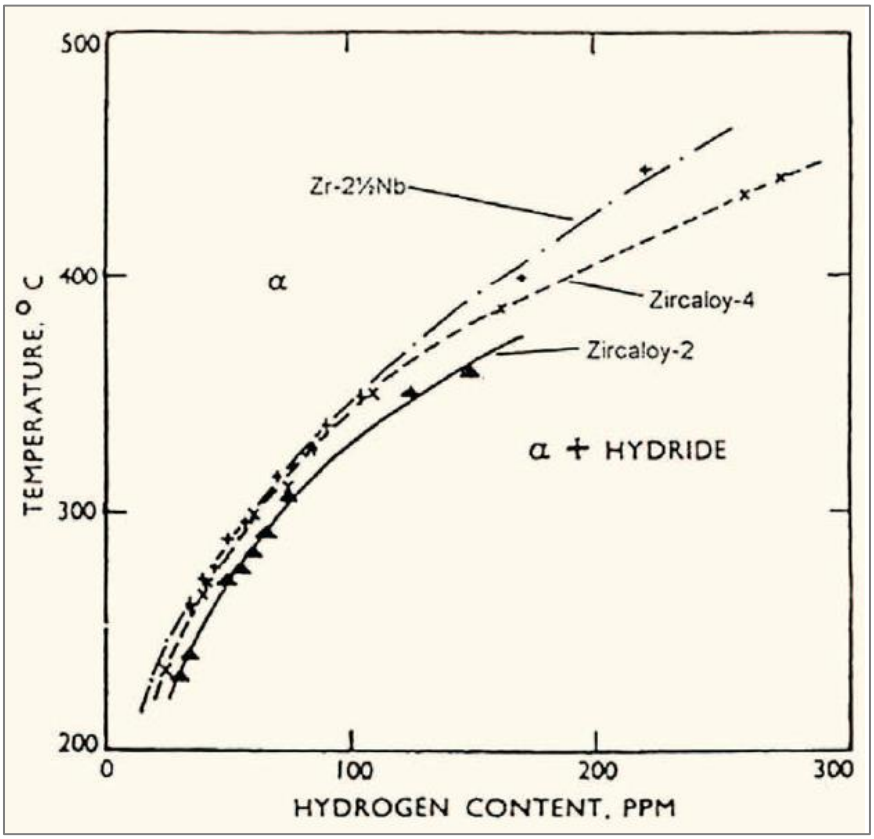

Figure 4-4: Solubility of hydrogen in zirconium alloys [28]

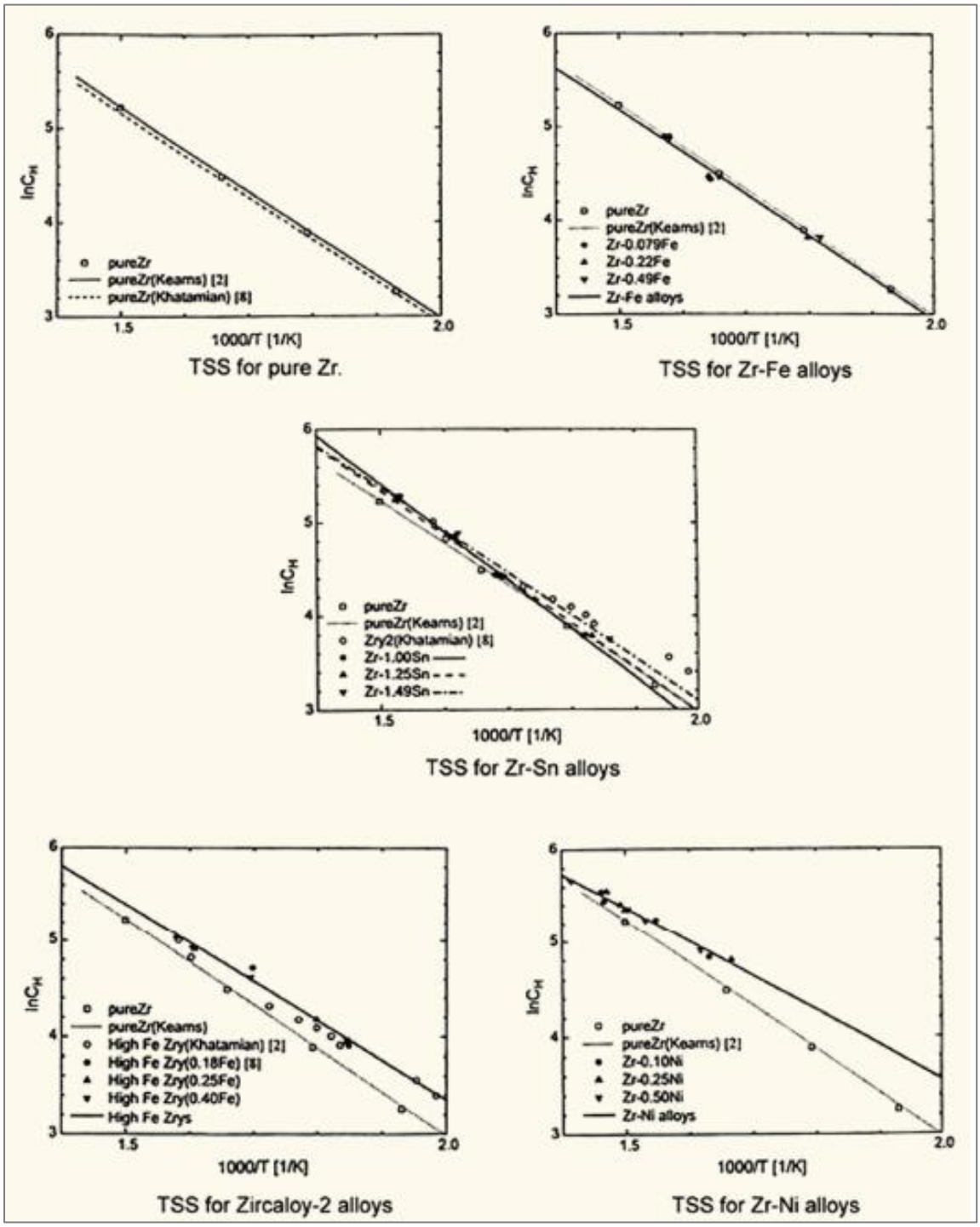

Figure 4-5: The effect of alloying elements on TSSd of hydrogen in zirconium [77]

4.2.1.4 Effect of stress

In part because data on the effect of stress on TSS is very limited, the effect of stress on hydrogen solubility is a subject of controversy. Experiments on Zircaloy-4 specimens show that an effect, that is much smaller than the effect of temperature, as illustrated in Figure 4-6. [78].

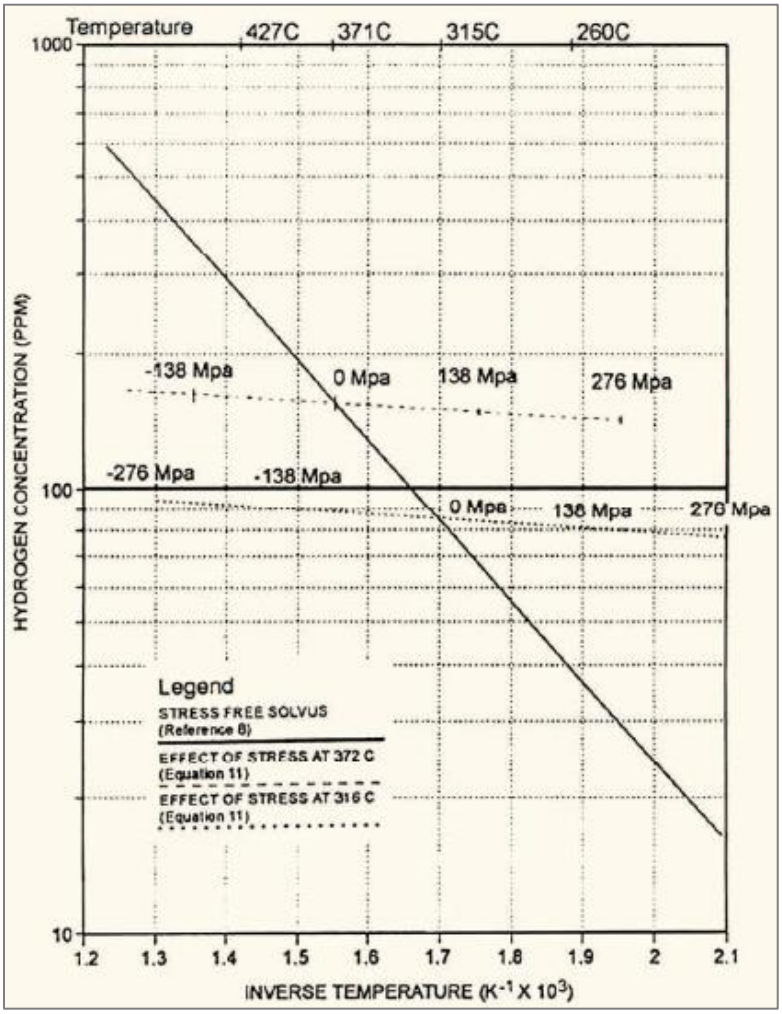

Figure 4-6: Hydride dissolution solvus, comparative effect of temperature and stress[78]

A theoretical evaluation by Puls et al. concluded that the effect of stress on TSS cannot be significant and that the determination of TSS on unstressed samples is reasonably valid [79]. As mentioned previously, hydrogen in solution in the α-zirconium lattice occupies the tetrahedral

interstices in the hexagonal α-zirconium unit cell and causes a small dilation of the lattice [80-82]. As a result hydrogen shows a tendency to segregate to regions (such as the core of dislocations) where the crystal lattice is already dilated [81]. Because of this effect, hydrogen in solution in zirconium tends to migrate up a tensile stress gradient (i.e. towards the region where the lattice is dilated by elastic stress). Whether or not there is an effect of stress on the hydrogen solubility in zirconium alloys is determined by the difference between the lattice dilation caused by the hydrogen atoms in solution and the lattice dilation resulting from the formation of a second-phase hydride. The effects of these dilations on the TSS are described by Eadie and Coleman by observing hydride precipitation at a flaw [83]. The equation they give governing the effect of stress on the TSS is:

$$\Delta \ln TSS = \frac{p\left(V_{H-Hydr} - V_H\right)}{RT} \qquad \textbf{4-8}$$

where the TSS is in wt.ppm, p is the hydrostatic stress in Pa, $V_{H\text{-}Hydr}$ and V_H are the partial molar volumes of hydrogen in the delta hydride and the alpha zirconium phases respectively (1.4×10^{-6} m^3 per mole and 1.67×10^{-6} m^3 per mole respectively).

After several studies using different techniques (such as time-of-flight neutron diffraction), stress was found to not have a strong effect on the TSS [83]. However, the effects of stress on hydrogen *migration* are critical to the mechanism of Delayed Hydride Cracking.

4.2.1.5 Summary of the additional effects

In summary, the main factors that influence hydride dissolution and precipitation in zirconium and its alloys are:

- Irradiation increases the solubility.
- Increasing O in solid solution decreases the solubility in the β phase and may also increase it in the α-zirconium phase. Pure, low oxygen zirconium has a lower solubility for hydrogen than the Zircaloys with 1000-1500 ppm of O.

- Increasing Ni and Cr alloying elements increase the solubility.
- Thermal cycling appears to increase solubility.

The following parameters appear to be less significant in affecting the hydrogen solubility:

- Increasing Fe and Sn alloying elements.
- Differences between Zircaloy-2, Zircaloy-4 and Zr-2.5 Nb of the same microstructures.
- Stress, although this is controversial.

4.3 Ideas and concerns regarding the hydrogen model

According to the simulation results described in section 2.5, the main issue regarding the model comes from the fact that it tends to predict a very high hydride concentration in the rim, which was never observed experimentally. The reason for this behavior is unknown. Two main explanations can be proposed. The first explanation is that the equilibrium between solid solution and hydride is modified when the total concentration of hydrogen is above 1000-1200 wt.ppm. This could be explained by a change in the stoichiometry or the structure of the hydride. The second explanation would be that there is a drastic change in precipitation kinetics at this concentration. If the precipitation parameter is lowered when the concentration is higher, it would explain why the hydrogen in solid solution diffuses further. It could be interesting to help the understanding of this limitation to do some TEM/SEM images of hydride zirconium samples with high hydrogen content (1000-2000 wt.ppm) in order to analyze the microstructure.

4.4 Improvement of the diffusion experiments

The first results with the diffusion experiment in section 3.1.5 are not fully conclusive. Furthermore, the data from the literature shows a wide range of values for Q*. It would be interesting to improve our understanding of Q*. First, a range of temperature gradients could be tested, using the same average temperature. Second, different temperatures could be used. The experimental setup is under modification at the time this thesis is being written. The new setup will have an automatic acquisition of the temperature value, in order to proceed to long time experiments (several weeks). This will allow the Q* measurement to be performed at lower temperatures.

It would be interesting to have a better understanding of the physical meaning of Q*. Thomas Garnier has done significant work at the CEA in order to explain the coupling between two particles diffusion phenomena.[84] He has shown interest in the understanding of the Soret effect and his work could be helpful regarding this question.

4.5 Next measurement of the precipitation parameter

The precipitation rate is not well known, according to section 3.2.1. The first results described in that section cannot conclude on the temperature dependence of this parameter. Moreover, the assumption of the linear relationship between the rate of precipitation and the hydrogen in super saturation is not based on any physical modeling. Other relationship such as a model with a quadratic law as explained in equation 4-9 could also be assumed. The shape of the precipitation curve tends to show a nonlinear behavior that could be assumed to be quadratic. Preliminary calculations tend to give better result with a quadratic model than with a linear model. Further analyses are necessary to confirm this hypothesis, but its testing would be worthwhile.

$$\frac{dC_p}{dt} = \gamma \cdot (C_{ss} - TSSp)^2 \qquad \textbf{4-9}$$

Where γ is a new proportionality coefficient.

Second, other physical parameters could affect the kinetics, such as stress or alloying elements. The APS experimental setup allows the testing of samples under stress, as shown in Kimberly Colas work [85]. The time remaining at APS to work on this kinetics could be devoted to measurements under stress.

Chapter 5: Conclusions

The goal of this research was to improve the understanding of the hydrogen redistribution in the zirconium fuel cladding. Progress has been made toward that end, from the modeling, the simulation and the experimental points of view. Since this thesis concludes the first two years of a three-year project, further developments on each of the studied areas still have to be conducted. However, the results and conclusions obtained from the current work allows for the understanding of the fundamental principle governing the distribution of hydrogen and zirconium hydride in a LWR fuel cladding.

1. Modeling

Hydrogen diffusion driven by concentration and temperature gradients are the two main phenomena that govern the distribution of hydrogen in solid solution. Once the terminal solid solubility for precipitation reached, hydride precipitation is in competition with diffusion, which can lead to the formation of specific features, such as a hydride rim. The equations governing these phenomena led to a model that has been used by other authors. Since the model is not microscopic, some of the parameters have to be found experimentally, and their physical meaning is not obvious. This is probably the main limiting factor to the model.

2. Simulation

The implementation of the model into computer codes has been one of the main parts of this work. The computational work made by the main research institutes involved in BISON (e.g. Idaho National Laboratory, Sandia National Laboratory) encourages modularity and continuous improvement. Thanks to this mindset, one of the most modern fuel performance codes (BISON) allowed the implementation of the new model. In this work, a hydrogen model was developed and fully implemented into a 3D fuel performance code. The hydrogen model source code is now

available for all the BISON users. The results show that the distribution of hydrogen cannot be understood using a simple radial model. The axial transfer from the hot region towards the cold region has been found to be the critical factor that will cause the initiation of the precipitation of hydrogen in the cold region. However, the radial distribution of hydrogen is critical in explaining why the hydrogen tends to precipitate close to the outer edge of the nuclear fuel cladding. The hydride rim calculated by the model is much thinner (<50 microns) and has a much higher total hydrogen concentration (~18,000 wt.ppm) than what is seen experimentally (~100 microns, <2000 wt. ppm). By setting a limitation to the amount of hydrogen in the hydrides, it was possible to get reliable results, consistent with experimental observation. With this new model, the rim thickness was about 200 microns and total concentration of hydrogen of about 1200 wt.ppm.

3. Experiments

In the experimental part of this work, the parameters Q* and α have been measured with different experiments. Although further experiments should be conducted, the results show that the experimental setups used can reliably measure these quantities. The hydrogen model contains several linear assumptions that can clearly be challenged for the future work.

The measurement of the heat of transport Q* was about 58.5 kJ/mol. This value is significantly higher that what is found in the literature (15-35 kJ/mol). Our measurement of Q* was made at a higher temperature than all the previous experiments. These previous experiments show a high dispersion of the results. No clear dependence of Q* on the temperature gradient or on the average temperature can be proven. Further experiments should be conduct to confirm this result and improve the understanding of factors influencing Q*.

The measurements of the rate of precipitation α found values between 0.013 and 0.034 $s^{-1/2}$, which are in the range of the previous measurements made by Kammenzind (0.009 and 0.0297). It was not possible to establish a clear temperature dependence of α. The scatter of

the results could be explained by experimental uncertainties or by other factor acting on the precipitation process during the experiment. Further experiments (in particular studying the influence of stress) should be performed to further refine the data obtained.

4. Parallel work on neutronics/thermohydraulics calculations

This project cannot be fully understood without considering the parallel work performed by Ian Davis in his thesis work, which focused on obtaining an accurate estimate of the temperature distribution in a nuclear fuel cladding. This was done by using three different codes, for the neutronics, thermal hydraulics and fuel performance calculations. Although the predictions of temperature based on these coupled calculations need further testing and application, they show promising results. The fact that the temperature distribution is internally coupled with the hydrogen model reduces the propagation of numerical errors and increases the reliability of the results.

5. Future work

The project has been designed for three years and a strong basis for the research has been developed. A 1D finite difference code has been created in order to model simple hydrogen distribution. A hydrogen model was added to the source code of the 3D fuel performance code BISON in order to allow 3D calculation of hydrogen distribution. Two experiments were designed, tested and performed to determine Q* and α, which are necessary to run the calculations. Future work will likely include more accurate 3D simulations and complementary experimental results, to address the remaining issues and will allow more precise determinations of locally high concentrations of hydride in nuclear fuel cladding.

References

1. Lamarsh, J.R., Baratta, A.J., *Introduction to Nuclear Engineering*. 3rd edition ed2001: Prentice Hall.
2. Lemaignan, C. and A.T. Motta, *Zirconium Alloys in Nuclear Applications*. Materials Science and Technology. Vol. 10B. 1994: VCH.
3. Coleman, C.E. and D. Hardie, *The hydrogen embrittlement of alpha-zirconium review.* Journal of the Less Common Metals, 1966. **11**: p. 168-185.
4. Garner, G.L.a.M., J.-P., *Alloy M5 in action* Nuclear Engineering International, 2002. **47(578)**: p. 36-37.
5. Sabol, G.P., *ZIRLO - An alloy developement sucess.* Zirconium in the nuclear industry: 14th international symposium, 2005. **ASTM STP 1467**: p. 3-24.
6. Clayton, J.C., *Cladding corrosion and hydriding in irradiated defected Zircaloy-4 fuel rods.* Corrosion, 1989. **45 (12)**: p. 996-1002.
7. IAEA, *Waterside Corrosion of Zirconium Alloys in Nuclear Power Plants*, 1998, International Atomic Energy Agency: Vienna.
8. Garzarolli, F., et al. *Review of Corrosion and Dimensional Behavior of Zircaloy under Reactor Water Conditions*. 1979. ASTM.
9. Yilmazbayhan, A., et al., *Transmission Electron Microscopy Examination of Oxide Layers Formed in Zr Alloys.* Journal of Nuclear Materials, 2006. **349**: p. 265-281.
10. Siefken, L.J., et al., *MATPRO - A Library of Materials Properties for Light-Water-Reactor Accident Analysis, SCDAP/RELAP5/MOD 3.3 Code Manual Vol.4, Rev. 2*, 2001.
11. Couet, A., Motta, A.T., Comstock, R.J., *Effect of alloying elements on hydrogen pick-up in zirconium alloys*, in *7th International Symposium on Zirconium in the Nuclear Industry*to be published: Hyderabad, India.
12. Couet, A., Motta, A.T., Comstock, R.J., *Hydrogen Pickup Measurements in Zirconium Alloys: Relation to Corrosion Rate*. Journal of Nuclear Materials, to be published.
13. Racine, A., "Influence de l'orientation des hydrures sur les modes de deformation, d'endommagement et de rupture du Zircaloy-4 hydrure," Ph.D. Thesis in Ph.D., Mecanique et Materiaux, L'Ecole Polytechnique, France, 2005
14. Elston, J., *Hydrures*, ed. G. Atomique1965: INSTN-PUF.
15. Daum, R.S., "Hydride Induced Embrittlement of Zircaloy-4 Under Plane Strain Tension Testing," PhD Thesis in Materials Science, Penn State University, 2007
16. Daum, R.S., et al., *Radial-hydride Embrittlement of High-burnup Zircaloy-4 Fuel Cladding.* Journal of Nuclear Science and Technology, 2006. **43**(9): p. 1054–1067.
17. Billone, M., et al., *Cladding Embrittlement During Postulated Loss-of-Coolant Accidents*, 2008, NRC.
18. Bossis, P., et al., *Comparison of the High Burnup Corrosion on M5 and Low Sn Zircaloy-4.* Journal of ASTM International, 2006. **3**(1): p. paper IDJAI12404.
19. J. Arborelius, M.D., L. Hallstadius, P. Jourdain, T. Andersson, R. Lisdat, M. Hahn, and a.E.H. Toscano5, *The Effect of Duplex Cladding Outer Component Tin Content on Corrosion, Hydrogen Pick-up, and Hydride Distribution at Very High Burnup.* Journal of ASTM International, 2005. **STP 1467**: p. 526-546.

20. Zhang, J.-H., "Hydruration du Zircaloy-4 et étude de la distribution de l'hydrogène dans une gaine de combustible REP," PhD thesis Thesis in Departement de Mecanique et de technologie, Commissariat à l'Énergie Atomique, 1993
21. Smith, G., *Evaluation and Demonstration of Methods for Improved Fuel Utilization*, in *ET/34013-15, CND-432*1994, DOE.
22. Guedeney, P., M. Trotabas, and M. Boschiero, *Fragema fuel behavior and rupture of Hydrdided Zircaloy-4.* ANS Topical Meeting on LWR fuel performance, 1991: p. 627-638.
23. Kearns, J.J., *Diffusion Coefficient of Hydrogen in Alpha Zirconium, Ziraloy-2 and Zircaloy-4.* J. Nuclear Materials, 1972. **43**: p. 330-338.
24. Bruce F. Kammenzind, D.G.F., H. Richard Peters and Walter J. Duffin, *Hydrogen Pickup and Redistribution in Alpha-Annealed Zircaloy-4.* Zirconium in the Nuclear Industry: 11th International Symposium, 1996. **ASTM STP 1295**: p. 338-370.
25. Prigogine, D.K.a.I., *Modern Thermodynamics*1998: John Wiley & Sons.
26. Sawatzky, A. and E. Vogt, *Mathematics of the Thermal Diffusion of Hydrogen.* Transactions of the Metallurgical society of AIME, 1963. **227**(4): p. 917-928.
27. Colas, K., "Fundamental experiments on hydride reorientation in Zircaloy," PhD Thesis in Mechanical and Nuclear Engineering, Pennsylvania State University, 2012
28. Kearns, J.J., *Terminal solubility and partitioning of hydrogen in the alpha phase of zirconium, Zircaloy-2 and Zircaloy-4.* Journal of Nuclear Materials, 1967. **22**: p. 292-303.
29. Puls, M.P., *Elastic and Plastic Accomodation Effects on Metal-Hydride Solubility.* Acta Metallurgica, 1984. **32**: p. 1259.
30. Puls, M.P., *Effects of Crack Tip Stress and Hydride-Matrix Internal Stresses on Delayed Hydride Cracking.* Metallurgical Transactions A, 1990. **21**: p. 2905.
31. Carpenter, G.J.C., *The precipitation of [gamma]-zirconium hydride in zirconium.* Acta Metallurgica, 1978. **26**(8): p. 1225-1235.
32. Zhao, Z., et al., *Identification and Characterization of a New Zirconium Hydride.* Journal of Microscopy, 2008. **232**: p. 410.
33. Kerr, M., et al., *Fracture of a minority phase at a stress concentration observed with synchrotron X-ray diffraction.* Scripta Materialia, 2009. **61**(10): p. 939-942.
34. Pan, Z.L., I.G. Ritchie, and M.P. Puls, *The terminal solid solubility of hydrogen and deuterium in Zr-2.5Nb alloys.* Journal of Nuclear Materials, 1996. **228**: p. 227-237.
35. McMinn, A., E.C. Darby, and J.S. Schofield. *The terminal solid solubility of hydrogen in zirconium alloys*. in *12th Int. Symp. on Zr in the Nuclear Industry*. 2000. Toronto, CA: ASTM.
36. Sawatzky, *Hydrogen in Zircaloy-2: Its distribution and heat of transport.* Journal of nuclear Materials, 1960. **4**: p. 321-328.
37. Shewmon, *Redistribution of second phase during annealing in temperature gradient.* Transactions of the Metallurgical Society of AIME, 1958. **212**: p. 642-647.
38. Marino, G.P., *Hydrogen Supercharging in Zircaloy.* Materials Science and Engineering, 1971. **7**(1971): p. 335-341.
39. Marino, G.P., *HYDIZ: A 2-dimensonal computer program for migration of interstitial solutes of finite solubility in a thermal gradient (LWBR Development Program)*, in *AEC Research and Developement Report - WAPD-TM-1157*1974.
40. McMinn, A., Darby, E.C., Schofield, J.S., *The Terminal Solid Solubility of Hydrogen in Zirconium Alloys.* Zirconium in the Nuclear Industry: Twelfth International Symposium, 2000. **ASTM STP 1354**: p. 173-195.

41. Kearns, *Diffusion coefficient of hydrogen in alpha Zr, Zircaloy-2 and Zircaloy-4.* Journal of nuclear Materials, 1971. **43**(1972): p. 330-338.
42. Davis, I., "High-fidelity multi-physics coupling for prediction of anisotropic power and temperature distributions in fuel rod : Impact on hydride distribution," MS Thesis in Nuclear Engineering, Pennsylvania State University, 2013
43. Williamson, R., S.H. Novascone, J.; , and B. Spencer, *BISON Workshop*, I.N. Laboratory, Editor 2012.
44. Derek Gaston, J.H., *MOOSE Workshop*, 2012, Idaho National Laboratory: MIT.
45. Zienkiewicz, O.C., R.L. Taylor, and J.Z. Zhu, *The finite element method: its basis and fundamentals*2005.
46. Chris Newman, G.H., Derek Gaston, *Three dimensional coupled simulation of thermodynamics, heat and oxygen diffusion in UO2 nuclear fuel rods.* Journal of nuclear Materials, 2009. **392**: p. 6-15.
47. Kochunas, B., Hursin, M. ,Downar, T., *DeCART-v2.05 Theory Manual*, 2009, University of Michigan.
48. RDFMG, P.S., *CTF, Technical Report*, 2010.
49. csimsoft, *Trelis*, 2013, Sandia National Laboratory.
50. Laboratory, K.I.L.A.N., *Paraview*, 2013: http://www.paraview.org.
51. IAEA, *Review of Fuel Failures in Water Cooled Reactors*, 2010, International Atomic Energy Agency.
52. U.S.NRC, *Standard Technical Specifications - Westinghouse Plants*, 2012: Office of Nuclear Reactor Regulation.
53. Cochran, R.G. and N. Tsoulfanidis, *The Nuclear Fuel Cycle: Analysis and Management*1999: American Nuclear Society.
54. Menibus, A.H.d., "Formation de blisters d'hydrures et effet sur la rupture de gaines en Zircaloy-4 en conditions d'accident d'injection de reactivite," Doctorat Thesis in Sciences et Genie des Materiaux, Ecole Nationale Superieure des mines de Paris, 2012
55. Jovanovic, M., Stern, A., Kneis, G., Weatherly, G., Leger, M., *Thermal diffusion of hydrogen and hydride precipitation in Zr-Nb pressure tube alloys.* Canadian Metallurgical Quarterly, 1988. **27**: p. 323-330.
56. Hong, H.S., S.J. Kim, and K.S. Lee, *Thermotransport of hydrogen in Zircaloy-4 and modified Zircaloy-4.* Journal of Nuclear Materials, 1998. **257**: p. 15-20.
57. Sawatzky, A., *The heat of transport of hydrogen in zirconium alloys.* Journal of nuclear Materials, 1963. **9**(3): p. 364.
58. Sugisaki, M., K. Hashizume, and Y. Hatano, *Estimation of hydrogen redistribution in zircaloy cladding of spent fuel under thermal conditions of dry storage and evaluation of its influence on mechanical properties of the cladding*, in *Effects of Radiation and Environmental Factors on the Durability of Materials in Spent Fuel Storage and Disposal, , IAEA-TECDOC-1316*, IAEA, Editor 2002, IAEA: Vienna, Austria. p. 63-78.
59. Morozumi, S., et al., *Effects of the alloying elements and cold work on the redistrivution of hydrogen in Zirconium under a temperature gradient.* Journal of Nuclear Materials, 1969. **33**: p. 261-270.
60. Hashizume, K., Hayakawa, M., Koganemaru, M., Sugisaki, M., *Temperature dependence of heat of transport of hydrogen in zirconium.* Defect and DiffusionForum, 1993. **95-98**: p. 323-328.
61. Markowitz, J., *The thermal diffusion of hydrogen in alpha-delta Zircaloy-2.* Transactions of the Metallurgical Society of AIME, 1961. **221**(819-823).

62. Kammenzind, B.F., *Hydrogen pickup and redistribution in alpha-annealed Zircaloy-4.* Zirconium in the Nuclear Industry: Eleventh International Symposium, ASTM STP 1295, 1996: p. 338-370.
63. http://www.surfaceigniter.com/, *Surface Igniter*.
64. Kammenzind, B.F., et al. *Hydrogen Pickup and Redistribution in Alpha-Annealed Zr-4*. in *Zirconium in the Nuclear Industry: 11th International Symposium*. 1996.
65. Douglass, D.L., *The Metallurgy of Zirconium*1971, Vienna: International Atomic Energy Agency Supplement.
66. *Analysis of Zirconium Alloys*, 1999, Luvak, Inc.: Boston, MA.
67. Zanellato, O., et al., *Syncrhotron diffraction study of dissolution and precipitation kinetics of hydrides in Zircaloy-4.* Journal of Nuclear Materials, 2012. **420**: p. 537-547.
68. Cullity, B.D., *Elements of X-ray Diffraction*. Second Edition ed1978: Addison-Wesley Publishing Company, Inc.
69. *The Powder Diffraction File*, 2006, International Center for Diffraction Data.
70. U.S.DOE, *The Advanced Photon Source, A National Synchrotron Radiation Research Facility at Argonne National Laboratory*, 1999.
71. Haeffner, D.R., J.D. Almer, and U. Lienert, *The use of high energy X-rays from the Advanced Photon Source to study stresses in materials.* Materials Science and Engineering: A, 2005. **399**(1-2): p. 120-127.
72. Larson, A.C. and R.B.V. Dreele, *General Structure Analysis System (GSAS)*, 2000, Los Alamos National Laboratory.
73. Vizcaíno, P., R.O. Ríos, and A.D. Banchik, *Hydrogen determinations in a zirconium based alloy with a DSC.* Thermochimica Acta, 2005. **429**(1): p. 7-11.
74. Yamanaka, S., et al., *Influence of Interstitial Oxygen on Hydrogen Solubility in Metals.* Journal of Alloys and Compounds, 1999. **293-295**: p. 42-51.
75. Bertolino, G., G. Meyer, and J. Perez Ipiña, *Degradation of the mechanical properties of Zircaloy-4 due to hydrogen embrittlement.* Journal of Alloys and Compounds, 2002. **330-332**: p. 408-413.
76. Brown, A. and D. Hardie, *The effect of Dissolved Oxygen on the Termina Solubility of Hydrogen in Alpha Zirconium.* Journal of Nuclear Materials, 1961. **4**: p. 110-112.
77. Setoyama, D., et al., *Influence of Additive Elements on the TSS for Hydrogen for Zirconium Alloy.* Journal of Nuclear Materials, 2005. **344**: p. 291.
78. Kammenzind, B.F., et al. *The long-range migration of hydrogen through Zircaloy in response to tensile and compressive stress gradients*. in *Zirconium in the Nuclear Industry: 12th International Symposium*. 2000.
79. Puls, M.P., C. Leitch, and S. Shi. *The Effect of Applied Stress on the Accomodtion Energy and Solvi for the Formation and Dissolution of Zirconium Hydride*. in *Proc. Int. Conference on Hydrogen Effects on Material Behavior* 2002. Moran, WY: TMS.
80. Martin, S. and A. Rees, *Interpretation of the Solubility of Hydrogen in Zirconium.* Trans. Faraday Society, 1954. **52**: p. 343-352.
81. Cox, B., *Hydrogen uptake during oxidation of zirconium alloys.* Journal of Alloys and Compounds, 1997. **256**(1-2): p. 244-246.
82. Cox, B. and P. Rudling, *Hydriding Mechanisms and Impact on Fuel Performance*, in *Advanced Nuclear Technology for ZIRAT5*2000.
83. Eadie, R.L. and C.E. Coleman, *Effect of stress on hydride precipitation in zirconium-2.5% niobium and on delayed hydride cracking.* Scripta Metallurgica, 1989. **23**(11): p. 1865-1870.
84. Garnier, T., "Transfert d'échelle dans la modélisation thermodynamique et cinétique des alliages," PhD Thesis in Université Paris Sud, 2012

85. Colas, K., et al., *Hydride Platelet Reorientation in Zircaloy studied with Synchrotron Radiation Diffraction.* Journal of ASTM International, 2011. **8**(No. 1): p. Paper ID JAI103033.
86. Coodington, E.A. and N. Levinson, *Theory of Ordinary Differential Equations*, ed. McGraw-Hill1955.

Appendices

Appendix A: HydruLab code simulating hydrogen behavior in Zircaloy plate

The following code simulates the linear decrease of temperature, in 24 hours.

```
% Physics constants
R_gaz=8.314;
    % Diffusion (Kearns)
    Q_diff=4.49e4;
    D_0=7.90e-3;
    %Soret effect
    Q_star=2.51e4;

%Geometry
slab_length=0.0660; %cm

TminK=273+320;
TmaxK=273+360;
TendmK=273+40;
TendMK=273+20;

%precipitation kinetick
Alpha_0=62.3;
Q_alpha=4.12e4;

%Initial condition
C_ini=100;

%Boundary condition
Flux_hot=0;

%Time (sec)
end_time=1e6 ;
ts=0;
num_hours=end_time/3600;
hoursstep=0;
frq=1;

%Discretization
n_tstep=1e6;
n_cell=20;
delta_t=end_time/n_tstep;
delta_x=slab_length/n_cell;
num_tstep=0;

%Tables
Hss=zeros(1,n_cell);
Hp=zeros(1,n_cell);
Ht=Hss+Hp;
TSSptable=zeros(1,n_cell);
TSSdtable=zeros(1,n_cell);
Dtable=zeros(1,n_cell);
alpha_table=zeros(1,n_cell);
```

```
Temperature_ini=zeros(1,n_cell);
Temperature_end=zeros(1,n_cell);
Temperature=zeros(1,n_cell);
x_table=zeros(1,n_cell);
Flux_left=zeros(1,n_cell+1);
Flux_left(n_cell+1)=Flux_hot;
max_hbyH=round(num_hours/frq);
HbyH_Hp=zeros(max_hbyH,n_cell);
HbyH_Hss=zeros(max_hbyH,n_cell);
HbyH_delta=zeros(max_hbyH,n_cell);
HbyH_temperature=zeros(max_hbyH,n_cell);

%initialization  of  temperature,  TSS,  diffusion  coefficient  and  initial
concentration
for i=1:1:n_cell;
    %all cell = initial temperature
    Hss(i)=C_ini;
    %Set up temperature gradient
    Temperature_ini(i)=TminK+(TmaxK-TminK)*(i-1)/(n_cell-1);
    Temperature_end(i)=TendmK+(TendMK-TendmK)*(i-1)/(n_cell-1);
    Temperature(i)=Temperature_ini(i);
    %Calculate TSS for each cell
    TSSptable(i)=TSSp(Temperature(i));
    TSSdtable(i)=TSSd(Temperature(i));
    %calculate diffusion coefficient for each cell
    Dtable(i)=D_0*exp(-Q_diff/(R_gaz*Temperature(i)));

    %calculate alpha coefficient for each cell
    alpha_table(i)=Alpha_0*exp(-Q_alpha/(R_gaz*Temperature(i)));

    %Precipitation due to initial concentration
    if Hss(i)>TSSptable(i)
        Hp(i)=Hss(i)-TSSptable(i);
        Hss(i)=TSSptable(i);
    end

   %create x table
   x_table(i)= slab_length*( i-1)/(n_cell-1);
end

%Theory
th_sol=zeros(1,n_cell);
xint=linspace(0,slab_length,n_cell);
yint=exp(Q_star./(R_gaz.*(TmaxK-(x_table)*(TmaxK-TminK)/slab_length)));
integral=trapz(xint,yint);
C_0=C_ini*slab_length/integral;

% C_0
for k=1:1:n_cell
    th_sol(k)=C_0*exp(Q_star/R_gaz/Temperature(k));
end
th_sol


% Time step loop
for t=0:delta_t:end_time;
    %Temperature update
     Temperature=Temperature_ini+ t/end_time*(Temperature_end-Temperature_ini);
```

```
    %Parameters update
    for u=1:1:n_cell;

        %Update TSS for each cell
        TSSptable(u)=TSSp(Temperature(u));
        TSSdtable(u)=TSSd(Temperature(u));

        %Update diffusion coefficient for each cell
        Dtable(u)=D_0*exp(-Q_diff/(R_gaz*Temperature(u)));
        %Update alpha coefficient for each cell
        alpha_table(u)=Alpha_0*exp(-Q_alpha/(R_gaz*Temperature(u)));
    end

    % Flux calculation
    for f=2:1:n_cell
        Flux_left(f)=-           (Dtable(f)*(Hss(f)-Hss(f-1))/delta_x           +
Dtable(f)*Hss(f)*Q_star/(R_gaz*Temperature(f)^2)*(Temperature(f)-Temperature(f-
1))/delta_x);
    end

    %Net flux and precipitation/dissolution loop
    for j=1:1:n_cell;
        %Net flux (grad J)
        gradJ=(Flux_left(j+1)-Flux_left(j))/delta_x;

        %Precipitation
        if Hss(j)>TSSptable(j)
            Hp(j)=Hp(j)+alpha_table(i)*alpha_table(i)*(Hss(j)-
TSSptable(j))*delta_t;
            Hss(j)=Hss(j)-delta_t*(alpha_table(i)*alpha_table(i)*(Hss(j)-
TSSptable(j))+gradJ);
        end

        %Hysteresis case
        if       (Hss(j)<TSSptable(j)       &&       Hss(j)>TSSdtable(j))       ||
(Hss(j)==TSSdtable(j) && Hp(j)>0 && gradJ<0)
            Hp(j)=Hp(j);
            Hss(j)=Hss(j)-delta_t*gradJ;
        end

        %Dissolution
        if Hss(j)==TSSdtable(j) && Hp(j)>0 && gradJ>0
            Hss(j)=Hss(j);
            Hp(j)=Hp(j)-delta_t*gradJ;
        end

       %Under TSSd dissolution (should not happen excepted numerical exception)
        if Hss(j)<TSSdtable(j) && Hp(j)>0
            Hp(j)=Hp(j)-(TSSdtable(j)-Hss(j))-delta_t*gradJ;
            Hss(j)=TSSdtable(j);
        end

        %Only solid solution
        if Hss(j)<=TSSdtable(j) && Hp(j)<=0
            Hss(j)=Hss(j)-delta_t*gradJ;
            Hp(j)=Hp(j);
        end
    end
```

```
    % Update of final tables
      ts=ts+delta_t/3600 ;
     num_tstep=num_tstep+1;
     if ts>hoursstep
       HbyH_Hss(hoursstep/frq+1,:)=Hss;
       HbyH_Hp(hoursstep/frq+1,:)=Hp;
       HbyH_delta(hoursstep/frq+1,:)=th_sol-Hss;
       hoursstep=hoursstep+frq;
       HbyH_temperature(hoursstep/frq+1,:)=Temperature;
       ts
     end

     num_tstep=num_tstep+1;

end

%Plot results
plot(x_table,transpose(HbyH_Hss), x_table)
xlabel('x(cm)')
ylabel('In solid solution hydrogen concentration (wt ppm)')
DeltaH=Hss-th_sol
plot(x_table,transpose(HbyH_Hp), x_table, th_sol,'x', x_table, TSSptable,'+')
```

The code calls the following functions:

```
function [ TSSp ] = TSSp( T )
%TSSp: Calculation of the Terminal Solid Solubility for Hydrogen
%according to McMinn,   Temperature in Kelvin
    N_TSSp=138746;
    R_gaz=8.314;
    Q_TSSp=4145.72*R_gaz;
    TSSp=N_TSSp*exp(-Q_TSSp/(R_gaz*T));
end

function [ TSSd ] = TSSd( T )
%TSSd: Calculation of the Terminal Solid Solubility for Hydrogen
%according to McMinn,    Temperature in Kelvin
    N_TSSd=106446.7;
    R_gaz=8.314;
    Q_TSSd=4328.67*R_gaz;
    TSSd=N_TSSd*exp(-Q_TSSd/(R_gaz*T));
end
```

The following functions have been use for specific purpose (but not in the example above):

```
function [ oxidationHflux] = oxidationHflux( t,T,thickness_cm )
% Flux of hydrogen due to oxidation%   in ppm*cm/s

%thickness in um
thickness=thickness_cm*1e4;
time=t/24/3600;
delta_star=4.35*exp(-550/T);
Kc=535*exp(-4533/T);
Kl=8.1e6*exp(-12500/T);
t_star=(delta_star/Kc)^3;
f=0.15;
M_H=1;
M_Zr=91;
if time<t_star
    %rate in um/h
    delta_rate=delta_star/t_star;
    delta_ox=delta_rate*time;
else
    delta_rate=Kl;
    delta_ox=Kl*(time-t_star)+delta_star;
end
oxidationHflux=4*f/1.56*M_H/M_Zr*thickness^2/(thickness-delta_ox)^2*
delta_rate/1e4/24/3600*1e6;
end


function [ Hppm ] = Hppm_lin( t,T,thickness_cm )
% Total amount of hydrogen, after a given time/temperature/thickness
thickness=thickness_cm*1e4;
delta_star=4.35*exp(-550/T);
Kc=535*exp(-4533/T);
Kl=8.1e6*exp(-12500/T);
t_star=(delta_star/Kc)^3;
%Hydrogen pick up
f=0.15;
M_H=1;
M_Zr=91;
time=t/24/3600;
if time<t_star
     delta_rate=delta_star/t_star;
    delta_ox=delta_rate*time;
else
    delta_ox=Kl*(time-t_star)+delta_star;
end
Hppm=4*f/1.56*delta_ox/(thickness-delta_ox)*M_H/M_Zr*1e6;
end
```

Appendix B: BISON Kernels source code

- **Diffusion of hydrogen kernel**

HDiffusionOC.h

```
#ifndef HDIFFUSIONOC_H
#define HDIFFUSIONOC_H
#include "Kernel.h"
//Forward Declarations
class HDiffusionOC;
template<>
InputParameters validParams<HDiffusionOC>();
class HDiffusionOC : public Kernel
{
public:
  HDiffusionOC(const std::string & name, InputParameters parameters);
protected:
  virtual Real computeQpResidual();
  virtual Real computeQpJacobian();
private:
  VariableValue  & _temp;
  VariableGradient & _grad_temp;
};
#endif                                                          //HDiffusionOC.h
```

HDiffusionOC.C

```
#include "HDiffusionOC.h"
template<>
InputParameters validParams<HDiffusionOC>()
{
  InputParameters params = validParams<Kernel>();
  params.addRequiredCoupledVar("temp", "Coupled Temperature");
  return params;
}
HDiffusionOC::HDiffusionOC(const    std::string    &    name,    InputParameters
parameters)
  :Kernel(name, parameters),
   _temp(coupledValue("temp")),
   _grad_temp(coupledGradient("temp"))
[49]
Real
HDiffusionOC::computeQpResidual()
{
//Flux calculation
  Real Qstar  = 2.51e4;
  Real D_diff = 7.90e-7*exp(-4.49e4/8.3142/_temp[_qp]);
  RealGradient          hflux          =          -D_diff*(_grad_u[_qp]          +
_u[_qp]*Qstar/(8.3142*_temp[_qp]*_temp[_qp])*_grad_temp[_qp]);
  return -hflux*_grad_test[_i][_qp];
}
//Jocabian calculation
Real
HDiffusionOC::computeQpJacobian()
{
  Real Qstar  = 2.51e4;
  Real D_diff = 7.90e-7*exp(-4.49e4/8.3142/_temp[_qp]);
  RealGradient        hflux        =        -(D_diff*_grad_phi[_j][_qp]        +
D_diff*_phi[_j][_qp]*Qstar/(8.3142*_temp[_qp]*_temp[_qp])*_grad_temp[_qp]);
```

```
  return -hflux*_grad_test[_i][_qp];
}
```

- **Precipitation/Dissolution kernel (Solid Solution)**

CssPreOcn.h

```
#ifndef CssPreOCn_H
#define CssPreOCn_H
#include "Kernel.h"

//Forward Declarations
class CssPreOCn;
template<>
InputParameters validParams<CssPreOCn>();
class CssPreOCn : public Kernel
{
public:
  CssPreOCn(const std::string & name, InputParameters parameters);
protected:
  virtual Real computeQpResidual();
  virtual Real computeQpJacobian();
private:
  VariableValue  & _temp;
  VariableGradient & _grad_temp;
  VariableValue  & _Cp;
};
       #endif //CssPreOCn.h
```

CssPreOCn.C

```
#include "CssPreOCn.h"
template<>
InputParameters validParams<CssPreOCn>()
{
  InputParameters params = validParams<Kernel>();
  params.addRequiredCoupledVar("temp", "Coupled Temperature");
  params.addRequiredCoupledVar("Cp", "Hydride concentration");
  return params;
}
CssPreOCn::CssPreOCn(const std::string & name, InputParameters parameters)
  :Kernel(name, parameters),
   _temp(coupledValue("temp")),
   _grad_temp(coupledGradient("temp")),
   _Cp(coupledValue("Cp"))
{
 }
Real
CssPreOCn::computeQpResidual()
{
//Flux calculation
  Real Qstar  = 2.51e4;
  Real TSSp = 1.39e5*exp(-3.45e4/8.314/_temp[_qp]);
  Real TSSd = 1.06e5*exp(-3.60e4/8.314/_temp[_qp]);
  Real alpha_kin=62.3*exp(-4.12e4/8.314/_temp[_qp]);
  Real beta_kin=alpha_kin*alpha_kin;
  if (_u[_qp]>TSSp)
   return alpha_kin*alpha_kin*(_u[_qp]-TSSp)*_test[_i][_qp];
  else if ((_u[_qp]<TSSd) && (_Cp[_qp]>0))
   return -beta_kin*(TSSd-_u[_qp])*_test[_i][_qp];
  else
```

```
   return 0;

}
//Jacobian calculation
Real
CssPreOCn::computeQpJacobian()
{
  Real Qstar  = 2.51e4;

  Real TSSp = 1.39e5*exp(-3.45e4/8.314/_temp[_qp]);
  Real TSSd = 1.06e5*exp(-3.60e4/8.314/_temp[_qp]);
  Real alpha_kin=62.3*exp(-4.12e4/8.314/_temp[_qp]);
  Real beta_kin=alpha_kin*alpha_kin;
  if (_u[_qp]>TSSp)
   return alpha_kin*alpha_kin*_phi[_j][_qp]*_test[_i][_qp];
  else if ((_u[_qp]<TSSd) && (_Cp[_qp]>0))
   return beta_kin*_phi[_j][_qp]*_test[_i][_qp];
  else
  return 0;
}
```

- **Precipitation/Dissolution kernel (Hydrides)**

CpPreOcn.h

```
#ifndef CpPreOCn_H
#define CpPreOCn_H
#include "Kernel.h"

//Forward Declarations
class CpPreOCn;
template<>
InputParameters validParams<CpPreOCn>();
class CpPreOCn : public Kernel
{
public:
  CpPreOCn(const std::string & name, InputParameters parameters);
protected:
  virtual Real computeQpResidual();
private:
  VariableValue  & _temp;
  VariableGradient & _grad_temp;
  VariableValue & _Css;
};
#endif //CpPreOCn.h
```

CpPreOcn.C

```
#include "CpPreOCn.h"
template<>
InputParameters validParams<CpPreOCn>()
{
  InputParameters params = validParams<Kernel>();
  params.addRequiredCoupledVar("temp", "Coupled Temperature");
  params.addRequiredCoupledVar("Css",     "Hydrogen     in     solid     solution
concentration");
  return params;
}
CpPreOCn::CpPreOCn(const std::string & name, InputParameters parameters)
  :Kernel(name, parameters),
```

```
    _temp(coupledValue("temp")),
    _grad_temp(coupledGradient("temp")),
    _Css(coupledValue("Css"))
{
}
Real
CpPreOCn::computeQpResidual()
{
//Flux calculation
  Real Qstar  = 2.51e4;

  Real TSSp = 1.39e5*exp(-3.45e4/8.314/_temp[_qp]);
  Real TSSd = 1.06e5*exp(-3.60e4/8.314/_temp[_qp]);
  Real alpha_kin=62.3*exp(-4.12e4/8.314/_temp[_qp]);
  Real beta_kin=alpha_kin*alpha_kin;
  if (_Css[_qp]>TSSp)
   return -alpha_kin*alpha_kin*(_Css[_qp]-TSSp)*_test[_i][_qp];
  else if ((_Css[_qp]<TSSd) && (_u[_qp]>0))
   return beta_kin*(TSSd-_Css[_qp])*_test[_i][_qp];
  else
   return 0;
}
```

Appendix C: BISON Auxiliary Kernel source code

CpPreOCnAux.h

```
#ifndef CpPreOCnAux_H
#define CpPreOCnAux_H
#include "AuxKernel.h"
class CpPreOCnAux : public AuxKernel
{
public:
  CpPreOCnAux(const std::string & name, InputParameters parameters);
  virtual ~CpPreOCnAux() {}
protected:
  virtual Real computeValue();
private:
  VariableValue  & _temp;
  VariableValue & _Css;
};
template<>
InputParameters validParams<CpPreOCnAux>();
#endif //CpPreOCnAux.h
```

CpPreOCnAux.C

```
#include "CpPreOCnAux.h"

template<>
InputParameters validParams<CpPreOCnAux>()
{
  InputParameters params = validParams<AuxKernel>();
  params.addRequiredCoupledVar("temp", "Coupled Temperature");
  params.addRequiredCoupledVar("Css",     "Hydrogen     in     solid     solution
concentration");
  return params;
}
CpPreOCnAux::CpPreOCnAux(const std::string & name, InputParameters parameters)
  :AuxKernel(name, parameters),
   _temp(coupledValue("temp")),
   _Css(coupledValue("Css"))
{
}
Real
CpPreOCnAux::computeValue()
{
//Flux calculation
  Real Qstar  = 2.51e4;
  Real TSSp = 1.39e5*exp(-3.45e4/8.314/_temp[_qp]);
  Real TSSd = 1.06e5*exp(-3.60e4/8.314/_temp[_qp]);
  Real alpha_kin=62.3*exp(-4.12e4/8.314/_temp[_qp]);
  Real beta_kin=alpha_kin*alpha_kin;
  Real value = _u_old[_qp];

  if (_Css[_qp]>TSSp)
  {
    value -= _dt * beta_kin*(TSSp-_Css[_qp]);
  }
  else if ((_Css[_qp]<TSSd) && (_u[_qp]>0))
  {
    value -= _dt * beta_kin*(TSSd-_Css[_qp]);
```

```
  }
  return value; }
```

Appendix D: Hydrogen picked up flux BISON boundary condition

HydrogenFluxBC.h

```
#ifndef HydrogenFluxBC_H
#define HydrogenFluxBC_H
#include "IntegratedBC.h"


//Forward Declarations
class HydrogenFluxBC;

template<>
InputParameters validParams<HydrogenFluxBC>();

class HydrogenFluxBC : public IntegratedBC
{
public:
  HydrogenFluxBC(const std::string & name, InputParameters parameters);
  virtual ~HydrogenFluxBC(){}

protected:
  virtual Real computeQpResidual();
  VariableValue & _temp;
};
#endif //HydrogenFluxBC_H
```

HydrogenFluxBC.C

```
#include "HydrogenFluxBC.h"

template<>
InputParameters validParams<HydrogenFluxBC>()
{
  InputParameters params = validParams<IntegratedBC>();
  params.addRequiredCoupledVar("temp", "Coupled Temperature");
  params.addParam<Real>("value", 0.0, "the value of the flux on the
boundary");
  return params;
}

HydrogenFluxBC::HydrogenFluxBC(const std::string & name,
InputParameters parameters)
  :IntegratedBC(name, parameters),
   _temp(coupledValue("temp"))
{
}
```

```
Real
HydrogenFluxBC::computeQpResidual()
{
  Real R_gas=8.314;
//Cubic Kinetics
  Real A_Kc=535;
  Real Q_Kc=37687.36;
  Real Kc=A_Kc*exp(-Q_Kc/R_gas/_temp[_qp]);

//linear Kinetics
  Real A_Kl=8.1e6;
  Real Q_Kl=103925;
  Real K_l=A_Kl*exp(-Q_Kl/R_gas/_temp[_qp]); //um/d

//transition
  Real delta_star=4.35*exp(-550/_temp[_qp]); //um

//other
  Real pickup=0.15;
  Real oxide_Zr_ratio=1; //(no oxidation model)
  Real big_ratio=1.56; //ratio of density and molar masses
  Real H_sto=4; //stoechiometric ratio
  Real H_mass=1;
  Real Zr_mass=91;

 Real    flux=H_sto/big_ratio*H_mass/Zr_mass*oxide_Zr_ratio*K_l;    //in
millions of wt.ppm*um/days <=> wt.ppm*m/days
 Real fluxSI=flux/3600/24;
  return -_test[_i][_qp]*fluxSI;
}
```

Appendix E: Input files for the BISON piece of cladding runs

- Case 1: First 23 days input file (Case 1 and 2 otherinput files are very similar and not reproduced)

```
[GlobalParams]
  # Set initial fuel density, other global parameters
  order = FIRST
  family = LAGRANGE
[]

[Problem]
  # Specify coordinate system type
[]

[Mesh]
  file = plate_test_7.e
 # displacements = 'disp_x disp_y disp_z'
  patch_size = 1000 # For contact algorithm
[]

[Variables]
  # Define dependent variables and initial conditions
  [./temp]

    [./InitialCondition]
     block=100
     function=toto
     type=FunctionIC
     variable=temp
    [../]
  [../]
  [./Css]
    initial_condition=0
    block=100
    scaling=1e6
  [../]
[]

[AuxVariables]
  [./Cp]
    initial_condition=0
    block=100
  [../]
[]

[Functions]
  [./toto]
    type = PiecewiseLinear
    axis=1
    x = '-0.00033 0.00033'
    y = '593 633'
```

```
  [../]
[]

[SolidMechanics]
[]

[Kernels]
  # Define kernels for the various terms in the PDE system
   [./time_temp]
     type=TimeDerivative
     variable=temp
     block=100
   [../]
  [./hdiffusion] # diffusion of hydrogen by OC
    type = HydrogenDiffusion
    variable = Css
    block=100
    temp=temp
  [../]
  [./csspre] # precipitation/dissolution of hydrogen by OC (for
solid solution)
    type = HydrogenPrecipitation
    variable = Css
    block=100
    temp=temp
    Cp=Cp
  [../]
  [./csstimeder] #time derivative of Css
    type=TimeDerivative
    variable = Css
    block=100
  [../]
[]

[Burnup]
[]

[AuxKernels]
  # Define auxilliary kernels for each of the aux variables

  [./cppre] # precipitation/dissolution of hydrogen by OC (for
hydrides)
    type = HydridePrecipitationAux
    variable = Cp
    block=100
    temp=temp
    Css=Css
    execute_on = residual
  [../]
[]

[AuxBCs]
[]

[Contact]
```

```
[]

[ThermalContact]
[]

[BCs]
# Define boundary conditions

  [./noCssinflux]
   # Infinite plate
    boundary= ' 20 30 40 50 60'
    type=NeumannBC
    value=0  #no incoming flux
    variable=Css
  [../]
  [./Hydrogen_influx] #calculated from oxide equation at 320 C
    boundary = '10'
    type=HydrogenFluxBC
    temp=temp
    variable=Css
  [../]
[]

[CoolantChannel]
[]

[Materials]
  # Define material behavior models and input material property data

  [./clad_thermal]                        # general thermal property
input (elk kernel)
    type = HeatConductionMaterial
    block = 100
    thermal_conductivity = 16.0
    specific_heat = 330.0
  [../]

  [./clad_density]
    type = Density
    block = 100
    density = 6551.0
  [../]

[]


[Executioner]

  type = AdaptiveTransient

  petsc_options = '-snes_mf_operator -ksp_monitor -
ksp_gmres_modifiedgramschmidt'
  petsc_options_iname = '-snes_type -snes_ls -ksp_gmres_restart -
pc_type  -sub_0_pc_hypre_type -sub_0_pc_hypre_boomeramg_max_iter -
```

```
sub_0_pc_hypre_boomeramg_grid_sweeps_all -sub_1_sub_pc_type -
pc_composite_type -ksp_type -mat_mffd_type'
  petsc_options_value = 'ls         basic   201
hypre         boomeramg            2
2                                        lu
multiplicative     fgmres    ds'

  l_max_its = 100
  l_tol = 8e-3
  nl_max_its = 15
  nl_rel_tol = 1e-6
  nl_abs_tol = 1e-13
  start_time = 0.0
  dt = 10
  end_time = 2e6
  num_steps = 50000000
  dtmax = 200
  dtmin = 1
  optimal_iterations = 60
  iteration_window = 0.4
  linear_iteration_ratio = 100
[]

[Postprocessors]
  # Define postprocessors (some are required as specified above;
others are optional; many others are available)
  [./_dt]                     # time step
    type = PrintDT
  [../]
  [./nonlinear_its]           # number of nonlinear iterations at
each timestep
    type = PrintNumNonlinearIters
  [../]
   []

[Output]
  # Define output file(s)

  interval = 1000
  output_initial = true
  exodus = true
  perf_log = true
  max_pps_rows_screen = 25
[]
```

- Case 3: Shutdown input file

```
[GlobalParams]
  order = FIRST
  family = LAGRANGE
[]

[Problem]
[]

[Mesh]
  file = plate_test_7.e
  patch_size = 1000 # For contact algorithm
[]

[Variables]
  [./temp]
    [./InitialCondition]
     block=100
     function=temp_ini
     type=FunctionIC
     variable=temp
    [../]
  [../]
  [./Css]
    initial_condition=120
    block=100
    scaling=1e6
  [../]
[]

[AuxVariables]
  [./Cp]
    initial_condition=0
    block=100
  [../]
[]

[Functions]
  [./temp_ini]
    type = PiecewiseLinear
    axis=1
    x = '-0.00033 0.00033'
    y = '593 633'
  [../]

  [./lowT_func]
    type = PiecewiseLinear
    x = '0 2e5 2.864e5 3e5'
    y = '593 593 293 293'
  [../]

  [./highT_func]
    type = PiecewiseLinear
```

```
    x = '0   1.9988e5 2e5  2.001e5  2.01e5  2.1e5  2.5e5  2.7e5
2.864e5 3e5'
    y = '633 633      595  594      590     559    420    350
293     293'
  [../]
[]

[SolidMechanics]
[]

[Kernels]
   [./heat]         # gradient term in heat conduction equation
     type = HeatConduction
     variable = temp
   [../]
   [./heat_ie]       # time term in heat conduction equation
      type = HeatConductionImplicitEuler
      variable = temp
   [../]
   [./time_temp]
     type=TimeDerivative
     variable=temp
     block=100
   [../]
   [./hdiffusion] # diffusion of hydrogen by OC
     type = HydrogenDiffusion
     variable = Css
     block=100
     temp=temp
   [../]
   [./csspre] # precipitation/dissolution of hydrogen by OC (for
solid solution)
     type = HydrogenPrecipitation
     variable = Css
     block=100
    temp=temp
     Cp=Cp
   [../]
   [./csstimeder] #time derivative of Css
     type=TimeDerivative
     variable = Css
     block=100
   [../]
[]

[Burnup]
[]

[AuxKernels]
  [./cppre] # precipitation/dissolution of hydrogen by OC (for
hydrides)
    type = CpPreOCnAux
    variable = Cp
    block=100
    temp=temp
```

```
    Css=Css
    execute_on = residual
  [../]
[]

[AuxBCs]
[]

[Contact]
[]

[ThermalContact]
[]

[BCs]
# Define boundary conditions
  [./noCssinflux]
   # Infinite plate
    boundary= ' 20 30 40 50 60'
    type=NeumannBC
    value=0  #no incoming flux
    variable=Css
  [../]
[./adiabT]
  boundary= '30 40  50 60'
   type=NeumannBC
   value=0 #adiabatic
   variable=temp
[../]
  [./hotT]
    boundary= '20'
    type=FunctionDirichletBC
    function=lowT_func
    variable=temp
  [../]
  [./lowT]
    boundary= '10'
    type=FunctionDirichletBC
    function=highT_func
    variable=temp
  [../]
  [./Hydrogen_influx]
    boundary = '10'
    type=HydrogenFluxBC
    temp=temp
    variable=Css
  [../]
[]

[CoolantChannel]
[]

[Materials]
   [./clad_thermal]                        # general thermal property
    type = HeatConductionMaterial
```

```
    block = 100
    thermal_conductivity = 16.0
    specific_heat = 330.0
  [../]
  [./clad_density]
    type = Density
    block = 100
    density = 6551.0
  [../]
[]

[Executioner]
    type = AdaptiveTransient
  petsc_options = '-snes_mf_operator -ksp_monitor -
ksp_gmres_modifiedgramschmidt'
  petsc_options_iname = '-snes_type -snes_ls -ksp_gmres_restart -
pc_type  -sub_0_pc_hypre_type -sub_0_pc_hypre_boomeramg_max_iter -
sub_0_pc_hypre_boomeramg_grid_sweeps_all -sub_1_sub_pc_type -
pc_composite_type -ksp_type -mat_mffd_type'
  petsc_options_value = 'ls         basic   201
hypre         boomeramg            2
2                                          lu
multiplicative     fgmres    ds'

  l_max_its = 100
  l_tol = 8e-3
  nl_max_its = 15
  nl_rel_tol = 1e-6
  nl_abs_tol = 1e-11
  start_time = 0.0
  dt = 10
  end_time = 5e5
  num_steps = 50000000
  dtmax = 200
  dtmin = 1
  optimal_iterations = 60
  iteration_window = 0.4
  linear_iteration_ratio = 100
[]
[Postprocessors]
  [./_dt]                     # time step
    type = PrintDT
  [../]
  [./nonlinear_its]           # number of nonlinear iterations at
each timestep
    type = PrintNumNonlinearIters
  [../]
[]
[Output]
  interval = 10
  output_initial = true
  exodus = true
  perf_log = true
  max_pps_rows_screen = 25
[]
```

Appendix F: Rough estimation of the axial diffusion flux through a full fuel rod

In the five pellet geometries, only the radial flux of hydrogen (after it is picked up by the cladding) is really accounted for. In reality, an axial flux is also possible due to the variation in axial temperature of the 360-pellet fuel rod, as seen in Figure A-1.

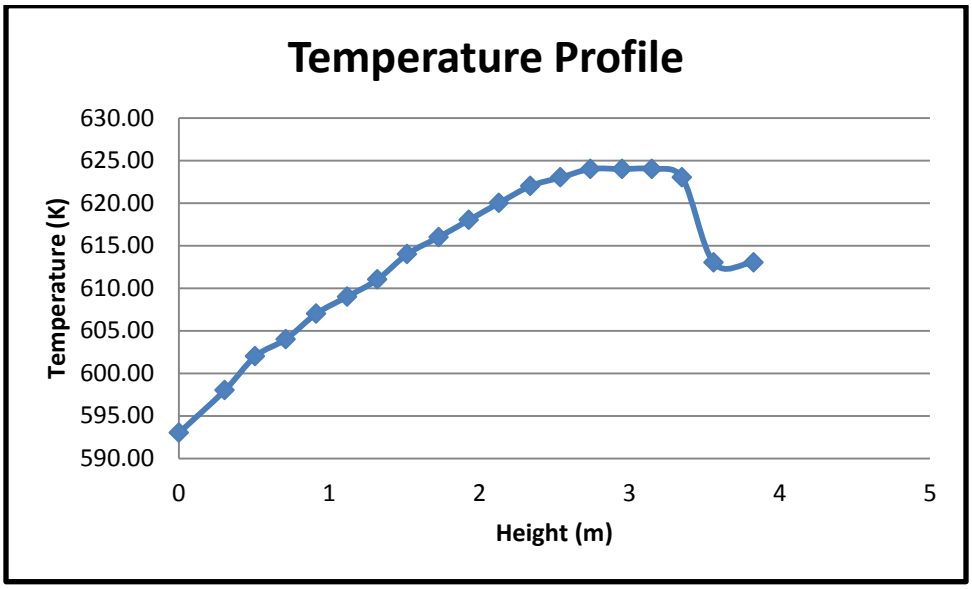

Figure A-1 - Axial Temperature profile of the cladding

The approximate axial flux is equal to:

$$J_{ax} = \frac{\Delta C_{ss}}{\Delta t} * L \qquad \text{A-1}$$

In this instance, ΔC is the change in concentration, Δt is the change in time, and L is the length where the flux is applied.

In order to find ΔC, two concentration points are needed. For this purpose the initial concentration (C_i) at t_i=0, the final concentrations (C_f) and the end time (t_f) have to be identified. C_i was found using the oxide model as defined in section 1.3.1. The variables in that equation largely depend on temperature, so the temperature profile of the entire rod was used to generate

the correct variable values at the given time. The result, shown in Figure A-2 mirrors the temperature profile.

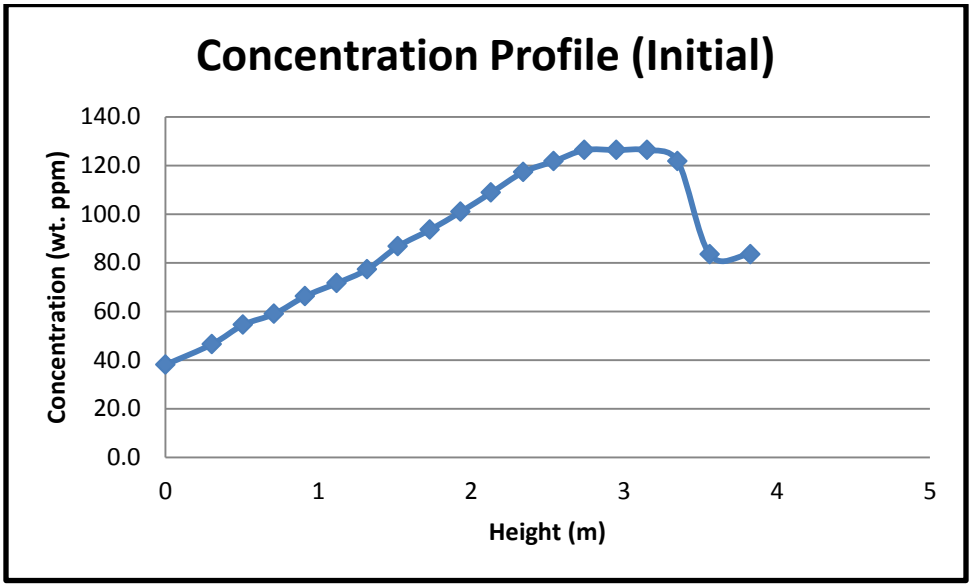

Figure A-2 - Initial Axial Concentration Profile

Once C_i was found, it had to be compared with C_f, which was based on the concentration predicted by the Soret Effect at t_f, using the derivation shown in section 1.4.3.3. The resulting profile is shown in Figure A-3

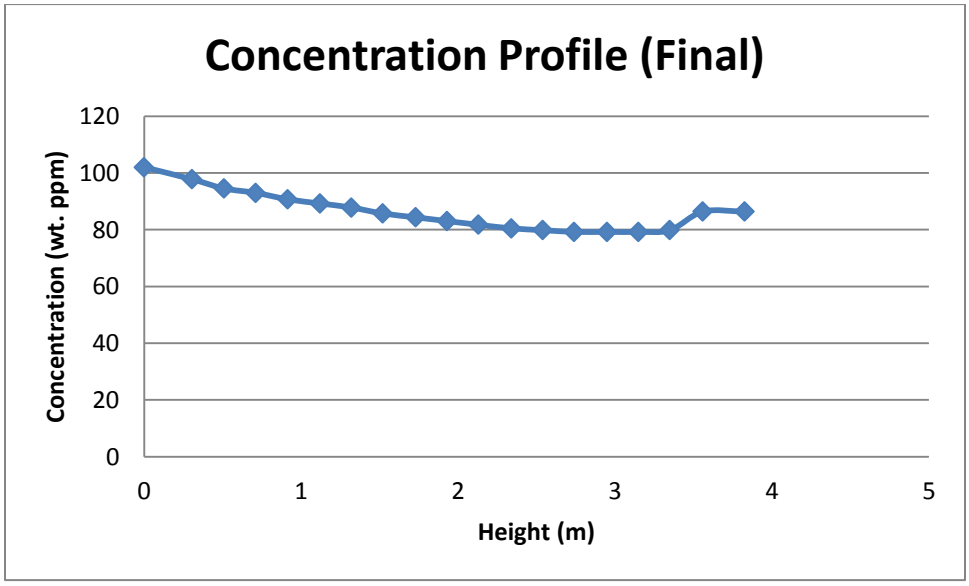

Figure A-3 - Final Axial Concentration Profile

Finally, a five-pellet section was selected for examination (from height = 0.00226 m to height = 0.053 m). Based on linear extrapolations, values for C_i and C_f were found at a height of 0.053 m to calculate the flux at the top of the selection. In this case, t_f was selected as 4 years, and L was the length of the 5 pellet model (approximately 0.5 cm). This led to a result of J_{ax}=2.23e-8 wt.ppm*m/s for the flux and a maximum radially average hydrogen concentration of 102 wt.ppm. at the bottom of the fuel cladding.

Appendix G: Derivation of the analytical rim calculation

The equation to be solved is:

$$D\frac{d^2C_{ss}}{dx^2} - \alpha^2 C_{ss} = \alpha^2 \cdot TSS \qquad \text{A-2}$$

In order to simplify the writing of the equations, **C_{ss} will be written C** in this Appendix.

The TSS is governed by an Arrhenius law, as described in equation A-3.

$$TSS = S * \exp(-\frac{Q}{RT}) \qquad \text{A-3}$$

Where S is the pre-exponential factor and Q is the heat of precipitation.

The parameter λ is defined as:

$$\lambda = \sqrt{\frac{\alpha^2}{D}} \qquad \text{A-4}$$

In order two solve the equation, it is needed to first solve the homogeneous form, and then to add the particular solution. The particular solution is found using what is called "the variation of parameter method". [86]

The homogeneous form of the equation A-2 is:

$$\frac{d^2C}{dx^2} - \lambda^2 C = 0 \qquad \text{A-5}$$

The general solution is:

$$C(x) = A * \cosh(\lambda x) + B * \sinh(\lambda x) \qquad \text{A-6}$$

- **We apply the variation of parameter method to find the solution:**

We call C_0 the particular solution of the equation A-2

$$C_0(x) = A(x) * \cosh(\lambda x) + B(x) * \sinh(\lambda x) \qquad \text{A-7}$$

Assuming:

$$A'(x)\cosh(\lambda x) + B'(x)\sinh(\lambda x) = 0 \qquad \text{A-8}$$

Then,

$$C_0'^{(x)} = A'^{(x)} * \cosh(\lambda x) + A(x) * \lambda \sinh(\lambda x) + B'(x) * \sinh(\lambda x) + B(x) * \lambda \cosh(\lambda x) \quad \textbf{A-9}$$

So,

$$C_0'^{(x)} = A(x) * \lambda \sinh(\lambda x) + B(x) * \lambda \cosh(\lambda x) \quad \textbf{A-10}$$

And

$$C''^{(x)}_0 = A'(x) * \lambda \sinh(\lambda x) + B'(x) * \lambda \cosh(\lambda x) + A(x) * \lambda^2 \cosh(\lambda x) + B(x) * \lambda^2 \sinh(\lambda x) \quad \textbf{A-11}$$

So,

$$\frac{d^2C}{dx^2} - \lambda^2 C = TSS \quad \textbf{A-12}$$

Becomes:

$$A'(x) * \lambda \sinh(\lambda x) + B'(x) * \lambda \cosh(\lambda x) = TSS \quad \textbf{A-13}$$

The following linear system is obtained:

$$A'(x) * \lambda \sinh(\lambda x) + B'(x) * \lambda \cosh(\lambda x) = TSS \quad \textbf{A-14}$$

$$A'(x) \cosh(\lambda x) + B'(x) \sinh(\lambda x) = 0 \quad \textbf{A-15}$$

So,

$$-\frac{B'(x) \sinh(\lambda x)}{\cosh(\lambda x)} * \lambda \sinh(\lambda x) + B'(x) * \lambda \cosh(\lambda x) = TSS \quad \textbf{A-16}$$

$$B'(x)\lambda \left(\frac{-\sinh^2(\lambda x) + \cosh^2(\lambda x)}{\cosh(\lambda x)} \right) = TSS \quad \textbf{A-17}$$

i.e.

$$B'(x) = \frac{TSS}{\lambda} * \cosh(\lambda x) \quad \textbf{A-18}$$

$$B'(x) = \frac{S}{\lambda} * \exp(-\frac{Q}{RT}) * \cosh(\lambda x) \quad \textbf{A-19}$$

Assuming a linear distribution of temperature:

$$T(x) = T_0 + \tau * x \qquad \textbf{A-20}$$

Where T_0 is the lower temperature and τ is the temperature gradient

So,

$$B'(x) = \frac{S}{\lambda} * \exp(-\frac{1}{\frac{R}{Q} * (T_0 + \tau * x)}) * \cosh(\lambda x) \qquad \textbf{A-21}$$

$$B'(x) = \frac{S}{\lambda} * \exp(-\frac{1}{\frac{R}{Q} * (T_0 + \tau * x)}) * \frac{\exp(\mathrm{x}) + \exp(-\mathrm{x})}{2} \qquad \textbf{A-22}$$

Using the linearity,

$$B(x) = B_1(x) + B_2(x) \qquad \textbf{A-23}$$

With:

$$B'_1(x) = \frac{S}{\lambda} * \exp(-\frac{1}{\frac{R}{Q} * (T_0 + \tau * x)}) * \frac{\exp(\mathrm{x})}{2} \qquad \textbf{A-24}$$

$$B'_2(x) = \frac{S}{\lambda} * \exp(-\frac{1}{\frac{R}{Q} * (T_0 + \tau * x)}) * \frac{\exp(-\mathrm{x})}{2} \qquad \textbf{A-25}$$

The following equations have to be solved:

$$B'_1(x) = \frac{S}{2\lambda} * \exp\left(-\frac{1}{\frac{R}{Q} * (T_0 + \tau * x)} + x\right) \qquad \textbf{A-26}$$

$$B'_1(x) = \frac{S}{2\lambda} * \exp\left(-\frac{1 + x * \frac{R}{Q} T_0 + x^2 * \frac{R}{Q}\tau}{\frac{R}{Q} T_0 + \frac{R}{Q}\tau * x}\right) \qquad \textbf{A-27}$$

Reorganizing:

$$B'_1(x) = \frac{S}{2\lambda} * \exp\left(-\frac{x^2 * \frac{R}{Q}\tau + x * \frac{R}{Q} T_0 + 1}{\frac{R}{Q}\tau * x + \frac{R}{Q} T_0}\right) \qquad \textbf{A-28}$$

Similarly,

$$B'_2(x) = \frac{S}{2\lambda} * \exp\left(-\frac{-x^2 * \frac{R}{Q}\tau - x * \frac{R}{Q}T_0 + 1}{\frac{R}{Q}\tau * x + \frac{R}{Q}T_0}\right) \quad \textbf{A-29}$$

This equation cannot be integrated using usual functions. We propose to solve the problem by simplifying the TSS expression.

$$TSS = \frac{S}{2\lambda} * \exp(-\frac{Q}{R * (T_0 + \tau * x)}) \quad \textbf{A-30}$$

This can be rewritten as:

$$TSS = \frac{S}{2\lambda} * \exp(-\frac{Q}{RT_0} * \frac{1}{1 + \frac{\tau}{T_0} * x}) \quad \textbf{A-31}$$

Experimentally,

$$\frac{\tau}{T_0} * x \ll 1 \quad \textbf{A-32}$$

Using a Taylor development, we can rewrite:

$$\frac{1}{1 + \frac{\tau}{T_0} * x} = 1 - \frac{\tau}{T_0} * x + \left(\frac{\tau}{T_0} * x\right)^2 \quad \textbf{A-33}$$

And the TSS becomes:

$$TSS \approx S * \exp\left[-\frac{Q}{RT_0} * \left(1 - \frac{\tau}{T_0} * x + \left(\frac{\tau}{T_0} * x\right)^2\right)\right] \quad \textbf{A-34}$$

Table Table A-1 shows the typical values for the TSS and the approximation between 320°C and 360°C

Temperature (°C)	SSS	Approx TSS
320.0	127.7	127.7
323.3	132.7	132.7
326.7	138.0	138.0
330.0	143.3	143.3
333.3	148.9	148.9
336.7	154.5	154.5
340.0	160.4	160.3
343.3	166.3	166.3
346.7	172.5	172.4
350.0	178.7	178.6
353.3	185.2	185.0
356.7	191.8	191.5
360.0	198.6	198.2

Table A-1: Approximation of the TSS

Recalling:

$$B'(x) = TSS * \cosh(\lambda x) \qquad \textbf{A-35}$$

In the next equations, we use the approximation for the TSS. We have:

$$B'(x) = \frac{S}{2\lambda} * \exp\left[-\frac{Q}{RT_0} * \left(1 - \frac{\tau}{T_0} * x + \left(\frac{\tau}{T_0} * x\right)^2\right)\right] * \frac{\exp(\lambda x) + \exp(-\lambda x)}{2} \qquad \textbf{A-36}$$

Dividing the equation in two parts, we get:

$$B_1'(x) = \frac{S}{2\lambda} * \exp\left[-\frac{Q}{RT_0} * \left(1 - \frac{\tau}{T_0} * x + \left(\frac{\tau}{T_0} * x\right)^2\right) + \lambda x\right] \qquad \textbf{A-37}$$

$$B_1'(x) = \frac{S}{2\lambda} * \exp\left[-\frac{Q}{RT_0} * \left(1 - \left(\frac{\tau}{T_0} + \frac{RT_0}{Q}\lambda\right) * x + \left(\frac{\tau}{T_0} * x\right)^2\right)\right] \qquad \textbf{A-38}$$

$$B_1'(x) = \frac{S}{2\lambda} * \exp\left[-\frac{Q}{RT_0} + \left(\frac{\tau}{T_0}\frac{Q}{RT_0} + \lambda\right) * x - \left(\frac{\tau}{T_0}\frac{Q}{RT_0} * x\right)^2\right] \qquad \textbf{A-39}$$

We call:

$$a_1 = -\left(\frac{\tau}{T_0^2}\frac{Q}{R}\right)^2 \quad \textbf{A-40}$$

$$a_2 = \left(\frac{\tau}{T_0^2}\frac{Q}{R} + \lambda\right) \quad \textbf{A-41}$$

$$a_3 = -\frac{Q}{RT_0} \quad \textbf{A-42}$$

We get:

$$B_1'(x) = \frac{S}{2\lambda} * \exp(a_1 x^2 + a_2 x + a_3) \quad \textbf{A-43}$$

The B function cannot be written with usual function. Thus we have to use the expansion with only 2 terms:

$$B_1'(x) = \frac{S}{2\lambda} * \exp(a_2 x + a_3) \quad \textbf{A-44}$$

Then,

$$B_1(x) = \frac{S}{2\lambda a_2}\exp(a_2 x + a_3) + cst \quad \textbf{A-45}$$

Similarly,

$$B_2'(x) = S * \exp\left[-\frac{Q}{RT_0} * \left(1 - \frac{\tau}{T_0} * x\right) - \lambda x\right] \quad \textbf{A-46}$$

We call:

$$b_2 = \left(\frac{\tau}{T_0^2}\frac{Q}{R} - \lambda\right) \quad \textbf{A-47}$$

$$b_3 = \frac{-Q}{RT_0} \quad \textbf{A-48}$$

We can notice that $b_3 = a_3$

We get:

$$B_2'(x) = S * \exp(b_2 x + b_3) \quad \textbf{A-49}$$

Finally,

$$B_2(x) = \frac{S}{2b_2}\exp(b_2 x + b_3) + cst \quad \textbf{A-50}$$

And

$$B(x) = \frac{S}{2b_2} * \exp(b_2 x + a_3) + \frac{S}{2a_2}\exp(a_2 x + a_3) + cst \quad \textbf{A-51}$$

- **We do a similar calculation for A(x):**

Recalling the system**:**

$$A'(x) * \lambda \sinh(\lambda x) + B'(x) * \lambda \cosh(\lambda x) = TSS \quad \textbf{A-52}$$

$$A'(x)\cosh(\lambda x) + B'(x)\sinh(\lambda x) = 0 \quad \textbf{A-53}$$

So,

$$A'(x) * \lambda \sinh(\lambda x) - A'(x) * \lambda \frac{\cosh^2(\lambda x)}{\sinh(\lambda x)} = TSS \quad \textbf{A-54}$$

$$A'(x)\lambda\left(\frac{\sinh^2(\lambda x) - \cosh^2(\lambda x)}{\sinh(\lambda x)}\right) = TSS \quad \textbf{A-55}$$

Id est,

$$A'(x) = -\frac{TSS}{\lambda} * \sinh(\lambda x) \quad \textbf{A-56}$$

$$A'(x) = -\frac{S}{\lambda} * \exp(-\frac{Q}{RT}) * \sinh(\lambda x) \quad \textbf{A-57}$$

Assuming a linear distribution of temperature, we have:

$$T(x) = T_0 + \tau * x \quad \textbf{A-58}$$

So,

$$A'(x) = -\frac{S}{\lambda} * \exp(-\frac{1}{\frac{R}{Q} * (T_0 + \tau * x)}) * \sinh(\lambda x) \quad \textbf{A-59}$$

$$A'(x) = -\frac{S}{\lambda} * \exp(-\frac{1}{\frac{R}{Q} * (T_0 + \tau * x)}) * \frac{\exp(\lambda x) - \exp(-\lambda x)}{2} \quad \textbf{A-60}$$

Using the linearity, we can set:

$$A(x) = A_1(x) - A_2(x) \quad \textbf{A-61}$$

With:

$$A'_1(x) = -\frac{S}{\lambda} * \exp(-\frac{1}{\frac{R}{Q} * (T_0 + \tau * x)}) * \frac{\exp(x)}{2} \quad \textbf{A-62}$$

$$A'_2(x) = -\frac{S}{\lambda} * \exp(-\frac{1}{\frac{R}{Q} * (T_0 + \tau * x)}) * \frac{\exp(-x)}{2} \quad \textbf{A-63}$$

We now have to solve both of the equations:

$$A'_1(x) = -\frac{S}{2\lambda} * \exp\left(-\frac{1}{\frac{R}{Q} * (T_0 + \tau * x)} + x\right) \quad \textbf{A-64}$$

$$A'_1(x) = -\frac{S}{2\lambda} * \exp\left(-\frac{1 + x * \frac{R}{Q} T_0 + x^2 * \frac{R}{Q} \tau}{\frac{R}{Q} T_0 + \frac{R}{Q} \tau * x}\right) \quad \textbf{A-65}$$

Reorganizing:

$$A'_1(x) = -\frac{S}{2\lambda} * \exp\left(-\frac{x^2 * \frac{R}{Q} \tau + x * \frac{R}{Q} T_0 + 1}{\frac{R}{Q} \tau * x + \frac{R}{Q} T_0}\right) \quad \textbf{A-66}$$

Similarly,

$$A'_2(x) = -\frac{S}{2\lambda} * \exp\left(-\frac{-x^2 * \frac{R}{Q} \tau - x * \frac{R}{Q} T_0 + 1}{\frac{R}{Q} \tau * x + \frac{R}{Q} T_0}\right) \quad \textbf{A-67}$$

This equation cannot be integrated using usual functions.

We propose to solve the problem by simplifying the TSS expression:

$$TSS = \frac{S}{2} * \exp(-\frac{Q}{R * (T_0 + \tau * x)}) \quad \textbf{A-68}$$

This can be rewritten as:

$$TSS = \frac{S}{2} * \exp(-\frac{Q}{RT_0} * \frac{1}{1 + \frac{\tau}{T_0} * x}) \quad \textbf{A-69}$$

Experimentally, we can show that $\frac{\tau}{T_0} * x \ll 1$

Using a Taylor development, we can rewrite:

$$\frac{1}{1 + \frac{\tau}{T_0} * x} = 1 - \frac{\tau}{T_0} * x + \left(\frac{\tau}{T_0} * x\right)^2 \quad \textbf{A-70}$$

We call:

$$a_1 = -\left(\frac{\tau}{T_0^2}\frac{Q}{R}\right)^2 \quad \textbf{A-71}$$

$$a_2 = \left(\frac{\tau}{T_0^2}\frac{Q}{R} + 1\right) \quad \textbf{A-72}$$

$$a_3 = -\frac{Q}{RT_0} \quad \textbf{A-73}$$

We get:

$$A(x) = -\frac{S}{2\lambda} * \exp(a_1 x^2 + a_2 x + a_3) \quad \textbf{A-74}$$

The A function cannot be written with usual function. Thus we have to use the expansion with only 2 terms:

$$A_1'(x) = -\frac{S}{2\lambda} * \exp(a_2 x + a_3) \quad \textbf{A-75}$$

Then,

$$A_1(x) = -\frac{S}{2\lambda a_2}\exp(a_2 x + a_3) + cst \qquad \textbf{A-76}$$

Similarly,

$$A_2'(x) = -S * \exp\left[-\frac{Q}{RT_0} * \left(1 - \frac{\tau}{T_0} * x\right) - x\right] \qquad \textbf{A-77}$$

We call:

$$b_2 = \left(\frac{\tau}{T_0^2}\frac{Q}{R} - 1\right) \qquad \textbf{A-78}$$

$$b_3 = \frac{-Q}{RT_0} \qquad \textbf{A-79}$$

We can notice that $b_3 = a_3$

We get:

$$A_2'(x) = -S * \exp(b_2 x + b_3) \qquad \textbf{A-80}$$

Finally,

$$A_2(x) = -\frac{S}{2b_2}\exp(b_2 x + b_3) + cst \qquad \textbf{A-81}$$

And

$$A(x) = -\frac{S}{2b_2} * \exp(b_2 x + a_3) + \frac{S}{2a_2}\exp(a_2 x + a_3) + cst' \qquad \textbf{A-82}$$

- **Final solution**

We know that:

$$C_0(x) = A(x) * \cosh(\lambda x) + B(x) * \sinh(\lambda x) \qquad \textbf{A-83}$$

Then,

$$C_0(x) = \left(-\frac{S}{2b_2} * \exp(b_2 x + a_3) + \frac{S}{2a_2}\exp(a_2 x + a_3) + cst\right)$$
$$* \cosh(\lambda x)$$
$$+ \left(\frac{S}{2b_2} * \exp(b_2 x + a_3) + \frac{S}{2a_2}\exp(a_2 x + a_3) + cst'\right) \quad \textbf{A-84}$$
$$* \sinh(\lambda x)$$

It can also be written as:

$$C_0(x) = \left(\frac{S}{2b_2} * \exp(b_2 x + a_3)\right) * (\sinh(\lambda x) - \cosh(\lambda x))$$
$$+ \left(\frac{S}{2a_2}\exp(a_2 x + a_3)\right) * (\sinh(\lambda x + cosh(\lambda x)) + cst \quad \textbf{A-85}$$
$$* \cosh(\lambda x) + cst' * \sinh(\lambda x)$$

- **Solution for a typical rim case**

There 2 areas. The first one has two phases, the second one only one. Since the second area is governed by Fick's law, we can assume it has a flat profile. Therefore the flux in the area is equal to 0. At the **moving** interface, the flux is equal to 0 (by continuity) and there is conservation of the hydrogen concentration. The coordinate of the moving boundary is called x0. In blue is plotted the shape of the concentration. The TSS is plotted in green

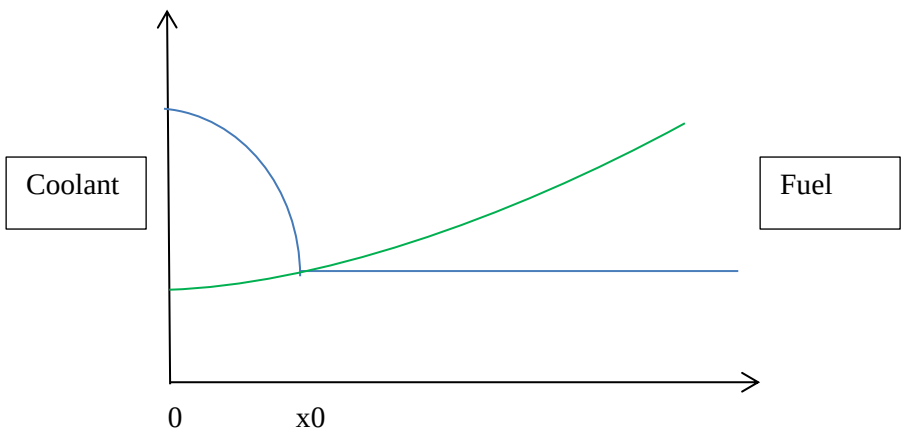

Figure A-4: Typical profile of the rim using the kinetics approach

Thus, we have the following boundary conditions:

The flux at the coolant/cladding interface is calculated from the oxidation rate and called J_0.

$$J(x=0) = J_0 \quad (oxidation * hydrogen\ pickup) \qquad \textbf{A-86}$$

The conditions at the interface are

$$J(x0) = 0\ (continuity\ of\ the\ flux) \qquad \textbf{A-87}$$

$$C(x0) = TSSp(x0) \qquad \textbf{A-88}$$

We use the continuity of the flux to find the value of x0:

We know that:

$$J = -D\nabla C \qquad \textbf{A-89}$$

So:

$$\frac{dC(x = x0)}{dx} = 0 \qquad \textbf{A-90}$$

$$0 = \frac{d}{dx}\left[\left(-\frac{S}{2b_2} * \exp(b_2x_0 + a_3) + \frac{S}{2a_2}\exp(a_2x_0 + a_3) + cst\right) * \cosh(\lambda x_0)\right.$$

$$+ \left(\frac{S}{2b_2} * \exp(b_2x_0 + a_3) + \frac{S}{2a_2}\exp(a_2x_0 + a_3) + cst'\right)$$

$$\left. * \sinh(\lambda x_0)\right]$$

$$= \frac{d}{dx}\left[\left(-\frac{S}{2b_2} * \exp(b_2x_0 + a_3) + \frac{S}{2a_2}\exp(a_2x_0 + a_3) + cst\right)\right. \qquad \textbf{A-91}$$

$$* \cosh(\lambda x_0)$$

$$+ \left(\frac{S}{2b_2} * \exp(b_2x_0 + a_3) + \frac{S}{2a_2}\exp(a_2x_0 + a_3) + cst'\right)$$

$$\left. * \sinh(\lambda x_0)\right]$$

$$0 = \left(-\frac{S}{2b_2} * \exp(b_2x_0 + a_3) + \frac{S}{2a_2}\exp(a_2x_0 + a_3) + cst\right) * \lambda \sinh(\lambda x_0)$$

$$+ \left(-\frac{S}{2} * \exp(b_2x_0 + a_3) + \frac{S}{2}\exp(a_2x_0 + a_3)\right) * \cosh(\lambda x_0)$$

$$+ \left(\frac{S}{2b_2} * \exp(b_2x_0 + a_3) + \frac{S}{2a_2}\exp(a_2x_0 + a_3) + cst'\right) * \lambda * \cosh(\lambda x_0)$$

$$+ \left(\frac{S}{2} * \exp(b_2x_0 + a_3) + \frac{S}{2}\exp(a_2x_0 + a_3)\right) * \sinh(\lambda x_0)$$

But also, J(x=0) =J0:

$$J0 = \left(-\frac{S}{2} * \exp(a_3) + \frac{S}{2}\exp(a_3)\right)$$

$$+ \left(\frac{S}{2b_2} * \exp(+a_3) + \frac{S}{2a_2}\exp(a_3) + cst'\right) \qquad \textbf{A-92}$$

$$* \lambda * \cosh(0)$$

So:

$$\frac{J0}{\lambda} = S\frac{\exp(a_3)}{2}(\frac{1}{b_2} + \frac{1}{a_2}) + cst' \qquad \textbf{A-93}$$

Then,

$$\frac{J0}{\lambda} - S\frac{\exp(a_3)}{2}(\frac{1}{b_2} + \frac{1}{a_2}) = cst' \qquad \textbf{A-94}$$

Recalling,

$$\alpha a_2 = \left(\frac{\tau}{T_0^2}\frac{Q}{R} + \lambda\right) \qquad \textbf{A-95}$$

$$b_2 = \left(\frac{\tau}{T_0^2}\frac{Q}{R} - \lambda\right) \qquad \textbf{A-96}$$

$$cst' = \frac{J0}{\lambda} - \mathrm{S} * \exp\left(-\frac{Q}{RT_0}\right)\left(\frac{\frac{\tau}{T_0^2}\frac{Q}{R}}{\left(\frac{\tau}{T_0^2}\frac{Q}{R}\right)^2 - \lambda^2}\right) \qquad \textbf{A-97}$$

Finally, the last equation gives:

$$\begin{aligned}\left(-\frac{S}{2b_2} * \exp(b_2x_0 + a_3) + \frac{S}{2a_2}\exp(a_2x_0 + a_3) + cst\right) * \cosh(\lambda x_0) \\ + \left(\frac{S}{2b_2} * \exp(b_2x_0 + a_3) + \frac{S}{2a_2}\exp(a_2x_0 + a_3)\right. \\ \left. + cst'\right) * \sinh(\lambda x_0) = TSSp(x_0)\end{aligned} \qquad \textbf{A-98}$$

$$\begin{aligned}\left(-\frac{S}{2b_2} * \exp(b_2x_0 + a_3) + \frac{S}{2a_2}\exp(a_2x_0 + a_3) + cst\right) * \cosh(\lambda x_0) \\ + \left(\frac{S}{2b_2} * \exp(b_2x_0 + a_3) + \frac{S}{2a_2}\exp(a_2x_0 + a_3)\right. \\ \left. + cst'\right) * \sinh(\lambda x_0) = S * \exp\left(-\frac{Q}{RT_0} * \left(1 - \frac{\tau}{T_0} * x\right)\right)\end{aligned} \qquad \textbf{A-99}$$

$$\left(-\frac{1}{2b_2} * \exp(b_2 x_0 + a_3) + \frac{1}{2a_2}\exp(a_2 x_0 + a_3) + cst\right) * \cosh(\lambda x_0)$$

$$+ \left(\frac{1}{2b_2} * \exp(b_2 x_0 + a_3) + \frac{1}{2a_2}\exp(a_2 x_0 + a_3)\right.$$

$$\left. + cst'\right) * \sinh(\lambda x_0) = \exp\left(-\frac{Q}{RT_0} * \left(1 - \frac{\tau}{T_0} * x\right)\right) \quad \textbf{A-100}$$

$$0 = \left(-\frac{S}{2b_2} * \exp(b_2 x_0 + a_3) + \frac{S}{2a_2}\exp(a_2 x_0 + a_3) + cst\right)$$

$$* \lambda \sinh(\lambda x_0)$$

$$+ \left(-\frac{S}{2} * \exp(b_2 x_0 + a_3) + \frac{S}{2}\exp(a_2 x_0 + a_3)\right)$$

$$* \cosh(\lambda x_0)$$

$$+ \left(\frac{S}{2b_2} * \exp(b_2 x_0 + a_3) + \frac{S}{2a_2}\exp(a_2 x_0 + a_3)\right. \quad \textbf{A-101}$$

$$\left. + cst'\right) * \lambda * \cosh(\lambda x_0)$$

$$+ \left(\frac{S}{2} * \exp(b_2 x_0 + a_3) + \frac{S}{2}\exp(a_2 x_0 + a_3)\right)$$

$$* \sinh(\lambda x_0)$$

Equation A-100 and A-101 cannot be solved analytically for x0.